



UNIVERSITÀ
degli STUDI
di CATANIA

DEPARTMENT OF CHEMISTRY
INTERNATIONAL PHD IN CHEMISTRY
XXXII CYCLE

Domenica Raciti

INTERACTIONS BETWEEN FLUCTUATING
AND SELF-RESHAPING SOFT BODIES:
FROM ELECTROSTATICS TO HYDRODYNAMICS

DOCTORAL DISSERTATION

SUPERVISOR:
PROFESSOR A. RAUDINO
UNIVERSITY OF CATANIA

ACADEMIC YEAR 2018/2019

Contents

I OVERVIEW OF THE PHD PROJECT	1
1 Introduction	2
1.1 Motivation	2
1.2 Objectives and overview of the research plan	3
1.3 Method	4
1.4 Originality and innovative aspects of the research	6
2 Overview of the thesis	7
II PRELIMINARY BACKGROUND	9
3 Capillary surfaces, bubbles and drops	10
3.1 Capillary surfaces	10
3.2 A quick overview	11
3.3 Stability of capillary interfaces	11
3.4 Capillary waves	13
4 "Bubble phenomenology"	15
4.1 Cavitation	15
4.2 Interacting bubbles	18
5 Biological background: from bubbles to cells	20
5.1 Cell membrane fluctuations	20
5.2 Mechanosensitivity of cell membranes	23

5.3	Intercellular coupling	24
5.4	From (hydrodynamic) interaction to (biochemical) synchronisation	26

III THEORETICAL BACKGROUND. FROM SINGLE TO INTERACTING BUBBLES 28

6	Theory of single oscillating bubbles 29
6.1	Background 29
6.2	The Navier-Stokes equation 30
6.3	Rayleigh-Plesset theory 31
6.4	Volume vs shape oscillations 34
6.5	Non-spherical RP equation 35
6.6	"Periodic table" of bubble oscillations 39
6.7	Bubbles vs drops 40
6.8	Damping 41
6.9	Free vs constrained bubbles 43
6.9.1	Comparison with our system 44
7	Nonlinear effects 47
7.1	Acoustic streaming and microstreaming 47
7.2	Bjerknes forces 50
7.2.1	Primary Bjerknes forces 50
7.2.2	Secondary Bjerknes forces 52
7.3	Inter-mode coupling 52
8	Hypotheses on coupling mechanisms 55
8.1	A naive (wrong) view of bubble interactions 55
8.2	Coupled oscillators 56
8.3	Coupling mechanisms 57
9	Background on interacting oscillating bubbles 59
9.1	Survey of the literature 59

10	Basis of "bubble spectroscopy"	62
10.1	Bubble resonant response to external excitation	62
10.2	"(Single) Bubble spectroscopy"	63
10.3	From single to interacting bubbles	64
IV	THEORETICAL MODELLING	65
11	A theoretical model of interacting bubbles	66
11.1	Formulation of problem	66
11.2	Approximate solution for two interacting bubbles undergoing shape oscillations . .	69
11.3	Two interacting bubbles undergoing volume oscillations	75
11.4	Numerical results	76
11.5	Approximations for the squeeze flow in the contact region between two bubbles . .	77
11.6	Qualitative predictions of the model	80
11.7	Electrostatic interaction energy between two bubbles undergoing shape deformations	82
12	Purely computational approaches	88
12.1	Lattice-Boltzmann methods	88
12.2	Other computational approaches	92
V	EXPERIMENTAL BACKGROUND.	
	THE SINGLE BUBBLE INTERFEROMETER	94
13	Measurement of surface deformations	95
13.1	Capillary waves	95
13.2	Bubbles and drops	96
13.3	Biomembranes and cells	101
14	Main features of interferometry	104
14.1	Principle	104
14.1.1	Optical interferometry	105

15 Interferometric measurement of capillary waves: “(single)-bubble interferometry”	110
15.1 Idea behind measurements	110
15.2 The single-bubble interferometer	111
15.2.1 The optical interferometer	112
15.2.2 The measurement cell	113
15.2.3 The detection system	113
15.3 Surface excitation	114
15.4 Relationship between excitation, interferometric response and detected signal	117
15.5 Spectral features	117
15.6 Covered bubbles	122
15.7 State of the art in the proposed method	123
VI THE <i>DOUBLE BUBBLE</i> INTERFEROMETER.	
EXPERIMENTAL RESULTS	124
16 Double interferometer	125
16.1 Functioning scheme	125
16.2 Actual setup	125
16.3 Spectral features	129
17 Experiments on double-bubble systems: interacting <i>axisymmetric</i> bubbles	130
17.1 Bare bubbles in water	131
17.2 SDS-covered bubbles	132
17.3 BSA-covered bubbles	133
17.4 Weakly viscous solutions	134
17.5 Absence of excitation	135
17.6 Feedback from the <i>slave</i>	136
17.7 Comment on the results	137
18 Experiments on double-bubble systems: interacting <i>spherical</i> bubbles	151

18.1 Experiment	151
18.2 Results	152
18.3 Comment on the results	153
VII CONCLUSIONS AND FUTURE PERSPECTIVES	158
19 Conclusions	159
19.1 Summary of the achieved results	160
19.2 Relevance and possible developments	161
VIII Appendices	163
Appendix A Theoretical remarks	164
A.1 Derjaguin approximation	164
A.2 Volume conservation	167
Appendix B Gaussian optics and origin of the fringe pattern	169
B.1 Gaussian beams	169
B.2 Origin of interference fringes	171
Appendix C Experimental remarks	174
C.1 Experimental issues and good working practice	174
C.2 Details of the <i>double</i> bubble interferometer	176
Acknowledgements	185
Bibliography	186

Part I

OVERVIEW OF THE PHD PROJECT

Chapter 1

Introduction

1.1 Motivation

The ability to undergo deformation, in response to mechanical/electrical stimulation or thermal fluctuations, distinguishes soft bodies from the well-known colloidal particles.

A typical example of soft bodies aggregation is represented by cell assemblies. Looking through an optical microscope at a culture of living cells, one of the most striking observations is the endless flickering motion of the membrane enveloping them. As will be detailed in Chapter 5, membrane fluctuations are closely linked to the viscous and elastic properties of the cell, such as cell tension, membrane thickness and elasticity, membrane-cytoskeleton coupling and so on [1]. These properties are also known to modulate fundamental membrane processes, such as intercellular communication and adhesion (see, e.g., [2]).

Intriguing questions stemming from the above observations are:

- How do membrane fluctuations affect chemoreception, that is, the transport rate of molecules from the bulk solution to the cell interior?
- Can the pressure waves associated to the cell surface trigger signalling pathways?

These questions are far from being trivial. Indeed, cell-cell communication relies on different coupling mechanisms, as will be discussed in Section 5.3. In particular, the sensing of pressure waves propagating in the surrounding fluid is of great relevance, since purely mechanical stimuli are known to influence the exchange of signalling factors between nearby cells (see, e.g., [3]).

My Thesis is intended to answer the simpler question of how a biomimetic cell can feel the oscillatory motion of a nearby cell. This goal will be pursued by a combination of experimental (interferometry), theoretical (Rayleigh-Plesset model) and computational (Lattice-Boltzmann techniques) approaches.

1.2 Objectives and overview of the research plan

In light of the crucial role played by membrane deformations in cell functionality (see, e.g., [2]), as well as in cell-cell interactions [3], the aim of my research project is to investigate the hydrodynamically-mediated interactions (e.g., synchronisation) between two nearby *biomimetic* cells (see panel C of Figure 5.2, page 24), which has been poorly investigated so far.

In particular, a key step in the understanding of these potentially long-range interactions is to evaluate the *decay length* of the cell surface oscillations inside the surrounding solvent due to viscous dissipation. This translates into finding the maximum distance at which such oscillations can be perceived by a nearby cell, initially at rest. Special focus will be given to *small-amplitude oscillations*, to find out the minimum perceivable deformations and to investigate the generation of hydrodynamic vortices by linear oscillators.

As pointed out in Section 6.5, bubble oscillations may assume a discrete spectrum of eigenfrequencies. A question then arises: what *kinds* of vibrations are worth investigating? It can be distinguished between "breathing" deformations – involving volume variations with maintenance of spherical shape – described in terms of one-dimensional motions, and shape deformations — occurring at constant volume – which are tridimensional and hence more complex to study.

Throughout this work, I will focus mainly on the *shape* fluctuations of *bubbles*. The reasons are as follows. First, volume modes are not relevant to biology, cells being incompressible (assuming negligible water exchange between the interior and the exterior through the membrane's pores during the fast cycles of oscillation). Secondly, surface modes are more insightful to interfacial properties. Finally, bubbles have some advantages over drops of immiscible fluids in terms of narrowness of the resonance peaks, accuracy and simplicity of the models. However, the information extracted from both experimental models is very similar [4, 5].

A biomimetic study

Due to the complexity of cells, the most effective way to isolate the key physical principles underlying their oscillation-mediated interactions is to use *biomimetic* models. Moreover, the possibility to finely tune all the chemico-physical properties of the investigated systems ("cell" radii, charge and chemical composition of their surface, relative distance, medium viscosity, intensity of the excitation field and so on) allows to effectively blend theoretical modelling with experimental measurements of this multi-scale problem.

The simplest conceivable model of soft, interacting cell membranes is represented by two identical gas bubbles, surrounded by water and set at a distance D apart (or, equivalently, two drops made up of an immiscible liquid). A layer of surface-active molecules on the bubbles surface may well mimic the cellular lipid membrane.

Further activities

The last part of my doctoral research was dedicated to the study of the interactions between oscillating microbubbles via an optical tweezers setup, in the framework of a six-month internship at the University of Tours, France, in the laboratory of professor Ayache Bouakaz (UMR Inserm U 1253 – Imag erie et Cerveau). Unfortunately I didn't obtain any significant results due to lack of time, hence they are not reported here. However, this activity gave me the opportunity to gain experience with optical trapping, besides providing an introduction to biomedical research.

1.3 Method

The hydrodynamic coupling between such deformable bodies will be studied by means of a "bubble spectroscopy". The theoretical basis of this approach is laid in Part III.

The proposed study, set on a collaboration basis, adopts a combined approach:

- *Theory.* Theoretical modelling is grounded on the hydrodynamic Rayleigh-Plesset theory of fluctuating interfaces [6], linearised by assuming small-amplitude oscillations. Following this method, the inter-bubble interaction is introduced as a distance-dependent perturbation to the system: this parameter is the clue of the theory and its analytical form depends on the invoked coupling mechanism. Two coupled differential equations are obtained for the bubble radii dynamics. Their solution yields the characteristic features of the two bubbles' oscillations – amplitude, frequency, damping and relative phase – whose variation over D marks the inter-bubble interactions.
- *Experiments.* The interaction between *millimetric* bubbles has been investigated interferometrically. The adopted method, detailed in Parts V and VI, is based on the extension of an interferometric technique recently developed by professors Mario Corti (Milan, Italy) and Antonio Raudino (Catania, Italy) [7]. Previous works from our laboratory [7–9] had proven that the eigen-frequencies of bubbles and drops can be selectively excited by a tunable local field (electric or acoustic) and that the associated vibrational parameters – amplitudes,

frequencies and width of resonance peaks and relative phases – can be measured with great accuracy.

In brief, the vibrational spectrum of an initially resting bubble (called the *slave* bubble, unexcited and acting as a "receiver"), induced by a nearby vibrating bubble (called the *master* bubble, excited by an external field and acting as a "transmitter") is measured as a function of inter-bubble distance D . The oscillation amplitudes of the *slave* bubble are evaluated in relation to the viscosity and ionic strength of the medium, to the chemical nature of the covering (bare water, pure lipid monolayers, lipid mixtures, proteins) and to the frequency and amplitude of the field applied on the *master* bubble. Measurements have been carried out in Milan in collaboration professor Corti and with his group at the LITA (Laboratorio Interdisciplinare di Tecnologie Avanzate) institute.

- *Simulations.* Computer simulations are set within the recently developed object-in-fluid framework [10], based on the coupling of the lattice-Boltzmann (LB) method to describe the fluid dynamics with the immersed boundary (IB) method to describe the immersed object. The distance between the two objects, the chemical nature of the covering (e.g., surfactants or proteins), the solvent viscosity, amplitude and frequency of the exciting field can be conveniently varied. Both the set-up and run have been performed by Doctor Martina Pannuzzo, from the Italian Institute of Technology, in Genoa, Italy.

Many are the advantages of the described method. The bubbles features (such as radii, compositions and mutual distances) and the different oscillation parameters (type of deformation, frequencies and amplitudes) can be finely tuned. Moreover, since bubbles are uniform bodies lacking in organelles, any variation in their mechanical properties can be directly related to the interfacial interactions induced by the motion of liquid. Finally, the technique allows to investigate independently the oscillation parameters with extreme sensitivity (of the order of 1 Å for amplitude measurements) and without the use of probes that could interfere with the system response.

Interdisciplinarity

The mechanical coupling of soft bodies, that this study aims to investigate, relies on an intricate meshwork of interactions set at the crossroads of chemistry (chemical nature of the surfactant, ionic strength and composition of the medium), physics (soft bodies undulations coupling, generating pressure forces) and biology (cell-cell communication, up-down regulated inter- and intracellular signalling). An interdisciplinary approach, combining theoretical modelling with computer

simulations and experiments, is the best way to tackle such a multifaceted problem.

Moreover, the inherent versatility of models allows to describe different systems, regardless of their peculiar features, or to apply them to disciplines other than biology.

1.4 Originality and innovative aspects of the research

The proposed method enables to focus selectively on the hydrodynamics-mediated interactions between biomimetic cells, excluding the complexity typical of cellular systems. Several and important experimental parameters can be finely tuned and the mechanical forces acting at the bubble interface can be quantitatively evaluated and easily related to the theory. Notably, the innovative experimental approach here proposed has unprecedented sensitivity, if compared to other interferometric techniques employed to measure cell deformations (see, e.g., [11]).

Chapter 2

Overview of the thesis

This thesis work is structured as follows:

- Part II introduces the concept of bubbles and cells oscillations. Chapter 3 introduces capillary surfaces, of which bubbles and drops are an example, and capillary waves generated at their oscillating interfaces. A phenomenological introduction to the rich bubble physics is given in Chapter 4. Chapter 5 deals with cell membrane oscillations and inter-cellular coupling, focusing on the hydrodynamic mechanism and drawing an analogy between oscillating cells and harmonic oscillators.
- Part III lays the theoretical background of bubble-bubble interactions, starting from linear oscillations of single bubbles (Chapter 6). Some noteworthy nonlinear effects are commented on in Chapter 7. Chapter 8 speculates on the possible interaction mechanisms. The basic theory on bubble interactions and the most pertinent literature on the topic are presented in Chapter 9. Finally, the brief, but important Chapter 10 explains the rationale underlying our "bubble spectroscopy".
- Part IV reports our theoretical calculations. Chapter 11 proposes a qualitative hydrodynamic model for interacting bubbles undergoing shape oscillations in the close-distance regime. Chapter 12 reports some preliminary results on bubble-bubble interactions obtained via computational approaches.
- Part V gives an overview of the experimental techniques employed in the measurement of capillary waves and membrane deformations (Chapter 13), followed by a theoretical introduction to optical interferometry (Chapter 14). Chapter 15 explains the functioning of the interferometric apparatus employed by our group to study single-bubble oscillations.

- Part VI concerns double-bubble experiments. Chapter 16 describes the interferometric apparatus purposely designed for this research project. Experimental results are presented in Chapter 17 (shape oscillations) and Chapter 18 (volume oscillations).
- Conclusions on the theoretical and experimental results, as well as future and ongoing activities, are discussed in Part VII.
- Part VIII collects appendices providing details on the employed theory (Appendix A), on the principle of interferometric detection (B) and on the experimental setup (C).

Part II

PRELIMINARY BACKGROUND

Chapter 3

Capillary surfaces, bubbles and drops

3.1 Capillary surfaces [12,13]

Fluid-fluid interfaces are ubiquitous in soft matter systems and appear in various shapes and sizes.

The simplest case is given by two (or more) immiscible fluid phases mixed with each other. The interface, called a *capillary surface*, is then defined by the common boundary between the phases. Basic capillary surfaces are the boundaries of *drops*, made up of two immiscible liquids, and *bubbles*, made up by a gas and a liquid. Typical systems encountered in everyday life are emulsions (liquid drops suspended in a liquid), foams (gas bubbles separated by thin liquid films), and liquid aerosols (liquid drops in gas). Such systems are of central importance, for instance, in food processing, cosmetics and pharmaceuticals and enhanced oil recovery.

A more complex and intriguing class of interfaces is represented by vesicles (closed membranes defined by a bilayer of phospholipid molecules), capsules (closed polymeric membranes), and all kinds of biological cells. Here, the interface is provided by an additional material whose constitutive behaviour (e.g., viscosity and compressibility) has to be specified. Understanding membrane dynamics is important for disease detection by measuring mechanical properties of living cell membranes and/or biofluids, for targeted drug delivery, and for the development of lab-on-chip devices. For many scopes, especially when the interfacial layer is thin, the concept of capillary surfaces and its implications may well be extended to covered interfaces and membranes.

The macroscopic behaviour of complex fluids – be they emulsions or cell suspensions – strongly depends on the microscopic properties of the constituting interfaces. The reason is that the ratio between interfacial surface and bulk volume – scaling as the inverse of the size of the phase enclosed by the interface – is usually large in this systems.

3.2 A quick overview

In light of their ubiquitous occurrence, as well as of emerging applications exploiting fluid confinement by surface tension on the micro- and nanoscale [14], capillary surfaces are both a classical and a modern topic. The first attempts date back to Aristotele in 350 B.C., but it was not until the development of proper mathematical methods – specifically calculus, calculus of variations, and differential geometry – that the theory on this topic could be made quantitative (for a detailed historical outlook, the reader may refer to Ref. [12]). Nevertheless, fluid-fluid interface stability is still a nontrivial problem, especially concerning dynamic systems, since the interface is usually deformable and its shape not known a priori.

Some experimental techniques commonly employed to characterise fluid interfaces are summarised in Section 13.2. Quantities of interest are the surface tension, the shear and dilational viscosities of the interface, as well as the dilational modulus if it is compressible (unlike typical bulk phases). Theoretical studies prove useful in complementing experiments, by providing hardly accessible observables via numerical calculation and simulations (analytical solutions being limited to few simple cases), as well as in the model-dependent interpretation of data [15].

3.3 Stability of capillary interfaces [13]

Capillary surfaces can reconfigure or exhibit oscillations, either spontaneously or in response to perturbations. Such behaviours are controlled by static and dynamic stability, respectively, which are in turn related, as well as by the presence of solid boundaries.

Free vs constrained

Many relevant physical configurations, starting from the well-known capillary tube, up to supported bubbles or drops, involve solid boundaries. In many cases the latter yield the dominant influence for determining the whole system configuration. The line intersection of the capillary surface with the solid surface, common to all of the involved phases, is called the contact line (CL) and is a key parameter in stability problems.

In summary, when a solid is introduced (for instance, to support a drop), the free surface becomes constrained. This is stabilizing as the surface is subject to fewer disturbances with respect to the free one. However, if the CL is free to wet or dewet the solid, a new degree of freedom arises, which is destabilising. The resulting capillary configuration may be unstable or not depending on

the two competing effects.

The situation gets foreseeably more involved in the case of dynamic systems. Remarkable effects are the onset of low-frequency modes and a global change in the oscillation spectra (detailed in Section 6.9 for the case of anchored bubbles/drops), contact-angle hysteresis dependent on the CL velocity [16], stick-slip behaviours dependent on deformation amplitudes (transition from sticking CL to slipping with increasing amplitudes) [17], or symmetry reduction (e.g., azimuthal instability) in the oscillation modes due to CL dissipation [18]. For a broad overview on wetting phenomena, we refer the reader to the De Gennes's review [19]. In our study, we disregarded such dynamic effects because of the extremely small oscillation amplitudes investigated. However, wetting experimental conditions were checked prior to any assumption.

Static vs dynamic

Following Gauss's approach, the stability problem can be faced from an energetic point of view. Accordingly, the potential energy U of a configuration is given by the sum of its interface areas A_{ij} weighted by the corresponding surface interfacial energies σ_{ij} :

$$U = \sum_{i,j} \sigma_{ij} A_{ij}.$$

In fact, $U = U[\mathbf{x}]$ is a functional of the local surface configuration \mathbf{x}^1 , which may be therefore obtained via calculus of variation. Apart from volume conservation, static and dynamic stability have different constraints.

- *Static* or configurational equilibrium entails bulk, surface, and (if solid boundaries are present) CL equilibrium. Bulk equilibrium requires an equilibrated hydrostatic pressure throughout the liquid (i.e., in the absence of gravity, a uniform pressure field, or a wavelength larger than the system dimension). Surface equilibrium requires the pressure at the liquid surface to match the Young-Laplace pressure, a condition highly exploited in interface studies (see Section 13.2). Finally, CL equilibrium imposes either a "pinned" CL, or a free CL with a fixed equilibrium contact angle.
- The *dynamic* stability is a more complex issue. Assuming irrotational flow, the velocity potential over the entire fluid domain must satisfy Laplace's equation (Equation 6.4). Interfaces

¹ $\mathbf{x} = \bar{\mathbf{x}} + \delta\mathbf{x}$, $\bar{\mathbf{x}}$ being the equilibrium configuration, perturbed by an amount $\delta\mathbf{x}$.

(fluid-liquid and, if present, solid-liquid) impose additional boundary conditions which constrain fluid motions with respect to the correspondent bulk behaviour. Typical constraints are the geometry of the supporting surface and the CL boundary conditions (e.g., no-penetration condition on the solid support), or the kinematic condition on free surface, relating the local velocity field to the interface disturbance. Since deformations are rarely small and linear, complex and time-dependent boundary conditions are generally expected.

It turns out that on scales smaller than the *capillary length*

$$l_c \equiv \sqrt{\sigma/\rho g} \quad (3.1)$$

the surface shape and dynamic behaviour are largely determined by surface tension σ . The term ρg is the buoyant force per volume according to the gravity level g and the density difference ρ between the fluids. Hence, for a finite, unperturbed two-phase system at equilibrium, a spherical shape is predicted, as for bubbles and drops. On the whole, static capillary surfaces have constant mean curvature.

For bare fluid-fluid interfaces (e.g. drops), or covered by a thin adsorbed film, ρ can be rather small, yielding up to tens-of-centimetre capillary lengths. In the case of gas-liquid systems (e.g. bubbles), l_c is of order of a few millimetres (values being lower than drops because of higher ρ). In space applications, the capillary length for a liquid against gas can be of 100 cm.

On scales larger than l_c , gravitational contributions are no longer negligible, and the equilibrium surface shape will depend on the balance between buoyancy and surface tension. For instance, large bubbles or drops will appear deformed, which is of critical importance to interfacial studies (see Section 13.2). Concerning the dynamic equations, body forces (see Equation 6.1) will have to be accounted for.

3.4 Capillary waves

Upon stimulation, planar and "infinite" fluid-fluid interfaces can undergo sinusoidal deformations, called surface waves, characterised by the following dispersion relation [20, 21]:

$$\omega^2 = |\mathbf{k}| \left(\frac{\rho - \rho'}{\rho + \rho'} g + \frac{\sigma}{\rho + \rho'} k^2 \right) \quad (3.2)$$

Here, ω is the angular frequency, ρ and ρ' are the fluid densities, σ the interfacial tension, g the gravitational constant and $|\mathbf{k}| = 2\pi/\lambda$ the wavenumber (compare with the familiar, linear relation

for electromagnetic waves in vacuum, $\omega = c |\mathbf{k}|$, where the phase velocity c is the speed of light in vacuum).

It can be seen from Equation 3.2 that the behaviour of surface waves strongly depends on the wavelength λ . At large wavelengths, fluid deformations are dominated by gravity effects ($\omega^2 \equiv \frac{\rho - \rho'}{\rho + \rho'} g k$, which simplifies to $\omega^2 \equiv g k$ for gas-liquid interfaces) and are referred to as *gravity waves*. When λ gets smaller (typically within 1 cm), the effect of gravity becomes negligible and fluid dynamics is regulated by the interfacial tension ($\omega^2 \equiv \frac{\sigma}{\rho + \rho'} k^3$, i.e. $\omega^2 \equiv \frac{\sigma}{\rho} k^3$ for gas-liquid interfaces). Those waves are defined *capillary waves* [20]. The transition between gravity and capillary waves corresponds to the capillary length (Equation 3.1), that is to say to $\lambda = l_c$ [21].

Capillary waves typically feature rounded crests and a V-shaped trough and the phase velocity $c = \omega/k$ increases with decreasing wavelength ($c \propto \lambda^{-1/2}$), unlike gravity waves, for which $c \propto \lambda$. The upper wavelength limit, observable in air-water interfaces, is 1.73 cm, corresponding to a minimum velocity c of 23.1 cm/s [21]. *Because of their sensitivity to surface tension, capillary waves are widely investigated for fluid interface characterisation [22].* An overview of the measurement techniques is given in Section 13.1.

In my thesis I will mainly study the capillary waves at the air-liquid interface of oscillating bubbles. As will be detailed later in the text, bubble interfaces differ from the planar, infinite ones by two main points, stemming from their finite and curved geometry:

- *The wavevector distribution of the waves at a bubble surface is discrete rather than continuous;*
- *Bubble deformations are better described by curvilinear coordinates (spherical for a single bubble, spheroidal for two bubbles), rather than Cartesian coordinates.*

Hence, the resulting equations are quite different than Equation 3.2.

Chapter 4

"Bubble phenomenology"

In the previous chapter we introduced bubbles and drops as capillary surfaces, and highlighted the role of *deformability* in determining their stability. When it comes to gaseous bubbles, interface deformations often involve compression-expansion motions. As illustrated in Figure 4.1, the two processes typically occur at two different timescales, compression being much faster than expansion. This asymmetric compressibility is responsible of the well-documented hydrodynamic and chemical instability of bubbles (see, for instance, [23]), associated to the phenomenon of *cavitation*.

In this chapter we will give an overview of the rich phenomenology related to bubble oscillations, and in particular to cavitation, without going into detail on this highly nonlinear process.

4.1 Cavitation

Acoustic cavitation [23] is the formation of gaseous cavities in a liquid when subject to rapid changes of pressure, for instance, when high-frequency sound waves are applied. In brief, cavities are formed in the liquid where the pressure is relatively low; when subjected to higher pressure, these voids implode and can generate an intense shock wave.

Cavitation is at the root of many interesting phenomena. Everyday manifestations may be found, for instance, in the sound of flowing water [25], as well as of cracking joints [26]. Other examples are illustrated in Figure 4.2 and discussed as follows:

- **Sonoluminescence and sonochemistry** [27]. When the change in pressure and corresponding bubble collapse are particularly fast the bubble effectively implodes with enough force to generate tremendous heat (local temperatures of the higher than a thousand degrees are reached). The heat generates radical species, which may react with each other, otherwise

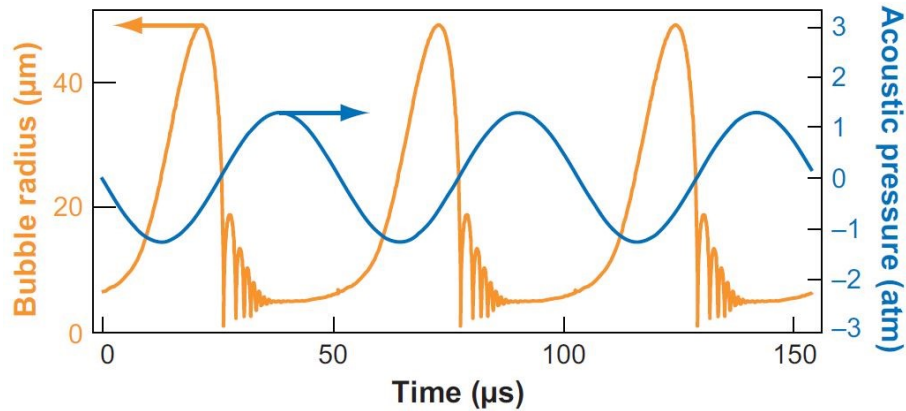


Figure 4.1: Calculated radial response of a bubble (orange curve) driven by a sinusoidal acoustic field (blue curve). No mass transport occurs at the bubble interface over any single acoustic cycle. Image retrieved from [24].

energy relaxation may lead to a burst of light. The spectrum of the emitted light is peaked in the ultraviolet and depends strongly on the type of gas dissolved in the liquid.

- **Vortex cavitation.** Regions of concentrated vorticity arise in many cases of high Reynolds number flows. In this cases, cavitation bubbles forms and concentrate in the lower pressure (highest velocity) regions (e.g. in the tip vortices of ships propellers or in the draft tube of water turbines, as shown in Figure 4.2, panel B).

The study of cavitation was first undertaken in 1894 by Reynolds [28]. Later on, Lord Rayleigh [6] investigated the collapse of a spherical bubble in an infinite fluid and thus developed the above described implosion mechanism of cavitation, leading to the generation of extremely high pressures during the last moments of the bubble collapse.

A more interesting behaviour arises when the bubble neighbourhood lacks spherical symmetry, as in proximity of a solid boundary (see, e.g., [29–31]): in this case, owing to symmetry breaking, vectorial microjets are formed instead of radial collapse (see Figure 4.2, panel C), which can be up to 200 ms^{-1} fast and point towards the surface. Interesting consequences stemming from this observation are:

- **Cavitation damage.** Repeated formation of microjets is responsible for structural damage to ship propeller blades, turbomachinery and hydraulic equipment, which can range from minor pitting to a total breach of the inside of the pump (see, e.g., [32, 33] and Figure 4.2,

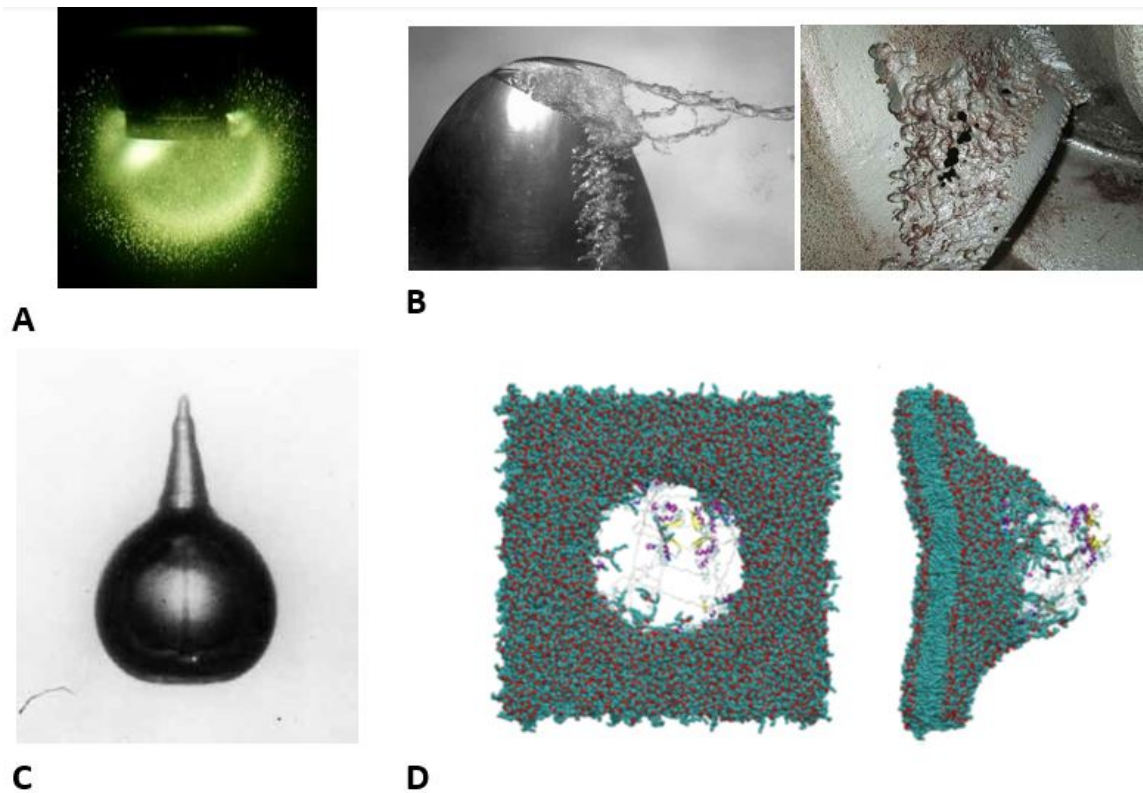


Figure 4.2: Examples of cavitation-related phenomena: **A)** A cloud of collapsing bubbles lit by their own sonoluminescence. **B)** Vortex cavitation: *left*, cavitation tip vortices on a hydrofoil; *right*, severe cavitation damage leading to the erosion of a pump impeller. **C)** Directional microjet formed by an imploding bubble. **D)** Sonoporation of a protein-ended lipid membrane in a shock wave simulation, similar to the effect induced by insonified microbubbles.

panel B). Due to the vortex cavitation phenomenon, the damage occurs in the external parts of the blades.

- **Sonoporation.** Insonified microbubbles in proximity of cells have been shown to induce pores or larger holes in membranes, a remarkable example being blood vessels endothelia [1]. The underlying mechanism, still not fully understood, has been explained in terms of many concurring events (see, for instance, [34–36]). Among them, a role seems to be played by the shock waves induced by bubble collapse at the cell wall (see Figure 4.2, panel D).

Applications

The ability of microbubbles to focus and concentrate energy paves the way to many applications in acoustics on the micrometre scale (microacoustics), spanning from cell manipulation to microfluidic devices. In particular, the use of shock waves and ultrasound in a biomedical context is appealing because of their non-invasiveness (see, e.g., [34, 37, 38]). Ultrasound-driven microbubbles have been used to enhance the acoustic contrast between blood and surrounding tissues in ultrasonic imaging, while sonoporation may find a therapeutical application in the delivery of drugs or chemotherapeutic agents as an alternative to cell-wall permeation techniques like electroporation and particle guns. The combined use of ultrasound contrast agent microbubbles (UCAs) for non-invasive, precise and targeted drug delivery and therapeutic monitoring has been demonstrated in a variety of animal models and clinical indications. Recent studies address the evaluation of the sonoporation mechanism(s), ultrasound parameters, drug type and dose in order to translate this technology into clinic use.

Typically, the bubbles used for biomedical purposes have a diameter on the order of a few micrometers and are encapsulated by a shell of albumin, polymer, or lipid, whose function is to prevent fast dissolution or coalescence. It should be noticed that special care is required when modelling encapsulated bubbles or comparing experimental results with the better-known free bubbles. The presence of a shell alters many of the functional properties of microbubbles, like the viscous and elastic parameters, and dramatically enhances the compression-expansion asymmetry. The reader may refer to [39] for a recent review on this topic.

4.2 Interacting bubbles

The onset of attractive interactions between bubbles was postulated by Bjerknes in 1917 [40]. Indeed, bubbles seldom appear isolated in real systems, but, regardless of their size and charge state, tend to aggregate into complex and specific ensembles like clusters, filaments and clouds (see Figure 4.3). The effects are emphasized in the presence of oscillating acoustic or electric fields (see left panel of Figure 4.3), where the pattern shapes depend on the strength and frequency of the applied field (see, e.g., [41–43]). Indeed, the nonlinear nature of the sound field and the complex inter-bubble interaction in a cloud present challenges to a comprehensive understanding of the physics of the bubble cloud in high-intensity focused ultrasound.

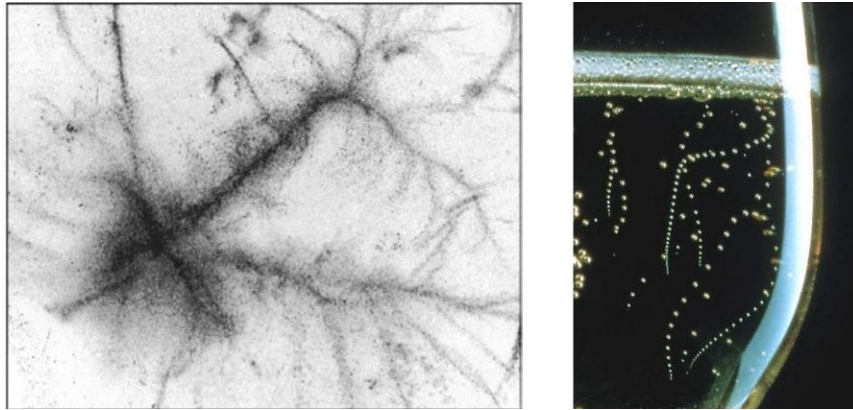


Figure 4.3: Patterns of interacting bubbles. *Left:* a characteristic web (resembling the "Lichtenberg figures" observed in electric discharges) of micrometer-sized bubbles subject to an acoustic field. Image retrieved from [43]. *Right:* bubble trains (millimetric) in motion in a champagne flute.

Chapter 5

Biological background: from bubbles to cells

The striking variety of terrestrial life has evolved thanks to the development of cell membranes, which allowed segregation of functional information and processes occurring inside the cell from the exterior. Meanwhile, cells continually take decisions concerning survival, proliferation, differentiation, migration or secretion based upon information on the surrounding environment. A major challenge in cell biology is to understand what kind of data cells extract from their environment and how fast the information decays in space and time.

Hydrodynamic effects, in the case of particles in proximity to a rigid surface, are generally considered negligible. However, they could become significant in the proximity of oscillating surfaces, as in the case of cells, owing to the possibility of synchronised oscillations. The degree of synchronization will depend on the distance between the oscillators, on their orientation and on the medium viscosity. Current knowledge suggests that oscillations of plasma membranes may play a pivotal role in the acquisition of environmental cues, thereby directing inter-cellular coupling.

5.1 Cell membrane fluctuations

The theoretical basis for the study of membrane fluctuations was laid in the 1970s by Helfrich, who applied the theory of thin elastic shells to lipid bilayers. According to his model [44], the deformation of a vesicle from the spherical (equilibrium) shape is ruled by the elastic modulus k , a constant depending on the lipid composition and lipid membrane status. The elasticity concept has proven useful in modelling several situations, such as the budding of a new vesicle from the membrane surface, phagocytosis events or the adhesion and fusion mechanisms between contiguous cells [45]. In line with theoretical predictions, simple lipid bilayers in aqueous solution have been observed to incessantly fluctuate around their average shape. These motions, called undula-

tions [46, 47], result from thermal excitation and occur with characteristic frequencies of order of 1000 Hz. Study of membrane undulations is highly informative of the mechanical properties of the bilayer and its interactions with the environment (e.g., membrane-bound proteins).

Cell membranes are no exception in this regard, their oscillating behaviour being more varied because of the variability in cell types and living conditions. These deformations have the capacity to strongly influence the signals generated by cell interaction with foreign surfaces. The associated timescales range between less than a second and several seconds.

Main features

First observations of cell membrane fluctuations (CMFs) were made in 1890 in red blood cell (RBC) suspensions by phase contrast optical microscopy [48], evidencing rhythmic membrane deformations accompanied by turbulence in the cytoplasm. The quantitative study of this “*flicker phenomenon*” was pioneered several years ago by Brochard and Lennon [49], who measured the frequency spectrum of RBCs under physiological conditions. Plasma membrane undulations of nucleated cells were first thought to be absent because of excessive surface tension and bending rigidity. However, they were later demonstrated using more sensitive microscopy techniques [46].

Recent data have improved our understanding of the physical properties of CMFs, which may be grouped into two categories [46]:

- “Conventional” membrane deformations – e.g., formation of finger- or sheet-like structures such as filopodia, microvilli and lamellipodia [50], or blebbing [51] – with membrane deformations extending up to several micrometres. The characteristic time-scales of these cell deformations range from several tens of seconds to one minute.
- Rapid membrane undulations, with frequency of 1 Hz or more. While RBCs display high frequency undulations (of order of 1000 Hz), with amplitudes ranging between a few tens and hundreds of nanometres [1, 52, 53], membrane undulations of nucleated cells are characterised by lower frequencies and amplitudes [54], due mainly to differences in size, surface tension and bending modulus. For instance, blood lymphocytes or monocytes display surface undulations with 0.2–30 Hz frequency and 20–30 nm amplitude, while human [55] or murine [56] fibroblasts fluctuate with a frequency between 0.5 and 0.01 Hz and amplitude of 1–4 nm.

Biological significance

The rhythmic movements of cells, as closely related to membrane deformability, were initially explained in terms of thermally excited undulations, i.e., as purely physical phenomena (see, e.g., [48, 49]). Metabolic regulation of CMFs – in terms, for instance, of ATP-dependence – has been widely debated since [1, 52, 57]. Membrane undulations and cell metabolism now appear to be intimately related, and changes in the biomechanic properties of membranes have been shown to reflect particular subcellular processes, as well as infectious or genetic diseases [46, 58, 59].

Moreover, the existence of different oscillation modes associated to specific time- and space-scales, as observed above, could allow cells to perform complementary tasks. For instance, formation of large-amplitude (micrometric) protrusions, exploited per se in sensory and explorative functions [60], may not allow cells to sense their environment with sufficient rapidity (say, less than 1 s), in such circumstances as in immune response (see, e.g., [61, 62]). This difficulty, by contrast, may well be overcome by the faster undulation modes.

Cell oscillation spectra

Erythrocytes (RBCs) provide an excellent model system to study CMFs, since they are easy to study and exhibit unique reversible shape deformability, essential both for their function of transporting oxygen and for their survival. Indeed, remarkable biomechanical membrane properties have been found altered in some pathological states including blood diseases [58, 59]. Human RBCs have a radius of 3–4 μm and display undulation frequencies of order of 10^3Hz with very large amplitudes (a fraction of a micron) [46, 49], as well as much slower motions (in the scale of seconds) associated to protrusions or blebbing [51]. Their vibration features are well explained by the harmonic model, as testified by the agreement between experimentally observed shapes and calculated eigenmodes (see Figure 5.1) [1, 63, 64]. In short:

Cell membranes behave as (round-shaped) spring-mass systems, with oscillation eigenmodes occurring at characteristic frequencies giving rise to oscillation spectra. As we shall see in Chapter 6, this is the same behaviour as the electron density fluctuation around a nucleus (atomic orbitals), or as a vibrating bubble/drop surface.

The oscillations of other cellular types are less pronounced and more complex to study, albeit observable (see, e.g., [54–56]), due to the presence of nuclei and organelles, which increase the cytoplasm (non-homogeneous) viscosity. In addition, most cells are part of tissues, hence they are at least partially anchored rather than freely floating and their oscillations may exhibit different features.

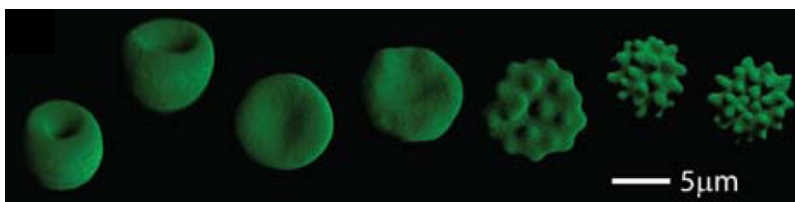


Figure 5.1: 3D confocal images of the canonical shapes of human RBCs, obtained at increasing concentrations of NaCl. The shape changes follow the spherical harmonic series expansions of the theoretical cell surfaces. Adapted from [64].

Finally, it should be noticed that membrane fluctuations are strongly influenced by the cytoskeleton-bilayer coupling [57]. Simpler model systems are provided by RBC *shells* (where the lipid membrane is removed by detergent solubilisation [65]) and *ghosts* (where all of the cytoplasmic content is removed by cell lysis, leaving only the outer membrane [66]).

Decay lengths of cell oscillations

While cell membrane fluctuations are widely studied, a much less explored field involves the decay length of such oscillations inside the surrounding medium due to viscous dissipation. Although some attempts date back to the end of the nineteenth century (the so-called secondary Bjerknes forces, discussed in Section 7.2), they apply to idealized systems (a pulsating sphere in a viscous fluid) and the overall understanding of this complex problem is poor so far.

The solution of the decay length around a fluctuating body is the clue to estimate the effectiveness of the hydrodynamic mechanism for cell-cell coupling (panel C of Figure 5.2, Section 5.3).

5.2 Mechanosensitivity of cell membranes

The conversion of physical signals, such as contractile forces or external mechanical perturbations, into chemical signalling events is a fundamental cellular process. Indeed, membrane deformations can generate forces capable to initiate and modulate early signalling cascades triggered by membrane receptors.

A plethora of mechanosensitive molecules is available to the cell [67], ranging from ion channels [68] to membrane receptors [3], making the exchange of signalling factors between nearby cells extremely regulated. In addition, a strong coupling between external mechanical stimuli and

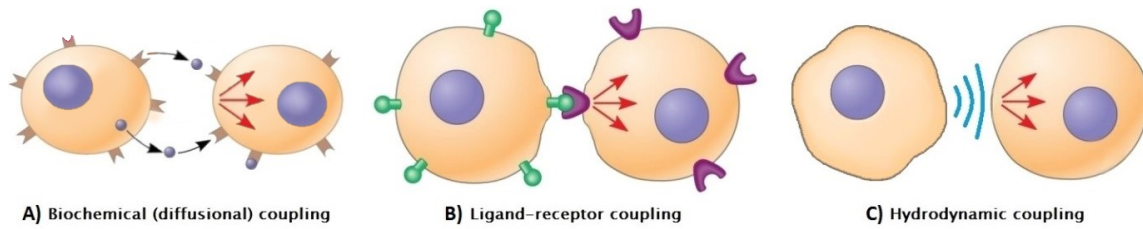


Figure 5.2: Different types of cell-cell coupling. **A)** *Biochemical*, relying on the diffusional exchange of signalling factors recognised by specific receptors on the cell membranes. **B)** *Ligand-receptor*, involving direct binding between membrane receptors; **C)** *Hydrodynamic*, triggered by the pressure waves of the medium, generated by cell membrane oscillations. Red arrows indicate the induced biochemical response. For simplicity, only one direction of communication (from a "sender" cell on the left to a "receiver" cell on the right) is illustrated.

cellular adhesion is provided by complex membrane structures, known as focal adhesions [69], related to both the extracellular matrix and the cell interior.

5.3 Intercellular coupling [70]

Intercellular communication is essential for the maintaining the functionality of tissues (both solid, where the cells are permanently linked and liquid, where they are floating in a liquid medium), as well as for cellular colonies (consider, for instance, the quorum sensing behaviour) and relies on different coupling mechanisms. The most important are sketched in Figure 5.2. In light of the pivotal role of mechanical sensing in cellular activities, pointed out in the previous section, these mechanisms appear to be intertwined rather than independent.

Each communication mode has specific time and distance ranges and its effectiveness will depend on the mutual distance and orientation between individual cells.

Biochemical coupling

This means of communication relies on the transport of chemicals – like signalling factors, hormones or neurotransmitters – from a "sender" secreting cell to a "receiver" cell. Being governed by diffusion processes, the timescale of transport and its efficiency in terms of length decay and information loss are dependent on molecular sizes and inter-cellular distances [71]. In particular, while the paracrine and the neuronal communication (*chemical synapse*) are extremely fast and occur over reduced scales (typical distances between the pre- and postsynaptic cells, for instance,

being of order of 500 Å), favoured by small and sheltered inter-cellular environments, the transport of hormones from endocrine to target cells is mediated by blood circulation.

Concerning the timescales (spanning from milliseconds in neurotransmission [70] to minutes in endocrine signalling, with rates of order of 10 mm/s [71]), both the rate of diffusion from the "sender" cell and that of interaction with the surface of the "receiver" cell (chemoreception) are affected by the motion of the fluid (advection-diffusion) and of the membrane surface. We are currently addressing a tightly related problem in a study of surfactant adsorption at the surface of a single bubble, in collaboration with Clarissa Astuto and Professor Giovanni Russo from the department of Mathematics and Informatics of Catania.

Ligand-receptor coupling

In this case, direct contact between molecules exposed at the cell membranes is required. This is achieved in two main ways. The former (*electrical synapse*, typical of muscle and cardiac tissues) involves molecular structures, called *gap junctions*, enabling the flow of electrical current or chemical species via low-resistance pores. The latter entails direct interaction between specific ligand-receptor couples (as those sketched in Figure 5.2), or less specific adhesion mediated by ions (mainly Ca^{2+}).

This is a highly efficient method (especially the communication between tight junctions, limited only by the pore resistance), but requires contact distances between the two cells (of order of a few nm). In the case of ligand-receptor binding, this is not extremely an easy task, owing to the long-range electrostatic repulsion between lipid membranes, as well as to the presence of sterically hindering molecules exposed at the cell surface [72]. I addressed this problem, within the framework of membrane adhesion, during my master thesis.

Hydrodynamic coupling

Mediated by fluid motions around the cells, this is still a poorly investigated method. However, it presents several potential advantages over the others, since hydrodynamic waves may propagate at high speeds and rather constant amplitudes over large distances, thereby enabling long-distance cell-cell communication.

Recent publications by the Prakash group in Stanford provided interesting theoretical and experimental insights to the question of fast cell-cell communication mechanisms [73]. In the investigated system, communication is mediated by long-ranged vortex flows stemming from contraction-

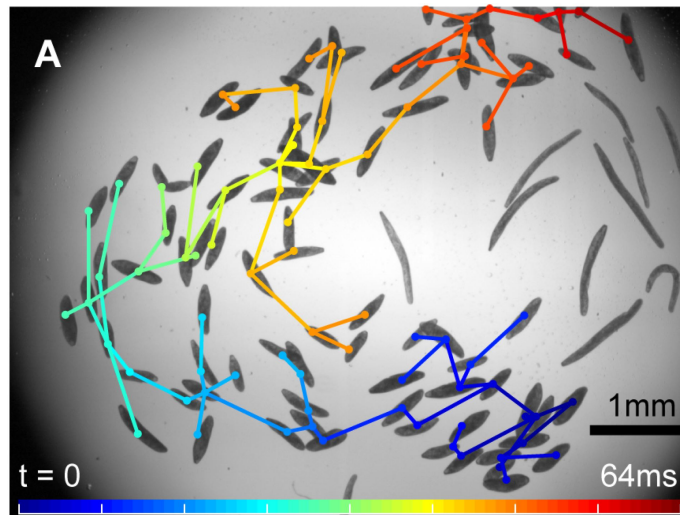


Figure 5.3: Trigger wave propagating through a *Spirostomum ambiguum* colony. The graph connects the triggered organisms during the observation time. As it can be seen, the waves propagate over distances of order of 1 cm in less than 0.1 s (cell contraction times of order of 1 ms). Image retrieved from [73].

elongation (i.e., oscillations) in a community of unicellular protists whose contractile response to electrical or mechanical applied stimuli is well characterised [74]. The trigger-wave propagation is found to require a critical concentration of individuals and to depend on distance and mutual orientation between the cells, with formation of directional interaction patterns in multi-cellular systems, evidenced in Figure 5.3.

5.4 From (hydrodynamic) interaction to (biochemical) synchronisation

The evidence presented above, concerning cell active fluctuations and the capability of neighbour cells to respond accordingly, suggests that two such soft systems could communicate by synchronizing their undulation modes. If the metabolism of a cell and then its stored energy suddenly change, this will in turn affect the corresponding membrane flickering. Neighbour cells within a threshold distance could feel these changes earlier than any biochemical change in the surrounding environment and synchronize in accordance their membrane oscillations thanks to hydrodynamic interactions. This mechanism may play a role, for instance, in the regulation of cell communities over large scales, similarly to quorum sensing.

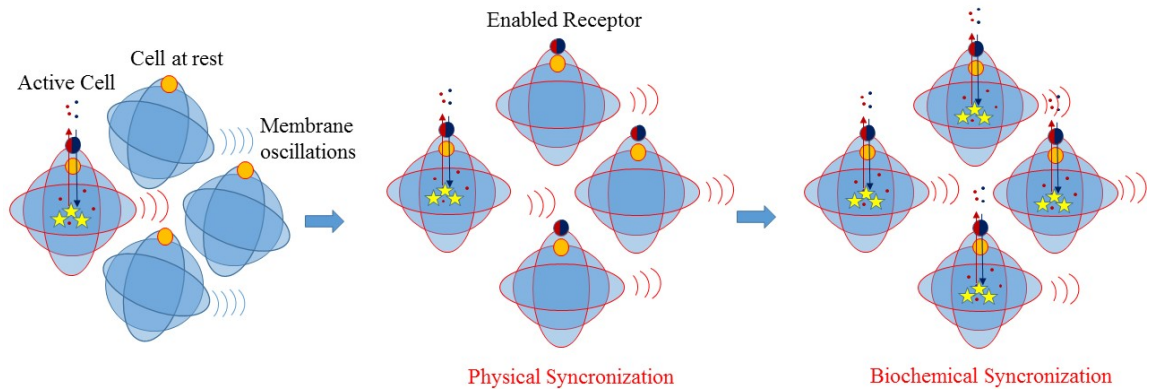


Figure 5.4: Cartoon representation of biochemical synchronisation between nearby cells, promoted by physical (hydrodynamic) synchronisation. Cells are shaded in light blue (*blue contours*: resting cells; *red contours*: active cells). Yellow stars inside the cells indicate an “activated” metabolic pathway. Small circles denote the membrane receptor responsible of the signalling cascade (*orange*: resting state; *blue/red*: activated).

An example of hydrodynamic synchronization has been unequivocally demonstrated in the case of flagella coupled solely through a fluid [75]. In the case of two cells, a successful synchronization could consequently promote more intense membrane oscillations, which could in turn influence important chemical-physical aspects of the membrane itself and the related permeability. As suggested earlier, cell communication mediated by an oscillatory synchronization could be reasonably more efficient and faster than the corresponding communication mediated by secretion/adsorption of metabolites. If cells oscillate in a concerted way, the signal can become effective almost instantaneously at long distances and concomitantly boost the excretion and spreading of second messengers, driving consequently to the well-known phenomenon of biochemical synchronization. A sketch representation of the whole process is drawn in Figure 5.4. The investigation of time scales typical for soft bodies synchronization mediated by hydrodynamic interactions could provide some clues on the order of events in biological systems.

A crucial point for the study of physical synchronisation between two interacting is the study of the relative phase between the two oscillators.

Part III

**THEORETICAL BACKGROUND.
FROM SINGLE
TO INTERACTING BUBBLES**

Chapter 6

Theory of single oscillating bubbles: the "bubble oscillator"

Individual bubbles and drops behave like spring-mass systems, undergoing linear oscillations around their equilibrium state in response to small sinusoidal perturbations. A more complex physics than mass-spring systems, like the distinction between volume and shape modes, arises from the dynamic deformations of the constituting fluids. These are commonly described by Rayleigh-Plesset-like equations.

6.1 Background

The small-amplitude oscillatory motion of bubbles and drops about their spherical shape is a classical problem in fluid mechanics. Besides the intrinsic scientific interest of this topic (see, e.g., [76–78]), a vast literature has focused on its widespread applications spanning, for instance, from chemical engineering [79, 80], to spray cooling [81], multiphase flow [82], nuclear physics [83], plasma [84] and meteorology [85].

The first pioneering studies were made in the late 19th century by Kelvin [86] and Rayleigh [87] for what concerns inviscid liquids, while Lamb [88, 89] introduced viscous effects to describe the decaying oscillatory waves at a liquid-liquid spheroidal interface. Since then, considerable efforts have been made to address bubble oscillations and their complex hydrodynamic regulation. Besides viscosity, special attention has been paid also to the fluid compressibility [90–95], to the oscillation regime (linear vs nonlinear, see next chapter) [96, 97], or to the presence of a covering shell at the bubble surface (see the review [39] and references therein). The above were only a few examples. A comprehensive treatment of the subject may be found, for instance, in Refs. [98, 99]. In the next

sections the basic theory of bubble oscillations will be presented as a starting frame for bubble-bubble interactions, focusing on the Rayleigh-Plesset theory which has set a standard for the field.

6.2 The Navier-Stokes equation

The standard way to describe the dynamics of Newtonian fluids, within the framework of continuum mechanics, is by the fundamental Navier-Stokes equations, which stand to fluid mechanics as Schroedinger equation stands to quantum mechanics. These are a set of nonlinear partial differential equations in the three spatial dimensions, arising from the momentum conservation principle. For the common case of incompressible fluids (for which the density $\rho = \text{const}$), they take the form:

$$\rho \left[\frac{\partial \mathbf{v}}{\partial t} + \nabla \times \mathbf{v} \times \mathbf{v} + \frac{1}{2} \nabla v^2 \right] = -\nabla p + \eta \nabla^2 \mathbf{v} - \rho \nabla \phi \quad (6.1)$$

where \mathbf{v} is the (three-component) velocity vector, ρ and η are the density and the dynamic viscosity of the fluid, p is the local pressure and ϕ is the body force potential (e.g., gravity). In brief, the general acceleration terms for the fluid are shown on the left side of the equation, while the forces acting on the fluid particles – pressure, viscous and (if present) body forces, respectively – are displayed on the right part.

In order to be solved, the Navier-Stokes equations must be supplemented by the continuity equation, stemming from the conservation of mass, which for incompressible fluids reads:

$$\nabla \cdot \mathbf{v} = 0 \quad (6.2)$$

Equations 6.1 and 6.2 apply to any Newtonian incompressible fluid system, provided the appropriate boundary conditions are applied. In practice, however, the Navier-Stokes equations (6.1) have no general solution and exact analytical solutions have only been found for a few systems, involving mainly incompressible fluids [100].

A considerable simplification of Equation 6.1 applies to the frequent case of slow fluid motions (low Reynolds numbers), where the quadratic terms in \mathbf{v} contained in Equation 6.1 can be safely neglected. Another simplification, independent of the stream rate, is to assume an irrotational velocity field ($\nabla \times \mathbf{v} = 0$), i.e. laminar flow. When both assumptions are made and the contribution of gravity or other body forces is negligible, Equation 6.1 reduces to:

$$\rho \frac{\partial \mathbf{v}}{\partial t} = -\nabla p + \eta \nabla^2 \mathbf{v} \quad (6.3)$$

This form can be applied to describe the behaviour of a gas bubble immersed in a liquid, or a liquid drop immiscible with the surrounding fluid, undergoing small-amplitude oscillations. Besides Equation 6.2, Equation 6.3 must be supplemented by the proper boundary conditions at the bubble (drop) interface, related to the fluid velocities at the inner and outer phases (the so-called *kinematic* boundary condition) and the balance of tangential and normal stresses upon bubble (drop) deformations (*dynamical* boundary conditions). In the course of this thesis we will follow an alternative, but related approach, presented in the following section.

6.3 Rayleigh-Plesset theory

The most popular equation for describing both the linear and the nonlinear response of a gas bubble in a Newtonian fluid to a driving field is the Rayleigh-Plesset (RP) equation. It can be derived either by integrating the Navier Stokes equation (6.3) or (6.1), or from the balance between the kinetic energy in the outer liquid and the potential energy in the gas [101].

The basic form of the RP equation proves especially useful in the case of individual *spherical* bubbles, using the radius R as the only dynamic parameter. Common assumptions are [101]:

- The bubble is surrounded by an infinite medium.
- The bubble maintains a spherical shape at all times.
- The gas content is constant (no mass exchanges).
- Spatially uniform conditions (e.g.: density, pressure) exist within the bubble.
- The density of the outer fluid is much greater than that of the internal gas.
- There are no body forces acting (e.g.: gravity).
- Bulk viscous effects are negligible. Hence, if present, viscous forces are confined to a thin layer around the bubble surface.
- The bubble radius is much smaller than the wavelength of the driving pressure field. This allows to regard the fluid as incompressible, leading to the velocity \mathbf{v} being expressed as the gradient of a potential Φ ($\mathbf{v} = \nabla\Phi$), with:

$$\nabla^2\Phi = 0 \quad (\text{Laplace equation}) \quad (6.4)$$

Similar arguments hold for drops immersed in an immiscible fluid. The main differences between the two systems are summed up in Section 6.7.

Under these assumptions, the dynamic motion of the bubble radius $R = R(t)$ is governed by [6, 102, 103]:

$$R \ddot{R} + \frac{3}{2} \dot{R}^2 = \frac{1}{\rho} [p(R) - p_\infty(t)] \quad (6.5)$$

From a physical standpoint, the left side of Equation 6.9 accounts for the kinetic energy of the fluid displaced by the oscillatory motion of the bubble surface ($\dot{R}(t)$ being the wall velocity and $u(r,t) = \frac{R^2(t)}{r^2(t)} \cdot \dot{R}(t)$ the velocity at distance r from the centre of the bubble), overdots denoting differentiation with respect to time. The right side, divided by the liquid density ρ , represents the work exerted on the bubble wall by that pressure which would exist at the position of the bubble centre, were the bubble not to be present. The latter, for incompressible fluids, coincides with the pressure far from the bubble:

$$p_\infty(t) = p_o + P_{ext}(t) \quad (6.6)$$

where p_o is the (constant) hydrostatic pressure and $P_{ext}(t)$ the dynamic component, dependent on the forcing. The pressure at the bubble wall, $p(R)$, is given by:

$$p(R) = \hat{p} - \frac{2\sigma}{R} - 4\eta \frac{\dot{R}}{R} \quad (6.7)$$

Here, \hat{p} is the total pressure inside the bubble, $\frac{2\sigma}{R}$ is the Laplace pressure at radius R (whose equilibrium value $\frac{2\sigma}{R_0}$ is known as the capillary pressure) arising from interfacial tension σ , while the last term accounts for viscous dissipation, with η being the dynamic viscosity. Concerning the form of \hat{p} , a polytropic compression behaviour of the inner gas is generally assumed [96, 104], yielding:

$$\hat{p} = \left(p_o + \frac{2\sigma}{R_0} - p_v \right) \left(\frac{R_0}{R} \right)^{3\kappa} + p_v \quad (6.8)$$

κ being the polytropic exponent¹ and p_v the vapour pressure (often neglected). The first term enclosed by parenthesis is the internal pressure at equilibrium \hat{p}_{eq} .

Substitution of Equations 6.6 and 6.7 into 6.5 gives:

$$R \ddot{R} + \frac{3}{2} \dot{R}^2 = \frac{1}{\rho} \left(\hat{p} - p_o - P_{ext}(t) - \frac{2\sigma}{R} - 4\eta \frac{\dot{R}}{R} \right) \quad (6.9)$$

¹The value of κ can range in the interval from 1 (in the isothermal limit: $PV = const$) to the ratio of specific heats of the gas, $\gamma = C_p/C_v$ (adiabatic limit: $PV^\gamma = const$). Appropriate criteria for the choice are available only for small-amplitude linear oscillations [96]. Typically, the proximity of the bubble behaviour to the isothermal or the adiabatic limit is estimated through the Péclet number, $Pe = R_0^2 \omega D_{th}$, where D_{th} is the gas thermal diffusivity and ω is the angular driving frequency. If $Pe \gg 1$ (as is the case, for instance, with modern contrast agents [105]), it is assumed that the bubble oscillates adiabatically and vice versa. For air bubbles in water it is commonly assumed $\kappa = 1.4$.

which will be used as a reference for single-bubble oscillations in this thesis.

If the bubble is subject to a sinusoidal, *isotropic* forcing sound field of frequency ω and amplitude $P_A \ll p_o$:

$$P_{ext}(t) = P_A \cos \omega t \quad (6.10)$$

it will pulsate about its equilibrium radius R_0 with amplitude $a(t) \ll R_0$:

$$R(t) = R_0 + a(t) \quad (6.11)$$

By substituting Equations 6.10 and 6.11 into Equation 6.9, a nonlinear differential equation in $a(t)$ is obtained. By linearising around $x = a(t)/R_0 \ll 1$, one finds a forced-damped harmonic-oscillator equation:

$$\ddot{x} + \beta \dot{x} + \Lambda^2 x = \alpha \sin \omega t \quad (6.12)$$

where

$$\beta = \frac{4\eta}{\rho \omega R_0^2} \quad (6.13)$$

is the damping constant (η being the viscosity of the liquid), $\Lambda \equiv \frac{\omega_0}{\omega}$, with ω_0 being the natural angular frequency²:

$$\omega_0^2 = 3\kappa \frac{\hat{p}_{eq}}{\rho R_0^2} - \frac{2\sigma}{\rho R_0^3} = \frac{1}{\rho} \left[3\kappa \frac{p_o}{R_0^2} + (\kappa - 1) \frac{2\sigma}{R_0^3} \right] \quad (6.14)$$

obtained assuming a linearised polytropic law (6.8) for the inner gas, and finally $\alpha \equiv \frac{P_A}{\omega^2 \rho R_0^2}$.

Equation 6.14, derived under the assumption of a perfectly spherical system, predicts one natural resonance frequency ω_0 for bubble oscillations. However, as will be introduced in the next section, spherical symmetry is actually broken in many real systems, resulting in different oscillation properties.

Exact solution of Equation 6.12 is:

$$R(t) = R_0 [1 + b \sin(\omega t + \psi)] \quad (6.15)$$

where:

$$b = \frac{\alpha}{\sqrt{(\Lambda^2 - 1)^2 + \beta^2}} \quad \text{and} \quad \tan \psi = \frac{\beta}{1 - \Lambda^2} \quad (6.16)$$

²Neglecting surface tension and assuming an adiabatic behaviour of the gas (with $\kappa = C_P/C_V$), Equation 6.14 reduces to the frequency originally estimated by Minnaert [25]: $\omega_0 = \sqrt{\frac{3\kappa \hat{p}_{eq}}{\rho R_0^2}}$.

Here, $b = b(\omega)$ is the amplitude (normalised to R_0) and $\psi = \psi(\omega)$ the phase of oscillation. Notice that the solution (6.15) exhibits a symmetric maximum, together with a π phase jump, around the natural angular frequency ω_o , meaning a resonance behaviour. On increasing the damping coefficient β , the resonance peak becomes broader and broader.

Equations 6.13, 6.14 and 6.16 confirm the similarity between the vibrational dynamics of a bubble (drop) and that of a mass-spring system oscillating in a viscous medium. In our case, the oscillation frequency depends on the bubble radius and on the interfacial tension, while the dissipation at resonance depends on the bubble radius and on the medium viscosity.

6.4 Volume vs shape oscillations

Most bubble systems observed in real life (or experiments) don't match the perfect spherical symmetry assumed in Section 6.3 for developing the RP equation. In brief, this may depend either on the system geometry – namely, if the bubble is tethered to a solid support (as discussed in Section 6.9), or a solid surface is present in the surroundings, albeit not in contact – or on the geometry of the forcing field – i.e., directional, rather than isotropic (as in our setup, described in Section 16.2) – or on nonlinear effects arising, for instance, from the intensity of the forcing field (see Chapter 7, Section 7.3). In this chapter we will neglect nonlinear effects and focus on linear oscillations.

Bubbles may undergo two different types of deformations, represented in Figure 6.1, referred to as volume and shape (surface) oscillations.

- *Volume* or "breathing" oscillations (left panel of Figure 6.1) retain the bubble's spherical symmetry over the entire motion and represent the best-described oscillation mode. This is the case treated in Section 6.3. Here, as we saw, the bubble shape dynamics is governed by the time-dependent radius only, $R(t)$ (Equation 6.11). The resulting oscillation dynamics is thus described by ordinary differential equations like Equation 6.9. Besides R , the other model parameters are the equilibrium (static) radius, R_0 , the fluid pressure inside the bubble, \hat{p} , and outside, p , and ρ , η and σ , i.e. the density, (dynamic) viscosity and surface tension of the liquid, respectively, and finally, the polytropic exponent of the gas in the bubble, κ .
- *Shape*, i.e. non-spherical oscillations (see Figure 6.1, right), involve surface deformations (and dilations) but retain constant bubble volume. In this case, the polar (θ) and azimuthal (ϕ) angle variables are needed to describe the bubble radius dynamics, $R(\theta, \phi, t)$. Due to

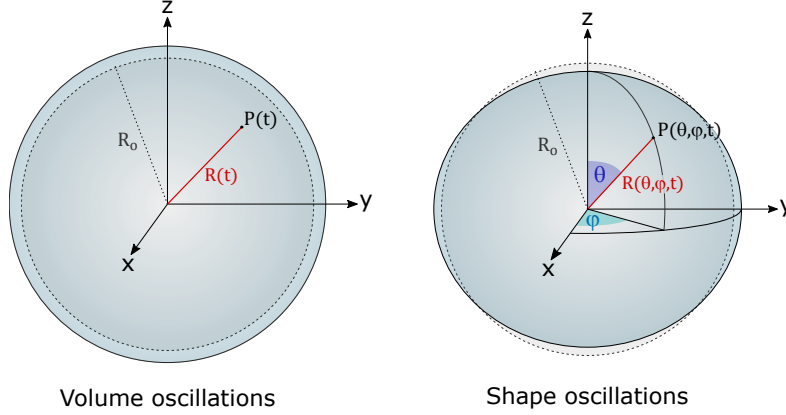


Figure 6.1: Oscillation modes of a free bubble in Cartesian (x, y, z) and spherical (r, θ, ϕ) coordinates. *Left:* a bubble undergoing volume oscillations remains spherical. Its dynamical shape is thoroughly described by the radial coordinate r , $R(t)$ being the radius at time t . *Right:* shape oscillations are non-spherical and occur at constant volume. The bubble spheroid is conveniently described adopting two further coordinates: θ (polar) and ϕ (azimuthal). The local radius is therefore $R(\theta, \phi, t)$. In case of axisymmetric deformations – where z becomes a symmetry axis – the local radius only depends on θ and t . In both panels, the bubble at rest has an equilibrium radius R_0 and the corresponding spherical profile is dashed and shaded in grey, while the deformed profiles are filled in blue.

the lower symmetry of the system, these modes are more complex to describe. A simplified treatment, valid for linear oscillations, is shown in the next section.

As will be pointed out in Section 7.3, combinations of the above described modes (e.g.: non-spherical and with time-dependent volume) can also take place, depending on the external forces acting on the bubble.

6.5 Non-spherical RP equation

As discussed in Section 6.3, the classical RP theory assumes that the bubble shape be spherical (i.e., *volume* oscillations). However, if the oscillation amplitude is sufficiently small, also *shape* modes can be described, to a good approximation, by simple forms like Equation 6.9.

A common procedure (see, for instance, Joseph [78], Brenn [106], and Prosperetti [107, 108]), is to assume that the bubble surface is only slightly perturbed from its equilibrium shape: by this way, the fluid-dynamical equation is linearised around the state of spherical symmetry. Following this perturbation approach, the local radius of the oscillating bubble at time t :

$$\mathbf{r}(\theta, \phi, t)|_S = [R(t) + l(\theta, \phi, t)] \cdot \hat{e}_r \quad (6.17)$$

$R(t)$ is the radius of a sphere of the same volume as the resting bubble (assumed to be constant), while l is the local deformation amplitude of an arbitrary point P on the surface S . Adopting a polar spherical coordinate system (R, θ, ϕ) centred at the bubble centroid (see Figure 6.1, right), θ and ϕ are the polar and azimuthal angles, and \hat{e}_r is the unit vector along the radial direction r . Since l is assumed to be much smaller than $R(t)$, it is appropriately expanded in terms of real orthonormal spherical harmonic functions $Y_n^m(\theta, \phi)$, of degree n and order m ,³ and factored into a time-dependent and a space-dependent component:

$$l(\theta, \phi, t) = \sum_{n,m} a_{n,m}(t) \cdot Y_n^m(\theta, \phi) \quad (6.18)$$

The summation spans over $n = 1, 2, \dots, \infty$ and $|m| \leq n$. $a_{n,m}(t)$ are complex time-dependent coefficients, while $Y_n^m(\theta, \phi) = P_n^m(\cos \theta) \cdot e^{im\phi}$, with $P_n^m(\cos \theta)$ the associated Legendre polynomial of the first kind.

Each spherical harmonic describes a surface mode with an oscillation pattern having n node lines in the θ -direction and $2m$ in the ϕ -direction. The coefficients $a_{n,m}$ are the oscillation amplitudes of the corresponding modes.

Further simplification arises in the case of *axisymmetric* deformations, as those assumed in our model and represented in Figure 6.2. Notably, the (azimuthal) ϕ -dependence disappears, together with the m parameter in Equation 6.18, and $P_n^m(\cos \theta)$ reduce to the Legendre polynomials $P_n(\cos \theta)$. Also in this case, different shape deformation modes are retrieved, corresponding to subsequent eigenmodes (see Section 6.6 for details).

Substitution of bubble radius as defined by Equation 6.17:

$$R(\theta, \phi, t) = R(t) + \sum_n a_n(t) \cdot Y_n(\theta, \phi) \quad (6.19)$$

into the traditional form of RP, Equation 6.9, yields a nonlinear differential equation. Upon linearisation, one obtains the following equation in the oscillation amplitude $a_n(t)$ [108]:

$$\ddot{a}_n(t) + B_n(t) \dot{a}_n(t) + C_n(t) a_n(t) = 0 \quad (6.20)$$

Where:

$$B_n(t) \equiv 3 \frac{\dot{R}(t)}{R(t)} + 2(n+2)(2n+1) \frac{\eta}{\rho R^2(t)}$$

³This approach is common to linearized descriptions of oscillator dynamics as a superposition of spherical harmonic contributions. A well-known example is given by quantum mechanics. Each of them represents an oscillation mode and obeys an independent equation of motion with characteristic frequency. Real functions $Y_n^m(\theta, \phi)$ can be obtained from a linear combination of the complex spherical harmonic functions $Y_n^{*m}(\theta, \phi)$.

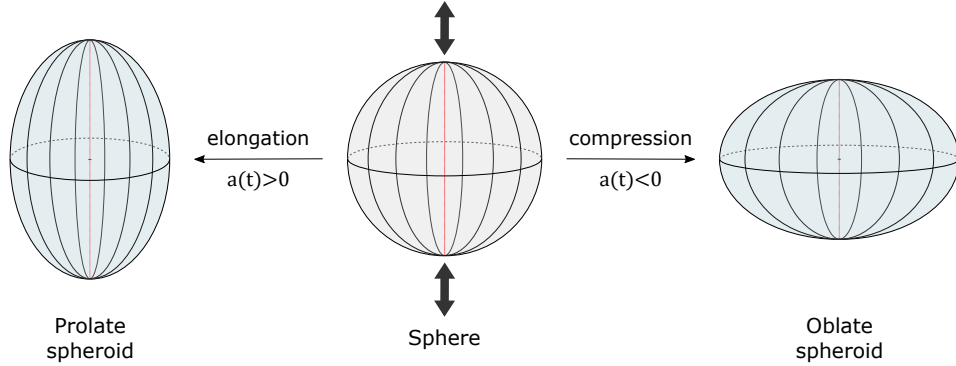


Figure 6.2: Axisymmetric deformations of an initially spherical bubble (centre), illustrated for the simplest case of sphere-to-spheroid deformation (quadrupolar mode, $n = 2$, or $n = 1$ of a constrained bubble). Vertical elongation (left, corresponding to $a_n(t) > 0$ in Equation 6.19) yields a prolate spheroid, while compression (right, corresponding to $a_n(t) < 0$) leads to an oblate spheroid. The vertical symmetry axis is shown in red.

and:

$$C_n(t) \equiv (n-1)(n+1)(2n+1) \frac{\sigma}{\rho R^3(t)} - (n-1) \frac{\dot{R}(t)}{R(t)} + 2(n-1)(n+2) \frac{\eta \dot{R}(t)}{\rho R^3(t)}.$$

R_o being the equilibrium bubble radius, ρ the fluid density, σ the interfacial tension and η the fluid viscosity.

In the relevant limit of constant $R(t)$ (i.e., $R(t) \rightarrow R_o = const$), Equation 6.20 reduces to $\ddot{a}_n(t) + \beta_n \dot{a}_n(t) + \omega_{on}^2 a_n(t) = 0$, with damping parameter:

$$\beta_n \equiv 2(n+2)(2n+1) \frac{\eta}{\rho R_o^2} \quad (6.21)$$

And natural frequency:

$$\omega_{on}^2 \equiv (n-1)(n+1)(2n+1) \frac{\sigma}{\rho R_o^3} \quad (6.22)$$

coincident with that obtained several years ago by Lamb [78, 89, 98].

Equation 6.20 is formally identical to Equation 6.12. However, unlike the spherical case, there exist a discrete spectrum of stationary nonspherical modes, with frequencies ω_{n0} , corresponding to the different terms of the spherical harmonic expansion of the bubble shape (Equation 6.19). Physically, this is due to the periodic boundary conditions naturally provided by the closed geometry of the finite-sized bubble surface.

In the most general case $R(t)$ is a periodic function of time. Performing the change of variables: $a_n(t) = b_n(t) \cdot (R(0)/R(t))^{3/2} \cdot \exp \left[-(n+2)(2n+1) \frac{\eta}{\rho} \int_0^t \frac{dt'}{R^2(t')} \right]$ and expanding Equation 6.20 in

terms of $\frac{R(t)-R_o}{R_o}$, one obtains, to the lowest-order terms, the well-known Mathieu equation:

$$\ddot{a}_n(t) + (\omega_{on}^2 - \beta_n^2 + \delta_n \cos(\omega t - \varphi_n)) a_n(t) = 0 \quad (6.23)$$

With:

$$\delta_n = \left\{ \left[-3\omega_{on}^2 + (n + \frac{1}{2})\omega^2 + 4\beta_n^2 \right]^2 + X_n^2 \omega^2 \right\}^{1/2} \quad \text{and} \quad \tan \varphi_n \equiv \frac{X_n \omega}{-3\omega_{on}^2 + (n + \frac{1}{2})\omega^2 + 4\beta_n^2}$$

with $X_n = 3(n+2)\frac{\eta}{\rho R_o^2}$. I do not pause on the solution of the Mathieu equation (6.23), which is very cumbersome and is reported in several papers (see, e.g. [109] and references in Section 7.3). Rather, I would like to emphasize the coupling between surface modes ($n \neq 0$) and the volume pulsation mode ($n = 0$), which may provide a mechanism for an indirect (parametric) excitation of surface modes (see Section 7.3).

Let us finally notice that the same results could also have been obtained by solving the linearised Navier-Stokes equations for incompressible flow (Equations 6.2 and 6.3), subject to the following boundary conditions at the interface⁴:

- a.** *Kinematic* boundary condition: the radial fluid velocities at the interface between the two different fluids must be identical. This is expressed as:

$$\hat{v}_r|_S = v_r|_S \approx \frac{\partial r(\theta, t)}{\partial t}$$

- b.** *Dynamical* boundary conditions, expressing the force balances as the bubble (drop) deforms:
- The *tangential stress* balance is a purely viscous term, as it assumes a uniform surface tension across the interface:

$$\hat{\eta} \left(\frac{1}{R_0} \frac{\partial \hat{v}_r}{\partial \theta} + \frac{\partial \hat{v}_\theta}{\partial r} - \frac{\hat{v}_\theta}{R_0} \right) \Big|_S = \eta \left(\frac{1}{R_0} \frac{\partial v_r}{\partial \theta} + \frac{\partial v_\theta}{\partial r} - \frac{v_\theta}{R_0} \right) \Big|_S$$

and considerably simplifies if either of the two fluids can be considered inviscid (e.g. bubble interior).

- The *normal stress* balance arises from the local curvature of the moving interface and depends on the interfacial tension σ (i.e. on temperature or chemical composition):

$$\left(p - \hat{p} + \frac{2\sigma}{R_0} \right) \Big|_S - \left(2\eta \frac{\partial v_r}{\partial r} - 2\hat{\eta} \frac{\partial \hat{v}_r}{\partial r} \right) \Big|_S - \frac{\sigma}{R_0^2} (2 + \Delta|_S) r(\theta, t) = 0$$

where: $\Delta|_S = \frac{1}{R_0^2 \sin^2 \theta} \frac{\partial}{\partial \theta} \left(\sin \theta \frac{\partial}{\partial \theta} \right)$. Under stationary conditions the well-known ‘‘capillarity condition’’, $\hat{p} - p = \frac{2\sigma}{R_0}$, is retrieved.

Under these conditions, the amplitude $a_n(t)$ can be shown to satisfy Equation 6.20.

⁴ v_r and v_θ are the radial and angular components of the velocity vector \mathbf{v} , carats denoting the inner fluid. $|_S$ means evaluation at the bubble (drop) interface. Other symbols were defined above in the section.



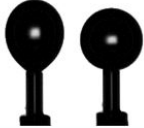
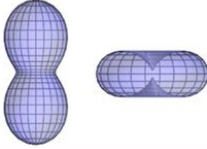
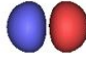

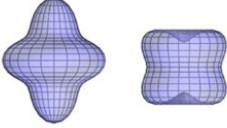
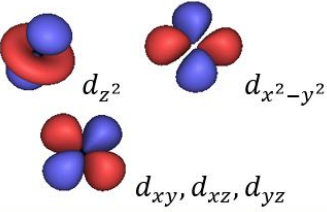

Mode number	Computed shape	Corresponding AO	A real bubble
$n=1$		 s	
$n=2$		 p_x, p_y, p_z	
$n=4$		 d_{z^2} $d_{x^2-y^2}$ d_{xy}, d_{xz}, d_{yz}	

Figure 6.3: Axisymmetric deformations of a bubble (drop). The lower-frequency eigenmodes are illustrated and compared to the shapes of the atomic orbitals (AO) corresponding to the same n (the degree of the Legendre polynomial P_n). The $n = 1$ mode corresponds to a mere translation of the center of mass without deformation (in the case of free bubbles) and has an analogue in the unpolarised orbital. The following modes always occur at non-zero frequencies. The last column shows the deformation of real bubbles attached to a capillary tip (pictures adapted from Refs. [84, 110]).

6.6 "Periodic table" of bubble oscillations

As observed in the previous section, shape oscillations differ from the volume ones in that they occur at various frequencies ω_{n0} , defined by Equation 6.22, corresponding to the different degrees of the spherical harmonic expansion of the bubble shape (Equation 6.19). In particular, the lowest vibration mode predicted by Equation 6.22 is the $n = 2$, corresponding to sphere-to-ellipsoid deformations of the bubble (quadrupolar mode), while the $n = 1$ is associated to degenerate ($\omega = 0$) displacements of its centre of mass. Higher modes occurring with even values of n ($n = 4, 6, \dots$) describe more corrugated (n -lobed) geometrical shapes, with no translation of the centre of mass.

Indeed, the equations describing bubble dynamics – namely the Navier-Stokes or related, like the Rayleigh-Plesset described in this chapter – bear a resemblance with the Schrödinger equation [13], the eigenvalue problem describing the fluctuations of electron density around atomic nuclei. The analogy appears much stronger if we write the bubble dynamics equations in the form

of eigenvalue problems, which turns out to be a convenient approach in several bubble studies, exploiting the relatively simple Hamiltonian formalism [111–113].

It should be noticed that the oscillation eigenfrequencies, whatever their nature, are intimately related to symmetry. In the case of the Schrödinger equation, we see that for the hydrogen atom it has spherical symmetry (s orbitals). Higher atoms, whose electron configurations have less symmetry (p , d , and f orbitals), break the symmetry of the corresponding equation, leading to a splitting of eigenvalues (i.e., of spectral lines). A similar symmetry breaking also takes place with oscillating bubbles (drops). Taking the RP as an example, it has spherical symmetry if the bubble is free from constraints and subject to an isotropic external environment, then it undergoes splitting as some kind of asymmetry is introduced. The conditions in which this degeneracy may be broken were briefly discussed in Section 6.4.

Figure 6.3 highlights the analogy between axisymmetric bubble deformations (left: computed shape for a free bubble; right: a real bubble pinned to a capillary) and electron density fluctuations around a nucleus (i.e., shapes of atomic orbitals, in the centre), for modes with $n = 1, 2, 4$. Accordingly, the $n = 2$ mode corresponds to p orbitals, the $n = 4$ to d orbitals, the $n = 6$ to f orbitals, and so forth, thereby forming a "periodical table" of shapes whose Aufbau principle is given – at least for free bubbles⁵ – by the order n of increasing eigenfrequency.

Interestingly, this analogy between predicted eigenmodes and observed shapes can be extended to real oscillating cells, like the RBCs illustrated in Figure 5.1 (page 23).

6.7 Bubbles vs drops

So far, we have considered exclusively oscillating gas bubbles, disregarding drops, since the former represent the more studied system. However, both bubble theory, as well as our experiments, can be extended to liquid drops as well, such that, to our scopes, the two systems can be almost treated as synonyms. Some differences, however, are worth noticing:

- Gaseous bubbles may undergo both shape deformations, at constant bubble volume, and volume or “breathing” deformations, preserving the spherical shape. By contrast, only the former are allowed for liquid drops (at commonly applied pressures). Breathing modes are by far more studied in literature, owing to their relative simplicity conferred by the spherical

⁵For constrained bubbles things get more involved, since two modes may share the same characteristic frequency, or the above-defined ordering of modes can be altered [13].

symmetry. Since cells are incompressible bodies, we will neglect breathing modes. focusing on the more complex shape fluctuations of both bubbles and drops.

- The interior of gaseous bubbles is practically inviscid, while the inner viscosity plays a role in drops thereby increasing dissipation. Likewise, the inner density $\hat{\rho}$ of a drop is not negligible as it is for air bubbles.

In this case, Equation 6.22 can be extended to [78, 98]:

$$\omega_{n0}^2 = \frac{\sigma}{R_0^3} \frac{n(n-1)(n+1)(n+2)}{n\rho + (n+1)\hat{\rho}}. \quad (6.24)$$

If we compare Equation 6.24 to 6.22, we also observe a frequency lowering in drops with respect to bubbles of the same size, since the higher density results in higher inertia, together with the decrease in interfacial tension σ .

As far as the damping is concerned, a form similar to Equation 6.21 is retrieved [114, 115]:

$$\beta_{n0} = \frac{(n+1)(n-1)(2n+1)\hat{\eta} + n(n+2)(2n+1)\eta}{[(n+1)\hat{\rho} + n\rho]R_0^2}. \quad (6.25)$$

By comparing the two forms it can be seen that drop resonances at $n \geq 2$ are broader than those of bubbles.

6.8 Damping

The derivation of the RP Equation 6.9 and the related forms proposed in the previous section exclude any sort of damping during bubble oscillations. This hypothesis may be more or less acceptable, depending on the system parameters. Extensive studies on this topic have followed the RP formulation, of which Ref. [116] provides an exhaustive review. Here we limit ourselves to reporting that damping arises from three main contributions:

- *Viscous damping*, caused by liquid viscosity;
- *Thermal damping*, due to thermal conduction between the gas and the surrounding liquid;
- *Radiation damping*, determined by liquid compressibility through acoustic radiation.

Commonly, their joint effect can be accounted for in Equation 6.9 or similar forms by considering an effective liquid viscosity $\mu_E = \mu_L + \mu_T + \mu_A$ (instead of the fluid viscosity μ_L), arising from the sum of each contribution, respectively.

Concerning the relative contributions of the three effects, it was found [117] that, for linear oscillations of individual free bubbles: A) thermal damping is dominant when the bubble is driven below resonance; B) radiation damping, on the contrary, prevails above resonance; and C) viscous damping is generally negligible, except for small (micrometric) bubbles, where it becomes dominant up to frequencies sufficiently exceeding the resonance frequency.

Viscous damping. Inertial terms

Although viscosity is a typical source of vorticity (see next chapter), several irrotational approaches have been developed to account for viscous dissipation around an oscillating bubble. A critical analysis of the problem has been performed by Joseph and coworkers, as summarised in Ref. [78]. Such approaches are valid if viscous forces are confined to the immediate proximity of the surface of the bubble, i.e. if the so-called "Stokes layers" are relatively thin in comparison with the wavelength of the distortion mode [89, 118, 119]. In this case, the fluid velocity can be expressed as the gradient of a potential ϕ and the Navier-Stokes equations reduce to the simple Bernoulli equation, which does not contain viscosity explicitly.

In the so-called *viscous potential flow* method [?], the viscosity effect is accounted for by a perturbative correction to the pressure field and by the viscous term in the normal stress balance at the interface. An alternative approach, called the *dissipation approximation* [?], derives from the evaluation of the mechanical energy equation on the fluid domain, imposing zero shear stress in the liquid and continuous tangential stress at the gas-liquid interface. In particular, for a spherical bubble viscous dissipation is related to the fluid velocity field \mathbf{u} by:

$$\frac{d}{dt} \int_V \rho \frac{|\mathbf{u}|^2}{2} dV = - \int_A \mathbf{n} \cdot \mathbf{T} \cdot \mathbf{u} dA - \int_A \mathbf{n} \cdot 2\mu \mathbf{D} \cdot \mathbf{u} dA \quad (6.26)$$

Where ρ and μ are the fluid density and viscosity, \mathbf{T} and \mathbf{D} are the stress and the strain-rate tensors, \mathbf{n} is the unit vector normal to the surface element dA and A and V are the bubble surface and the volume of the bulk fluid respectively. The viscous dissipation, proportional to the resonant peak width, is represented by the last term of Equation 6.26.

Both methods yield similar quantitative results, especially for moderate viscosities and relatively small eigenmode numbers, predicting the effects of viscosity on both the peak width (leading to expressions like Equation 6.13 and 6.21 under the assumption of purely viscous dissipation) and on the resonance frequency (i.e., shift from oscillatory to monotonically decaying waves over a certain viscosity threshold).

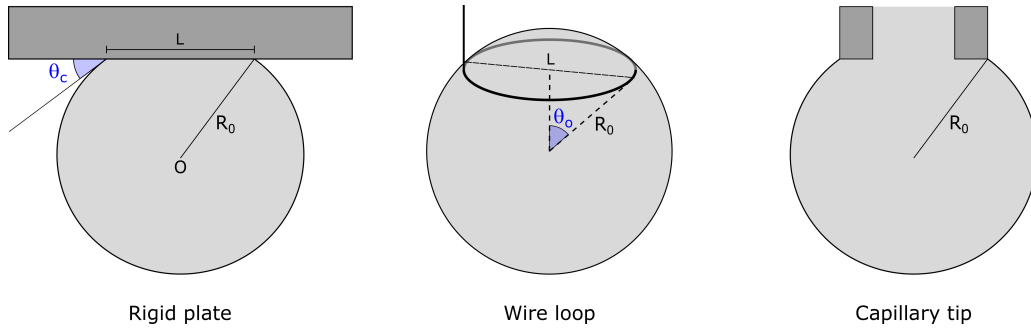


Figure 6.4: Common constraints used in bubble/drop studies. *Left:* tethering to a plane surface (e.g. glass). The equilibrium bubble shape is a spherical segment. The value of L , as well as of contact angle θ_c , will depend on wetting ($L \rightarrow 0$, $\theta_c \rightarrow 0$ meaning zero wetting, while $L \rightarrow \infty$, $\theta_c \rightarrow \pi$ full wetting). *Centre:* tethering to a wire (glass or metallic) loop. The bubble retains an approximately spherical shape (provided the wire thickness is much smaller than the ring diameter L and wetting is negligible) and the contact surface tends to a circular line of diameter L . *Right:* tethering to a capillary tip. The dead volume of fluid inside the capillary (and the related contact surface), depending on the experimental conditions, must be considered as well. In all cases, buoyancy effects leading to deviations from constant curvature, observable in large bubbles and especially drops, have been neglected for simplicity.

6.9 Free vs constrained bubbles

To avoid disturbances due to buoyancy (and to coalescence, when multiple bubbles are considered), it is common practice in experiments to constrain the bubble (drop) to a solid support. Typical configurations, illustrated in Figure 6.4, are the wire loop (left), the rigid plate (centre) and the capillary tip (right). Likewise, as we will discuss in Chapters 15 and 16, the bubbles used in our experiments are not freely floating, but anchored to one or two solid electrodes (see Figure 6.5).

Albeit necessary, this practice inevitably modifies the inherent properties of the capillary surface (see Section 3.3) and hence, the experimentally observed resonance modes. The most prominent effects are the following:

- Preference for nonspherical (e.g., axisymmetric) modes, due to the decreased symmetry of the system;
- Onset of eigenmodes which are degenerate ($\omega = 0$) in free bubbles/drops, like the ones with odd values of n ($n = 1, 3, \dots$), corresponding to translational modes [120, 121];
- Variation in the resonance frequency of a given mode.

Knowing the extent of such modifications allows to properly assign the observed resonance peaks and to extract information concerning the restoring force (e.g., surface tension) from them.

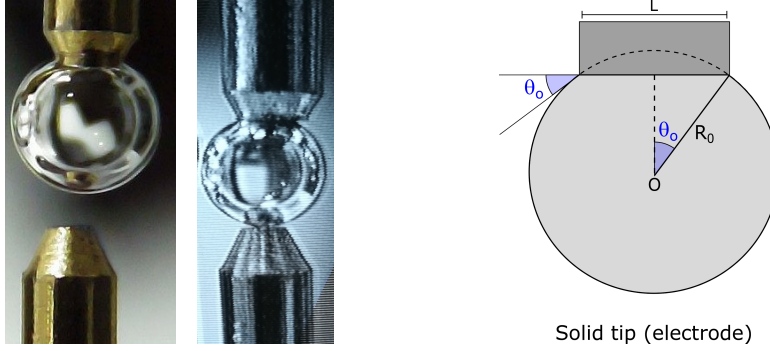


Figure 6.5: *Left:* a bubble ($R_0 = 0.76$ mm) anchored to an upper, solid electrode and a doubly-anchored bubble ($R_0 = 0.6$ mm), from our two-bubble experimental apparatus. In both pictures, the diameter of the anchoring electrodes is $L = 1$ mm. *Right:* schematics of a bubble tethered to a solid tip (electrode) of diameter L . If the profile is spherical, the contact angle θ_c and the attachment angle θ_o are equal.

This entails a good understanding of the interaction between the bubble (drop) and the solid boundary, as a function of the adopted experimental setup and of the external driving (acoustic, mechanical, electric). Accordingly, many attempts have been made by numerous researchers [110, 115, 120–126] for different rigid boundaries. Some of them have also addressed the case of multiple constraints, of great relevance, for instance, to microfluidics. However, the influence of the boundary on the bubble dynamics in an oscillating pressure field remains unclear.

On the whole, a pivotal role is found to be played by surface wetting, via the contact angle θ_c , affecting the inertial mass of the system in a non-monotonic way. Accordingly, the predicted l -mode eigenfrequency $\Omega_{0,l}$ follows a relationship of the kind:

$$\Omega_{0,l} = \Omega_{0,l}^* \cdot f(l, a) \quad (6.27)$$

where $\Omega_{0,l}^*$ is the frequency of the corresponding mode for a free bubble and $f(l, a)$ depends on the mode l and on the attachment conditions via the (θ_c -related) parameter a .

6.9.1 Comparison with our system

To get a physical insight into the dynamics of our tethered bubbles and estimate the anchoring-dependence of the observed spectral features, we will consider the literature models which best match the attachment geometry shown in Figure 6.5. A distinction will be made between volume and shape oscillations (Section 6.4).

Volume mode

To describe the breathing oscillations of a bubble anchored to a solid electrode we will follow the results by Maksimov [124], referred to a gas bubble attached to a rigid plate. The geometry of the problem is illustrated in the left panel of Figure 6.4. The equilibrium shape profile is represented by a spherical segment of radius R_0 , L being the diameter of the contact ring. Besides R_0 , the key parameter to predict the bubble behaviour is the *contact angle* θ_c with the adjacent solid surface. Its magnitude depends on wetting of the material of the boundary by the liquid and on the surface tension of the bubble wall. The analytical approach makes use of image theory, whereby the rigid boundary is replaced by the mirror image of the bubble relative to the boundary plane.

The fundamental frequency of the breathing mode for the tethered bubble is found to be [124]:

$$\Omega_0(R_0, \theta_c) = \Omega_0^*(R_0) \cdot f(\theta_c) \quad (6.28)$$

with $\Omega_0^*(R_0) = \sqrt{\frac{3\kappa\hat{p}}{\rho R_0^2}}$ being the Minnaert frequency of the *free* bubble⁶ [25] (see Section 6.3). As the boundary-dependent part, $f(\theta_c)$, takes an integral form, closed solutions of Equation 6.28 can be obtained only for a set of particular values of θ_c . Notably, in the limit of $\theta_c \rightarrow 0$ – that is to say, when the bubble is tangent to the solid substrate at a single point (i.e., zero wetting or spreading) – it is obtained $\Omega_0 = \sqrt{\ln 2} \Omega_0^* \approx 0.83 \Omega_0^*$ (see also [127]). The behaviour of Ω_0 over θ_c is represented in Figure 6.6 (solid line, frequency normalised on the normal mode Ω_0^* of a free bubble of equal volume), showing that for moderate θ_c values, say up to $\pi/2$, Ω_0 is of the order of $0.8 \Omega_0^*$, while at higher values it may exceed Ω_0^* . However, values of θ_c larger than $\pi/2$ (corresponding to a hemispherical equilibrium shape of the bubble), are not of great interest, since we are no more in the presence of a "bubble". From a physical standpoint, the results for $\theta_c \leq \pi/2$ indicate that the constraint hampers acceleration of liquid at the bubble wall. This leads to an increase in the inertial mass, and thus to a *lowering* of the natural frequency of the volume oscillations. Similar results are obtained also for bubbles attached to a wire loop of diameter L (Figure 6.4, centre), where $f(\theta_c)$ appearing in Equation 6.28 takes the simpler form $\sqrt{1 - \frac{a}{R_0 \sin \theta_c}}$, $a \ll L$ being the wire radius [126].

As far as viscous damping is concerned, it is obtained (under the assumption of inviscid and irrotational fluid flow) [125]:

$$\gamma_0 = \sqrt{\frac{2\omega\eta}{R_0^2}} F(\theta_c) \quad (6.29)$$

which can be related to the damping factor of the free bubble Equation 6.13. $F(\theta_c)$ is the anchoring-dependent factor, whose behaviour is reported in Figure 6.6 as a dashed line. As it can be seen,

⁶ κ is the polytropic exponent, \hat{p} is the equilibrium pressure in the bubble (equal to 1.4 for air), ρ the fluid density

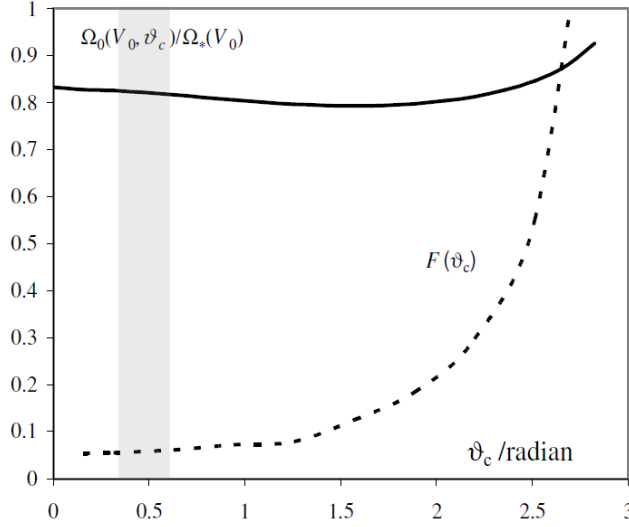


Figure 6.6: Breathing oscillations of a bubble of fixed volume V_0 tethered to a plane surface (see left panel of Figure 6.4) at varying contact angle θ_c (in radian units), from Ref. [125]. *Solid line:* natural frequency $\Omega_0(V_0, \theta_c)$, normalised on the normal mode $\Omega_0^*(V_0)$ of a free bubble of the same volume. *Dashed line:* normalised viscous damping $F(\theta_c)$ (Equation 6.29). The area shaded in gray encloses the highest variability region of θ_c in our experiments (typical figures lying in the range 0.45–0.50 rad).

unlike the resonance frequency, $F(\theta_c)$ can vary as much as two orders of magnitude over θ_c . In particular, viscous damping is generally increased, owing to the greater dissipation near rigid walls in comparison with the free fluid-fluid interface, as well as to a contact line dissipation effect (see Section 3.3). However, within the θ_c interval of our experiments (shaded in gray in Figure 6.6), both the resonance frequency and viscous damping stay approximately constant.

Shape modes

The effect of contact line on the shape oscillations of bubbles and drops has been widely investigated in the literature, taking into account different constraint geometries, like the above-mentioned capillary tip (see, e.g., [110, 121]) and wire loop [120, 122].

A geometry similar to our setup, consisting of a bubble/drop supported on a slightly concave solid support, has been described by Vejrazka [115]. Here, the reported numerical values show that: *a)* the eigenfrequencies of a given l -th mode vary as a function of the contact angle θ_c in a non-monotonous way and may assume higher values than the corresponding free-bubble case; *b)* the relative amplitudes of the resonance peaks in a spectrum also vary with θ_c , such that, for instance, the highest-intensity experimental peak is not necessarily, as one would expect, the $l = 1$.

Chapter 7

A sadder and wiser view: nonlinear effects

So far, when describing single-bubble oscillations, we only considered *linear* effects, as we assumed small-amplitude deformations. However, nonlinearity plays a prominent role in bubble dynamics, even for slow fluid motions, especially in the case of multi-bubble systems [97].

The nonlinear response of a fluid subjected to an acoustic field can be explained in terms of the law of momentum conservation (Euler equation):

$$\frac{\partial v}{\partial t} + \boxed{v \frac{\partial v}{\partial r}} = -\frac{1}{\rho} \frac{\partial p}{\partial r} \quad (7.1)$$

where v is the fluid velocity at time t along direction r , ρ is the density and $p(r,t)$ the pressure. While for ideal linear flows the nonlinear (boxed) term of Equation 7.1 can be neglected, this is not the case in most real systems.

In the following sections we will discuss some intriguing consequences of this observation.

7.1 Acoustic streaming and microstreaming

Acoustic streaming is a steady fluid flow formed by the viscous attenuation of a propagating sound wave [128]. This phenomenon seems to contrast with the basic notion that fluids undergoing small-amplitude (linear) oscillations have a zero time-averaged net displacement. In fact, in real fluids, the nonlinear term appearing in Equation 7.1 may result in second-order mean flow velocities, which are much lower in magnitude than the (first-order) oscillatory flow, but, unlike the latter, do not cancel out at each oscillation cycle and hence generate a net drift of the fluid.

The occurrence of streaming strictly depends on the fluid flow properties and, as implied by Equation 7.1, it is accompanied by a gradient in the acoustic field. In particular, streaming is significant in case of:

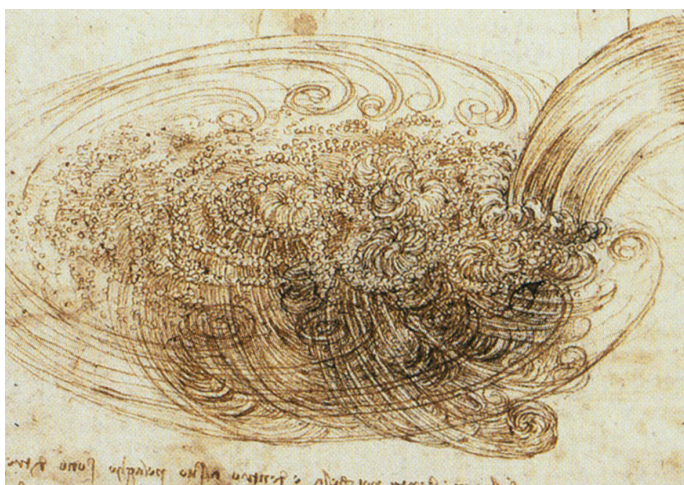


Figure 7.1: Leonardo da Vinci's study of turbulence (1508–1513). The drawing illustrates the velocity streamlines of water entering in a tank from a channel, giving rise to vortices around the main flow.

- a) Large v : *acoustic streaming*.
- b) Large $\frac{\partial v}{\partial r}$: *acoustic microstreaming*.

Mechanism

The first theoretical description of acoustic streaming was given by Rayleigh in 1884 [129]. Since then, a large volume of related work has been published, complementing Rayleigh's theory (see, e.g., [128, 130]) and providing experimental insights (see, e.g., [131–133]), as well as numerical solutions to existing theoretical models and application problems [134].

The main (but not only) mechanisms underlying acoustic streaming involve viscous attenuation of an acoustic wave [128], either within the bulk fluid or in the boundary layer with a solid (comparable or greater in length than a quarter of the acoustic wavelength) [135]. The first case gives rise to the so-called Eckart streaming [136]. Basically, as an acoustic wave propagates in a fluid, part of its energy is adsorbed by the fluid, at a rate proportional to the square of the sound frequency (Stoke's law of sound attenuation). The consequent attenuation of the wave amplitude generates a gradient in the pressure amplitude along the propagation distance from the wave source. This results in a steady momentum flux, forming a jet of fluid in the direction of acoustic propagation. The second case behaves similarly, but the dissipation into the boundary layer is larger than bulk dissipation, because of the steep velocity gradient that is formed perpendicular to the solid boundary as the acoustic wave propagates parallel to the boundary. This argument provides an explanation to

the phenomenology observed in Section 4.1.

When the boundary layer is a gas-liquid interface, the gas compressibility comes into play and the associated streaming flows are termed cavitation microstreaming [137–139]. Microstreaming is usually noticeable when the obstacle is a bubble, because of its special ability to locally amplify and transform an acoustic field. In short, bubble oscillation results in an increase of acoustic scattering so that the local amplitude of the bubble-scattered field is much larger than that of the incident field [128]. The consequence of this is a much larger boundary layer oscillation and hence higher velocity flows. The first detailed characterization of microstreaming around an oscillating microbubble was carried out by Elder [137]. For more recent works, see, for instance, [139–143].

Streaming patterns

Back in the XVI century, Leonardo da Vinci addressed the problem of turbulence and represented water flow as curved lines forming tight vortices (Figure 7.1). First observations of streamlines concern the patterns assumed by sand and fine powders on Chladni's vibrating plates [144]. The same principle is at the basis of Particle Image Velocimetry (PIV), the optical method commonly employed for instantaneous visualisation of fluid velocity flows [132, 133] (see Figure 7.4).

Streaming patterns may vary considerably from one another in velocity, length scale and geometry (e.g., jets vs vortices), depending on the mechanism of acoustic wave dissipation [145]. However, a common characteristic of acoustic streaming is that the flows are time-invariant, as long as the acoustic excitation is kept unaltered: in other words, they are stationary from an "Eulerian" (velocity field) point of view, albeit dynamic from a "Lagrangian" (single-particle) perspective.

Let us now look at Figure 7.2, showing microstreaming around oscillating bubbles. As reported in Ref. [138], the observed patterns vary on the bubble radius and on the amplitude, frequency and mode of vibration.

It is easy to imagine that, in the case of two (or more) vibrating bubbles, streaming flows may impact both the direction and the length scales of their mutual hydrodynamic interactions. Namely, anisotropic interaction patterns and long-range interactions are expected, which could not be accounted for by purely irrotational models.

Relevance and applications

Streaming phenomena typically give rise to vortex fluid flows, especially for what concerns microstreaming. An interesting consequence is that fluid mixing is considerably enhanced (with

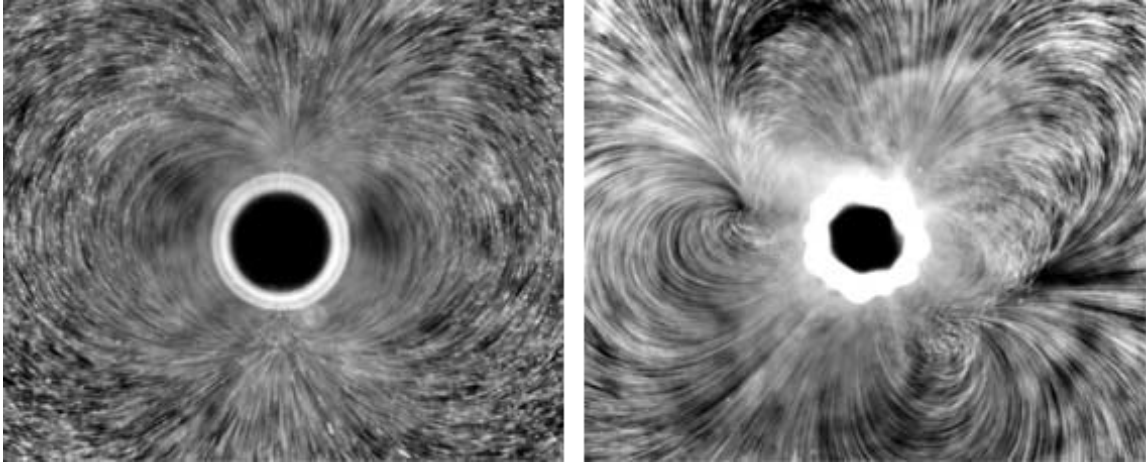


Figure 7.2: Microstreaming patterns around an oscillating supported bubble. *Left:* volume oscillations; *right:* shape oscillations ($n = 6$). The reported streak photographs were taken along the plane of the solid support by Manasseh et al. [138], as part of a micro-PIV study.

respect to diffusion rates) whenever cavitation bubbles are present [138, 139, 146]. This finds application, for instance, in engineered micromixers operating on volumes of order of $1 \mu\text{l}$ [147], of great interest for biochemical assays, or in enhanced mass transfer in sonochemistry [148]. Recent biological applications of microstreaming involve sonothrombolysis [149] and sonoporation [150], based on the possibility to generate local shear stress on cell membranes [151], in a more gentle way than inertial cavitation (see Section 4.1) and hence less likely to cause cell death.

7.2 Bjerknes forces

Another nonlinear effect that can be important for bubbles placed in an acoustic field is represented by the Bjerknes forces. Named after their first observers [40], they are commonly divided into two types: the force on an individual bubble is called the acoustic radiation pressure or the *primary* Bjerknes force, while that between bubbles is called the *secondary* (or mutual or merely) Bjerknes force. However, both are identical in nature and originate from the finite wavelength of sound waves crossing the liquid.

7.2.1 Primary Bjerknes forces

Propagation of a finite-wavelength pressure wave implies an instantaneous pressure gradient in the liquid (right term in Equation 7.1, which in turn raises the nonlinear term). Like any other pressure

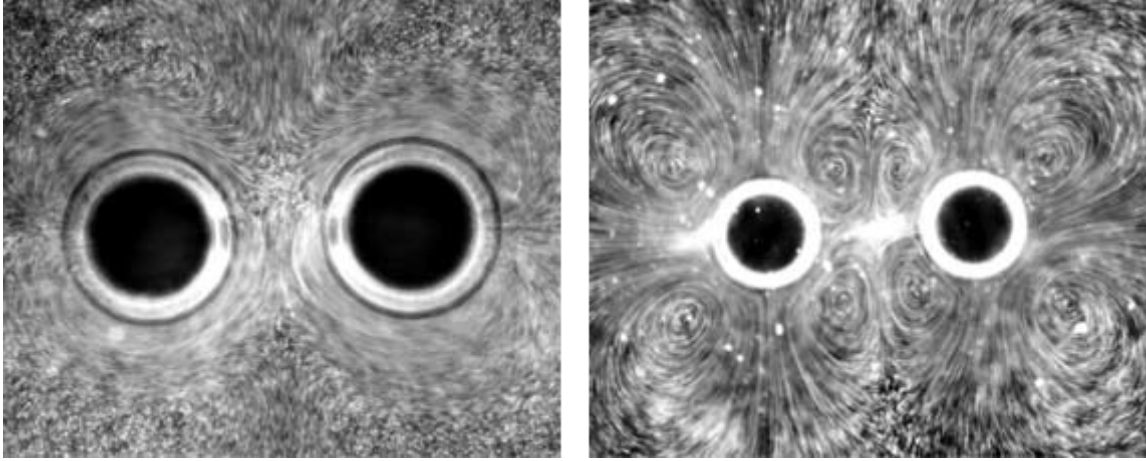


Figure 7.3: Streaming flows between two supported bubbles. *Left:* bubbles undergoing volume oscillations; *right:* bubbles undergoing mutual translations along their joining axis. Images taken from [138].

gradient, this produces an instantaneous force F_i on the bubble in the direction of the pressure field x_i (see Figure 7.5). In the case of a spherical bubble we have:

$$F_i = -\frac{4}{3}\pi R^3 \left(\frac{dp}{dx_i} \right) \quad (7.2)$$

with R being the instantaneous radius of the bubble, governed by the Rayleigh-Plesset equation (Equation 6.9, Section 6.3). Since both R and $\frac{dp}{dx}$ contain oscillating components, their combination in Equation 7.2 will lead to a nonlinear, time-averaged component in F_i , that we will denote by \bar{F}_i . A good approximation for this force component, valid if p_a is small and the natural frequency of the bubble ω_0 is not too close to the excitation frequency ω , is found to be (see, e.g., [152, 153]):

$$\bar{F}_i \approx -\frac{\pi \kappa R_0 p_a^2 \sin(2\kappa x_i)}{\rho (\omega^2 - \omega_0^2)} \quad (7.3)$$

This is the form of the *primary* Bjerknes force. Here, R_0 is the equilibrium radius of the bubble, ρ the liquid density, and p_a and $\kappa \propto \omega$ the density and wavenumber of the applied pressure field. If $\omega < \omega_0$, then the force will cause migration of the bubbles away from the nodes in the pressure field and toward the antinodes (points of largest pressure amplitude). On the other hand, if $\omega > \omega_0$, the force is directed towards the nodes.

Note that Equation 7.3 is an average form. Since the bubble natural frequency is related to the radius (see Section 6.3, Equation 6.14), which may vary during excitation (particularly if $\omega \approx \omega_0$), primary Bjerknes forces may produce some interesting bubble migration patterns in a stationary

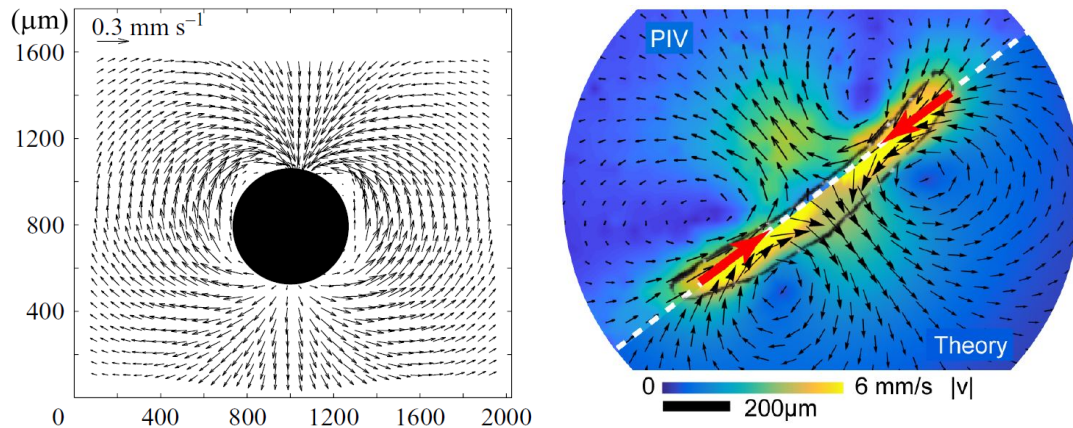


Figure 7.4: Examples of streaming flow visualisation. *Left:* micro-PIV velocity field of a supported bubble undergoing radial oscillations (the same shown in Figure 7.2, left) along the plane of the solid support. *Right:* Particle Image Velocimetry (PIV) measurement on a vibrating protist (image retrieved from [73]) against numerical calculation. The velocity vector field is indicated by arrows. PIV involves photographic recording of the motion of microscopic particles, seeded in the fluid, that follow the flow dynamics. Photographic recordings are then processed to determine the particle motion, and hence the flow velocity.

sound field. An example is provided by the "bubble dancing" phenomenon abundantly reported in the literature (see, for example, [154, 155]).

7.2.2 Secondary Bjerknes forces

An oscillating bubble may be considered itself as a source of acoustic waves. Hence, in multi-bubble systems, the contributions coming from each oscillating bubble combine with the effects of the applied external field (Equation 7.3) and cause the bubbles to interact with each other. These inter-bubble forces are in all ways similar to the primary Bjerknes forces, although they are customarily distinguished and denoted as *secondary* Bjerknes forces [152, 156–162].

The observed interacting patterns often give rise to bubble clusters or "grapes" (resembling the one shown in Figure 4.3), depending on the features of the bubbles and of the applied field.

7.3 Inter-mode coupling

Theory of coupled oscillators describes the coupling between two (or more) linear oscillators as a linear combination of their normal modes. A requisite for effective coupling is that they display similar energy and symmetry. However, these "selection rules" are often broken in real systems,

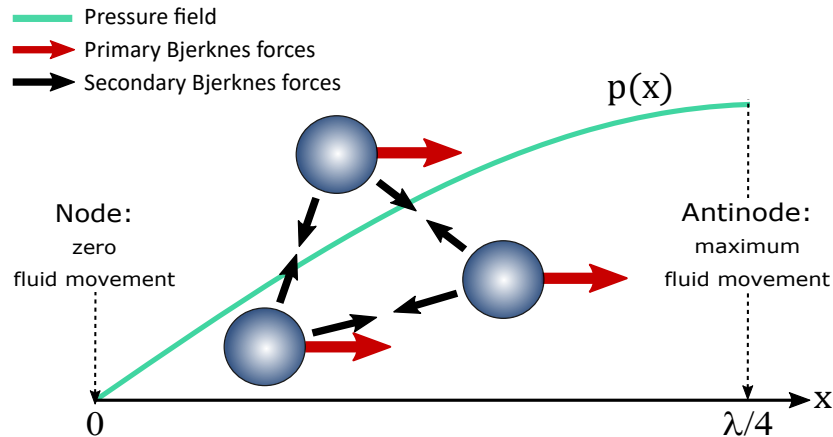


Figure 7.5: Oscillating bubbles (blue spheres) immersed in a pressure field of wavelength λ (green curve on the background) experience an average force, called the *primary* Bjerknes force (red arrows), along the field direction x . The force depends on the bubble's resonance frequency and in this case is directed towards the pressure antinodes. Each bubble, in turn, exerts *secondary* Bjerknes forces (black arrows) towards the other bubbles, which can be either repulsive or attractive like in this picture.

where most coupling events are intrinsically nonlinear. A prominent example, familiar to chemists, is given by atomic and molecular orbitals, in the so-called orbital hybridisation and in the formation of molecular bonds. In any case, the coupling strength depends on energy and symmetry differences.

Referring to our bubble system, two cases are worth mentioning:

- a) Coupling between different oscillation modes, within a single oscillating bubble.

In Chapter 6, we described the overall shape of a bubble as a linear combination of individual eigenmodes (Equation 6.20), with different symmetries and characteristic frequencies. Accordingly, we can assume each peak to represent an individual oscillation mode (e.g., $n = 2$, $n = 4$ etc.). In reality, inter-mode coupling is widely documented in literature [97, 109]. Not only combinations of different shape modes are observed (occurring at rather similar frequencies), but also between shape and volume modes (the frequency gap being of one order of magnitude), up to vibro-translational coupling, yielding "dancing" phenomena. Below we will consider a relevant case of inter-mode coupling.

- b) Coupling between different oscillation modes from two (or more) bubbles.

Indeed, our experiments described in Chapter 17 report the interactions between the $n = 2$ mode of one bubble (the *master*) and the $n = 1$ mode of a second bubble (the *slave*). Hence,

as we will see, the coupling between two identical oscillators, sketched in Section 8.1 and in Figure 8.1, is an oversimplified picture of bubble-bubble interactions not reflected by our experiments.

Careful choice of the experimental setup, especially the geometry, frequency and intensity of the excitation field, can strongly minimise (or emphasize at will) the occurring of such nonlinear couplings by focusing on specific oscillation modes, in order to get results comparable with theoretical predictions.

Parametric resonance

In the linear steady-state limit, a bubble driven by an isotropic pressure field will exhibit volume oscillations of the same frequency as the applied field, with an amplitude maximum at the breathing-mode resonance. As observed in Chapter 6, the excitation of shape modes requires a loss of degeneracy of the system, for instance some anisotropy in the applied pressure field or in the surrounding environment.

However, shape modes can be excited as well in isotropic environments, as long as the amplitude of the applied field exceeds a certain threshold. This phenomenon is known as *parametric resonance* and arises from a form of nonlinear coupling between the volume and shape bubble modes. The lowest-order description of this effect is based on similar arguments to those used in Section 6.5, leading to Mathieu equations like Equation 6.23, and was first given by Benjamin and Strasberg [163]. A higher-order approximation was provided by Eller and Crum [154].

Parametric resonance has been exploited to excite shape modes by means of acoustic field (see, e.g., [?, 164]). The excited mode will be the one whose natural frequency is closest to the subharmonic frequency of the applied driving, the minimum frequency being that of the breathing mode, ω_0 . Hence, the most easily excited surface mode is the $n = 2$, the threshold of which has a minimum in the vicinity of $\omega = 2\omega_0$. The intensity and frequency of the threshold are very sensitive to the external parameters [126, 165]. Recent studies have addressed transient and near-threshold processes, motivated by the discrepancies between the existing theory and the experimentally observed thresholds [165, 166].

Chapter 8

Hypotheses on coupling mechanisms

8.1 A naive (wrong) view of bubble interactions: Interacting bubbles as coupled oscillators

In Chapter 6 we drew an analogy between the oscillations of isolated bubbles and drops and the behaviour of spring-mass systems, based on the (harmonic) oscillator theory. We may then wonder whether the analogy can be extended to the case of two nearby interacting bubbles (drops), that is, if these objects may behave like coupled harmonic oscillators. Based on this argument, we formulated a working hypothesis on the interaction between two oscillating bubbles (identical for simplicity), as described by Figure 8.1:

- Two equal bubbles set at infinite – i.e., sufficiently large – distance will act as degenerate oscillators (panel **A** of the figure).
- When the two bubbles are brought at a finite distance D apart, the displacement of the fluid near their surfaces causes them to interact: the two oscillators are thus coupled by hydrodynamic motions. This breaks down the degeneracy of their frequencies, giving rise to low-frequency (populated) and high-frequency (unpopulated) states, as shown in panel **B**. In other words, the system evolves from a separated to a bound state.

Under this hypothesis, the red shift in the natural frequencies of the two oscillators gives a measure of their interaction strength.

This mechanism is similar to that employed to describe the formation of molecular bonds from atomic systems (recalling the analogy evidenced in Section 6.6), as well as the London or the van der Waals forces in molecular systems, where *synchronised* electron fluctuations determine significant attractive forces among apolar molecules [167, 168].

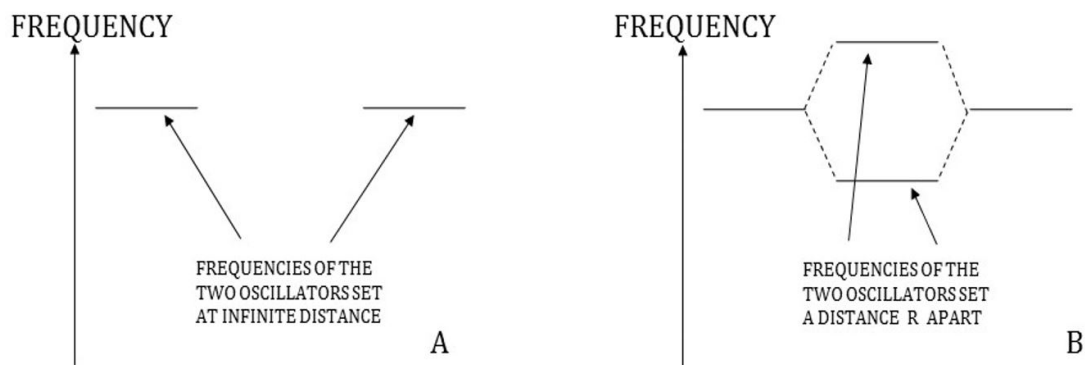


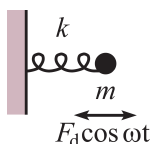
Figure 8.1: Vibrational behaviour of two identical harmonic oscillators (like two identical atoms, or bubbles undergoing small deformations). *Panel A:* independent oscillators (set at an infinite distance D) are degenerate. *Panel B:* interacting oscillators (finite distance D) give rise to frequency splitting.

Albeit intriguing, this hypothesis turned out to be wrong. As we shall see in the following chapters, other more sound models work better in explaining the experimental findings.

8.2 Coupled oscillators

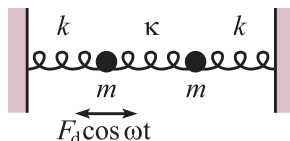
In this section we will describe the coupling mechanism between two spring-mass harmonic oscillators (mimicking the interacting bubbles), subject to (viscous) damping and selective excitation of one of the two masses.

Let us first consider a driven-damped harmonic oscillator of mass m and spring modulus k , immersed in a viscous fluid and excited by a periodic force $f(t) = F_d \cos \omega t$:



As is known, its natural frequency is $\omega_0 = \sqrt{k/m}$.

One first coupling option is to add a second identical oscillator, connected to the first one via a spring of modulus $\kappa \neq k$. We obtain the two-mass, three-spring system depicted below:



Here, the second mass, not directly excited, will respond as a "receiver" to the oscillations of the first mass ("transmitter"), excited by $f(t)$. The dynamics of the system can be expressed by two coupled $F = ma$ equations in x_1 and x_2 , i.e. the displacements from the (unstretched) equilibrium positions of the left and the right mass, respectively:

$$\begin{aligned} m\ddot{x}_1 &= -kx_1 - \kappa(x_1 - x_2) - b\dot{x}_1 + F_d \cos \omega t \\ m\ddot{x}_2 &= -kx_2 - \kappa(x_2 - x_1) - b\dot{x}_2 \end{aligned} \quad (8.1)$$

where b is a (viscous) drag coefficient.

The steady-state behaviour of the system, reached after damped oscillations have vanished and regulated by the driving force $f(t)$, is given by the particular solution of Equations 8.1:

$$\begin{aligned} x_1(t) &= C_- \cos(\omega t + \phi_-) + C_+ \cos(\omega t + \phi_+) \\ x_2(t) &= C_- \cos(\omega t + \phi_-) - C_+ \cos(\omega t + \phi_+) \end{aligned} \quad (8.2)$$

where

$$C_{\pm} = \frac{F}{2\sqrt{(\omega_{\pm}^2 - \omega^2)^2 - \gamma^2 \omega^2}}, \quad \tan \phi_{\pm} = \frac{-\gamma \omega}{\omega_{\pm}^2 - \omega^2}, \quad (8.3)$$

and

$$\omega_- = \sqrt{\frac{k}{m}}, \quad \omega_+ = \sqrt{\frac{k + 2\kappa}{m}}. \quad (8.4)$$

Hence, two identical, interacting masses can oscillate at two frequencies (normal modes):

- The first, ω_- , is the resonance frequency of the isolated oscillators and is independent of the coupling force κ . If γ is small, and if the driving frequency ω matches ω_- the two masses undergo stable oscillations of the same amplitude C_- and phase ϕ_- . The distance between the two masses remains constant.
- The second, ω_+ , depends on the coupling spring via κ . In this case, for small γ and $\omega \approx \omega_+$, the two masses oscillate out of phase with equal amplitudes C_+ (as indicated by the relative minus sign in Equation 8.2). The centre of mass of the system remains fixed.

8.3 Coupling mechanisms

Unlike the interaction potential between two nearby dipole oscillators, which is exquisitely electrostatic and governed by the dielectric constant of the medium, with a decay length over the dipole-dipole distance comparable with the Debye length of the solution (lying in the 0.1–1000 nm range), the coupling between two oscillating bubbles (drops) is mainly of hydrodynamic nature. As

such, the decay of these hydrodynamic forces with bubble-bubble distance D is much smoother (of the order of bubble radii, see Chapter 17) and strictly associated to the solvent viscous dissipation.

However, other coupling mechanisms can be considered as well. For instance, if a bubble is covered by a distribution of surfactants (like SDS), oscillations will induce a surfactant redistribution towards the more curved regions to minimize the electrostatic repulsion. The electric field around the bubble loses its spherical symmetry giving rise to oscillating multipoles. In the case of two adjacent bubbles, their synchronized motion will give rise to favourable attraction between the fluctuating multipoles located on their surfaces. These forces contrast the expected repulsion between identically charged spheres (bubbles) and have been invoked to interpret the attractive interactions in charged colloids.

Proper choice of the coupling mechanism is crucial for the success of our model in predicting the spectral features and the decay length of bubble-bubble interactions.

Chapter 9

Background on interacting oscillating bubbles

9.1 Survey of the literature

The interaction between two (or many) oscillating bubbles under the effect of an external perturbation (typically an acoustic field) has been extensively investigated – both theoretically and experimentally, as well as by calculation – over the years, although not as much as single-bubble vibrations (Section 6.1).

In this section we will give a general and by no means exhaustive outlook of the available literature. Extreme conditions lying beyond the scopes of our study – such as very small (sub-micrometric) bubbles, large-amplitude oscillations, or high-energy phenomena like cavitation – will be mostly neglected.

It is worth noticing that, in spite of the wealth of published works on bubble-bubble interactions, theoretical and experimental works have generally been conducted separately. Hence, very little data exist from well-controlled laboratory experiments for which comparison with theoretical predictions can be performed [169, 170].

Theory

The starting modelling step for multi-bubble systems is clearly the two-bubble system. The first attempt was made by Shima in 1971 [171], albeit under rather restrictive assumptions (e.g.: radial oscillations, incompressible and inviscid fluid, distance larger than bubble radii). Later studies dealt with different system parameters, such as bubble sizes and mutual distances, oscillation modes, or fluid properties like viscosity and compressibility.

Notice that most of the literature has focused on bubbles undergoing radial oscillations (see, for instance, [143, 161, 162, 172–174]) and/or on relative translation along their line of centres (see

also [175, 176]). A smaller, but significant number of papers, like Refs. [156, 157, 177–179], have dealt with shape oscillations, which are the focus of the present thesis.

Moreover, because of the mathematical intricacies, many of them have been discussed in Chapter 7, most theoretical models address the case where the distance between the centres of the bubbles significantly exceeds the sum of their radii. In such a limit, the angular dependence in the bubble-bubble interaction can be neglected and a perturbation approach is quite natural. This approach often leads to simple analytical expressions, of which the works by Doinikov and his coworkers are self-explicating exempla (see the above references), allowing also to model many complex physical effects, like the formation of stable bubble clusters or "grapes" mentioned in Section 7.2.2 [158, 159, 180, 181].

Much less investigated is the opposite limit, where the centre-centre distance is comparable with the sum of bubbles radii. In this case, the most natural procedure is that of adopting a specific coordinate system (e.g., bi-spherical coordinates) that enables to decouple the equation of motions for the fluid around the oscillating and interacting bubbles. This approach has been pioneered by Morioka [182] within the large-distance frame. Later on, Maksimov was able to deduce different analytical expressions for this kind of difficult problems also in the short-distance regime [183, 184], based on a symmetry approach (for a recent review on this topic, see [185] and references therein).

Experiments

A broad variety of experiments have been conducted on bubble-bubble interactions, starting from two-bubble systems, up to complex ensembles like clusters and grapes. However, the lack of data from well-controlled experiments prevents direct and fruitful comparison with the existing theory.

Most studies address micrometer-sized bubbles, in light of their applicative interest (see Section 4.1). In this case, especially for large bubble ensembles, the most common observable is the acoustic backscattered signal (see, for instance, [169, 186]). Typically, volume oscillations are excited by an acoustic transducer and the backscattered waves are recorded by a second transducer. The occurrence of shape deformations is related to instability phenomena as those discussed in Section 7.3. Since the recorded signal is extremely sensitive to the interaction forces between the bubbles – in terms of mutual distances, directions and of their attractive or repulsive nature – it provides a "fingerprint" of the interacting system. Exciting frequencies lie in the range of 10^2 kHz, detected frequencies decrease with the number of bubbles and may differ significantly from those of isolated bubbles. Videometry measurements are also feasible by use of modern ultrafast cam-

eras, however they require rather large oscillation amplitudes and contained frequencies due to the spatial and temporal resolution limits of optical imaging.

Experiments on the interactions between larger (millimetric) bubbles, often tethered or supported on solid surfaces, have been performed as well. Interestingly, results for the typical 1 kHz acoustic frequency on a pair of equal sized bubbles of 1 mm have confirmed the existence of symmetrical (low-frequency) and anti-symmetrical (high-frequency) eigenmodes [170]. The close-distance regime, in particular, has been addressed by several numerical and experimental studies, like Refs. [187–193].

More complex systems have been investigated as well. Many involve bubble interactions in proximity of solid boundaries, like Ref. [192] or Refs. [187, 188], providing some clues on the formation of bubble clusters, or acoustic emission by coalescing bubbles [189, 190].

Chapter 10

Basis of "bubble spectroscopy"

10.1 Bubble resonant response to external excitation

As it can be observed from Equations 6.12 and 6.20, unexcited bubbles undergo only small, random perturbations caused by the temperature or pressure fluctuations in the thermal bath (damped oscillations). By contrast, resonant fluctuations with characteristic Lorentzian decay (damped and forced oscillations) can be observed in the presence of controlled external excitation (the $F(t)$ term in Equations 6.12 and 6.20). The excitation may be applied in several ways:

- For instance, charged bubbles (drops) can be excited by applying an oscillating electric field. *Electric excitation* may take place also in the absence of a net interfacial charge, due to the difference in the dielectric constant between the fluid (gas or liquid) inside the bubble (drop) and the surrounding liquid, although the resulting force is very small compared to the direct excitation obtained with a net surface charge. The latter case is easily distinguishable from direct excitation since the coupling is quadratic in the electric field, thus, given a field of frequency f , the force acts at a frequency $2f$.
- For the broadly investigated *acoustic excitation*, the mismatch in compressibility and density between the facing media is at the basis of the bubble or drop response.
- Bubbles (drops) can also be deformed from their equilibrium shape by simple shear, due to the flow properties of the surrounding medium [194] or to the movement of a contacting surface [115], as in the case of anchored bubbles (drops). The response to this *mechanical excitation* is particularly sensitive to interfacial properties like surface tension.

Bubble resonances are extremely reproducible and bring a lot of information on the bubble itself:

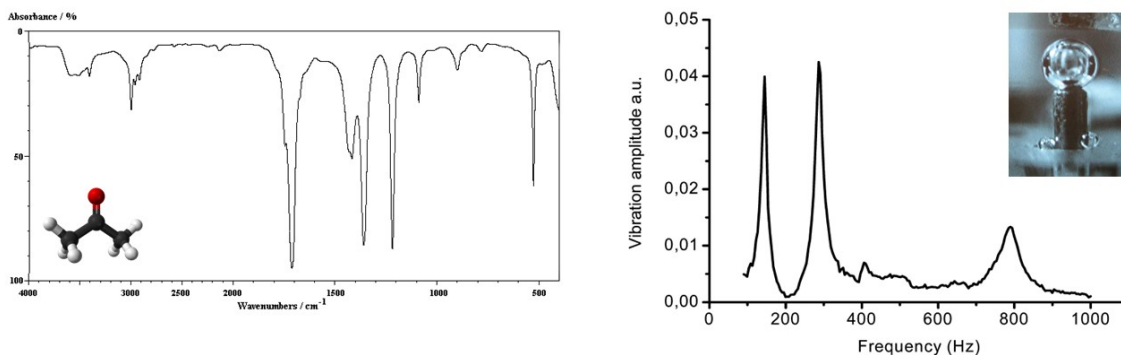


Figure 10.1: Molecular vibrational (IR) spectroscopy (source: web), vs bubble vibrational spectroscopy obtained with our setup. The former allows to study the vibrational modes of single molecules, whose typical frequencies are of order of 10^{12} Hz (100 cm^{-1}). The latter, by contrast, refers to the collective vibrations of the bubble (drop) interfaces, which occur at much lower frequencies (10^2 Hz for radii $R \approx 500\text{ }\mu\text{m}$). The underlying principle, however, is markedly similar. Moreover, in both cases the detected amplitudes are, in terms of sensitivity, of order of 0.1 nm (length of molecular bonds).

- The oscillation *amplitude* at resonance depends on the net surface charge;
- The resonance *width* reflects the energy dissipation at the interface;
- The resonance *frequency* is connected to the dilation restoring force at the interface.

All of the above parameters are experimentally accessible for every harmonic (n), as will be discussed in detail in Chapter 15. This lays the theoretical basis for a “bubble spectroscopy”.

10.2 "(Single) Bubble spectroscopy"

If we record the oscillation response of an excited bubble over the applied frequency, we get a *vibrational spectrum* of the bubble, like that shown in the right panel of Figure 10.1 (obtained by the interferometric apparatus described in Chapter 15). Here, the first detected peaks denote shape oscillation eigenmodes with increasing n (for a free bubble, the frequency is given by Equation 6.22); the volume mode generally falls at higher frequency (see Equation 6.14 for free bubbles). As anticipated in Section 6.9, anchored bubbles display a somewhat different spectrum, characterised by a shift in resonance frequencies and by the appearance of the degenerate $n = 1$ mode; however, apart from the frequency shift, the information that can be extracted is the same.

The left part of Figure 10.1 shows by comparison a *molecular* vibrational spectrum (obtained by a customary FT-IR spectrometer). Resonance frequencies differ as much as 10 orders of mag-

nitude in the two cases: while molecular vibrational spectroscopy measures the oscillations of *single* molecular bonds (with energies falling in the infrared region, corresponding to 10^{12} Hz frequencies), bubble spectroscopy addresses the *collective* motions of molecules at the bubble (drop) interfaces (lying at much lower frequencies, of order of 10^2 Hz for shape modes and 10^3 Hz for volume modes). The principle underlying these two spectroscopies, however, is markedly similar: both study the characteristic resonances of a mass-spring oscillator (molecular bonds linking atoms in a molecule, and the closed interface between two immiscible fluids, respectively) in order to infer its properties (e.g., bond strength, or interfacial tension), with amplitude sensitivity of order of 1 \AA (length of molecular bonds).

10.3 From single to interacting bubbles

The spectroscopic approach described above has been exploited to study oscillations of single bubbles and drops at different amplitudes and with different coverages. Details are given in Chapter 15. We now want to extend it to measure the interaction forces between two nearby bubbles.

Many studies have addressed force measurements involving soft interfaces. For instance, the well-assessed atomic force microscopy (AFM) techniques have been applied to numerous systems, from the simple air-liquid interfaces to membranes (for a comprehensive review on the topic, see Ref. [195]). In such measurements, the interaction force between the interface and a probe tip mounted on a cantilever is measured by monitoring the distance between the tip and the sample, while a feedback loop ensures that the force is kept constant.

On the contrary, in our experiments the relative distance D between the oscillating bubbles (drops) is held constant (see Chapter 16). Hence, their weak attractive forces cannot be measured directly. Instead, following the arguments of Section 8.1, we may exploit the frequency shift of the interacting bubbles set at different distances D . This frequency shift can be theoretically linked to the distance D in order to fit the strength of the bubble-bubble interactions.

Part IV

THEORETICAL MODELLING

Chapter 11

A theoretical model of interacting bubbles

In this chapter, I propose an intuitive and qualitative approach aimed at rationalizing the experimental trends of the bubbles vibrational properties – amplitudes, viscous dissipations (proportional to the resonance width), phases and frequencies – as a function of the inter-bubble distance.

11.1 Formulation of problem

The basis for the description of two interacting pulsating bubbles lies in the theory of single oscillating bubbles. In particular, the Rayleigh-Plesset (RP) theory, introduced in Chapter 6, provides a convenient framework for our task.

The modelling entails modifying the equations for a single bubble, seen in Section 6.5, by introducing a perturbation term that depends on the relative inter-bubble distance D and on the invoked coupling mechanism.

However, the two-bubble system investigated in our study – and in particular the experimental setup, described in Chapter 16 – is much more complex than that assumed by the RP theory. To best match our experimental conditions while preserving model simplicity, we will have to consider precise system geometry and bubble oscillation modes. In particular, we are looking for the simplest analytical model of two interacting bubble oscillators with the following features:

- Two axially symmetric anchored bubbles, with a partially charged surface, undergoing shape (at least quadrupolar) oscillations.
- Inter-bubble distance spanning from the order of bubble radii to contact. Hence, crucially, it must account for the close-distance range (see Chapter 9).

- Directional driving field (acoustic and electric) selectively applied on one bubble: this so-called "master" bubble will in turn act as a pressure wave source (transmitter) towards the second one (receiver), denoted as "slave" bubble.
- Possibility of mixed interaction mechanisms (mainly hydrodynamic and electrostatic).

To a first approximation, we will assume irrotational flow, leaving out the highly nonlinear mathematics related to vorticity (see Chapter 7). Moreover, we will not make hypotheses on the nature of the applied field and on the bubble response to the driving. Indeed, as our experiments are mainly based on electrical or mechanical stimulation of the master bubble by a contacting electrode, the response may differ from the typical case of an applied pressure field at "infinite" distances. Such a difference would in turn affect the bubble dynamics via the $F(t)$ term in Equation 6.20 (or similar forms). We have addressed this problem for the case of electric excitation in collaboration with Professor Alexey Maksimov, from the Oceanographical Institute of Vladivostok (Russia). Results are still preliminary, some information will be given in a later version.

System description

The problem of a spherical bubble (the *slave* bubble) locally excited by an oscillating bubble (the *master* bubble) can be addressed by introducing two local spherical coordinates centred at the bubbles centroids, as depicted in Figure 11.1, in a similar way to the first two-bubble models like [171].

We recall from Section 6.5 that, in local spherical coordinates, an axisymmetric deformation of the radius R_j of bubble j is described by an angular modulation of the radius:

$$R_j(\theta_j, t) = R_{0j} + \sum_n^{\infty} a_{jn}(t) P_n(\cos \theta_j) \quad (11.1)$$

where R_{0j} is the unperturbed radius ($j = 1, 2$), $P_n(\cos \theta_j)$ is a Legendre polynomial and $a_{jn}(t) \ll R_{0j}$ is the time-dependent amplitude of the bubble maximum surface deformation. Strictly speaking, R_{0j} is a function of time, oscillating around the equilibrium position of the bubble radius. This point will be addressed shortly later.

The presence of a second oscillating bubble (the *master* bubble) induces an oscillatory motion of the *slave* bubble (otherwise unexcited). The master-slave interaction is mainly localized within a relatively small surface area, hereinafter referred to as the "*contact region*". The calculation of the fluid-mediated vibrational properties of the system depicted in Figure 11.1 in the case of shape deformations and is described in the following section.

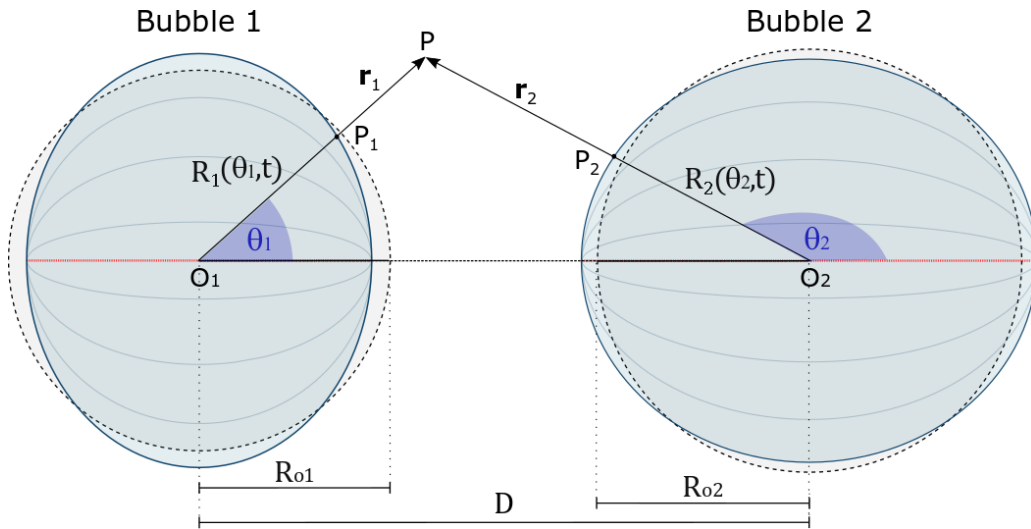


Figure 11.1: Representation of two interacting bubbles in local spherical coordinate systems. The bubbles are described as axially symmetric spheroids (axes in red) of equilibrium radius R_{0j} , with $j = 1$ (*master* bubble) or $j = 2$ (*slave* bubble). Their centroids O_j are vertically aligned and set at a distance D . The bubbles' deformed profiles – set in antiphase in this representation – are filled in blue and their equilibrium (spherical) shapes are shadowed in grey. Since the system has global axial (C_∞) symmetry, the azimuthal (ϕ_j) dependence is suppressed, thus simplifying calculations. Given a point P in the surrounding fluid, \mathbf{r}_j is the local radial coordinate, θ_j being the angular coordinate and $R_j(\theta_j, t)$ the local radius of Bubble j .

11.2 Approximate solution for two interacting bubbles undergoing shape oscillations

If we neglect the relatively small *contact region*, the oscillation of the bubble surface can be described by the standard equations set forth for the isolated bubble. Of course, the oscillation properties will be modified by the presence of a contact region. As we shall see shortly, the effect of a second bubble will be considered as a perturbation to the oscillation of the free bubble.

I will restrict the analysis to incompressible fluids (i.e., sound velocity $c \rightarrow \infty$), but more complete descriptions valid also to compressible fluid, like the Keller-Miksis equation [91], have been widely reported in the literature. In incompressible fluids, the starting equation to describe the motion of a free bubble is the well-known Rayleigh-Plesset, Equation 6.9 (see Section 6.3), here rewritten as:

$$\rho \left(R\ddot{R} + \frac{3}{2}\dot{R}^2 \right) + 4\eta \frac{\dot{R}}{R} + \frac{2\sigma}{R} + \Delta P(\mathbf{r}, t) = 0 \quad (11.2)$$

where ρ is the fluid density (assumed to be constant), R the bubble radius, σ the surface tension at the liquid-gas interface and $\Delta P(\mathbf{r}, t) = P_{ext}(\mathbf{r}, t) - P_B(t)$ the difference between the pressure far from the bubble $P_{ext}(\mathbf{r}, t)$ (that may depend on space \mathbf{r} and time t) and that within the bubble $P_B(t)$. From a physical standpoint, the first term accounts for the kinetic energy of the fluid displaced by the oscillatory motion of the gas-liquid boundary of the bubble. The second term derives from the viscous dissipation energy, the third accounts for the energy spent to deform the liquid-gas surface area and the last describes the master-slave interactions.

In the case of two interacting bubbles, I have to consider two RP equations coupled through a term dependent on their mutual distance. Labelling with 1 and 2 the two bubbles and letting D be the relative distance between their centres ($D = R_1 + R_2 + h$, where h is the shortest distance between the bubbles walls), I write, up to $O(D^{-2})$ terms:

$$\begin{aligned} \rho \left(R_1\ddot{R}_1 + \frac{3}{2}\dot{R}_1^2 \right) + 4\eta \frac{\dot{R}_1}{R_1} + \frac{2\sigma}{R_1} + \Delta P_1(\mathbf{r}, t) &= -\frac{\rho}{D} \left(2R_2\dot{R}_2^2 + R_2^2\ddot{R}_2 \right) \\ \rho \left(R_2\ddot{R}_2 + \frac{3}{2}\dot{R}_2^2 \right) + 4\eta \frac{\dot{R}_2}{R_2} + \frac{2\sigma}{R_2} + \Delta P_2(\mathbf{r}, t) &= -\frac{\rho}{D} \left(2R_1\dot{R}_1^2 + R_1^2\ddot{R}_1 \right) \end{aligned} \quad (11.3)$$

The coupling term $\frac{\rho}{D} \left(2R_j\dot{R}_j^2 + R_j^2\ddot{R}_j \right)$, with $j = 1, 2$, describes to the lowest order the dynamic effect of a nearby bubble set a distance D apart. Its analytical expression can be derived following, for instance, the reasoning reported in [196]. Higher-order terms in D^{-n} (with $n \geq 2$) can be calculated, their analytical expressions can be found for instance in Refs. [162, 174]. In this Thesis,

only the lowest-order approximation will be used. Notice that, in the case of surface-active species (e.g., surfactants) adsorbed on the bubble surface, possible direct interactions may arise, mediated by the surface layers. Such interactions may be taken into account by adding an additional distance-dependent term, $\Phi(R_j, |D|)$, to the purely hydrodynamic coupling term. This effect is generally neglected in standard models of bubble-bubble interactions, but can be important if one considers "dressed" bubbles as we did in many experiments. In Section 11.7 I report an analytical expression for $\Phi(R_j, |D|)$, based on the Derjaguin approximation (Appendix A.1), for the case of charged bubbles suspended in an electrolyte solution.

At variance with the overwhelming number of papers present in the literature, our experimental setup used imposes that the forcing term acting on the second (slave) bubble be zero. Indeed, researchers customarily employ acoustic fields to excite the bubbles oscillations. Generally, the acoustic field is homogeneous in the scale of the bubbles dimensions, so all of the bubbles feel an identical exciting field. On the contrary, in my experiments I purposely used a strongly localized excitation that enables to trigger selectively the oscillations of a single bubble (the master). Several control experiments performed in our laboratory confirm that the exciting field is confined over a single bubble alone even at short bubble-bubble distances. Consequently:

$$\begin{aligned}\Delta P_1(\mathbf{r}, t) &= P_{ext}(R_1, \theta_1, t) + P_o - P_B(t) \\ \Delta P_2(\mathbf{r}, t) &= P_o - P_B(t)\end{aligned}\tag{11.4}$$

where P_o is the atmospheric pressure (a constant) and $P_{ext}(R_1, \theta_1, t)$ is the additional pressure generated by an external field applied to the first bubble (the master bubble) alone.

I pause for a moment and stress the key conceptual differences between the setup employed in our experiments and that commonly adopted to investigate volume or shape oscillations, relying on intense, homogeneous acoustic fields. Because of the relative size of the acoustic wavelength and bubble radius, the time-dependent pressure of the acoustic wave can be considered spatially uniform in the scale of bubble dimensions. If one assumes a constant bubble radius, such a homogeneous pressure field cannot excite shape deformations. On the contrary, if the bubble radius is allowed to change in time during bubble oscillations, one can observe a parametric excitation of the different shape oscillation modes above a some critical threshold. The mechanism of this parametric excitation has been briefly discussed in Section 7.3.

In the setup used in my laboratory, the exciting field is strongly inhomogeneous. Electric or mechanical (piezoelectric) excitation is focused on a part of the bubble by exploiting the needle

shape of the electrodes to which the bubble is supported. One may wonder if the classical parametric excitation still persist even in our experiments. To answer this question, we performed several experiments by using drops instead of bubbles. We investigated shape oscillations of immiscible drops suspended in water using different hydrophobic fluids and exciting them with strongly inhomogeneous fields as described above [4, 5]. Because of the virtual incompressibility of liquids with respect to gas, no significant variations of the bubble radius is to be expected during the drops oscillations. Results constantly show only tiny differences in the oscillatory behaviour of drops and bubbles, ruling out significant contribution of the parametric excitation mechanism. On the basis of these experimental results, I neglected radius variations during the shape oscillations of the bubbles. Moreover, the pressure of the gas, $P_B(t)$, inside the bubbles is assumed to be identical and spatially homogeneous.

From a modelistic point of view, the *direct* excitation of the shape modes through spatially inhomogeneous fields introduces important simplifications. Indeed, the standard parametric excitation mechanism for shape modes requires a modulation of the bubble radius that, upon linearization, leads to coupled Mathieu-like equations. On the contrary, direct excitation of the shape modes through a inhomogeneous field leads, upon linearization, to the classic (damped) driven oscillator equations that can be easily solved even in the case of interacting bubbles. Even if the theory of coupled Mathieu equations exists in the literature (see, e.g., [197]), it is very cumbersome and difficult to apply. Therefore, a direct excitation of the shape modes could be advantageous in studying the dynamics of interacting bubbles.

For a bubble undergoing shape oscillations alone, the spatial profile of the radius reads: $R_j(\theta_j, t) = R_{0j} + \sum_n^\infty a_{jn}(t)P_n(\cos \theta_j)$ as defined by Equation 11.1. Replacing this expression into the coupled RP equations (11.3) and expanding in linear terms of $a_{jn}(t)/R_{0j}$ (a permissible approximation since in our experiments $a_{jn}(t)$ is in the nanometre scale and R_{0j} falls in the millimetre scale), I find:

$$\sum_n^\infty [\ddot{a}_{1n}(t) + b_{1n}\dot{a}_{1n}(t) + \omega_{1o}(n) \cdot a_{1n}(t)P_n(\cos \theta_1) + c_{2n}(D) \cdot \ddot{a}_{2n}(t)P_n(\cos \theta_2)] = \frac{1}{\rho} P_{ext}(R_1, \theta_1, t) \quad (11.5)$$

$$\sum_n^\infty [\ddot{a}_{2n}(t) + b_{2n}\dot{a}_{2n}(t) + \omega_{2o}(n) \cdot a_{2n}(t)P_n(\cos \theta_2) + c_{1n}(D) \cdot \ddot{a}_{1n}(t)P_n(\cos \theta_1)] = 0 \quad (11.6)$$

where: $b_{jn} \equiv 2(n+2)(2n+1)\frac{\eta}{\rho R_{0j}^2}$, $\omega_{jo}^2(n) \equiv (n-1)(n+1)(n+2)\frac{\sigma}{\rho R_{0j}^3}$ and:

$$c_{1n}(D) = \frac{R_{o2}^2}{R_{o1}D}; \quad c_{2n}(D) = \frac{R_{o1}^2}{R_{o2}D}. \quad (11.7)$$

Equations 11.5 and 11.6 are the classical equations for two driven-damped harmonic oscillators with damping coefficients b_{jn} and characteristic frequencies $\omega_{jo}(n)$. The forcing term $\frac{1}{\rho}P_{ext}(R_1, \theta_1, t)$ arises from the spatially inhomogeneous field (either electric or acoustic) used to excite the master bubble. In the geometry employed in this Thesis, the field is essentially dipolar (a bubble pinned at the poles by two oppositely charged electrodes), however, higher -order multipoles (mainly quadrupole) show non-vanishing amplitudes.

In writing the above equations, I neglected any distortion of the bubble geometry and eigenfrequencies due to bubble adhesion to the electrodes. This approximation stems from the observation that: i) the bubbles maintain a thin layer of water when approaching to the electrodes as observed by an optical microscope; and ii) the geometry of the bubble does not deviate appreciably from the spherical shape when it is gently adhering to the electrode. So, by properly selecting the electrodes coating, we can minimize the wetting phenomena between the drop and the electrodes. In any case, more advanced theories enable us to include the strong adhesion effects (see, e.g., [120, 122, 126]). It must be recalled that bubble adhesion enables to observe the bubble deformation motion $n = 1$ (displacement of the centre of mass, i.e., translation), that is degenerate for free bubbles. For an anchored bubble, the associated frequency differs from zero and increases with the strength of bubble-electrode binding. Indeed, we experimentally observed the motion $n = 1$ in most of our measurements.

Without loss of generality, one may multiply both sides of Equation 11.5 by $\sin \theta_1 P_m(\cos \theta_1)$ and integrate over $d\theta_1$ obtaining:

$$\sum_n^{\infty} \left[(\ddot{a}_{1n}(t) + b_{1n}\dot{a}_{1n}(t) + \omega_{1o}^2(n) \cdot a_{1n}(t)) \int_{-\pi}^{+\pi} P_n(\cos \theta_1) P_m(\cos \theta_1) \sin \theta_1 d\theta_1 + c_{2n}(D) \cdot \ddot{a}_{2n}(t) \int_{-\pi}^{+\pi} P_n(\cos \theta_2) P_m(\cos \theta_1) \sin \theta_1 d\theta_1 \right] = \frac{1}{\rho} \int_{-\pi}^{+\pi} P_{ext}(R_1, \theta_1, t) P_m(\cos \theta_1) \sin \theta_1 d\theta_1 \quad (11.8)$$

The first integral is easily calculated by exploiting the well-known orthogonality relationships for Legendre polynomials:

$$\int_{-\pi}^{+\pi} P_n(\cos \theta_2) P_m(\cos \theta_1) \sin \theta_1 d\theta_1 = \begin{cases} \frac{2}{2n+1} & \text{if } n = m \\ 0 & \text{otherwise} \end{cases} \quad (11.9)$$

More difficult is the evaluation of the second integral $\int_{-\pi}^{+\pi} P_n(\cos \theta_2) P_m(\cos \theta_1) \sin \theta_1 d\theta_1$. Making use of the mathematical relationships [198]:

$$\frac{P_n(\cos \theta_2)}{R_{o2}^{n+1}} = \frac{(-1)^n}{D^{n+1}} \sum_{k=0}^{\infty} C_{nk} \left(\frac{R_{o1}}{D} \right)^k P_k(\cos \theta_1) \quad (11.10)$$

where $C_{nk} \equiv \frac{(n+k)!}{n!k!}$, and of the orthogonality condition Equation 11.9, the above integral becomes:

$$\begin{aligned} & \int_{-\pi}^{+\pi} P_n(\cos \theta_2) P_m(\cos \theta_1) \sin \theta_1 d\theta_1 = \\ & (-1)^n \frac{R_{o2}^{n+1}}{D^{n+1}} \sum_{k=0}^{\infty} C_{nk} \left(\frac{R_{o1}}{D} \right)^k \int_{-\pi}^{+\pi} P_m(\cos \theta_1) P_k(\cos \theta_1) \sin \theta_1 d\theta_1 = \quad (11.11) \\ & (-1)^n 2 \left(\frac{R_{o2}}{D} \right)^{n+1} \sum_{k=0}^{\infty} \frac{C_{nk}}{2k+1} \left(\frac{R_{o1}}{D} \right)^k \end{aligned}$$

Finally, the third integral $\int_{-\pi}^{+\pi} P_{ext}(R_1, \theta_1, t) P_m(\cos \theta_1) \sin \theta_1 d\theta_1$ can be calculated by expanding the applied pressure $P_{ext}(R_1, \theta_1, t)$ in terms of Legendre functions, that is: $P_{ext}(R_1, \theta_1, t) = \sum_n^{\infty} A_n(t) \cdot P_n(\cos \theta_1)$, where A_n are multipolar terms that can be theoretically calculated or experimentally determined from the geometry of the applied excitation field. Hence:

$$\int_{-\pi}^{+\pi} P_{ext}(R_1, \theta_1, t) P_m(\cos \theta_1) \sin \theta_1 d\theta_1 = \frac{2}{2n+1} A_n(t) \quad (11.12)$$

With the aid of the integrals (11.9), (11.11) and (11.12) and setting $A_n(t) = A_{on} \cdot e^{i\omega t}$ (periodic applied force), I transform Equation 11.8 into a much simpler expression:

$$\left(\ddot{a}_{1n}(t) + b_{1n} \dot{a}_{1n}(t) + \omega_{1o}^2(n) \cdot a_{1n}(t) \right) + Q_1(n, D) \cdot \ddot{a}_{2n}(t) = A_{on} \cdot e^{i\omega t} \quad (11.13)$$

where the dimensionless coupling parameter $Q_1(n, D)$ takes the simple form: $Q_1(n, D) \equiv c_{2n}(D) \cdot (-1)^n (2n+1) \left(\frac{R_{o2}}{D} \right)^{n+1} \sum_{k=0}^{\infty} \frac{C_{nk}}{2k+1} \left(\frac{R_{o1}}{D} \right)^k$, that is, from Equation 11.5:

$$Q_1(n, D) \equiv (-1)^n (2n+1) \frac{R_{o2}^{n+3}}{R_{o1} D^{n+2}} \sum_{k=0}^{\infty} \frac{C_{nk}}{2k+1} \left(\frac{R_{o1}}{D} \right)^k, \quad n \geq 1.$$

By repeating exactly the same procedure, a form similar to Equation 11.13 is deduced from (11.6):

$$\left(\ddot{a}_{2n}(t) + b_{2n} \dot{a}_{2n}(t) + \omega_{2o}^2(n) \cdot a_{2n}(t) \right) + Q_2(n, D) \cdot \ddot{a}_{1n}(t) = A_{on} \cdot e^{i\omega t} \quad (11.14)$$

where

$$Q_2(n, D) \equiv (-1)^n (2n+1) \frac{R_{o1}^{n+3}}{R_{o2} D^{n+2}} \sum_{k=0}^{\infty} \frac{C_{nk}}{2k+1} \left(\frac{R_{o2}}{D} \right)^k, \quad n \geq 1.$$

Notice that Equations 11.13 and 11.14 are valid only for the shape deformation modes ($n \geq 1$) and were obtained under the approximation of a constant radius of the bubble during the oscillations. The case $n = 0$, that is, the pure volume mode, entails a compression/dilation response of the bubble and will be treated separately.

In order to numerically estimate $Q_1(n, D)$ and $Q_2(n, D)$, we need to calculate the convergent series $\Sigma(n) \equiv \sum_{k=0}^{\infty} \frac{C_{nk}}{2^{k+1}} \left(\frac{R_{oj}}{D}\right)^k$ with $C_{nk} \equiv \frac{(n+k)!}{n!k!}$. A general closed formula valid for all n values cannot be obtained. However, only the oscillation eigenmodes with small n are of experimental interest, namely the $n = 1$ (dipolar mode) and $n = 2$ (quadrupolar mode). Higher oscillation modes like $n = 4$ and $n = 6$ can be experimentally detected, but their intensity decreases with n . Letting $X \equiv \frac{R_{oj}}{D} < 0.5$, simple algebra yields:

$$\begin{aligned}\Sigma(n=1) &= \frac{(X-1)\tanh^{-1}(\sqrt{X}) - \sqrt{X}}{2(X-1)\sqrt{X}} \\ \Sigma(n=2) &= \frac{3(X^2 - 2X + 1)\tanh^{-1}(\sqrt{X}) + 5\sqrt{X} - 3\sqrt{X^3}}{8(X-1)^2\sqrt{X}}\end{aligned}\quad (11.15)$$

where $\tanh^{-1}(\sqrt{X})$ is the inverse hyperbolic tangent. In the limit $X \rightarrow 0$ (large inter-bubble distances), I get: $\Sigma(n=1) = 1 + \frac{2}{3}X + \dots$, and: $\Sigma(n=2) = 1 + X + \dots$, that is, the series is weakly dependent on R_{oj} and D . The system of second-order ordinary differential Equations 11.13 and 11.14 can be easily solved. Neglecting irrelevant transient terms that occur near $t = 0$, I seek for a solution of $a_{1n}(t)$ and $a_{2n}(t)$ of the form: $a_{jn}(t) = a_{jn}^o e^{i\omega t}$. Replacing this formula into Equations 11.13 and 11.14, I get:

$$\begin{aligned}(\omega_{1o}^2(n) - \omega^2 + i\omega b_{1n}) a_{1n}^o - \omega^2 Q_1(n, D) a_{2n}^o &= A_{on} \\ -\omega^2 Q_2(n, D) a_{1n}^o + (\omega_{2o}^2(n) - \omega^2 + i\omega b_{2n}) a_{2n}^o &= 0.\end{aligned}\quad (11.16)$$

Exact solution to Equations 11.16 reads:

$$\begin{aligned}a_{1n}^o &= \frac{(\omega_{2o}^2(n) - \omega^2 + i\omega b_{2n})}{(\omega_{1o}^2(n) - \omega^2 + i\omega b_{1n})(\omega_{2o}^2(n) - \omega^2 + i\omega b_{2n}) - \omega^4 Q_1(n, D) Q_2(n, D)} A_{on} \\ a_{2n}^o &= -\frac{\omega^2 Q_2(n, D)}{(\omega_{1o}^2(n) - \omega^2 + i\omega b_{1n})(\omega_{2o}^2(n) - \omega^2 + i\omega b_{2n}) - \omega^4 Q_1(n, D) Q_2(n, D)} A_{on}.\end{aligned}\quad (11.17)$$

The phase of the amplitude oscillations of the two bubbles are defined through the relationships: $a_{1n}^o = |a_{1n}^o| e^{-i\phi_1(\omega)}$ and $a_{2n}^o = |a_{2n}^o| e^{-i\phi_2(\omega)}$, thus the phase difference between the two oscillators (master and slave) can be calculated as $\phi_1(\omega) - \phi_2(\omega)$, yielding:

$$\phi_1(\omega) - \phi_2(\omega) = \pi - \tan^{-1}\left(\frac{b_{2n}\omega}{\omega_{2o}^2(n) - \omega^2}\right)\quad (11.18)$$

which reproduces the classical sigmoidal shape with a π jump at the resonance frequency, observed also for a single harmonic oscillator.

Once the coefficients a_{1n}^o and a_{2n}^o have been calculated through Equations 11.17, the averaged response of the bubbles, $\langle A_{jn}^2 \rangle^{1/2}$, can be easily calculated by performing a space and time averaging. This quantity can be directly compared with the experimental data on the amplitudes of the surface deformations obtained from the interferometric apparatus.

$$\langle A_{jn}^2 \rangle^{1/2} = \left(\frac{1}{T} \int_0^T \left[a_{jn}(t) \cdot a_{jn}^*(t) \int_{-\pi}^{+\pi} P_n(\cos\vartheta_j) P_n(\cos\vartheta_j) \sin\vartheta_j d\vartheta_j \right] dt \right)^{1/2} \quad (11.19)$$

where T is the oscillation period ($T = 2\pi/\omega_{oj}(n)$), $a_{jn}^*(t)$ denotes the conjugate complex of $a_{jn}(t)$ and $j = 1, 2$. Performing the integrations:

$$\langle A_{jn}^2 \rangle^{1/2} = \left(\frac{1}{2n+1} \text{Re} \{ a_{1n}^o a_{1n}^{o*} \} \right)^{1/2}, \quad n \geq 1. \quad (11.20)$$

Separating real and imaginary parts, from Equation 11.19 it is obtained:

$$\begin{aligned} \langle A_{1n}^2 \rangle^{1/2} &= \frac{\sqrt{F(n, \omega)}}{\sqrt{P^2(n, \omega, D) + \omega^2 S^2(n, \omega)}} A'_{on} \\ \langle A_{2n}^2 \rangle^{1/2} &= \frac{\omega^2}{\sqrt{P^2(\omega, D) + \omega^2 S^2(\omega)}} |Q_2(n, D)| A'_{on} \end{aligned} \quad (11.21)$$

where:

$$\begin{aligned} P(n, \omega, D) &\equiv (\omega_{1o}^2(n) - \omega^2) (\omega_{2o}^2(n) - \omega^2) - \omega^4 Q_1(n, D) Q_2(n, D) - \omega^2 b_{1n} b_{2n} \\ S(n, \omega) &\equiv b_{1n} (\omega_{2o}^2(n) - \omega^2) + b_{2n} (\omega_{1o}^2(n) - \omega^2) \\ F(n, \omega) &\equiv (\omega_{1o}^2(n) - \omega^2) (\omega_{2o}^2(n) - \omega^2) + \omega^2 b_{2n} S(\omega) \\ A'_{on} &\equiv \frac{A_{on}}{\sqrt{2n+1}}. \end{aligned}$$

11.3 Two interacting bubbles undergoing volume oscillations

Before discussing the numerical results, let me briefly report the equations for the vibrational properties of two interacting bubbles submitted to radial deformations.

Two main points are worth noticing:

- First, the eigenfrequency of the radial mode is generally higher than those of the lower-energy surface modes. This is because the restoring force to volume bubble deformation arises from a combination of surface area variation and compression of the gas inside the bubble. On the contrary, for surface modes, the compression of the gas during the bubble deformation is negligible.

- Secondly, the formulas reported in the literature for two pulsating bubbles set a distance D apart cannot be used because they have been derived under the assumption of a perturbing field identically acting on both bubbles. However, the extension of the model to the case of radial oscillations is straightforward.

By repeating the procedure employed to derive Equations 11.21, I look for a variation of the bubble radius during a volume deformation of the kind: $R_j(t) = R_{oj} + \varepsilon_j(t)$, where $\varepsilon_j(t)$ is the amplitude of the oscillation around the equilibrium radius R_{oj} , obtaining:

$$\begin{aligned} \langle A_{10}^2 \rangle^{1/2} &= \frac{\sqrt{F(n=0, \omega)}}{\sqrt{P^2(n=0, \omega, D) + \omega^2 S^2(n=0, \omega)}} A_{oo} \\ \langle A_{20}^2 \rangle^{1/2} &= \frac{\omega^2}{\sqrt{P^2(n=0, \omega, D) + \omega^2 S^2(n=0, \omega)}} |Q_2(n=0, D)| A_{oo} \end{aligned} \quad (11.22)$$

where $\langle A_{10}^2 \rangle^{1/2}$ and $\langle A_{20}^2 \rangle^{1/2}$ are the mean amplitudes of the master ($j = 1$) and slave ($j = 2$) bubbles. Explicit expressions for $P(n=0, \omega, D)$, $S(n=0, \omega)$ and $F(n=0, \omega)$ have been defined after Equations 11.21, while the coupling terms $|Q_j(n=0, D)|$ are given by: $|Q_1(n=0, D)| \approx \frac{R_{o1}^2}{R_{o2}D}$ and $|Q_2(n=0, D)| \approx \frac{R_{o2}^2}{R_{o1}D}$. The resonance frequencies of the two bubbles are: $\omega_{jo}^2(n=0) = \frac{1}{\rho} \left(\frac{3\gamma}{R_{oj}^2} + \frac{2\sigma}{R_{oj}^3} (3\gamma - 1) \right)$, where γ is the gas polytropic exponent ($\gamma = 1.4$ for air) and P_o is the atmospheric pressure.

11.4 Numerical results

The resonance spectrum of the slave bubble, i.e. the oscillation amplitude $\langle A_{jn}^2 \rangle^{1/2}$ against the frequency ω of the perturbing field (applied to the master bubble alone), is shown in Figure 11.2. For the sake of simplicity, the bubbles were assumed to be identical. Curves have been calculated for different values of the bubble-bubble distance D (more intense curves refer to shorter master-slave distances, D ranging from 100 to 300 μm , respectively). Arbitrary units were always used.

Analogous calculations have been made for what concerns the master bubble. As expected, variations are much smaller and slightly depend on the bubble-bubble distance D .

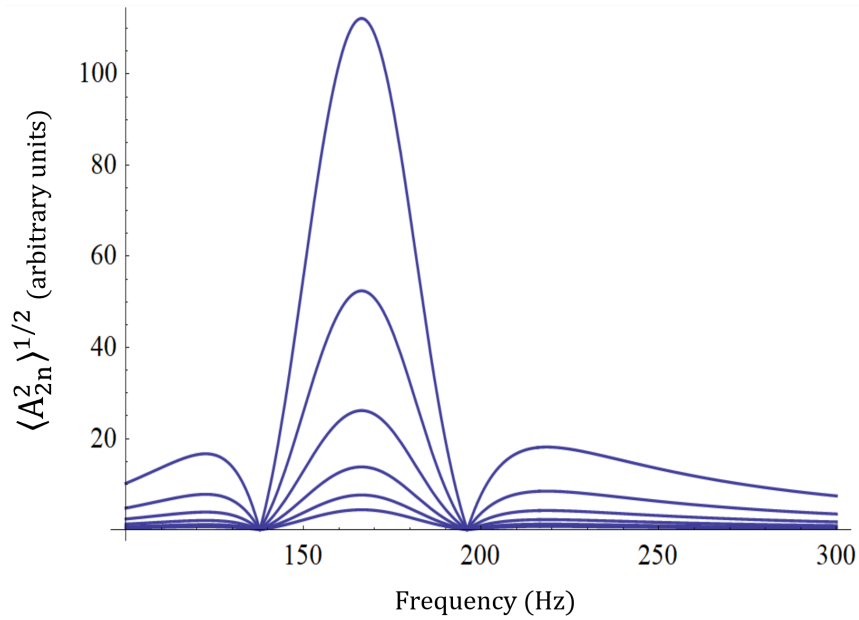


Figure 11.2: Amplitude $\langle A_{2n}^2 \rangle^{1/2}$ of the “slave bubble” against the frequency ω applied to the “master bubble”. Data refer to the vibrational mode $n = 2$. The different curves have been calculated at increasing inter-bubble distance D . Notice that when $D \rightarrow \infty$, the amplitude $\langle A_{2n}^2 \rangle^{1/2}$ goes to zero.

11.5 Approximations for the squeeze flow in the contact region between two bubbles

At short distances, hydrodynamic forces are strong and the fluid motion inside a narrow gap between two bubbles can be described in the framework of the lubrication approximation (see, e.g., [199]). This approach is particularly suitable to describe the deformations of a fluid contained in an oscillating gap of thickness $h(t)$.

Since extremely simple formulas can be obtained in the limit of flat plates, I assume that the gap between two nearby bubbles can be approximately considered as planar, with an effective radius of the upper and lower circular plates r_{eff} (see Figure 11.3). Let δ be a cutoff distance beyond which the squeeze flow characteristics sharply decay, and let $h(t)$ be the shortest distance of the oscillating gap and R_o the unperturbed radius of the bubbles (assumed identical), simple geometry shows that: $R_o - \frac{1}{2}\delta = \sqrt{R_o^2 - r_{eff}^2}$, which is trivially solved yielding to the leading terms:

$$r_{eff} \approx \sqrt{\delta R_o} \quad (11.23)$$

The next step is to calculate the fluid velocity in the region limited by the plates of effective radius

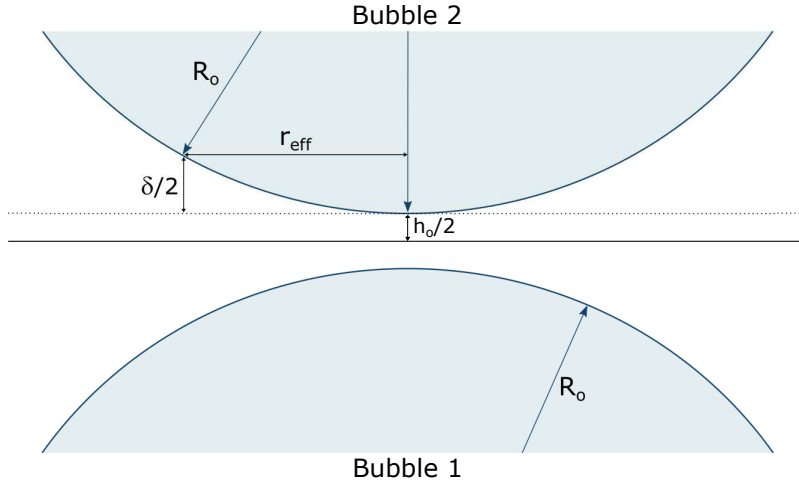


Figure 11.3: A zoomed representation of the two interacting bubbles of Figure 11.1 (rotated by $\pi/2$). The equilibrium radii R_o have been assumed to be equal for model simplicity, and the closest equilibrium distance between the surfaces is $h_o \ll R_o$. The so-called "contact region", where the interaction between the bubbles is the most effective, is defined by the spherical segments on their surfaces with a base of radius r_{eff} , determined by the cutoff distance assumed for effective interactions, $h_o + \delta$.

r_{eff} and relative distance $h(t) = h_o + \varepsilon e^{i\omega t}$, where ε is the oscillation amplitude, ω the oscillation frequency and t is the elapsed time.

To solve the problem, I adopt a local system of cylindrical coordinates (r, z, φ) , centred in the middle of the contact region between two nearby bubbles. The starting point is the usual Navier-Stokes, Equation 6.3. For a squeeze flow originated from the oscillatory motion of the boundary, the i -th component of the fluid velocity vector $U_i(r, z, \varphi, t)$ (with $i = r, z, \varphi$) can be written as:

$$U_i(r, z, \varphi, t) = u_i(r, z, \varphi) e^{i\omega t} \quad (11.24)$$

This particular form of U_i enables us to write the Navier-Stokes equations as:

$$\begin{aligned} i\omega\rho u_r &= -\frac{\partial P}{\partial r} + \eta \left(\frac{\partial^2 u_r}{\partial r^2} + \frac{1}{r} \frac{\partial u_r}{\partial r} + \frac{\partial^2 u_r}{\partial z^2} - \frac{u_r}{r^2} \right) \\ i\omega\rho u_z &= -\frac{\partial P}{\partial z} + \eta \left(\frac{\partial^2 u_z}{\partial r^2} + \frac{1}{r} \frac{\partial u_z}{\partial r} + \frac{\partial^2 u_z}{\partial z^2} \right) \end{aligned} \quad (11.25)$$

where ρ and η are the density and dynamic viscosity of the fluid, respectively, while u_r and u_z are the radial and perpendicular components of the velocity within the gap (see Figure 11.3). In writing Equations 11.25 we dropped out the angular component of the fluid velocity u_φ because, by symmetry reasons, the fluid rate is angular independent. Equations 11.25 must be supplemented

by the equation of continuity, that for incompressible fluids reads:

$$\frac{\partial(ru_r)}{\partial r} + r \frac{\partial u_z}{\partial z} = 0 \quad (11.26)$$

Symmetry arguments and use of Equation 11.26, lead to the fact that, in planar (or quasi-planar) geometries, the radial and perpendicular components of the velocity behave as:

$$u_r = \frac{1}{2}f'(z) \cdot r; \quad u_z = -f(z) \quad (11.27)$$

where $f(z)$ is a function of z alone and the dash refers to differentiation with respect to z . Inserting Equations 11.27 into Equations 11.25 yields:

$$\frac{1}{2}i\omega\rho r f'(z) = -\frac{\partial P}{\partial r} + \frac{1}{2}\eta r f'''(z) \quad \text{and:} \quad i\omega\rho f(z) = \frac{\partial P}{\partial z} + \eta f''(z) \quad (11.28)$$

Eliminating P by cross-differentiation and combining together Equations 11.28, I obtain:

$$f''''(z) + \alpha^2 f''(z) = 0 \quad (11.29)$$

where $\alpha^2 \equiv -i\frac{\omega\rho}{\eta}$. Boundary conditions at the wall of the slave bubble are: $U_r|_{z=0} = U_z|_{z=0} = 0$ (no-slip conditions) and: $U_z|_{z=h(t)} = 0$ (no-slip condition) and: $U_z|_{z=h(t)} = \frac{dh}{dt} = i\omega\varepsilon e^{i\omega t}$ (kinematic condition) at the wall of the *master* (i.e., directly excited) bubble. The above conditions imply: $f(0) = f'(0) = 0$ and: $f(h_o) = 0, f'(h_o) = 1$.

Analytical solution to Equation 11.29 satisfying the boundary conditions defined above is feasible, but not very informative; an useful formula is recovered in the limit $\alpha \rightarrow 0$ (i.e., negligible inertia):

$$f(z) = -2\left(\frac{z}{h_o}\right)^3 + \left(\frac{z}{h_o}\right)^2 \quad (11.30)$$

More precise results can be obtained by adding the α -dependent terms as a perturbation, these formulas will not be reported here. Once the explicit, approximate expression for $f(z)$ has been obtained, with the aid of Equation 11.27 the components of the velocity vector can be easily calculated:

$$U_r = \frac{1}{2}i\omega\varepsilon e^{i\omega t} r f'(z) \quad (11.31)$$

Thus, the z - and r -averaged mean flow within the contact region ($r = r_{eff} = \sqrt{\delta R_o}$, see Equation 11.23) is:

$$\langle U_r \rangle = \frac{1}{h_o} \int_0^{h_o} \frac{1}{r_{eff}} \int_0^{r_{eff}} U_r dr dz = i\omega\varepsilon \frac{\sqrt{\delta R_o}}{4h_o} e^{i\omega t} \quad (11.32)$$

The above result clearly evidences the different behavior of the fluid near the contact region of two close oscillating bubble and that of a fluid oscillating in a narrow layer of fluid lying between the two bubbles. Indeed, if we compare Equation 11.32 (the averaged radial velocity just outside the contact region), with the radial component of the interfacial velocity far from the contact region, $U_r|_R \approx i\omega\epsilon e^{i\omega t}$, I obtain that their ratio scales as:

$$\frac{\langle U_r \rangle_{\text{contact region}}}{U_r|_R} \approx \left(\frac{\delta R_o}{16h_o^2} \right)^{1/2} \quad (11.33)$$

where the length δ is of the same order of magnitude as the shortest bubble-bubble distance h_o . Equation 11.33 clearly shows a divergence of the local velocity in the limit $h_o \rightarrow 0$ (touching bubbles). Even at non-vanishing distances the fluid rate enhancement is significant, in our experiments h_o is in the micron range and R_o is in the millimetre range, it follows that the fluid velocity in the gap between the bubbles is estimated to be about 10 times faster than in regions far from the contact region¹.

The occurrence of unusually large velocities makes questionable some approximations widely adopted in solving the Navier-Stokes equation, at least in the critical contact region. The fluid motion cannot be considered any more irrotational and non-linear terms in the fluid velocity cannot be neglected as usually made at low Reynolds numbers. Both effects are well-known since long time (see, e.g., [140–143]) and belong to the microstreaming phenomena described in Section 7.1.

11.6 Qualitative predictions of the model

The model we have developed in my laboratory foresees a number of effects associated to the same variation of the inter-bubble distance. I summarize the main results:

- Because of the greater fluid velocity inside the inter-bubble spacing gap, the fluid kinetic energy is larger than in distal regions near the surface bubble. The resulting apparent “added mass” lowers the oscillation frequency of the slave bubble, the effect being more pronounced at short distances.
- The great fluid velocity in the gap induces a strong dissipation of the kinetic energy (the dissipated energy is proportional to the square of the fluid velocity times the fluid viscosity). As

¹Strictly speaking, the radial flow in the gap and far from the gap have different orientations. Inside the gap, the fluid motion is almost parallel to the bubble surface, while far from the gap, the radial motion is perpendicular to the oscillating surface. This difference, however, does not modify the conclusions.

a consequence, the viscous dissipation (experimentally related to the width of the resonance peak) must decrease with the distance. Since the behaviour of the fluid patterns strongly depends upon the bubble distance, the dissipation behaviour is very intricate.

- The amplitudes of the oscillation modes decrease with the distance with different powers for volume and shape modes.
- The form of Equations 11.21 and 11.22 predicts only a slight variation in the oscillation frequency along with the inter-bubble distance, especially for what concerns shape oscillations (see Figure 11.2), meaning weak interactions.
- In the absence of strong inter-bubble attraction forces (e.g., “stickers-receptors” couples uniformly distributed at the bubble surfaces), the oscillations of the master and the slave bubbles must be always out of phase.
- The decay law for the vibrational parameters with the inter-bubble distance D is faster on increasing the eigenmodes number n . Therefore, for a volume oscillation ($n = 0$) the decay roughly behaves as D^{-1} while for a quadrupolar mode ($n = 2$), the decay approximately follows a D^{-4} law. This result implies that the shift of the spectroscopic parameters is smaller for shape oscillation modes than for the radial mode, as seen in our experiments.

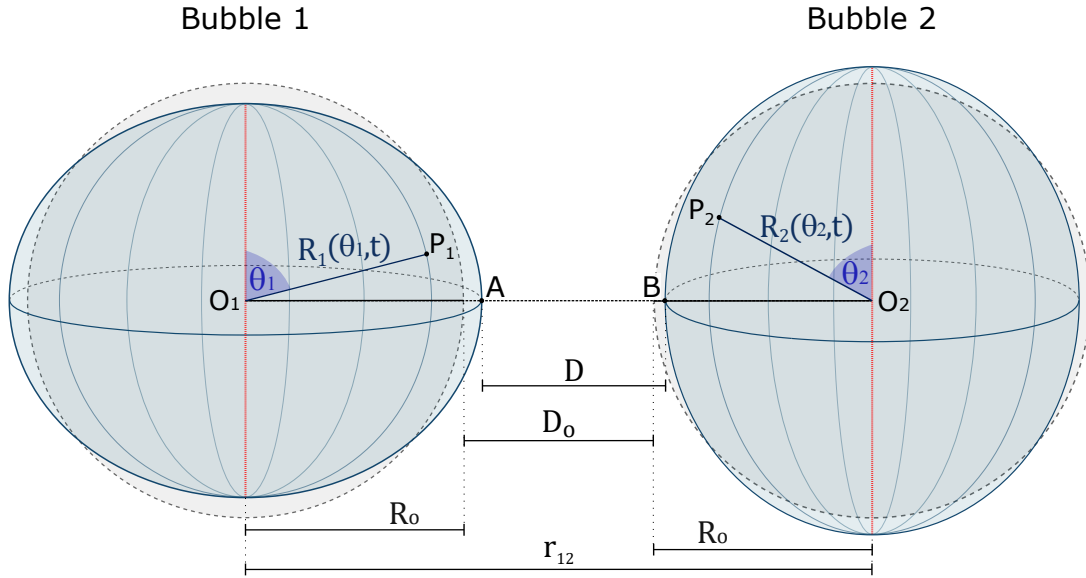


Figure 11.4: Representation of two interacting bubbles in local spherical coordinate systems, similar to Figure 11.1. The most notable difference is that here the symmetry axes (shown in red) are vertical, as in the real experimental setup. For convenience, both bubbles have equal equilibrium radii R_0 . The distance between their centroids O_1 and O_2 (vertically aligned) is constant and equal to r_{12} . As the bubbles vibrate, the distance of closest approach D (length of the segment \overline{AB}) varies about the equilibrium distance D_0 . Given a point P_i on bubble i surface, R_i is the local radius of the bubble.

11.7 Electrostatic interaction energy between two bubbles undergoing shape deformations

In this section I will suggest an approximate form of the coupling term $\Phi(R_j, |D|)$ required in Equations 11.3 to account for direct bubble-bubble interactions mediated by the surface charge.

A word of caution is needed. The calculations made in this section refer to a slightly different system, as shown in Figure 11.4. The adoption of this symmetry, dictated by the real experimental setup, changes slightly the final form of Equation 11.47 with respect to the system described in Figure 11.1, via the radius form, Equation 11.38. However, the numerical differences are small and the qualitative behaviour is unaltered.

System description

Let bubbles 1 and 2 be axially symmetric spheroids, as those represented in Figure 11.4, whose centroids are vertically aligned (a simplification with respect to the real system) and located at a constant distance r_{12} , and with their symmetry axes oriented vertically. We shall denote as A and B the points of least separation between the two bubbles, which define the distance of closest approach D . While r_{12} is held constant (as is done experimentally by anchoring the bubbles to the electrodes), D varies along with the oscillation motion.

Since, for the purpose of describing shape oscillations, the bubble volume is assumed to be constant, the local radius of the bubble must be rescaled to ensure bubble (drop) incompressibility, yielding (see Appendix A.2):

$$R_i(\theta_i, t) \approx R_{0i} + \left[1 + 2x_i(t) \cdot P_2(\cos \theta_i) + \frac{4}{5} x_i(t)^2 \right] + O(x_i^3) \quad (11.34)$$

where R_{0i} is the initial radius of the resting bubble and the variable change $x_i(t) = \frac{a_{2i}(t)}{2R_{0i}}$ was introduced for convenience.

For the sake of simplicity, we shall first consider two equal bubbles (drops) of initial radius R_0 . Then, D_0 is the distance between the bubbles at rest. We shall also assume that they both bear an overall surface charge q , i.e. a global charge density:

$$\sigma = q/4\pi R_0^2 \quad (11.35)$$

If the bubbles bear a *net* electric charge, the surface charge density is related to the electrostatic potential at the bubble surface by the Grahame equation [200, 201]:

$$\sigma = \sqrt{8RT\varepsilon\varepsilon_0 C_\infty} \sinh \frac{ze\Psi}{2kT} \quad (11.36)$$

where ze is the charge of the covering ions, ε and ε_0 are the medium and vacuum dielectric permittivity, k and R the Boltzmann and the gas constants, T the temperature and C_∞ the ion concentration in the bulk².

Calculation via Derjaguin's Approximation

Let us now evaluate the electrostatic interaction energy between two bubbles (drops) undergoing shape deformations, in terms of the pair potential between two axisymmetric spheroids immersed

²Notice that in the absence of charges in the medium ($C_\infty = 0$) an unphysical infinite potential Ψ would be obtained: physically, this means that there must always be charges. In the case of pure water, or very small concentrations of electrolyte, the contribution from the auto-dissociation of water must be taken into account, hence: $C_\infty = \sqrt{K_w} = 10^{-7}$.

in a fluid. We shall follow an approach based on Derjaguin's approximation [202] (DA, detailed in Appendix A.1) and refer to the scheme presented in Figure 11.4. In brief, provided the applicability conditions are met, this method enables us to evaluate the *global* inter-bubble electrostatic interaction in terms of *local* properties, that is, the curvature and charge density of the two bubbles in proximity of the closest-distance points.

We begin by imposing (ideal case of perfectly identical bubbles) that the equally-charged bubbles bear the same *and locally uniform* surface potential ψ as well³. Then, for $\psi_1 = \psi_2 = \psi$ the electrostatic free energy U becomes (see Equations A.3 to A.6):

$$U = \frac{4\pi \epsilon_0 \epsilon_r \psi^2}{\sqrt{\lambda_{\parallel} \lambda_{\perp}}} \cdot \log(1 + e^{-\kappa D}) \quad (11.37)$$

where ϵ_0 is the vacuum dielectric permittivity, ϵ_r the relative permittivity, κ the inverse Debye length of the medium and D the distance of closest approach. λ_{\parallel} and λ_{\perp} are the effective curvatures as defined in Equations A.5 and A.6. As expected for two bodies of the same charge, U is repulsive.

We proceed by calculating the local curvatures at the points of closest approach on bubbles 1 and 2, to determine the curvature factor $(\lambda_{\parallel} \lambda_{\perp})^{-1/2}$ in Equation 11.37. We first calculate the local radius R_i at the closest-approach points of bubbles 1 and 2. As the bubble centroids are vertically aligned, points A and B lie on the equator lines (corresponding to $\theta_i = \pi/2$), hence, using Equation 11.34:⁴

$$R_i\left(\frac{\pi}{2}, t\right) = R_0 \left[1 - x_i + \frac{4}{5} x_i^2\right] = R_i(t) \quad (11.38)$$

The assumption of small-amplitude vibrations simplifies the calculation of the curvature radii $R_{\parallel i}$ and $R_{\perp i}$ with respect to their analytical definition (see, e.g., [203, 204]). In fact, the local radius $R_i\left(\frac{\pi}{2}, t\right)$, coinciding with the equatorial radius $R_{\parallel i}$ and may well approximate the longitudinal radius $R_{\perp i}$, that is:

$$R_{\perp i} \approx R_{\parallel i} = R_i(t) \quad (11.39)$$

$$\lambda_{\perp} \approx \lambda_{\parallel} = \frac{1}{R_1(t)} + \frac{1}{R_2(t)} \quad (11.40)$$

$$\frac{1}{\sqrt{\lambda_{\parallel} \lambda_{\perp}}} \approx \left(\frac{1}{R_1(t)} + \frac{1}{R_2(t)}\right)^{-1} \quad (11.41)$$

We substitute Equation 11.38 into Equation 11.41 and expand in Taylor series truncating to second order:

$$\frac{1}{\sqrt{\lambda_{\parallel} \lambda_{\perp}}} \approx \frac{R_0}{2} \left[1 - \frac{1}{2}(x_1 + x_2) + \frac{3}{20}(x_1^2 + x_2^2) + \frac{1}{2}x_1 x_2\right] + O(3) \quad (11.42)$$

³This assumption is not straightforward, since, even for identical bubbles bearing the same global charge, the local density may differ due to charge redistribution at the surface, depending in turn on local curvature.

⁴If we assume $\theta_i = 0$ (horizontal symmetry axes as in Section 11.2), then it becomes $R_i\left(\frac{\pi}{2}, t\right) = R_0 \left[1 - x_i + \frac{4}{5} x_i^2\right] = R_i(t)$ and the following equations change accordingly.

We now determine the electrostatic shielding factor $\log(1 + e^{-\kappa D})$ appearing in Equation 11.37. Looking at Figure 11.4, the distance D can be written as:

$$D = D_0 - [a_{21}(t) \cdot P_2(\cos \theta_1) + a_{22}(t) \cdot P_2(\cos \theta_2)]$$

which, after normalising (see Appendix A.2) and substituting $x_i = \frac{a_i}{2R_0}$ as above, yields:

$$D \approx D_0 + R_0(x_1 + x_2) + O(3) \quad (11.43)$$

Therefore:

$$\log(1 + e^{-\kappa D}) = \log\left[1 + e^{-\kappa(D_0 + R_0(x_1 + x_2))}\right] \quad (11.44)$$

$$\approx k_0 + k_1(x_1 + x_2) + k_2(x_1^2 + x_2^2) + k_{2m}x_1x_2 + O(3) \quad (11.45)$$

with:

$$k_0 = \log(1 + e^{-\kappa D_0})$$

$$k_1 = -\frac{\kappa R_0}{1 + e^{-\kappa D_0}}$$

$$k_2 = \frac{\kappa^2 e^{\kappa D_0} R_0^2}{2(1 + e^{-\kappa D_0})^2}$$

$$k_{2m} = \frac{\kappa^2 e^{\kappa D_0} R_0^2}{(1 + e^{-\kappa D_0})^2}$$

Hence, the pre-logarithmic factor reads:

$$\frac{\log(1 + e^{-\kappa D})}{\sqrt{\lambda_{\parallel} \lambda_{\perp}}} \approx \alpha_0 + \alpha_1(x_1 + x_2) + \alpha_2(x_1^2 + x_2^2) + \alpha_{2m}x_1x_2 + O(3) \quad (11.46)$$

with:

$$\alpha_0 = \frac{R_0}{2} \log(1 + e^{-\kappa D_0})$$

$$\alpha_1 = -\frac{R_0}{4} \log(1 + e^{-\kappa D_0}) - \frac{\kappa R_0^2}{2(1 + e^{\kappa D_0})}$$

$$\alpha_2 = -\frac{R_0}{8} \log(1 + e^{-\kappa D_0}) + \frac{\kappa R_0^2}{4(1 + e^{\kappa D_0})} + \frac{\kappa^2 e^{\kappa D_0} R_0^3}{4(1 + e^{\kappa D_0})^2}$$

$$\alpha_{2m} = \frac{R_0}{4} \log(1 + e^{-\kappa D_0}) + \frac{\kappa R_0^2}{2(1 + e^{\kappa D_0})} + \frac{\kappa^2 e^{\kappa D_0} R_0^3}{2(1 + e^{\kappa D_0})^2}$$

We finally obtain the form of the electrostatic interaction energy between two identical, uniformly charged bubbles:

$$U \approx \left[\alpha_0 + \alpha_1(x_1 + x_2) + \alpha_2(x_1^2 + x_2^2) + \alpha_{2m}x_1x_2 \right] 4\pi\epsilon_0\epsilon_r\psi^2 + O(3) \quad (11.47)$$

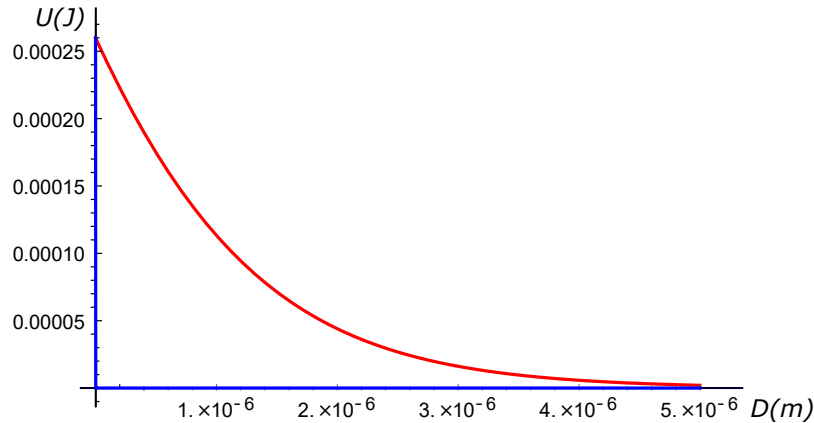


Figure 11.5: Electrostatic interaction energy U (calculated from Equation 11.47) between two equally charged deformed spheroids ($x = 10^{-6}$, corresponding of bubble deformation of about 1 nm), as a function of their closest distance D . *Red curve:* spheroids in pure water (Debye length $\kappa^{-1} = 960$ nm); *Blue curve:* NaCl solution 1M ($\kappa^{-1} = 0.3$ nm). While the (repulsive) interactions in pure water decay over a distance of order of 1 μm , the decay length (comparable with the Debye length of the solution) decreases up to sub-nanometric distances in the NaCl solution.

where numerical coefficients α_i were defined above.

Differentiation of Equation 11.47 with respect to x_1 and x_2 yields the force (per unit surface) exerted by a charged bubble upon a surface deformation of magnitude x_1 and x_2 , respectively, giving an estimate of the electrostatic contribution $\Phi(R_j, |D|)$ to the coupling between two identical bubbles, as defined after Equations 11.3. A word of caution is in order, however. Equation 11.47 is *not* the most general form for two interacting charged spheroids. In fact, it contains three important approximations:

- The DA to calculate the electrostatic interactions among curved charged surfaces;
- The assumption of two identically charged spheres;
- The assumption that no charge redistribution occurs at the interface;
- The assumption that deviations from spherical shapes can be described by a single term in the Legendre functions expansion (sphere-to-ellipse deformation).

The behaviour of $U(D)$, Equation 11.47, is shown in Figure 11.5 for typical experimental values of bubble radii and deformation amplitudes and for two limit values of the Debye length. Unsurprisingly, the electrostatic contribution to the interactions between two identical deformed bubbles (drops) with uniform surface charge distribution is repulsive and decays over extremely

short ranges (comparable with the Debye length of the medium).

While the decay length of bubble-bubble interactions (long-ranged, as observed in Chapter 17) is determined by hydrodynamic effects, electrostatic effects will contribute to modulate the interactions, via a repulsion effect, within the close-distance regime. At larger distances the contribution of $\Phi(R_j, |D|)$ to Equations 11.3 will be negligible.

Chapter 12

Purely computational approaches

The simple arguments put forward in Section 11.5 have proven the need of an accurate estimate of the fluid rate in the contact region, by means of non-linear hydrodynamics. Owing to the difficulties of this theory, requiring non common technical skills, I decided not to tackle the problem from an analytical point of view and to rely instead on computational approaches, on a collaborative basis.

12.1 Lattice-Boltzmann methods

I started an intense collaboration with Dr. Martina Pannuzzo, a researcher from the Italian Institute of Technology (IIT) in Genoa. Dr. Pannuzzo is an expert of numerical calculations of mesoscopic systems and has already set up simulations on bubble dynamics. In previous works, coarse-grained Molecular Dynamics (MD) approaches were used to describe the oscillatory behaviour of a surfactant-covered bubble [9]. These computer simulations are very accurate and produce results in good agreement with the experimental findings. Unfortunately, MD simulations are very long and demand nontrivial computational facilities. Despite many simulations had been performed with the help of international networks of computer clusters, the extension of MD simulations to two-bubbles systems is hardly feasible in terms of time and costs. After different attempts, we found that the best computational tool to address my two-bubble problem are the so-called Lattice-Boltzmann techniques.

Unlike the classical Navier-Stokes equations, Lattice-Boltzmann (LB) approaches are based in essence on the numerical simulation of fictive particles that perform consecutive propagation and collision processes over a discrete lattice mesh. LB techniques blend together a reasonably good accuracy in the results and fast computational times, for this reason they are becoming very popular among researchers working on complex fluids. The calculation procedure we used follows

the one recently developed by Cimrak, Gusenbauer and Jancigova [10,205], set within the recently developed object-in-fluid framework, based on the coupling of the LB method to describe the fluid dynamics with the immersed boundary (IB) method to describe the immersed object. This allows to get reliable information on the fluid velocity around deformable objects that continuously change their shape with time. Despite the growing number of papers dealing with LB techniques, I will refer to their works for the relevant literature concerning LB calculations of mesoscopic systems.

Setup

Briefly, we simulated two spherical deformable objects (mimicking the oscillating bubbles) weakly adsorbed to solid supports (mimicking the electrodes) and immersed in an isotropic and homogeneous fluid. The distance between the oscillating bubbles and their radii can be changed at will together with the fluid properties (e.g., viscosity) and bubble surface (e.g., charge, air-solvent interfacial tension). A driving pressure field stemming from the surface of a single electrode was applied to the system to simulate the experimental conditions. Intensity and frequency of the pressure field can be varied over a wide range. In this way, we can simulate the interaction of master and slave bubbles, using relative scales similar to those used both in our interferometric measurements and in the theoretical modelling (the individual parameters being adimensional instead). Hence, apart from some details, our LB setup is not too far from the experimental conditions.

To describe the oscillating air-water interface, we partitioned the curved surface of the bubble into an array of close small triangular meshes. By increasing the number and decreasing the size of the meshes, we were able to simulate with a good accuracy the relevant properties of an oscillating and curved interface.

Results

Results from simulations are summarized in Figure 12.1, reporting a series of snapshots of the dynamics of the two bubbles, spanning approximately half an oscillation period. For the sake of clarity, we show in the movie also the velocity vector of tagged fluid particles (a very informative and widely used parameter obtained from both theory and experiments). Different colours, shown in a legend aside the movie, label the intensity of the fluid velocity.

Although these results are preliminary and a lot of additional computer experiments are needed to test the validity and limitations of the LB technique (see below), altogether our results qualitatively confirm a couple of hypotheses.

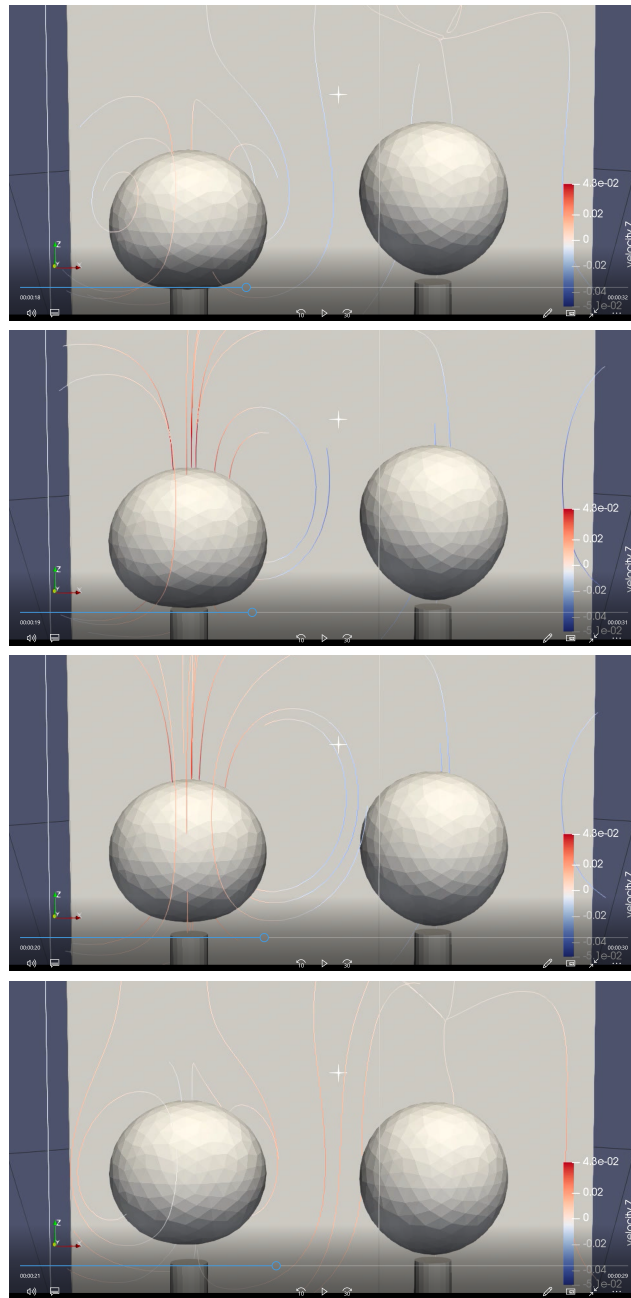


Figure 12.1: Snapshots from a LB simulation of two interacting oscillating objects (mimicking bubbles) gently adsorbed on solid supports (electrodes), along approximately half of an oscillation cycle. On the left is Bubble 1 (the master, directly excited), on the right Bubble 2 (the slave). The time-changing streamlines are shown in colour velocity scale. Deformation amplitudes were amplified with respect to real experiments for clarity. The inter-bubble distance D was varied in the simulations from values comparable to the bubble radii (as in the reported snapshots) to the contact distance.

- The fluid motion around two oscillating bubbles is very complex and akin to that of a turbulent motion, as evidenced by the flux lines in Figure 12.1.
- The master and slave bubbles communicate at great distances through the oscillation-induced fluid motion that strongly depends on the distance between the oscillating bubbles and on the fluid properties. In particular, the non-monotonous behaviour of the fluid velocity and the dependence on viscosity are clear from Figure 12.2.
- *The oscillations between the two bubbles are always out-of-phase*, as evident both from Figure 12.1 and from the analysis of the gyration radii of the individual bubbles over the simulation time (data not shown), *thereby ruling out the hypothesis of attractive forces mediated by correlated turbulent motions*.

To obtain more quantitative results we are proceeding through a statistical analysis of our results. A first and still preliminary analysis concerns the calculation of the total *viscous dissipation*. It is well known that the energy dissipated by a moving fluid depends on the square of the particles velocity times the fluid viscosity (see Section 6.8). Using the data on the fluid velocity calculated in our LB simulations (like those illustrated in Figure 12.2) and the experimental value of solvent viscosity (we used water + sucrose mixtures in our interferometric experiments) and integrating over the whole volume of the fluid, we were able to extract the first data on dissipation. This parameter is particularly interesting because the width of the resonance peaks detected experimentally is proportional to the energy dissipated during the oscillations at different frequencies, which is in turn proportional to the average of the squared velocity. Apart from the obvious viscosity-dependent enhancement of dissipation, our LB results show a nontrivial bell-shaped variation of the dissipation with the inter-bubble distance (Figure 12.2). The explanation of this seemingly strange behaviour is probably simple. Indeed, at large distances, the mutual effect of the bubbles is small, so the viscous dissipation is similar to that of the isolated bubbles. Conversely, at very short distances the mutual perturbation is strong but it is localized in a quite small region of the fluid. At intermediate distances, the perturbed flow patterns span over large portions of the fluid, so the viscous dissipation attains the largest values. It is worth noticing that a non-monotonous trend in peak widths vs distance has been observed in our experiments of interacting bubbles undergoing volume oscillations (albeit not for shape oscillations) and analytically predicted by Maksimov [183] for a very similar system (see Section 18.2).

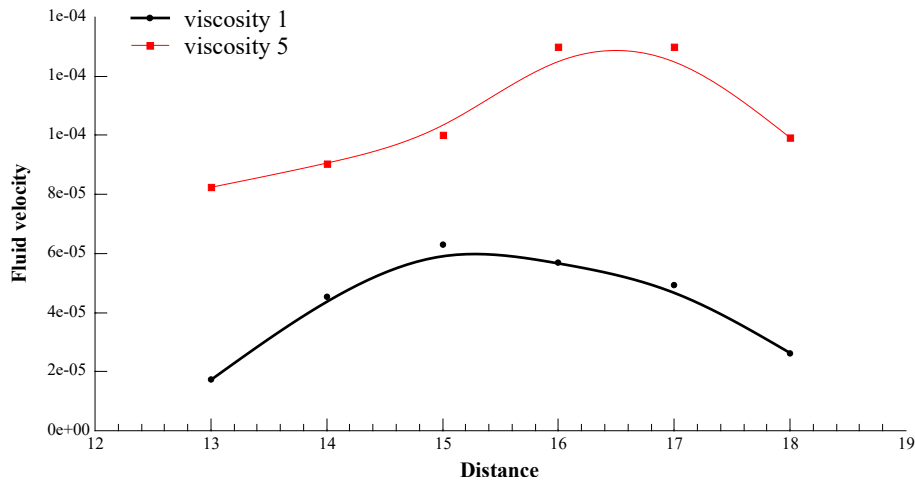


Figure 12.2: Averaged fluid velocity vs inter-bubble distance for two different fluid viscosities, calculated by LB method. The black scatter (viscosity 1) mimicks water, the black scatter (viscosity 5) corresponds to an increased 5X viscosity. A nontrivial non-monotonous (bell-shaped) behaviour of the velocity (and hence, of viscous dissipation) with distance can be observed, together with the expected increase with viscosity. Notice that the average of the squared velocity is proportional to the viscous dissipation and then to the (experimental) peak width.

12.2 Other computational approaches

To confirm the validity of the used LB techniques, we are facing the problem using a more standard procedure based on the numerical resolution of the classical Navier-Stokes equations. The difficult issue is the presence of curved and moving boundary conditions at the air-liquid interface the modelling of which requires the use of unconventional discretization approach. This part of the research has been conducted in collaboration with Prof. Armando Coco, Associate Professor of Mathematics at Oxford Brookes University, UK. The problem has been successfully solved in the case of a single oscillating bubble, within the PhD activity of Clarissa Astuto (University of Catania, Department of Mathematics). Numerical results are very accurate and do not require excessively long computational times. The procedure will be extended soon to the case of two interacting bubbles. A hint at results is given in Figure 12.3. I will not comment any longer on this active and interesting topic because my contribution to this research has been up to date partial.

Furthermore, to confirm the validity of our results, we are comparing the results obtained by numerical simulations with those coming from particles tracking velocimetry, a powerful technique that enables a direct visualization of the fluid streamlines around the oscillating bubbles (see, e.g., [206]). Results, at the moment, are preliminary.

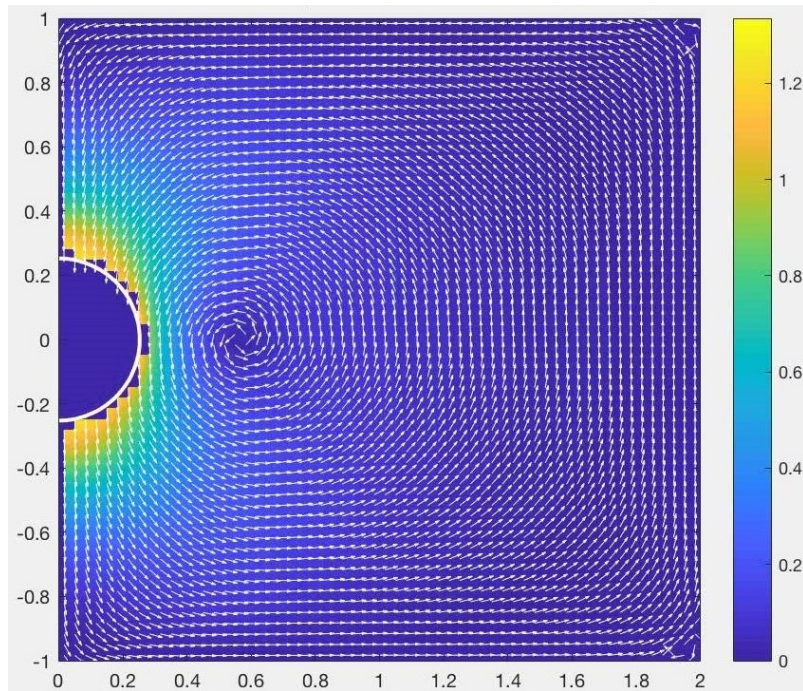


Figure 12.3: Snapshot of a numerical simulation of an axisymmetric oscillating bubble, calculated from the Stokes equation. Notice the presence of a vortex even in the irrotational assumption. The snapshot was taken at the equilibrium position (maximum velocity of the bubble wall, as indicated by the colour bar on the right). Distances are expressed in mm. Calculations were performed by Armando Coco, Oxford UK, and Clarissa Astuto, Catania.

Part V

**EXPERIMENTAL BACKGROUND.
THE *SINGLE* BUBBLE
INTERFEROMETER**

Chapter 13

Measurement of surface deformations: from air-water to cells

A plethora of experimental techniques have been applied so far to the measurement of surface oscillations. Based on the aim of the study – from surface characterisation up to molecular detail, to rheology, to biology and biomimetics – they will vary in: scale (from nanometric to macroscopic) and nature of the investigated system (from the bare air-water interface to complex fluids and reconstituted membranes, up to living cells); nature of deformations (equilibrium or out-of-equilibrium, spontaneous or forced); measurement principle (optical imaging, acoustics, interferometry, scattering, ...). Performances, such as time- and scale- sensitivity, vary accordingly.

This chapter provides a broad, not exhaustive overview of these techniques, functional to comparison with the one adopted in this thesis. For convenience, the review has been divided based on the investigated system, starting from generic capillary waves to finish with cells.

13.1 Capillary waves

The study of capillary waves, introduced in Section 3.4, has mostly been focused on large planar interfaces. Here, due to the “infinite” nature of the flat interface, a continuous frequency spectrum can be observed (see Equation 3.2).

In the case of gas/liquid systems, experimental measurements are typically based on the scattering of incident light at the surface, whereby capillary waves act as gratings and diffuse light in directions related to their wave-vector \mathbf{k}^1 [21, 22, 207–210] (see Figure 13.1). Such experiments have been applied to determine the surface tension and surface viscoelasticity of both pure and

¹whose modulus is the wavenumber mentioned in Equation 3.2 and direction is normal at every point to the phase front of the wave.

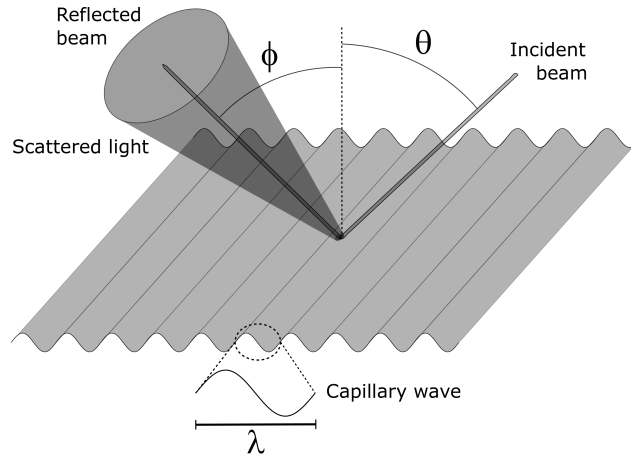


Figure 13.1: Scheme of capillary wave measurement on a planar interface via dynamic light scattering. The shaded cone indicates the solid angle of scattered light detection. The direction of maximum intensity is related to the wavenumber \mathbf{k} .

complex bidimensional fluids and allow to investigate large (electrically or acoustically excited) to small-amplitude (thermal) surface oscillations.

In the case of thermal motions, which generate capillary waves of all wavelengths, the wavelength selection is made by the scattering angle, and then the frequency response is measured [22, 207, 209]. Typical values are $\lambda = 100\mu\text{m}$, corresponding to $\nu = 10\text{kHz}$. With excited waves, by contrast, the frequency is fixed and the wavelength is measured [22, 211]. Sinusoidal waves can be generated by mechanical (movable surface barriers), acoustical (loudspeakers) or electrical (electrocapillarity) methods. Frequencies and wavelengths vary accordingly, within the ranges of 1–100 Hz and 1–100 mm, respectively. Typical accuracies are 0.1% for wavelengths and 1% for frequencies [21].

13.2 Bubbles and drops

As mentioned in Chapter 3, gas bubbles in a liquid, or liquid drops in an immiscible liquid, represent a special case of capillary surfaces. The main difference with the flat-surface case discussed in the previous section lies in their finite and closed geometry, which imposes periodic boundary conditions on the propagation of capillary waves. Hence, as discussed in Chapter 6, the vibrational spectrum is no more continuous, but composed of a discrete set of stationary oscillation modes (see, for instance, Equations 6.22 and 6.24).

The experimental tools to study non-flat interfaces are on a good level and several techniques are commercially available. In particular, a lot of different setups have been devised for measuring surface tension— e.g., the Wilhelmy plate, spinning drop, or capillary rise method – varying in geometry as well as in the detection principle [212–214]. Here we will focus only on the oscillating drop and bubble methods. Measurements usually rely on videometry and digital image processing of a drop (bubble) shape oscillating in a solvent where surface-active molecules (e.g.: surfactants, proteins, polymers, nano/micro-sized particles) can be dissolved. This procedure yields a two-dimensional image of the cross section of the vibrating drop (bubble). From these data surface oscillations can be carefully reconstructed and the mechanisms underlying the surface dynamics can be unveiled. Typically, the drops or bubbles are anchored at a solid support, similarly to our experiments, although the anchoring mode can vary (see Section 6.9).

Interesting observables are, for instance, the interfacial tension, the surface dilational viscoelasticity and the viscous dissipation. The dynamic properties of interfacial layers also give information on adsorption/desorption mechanisms, such as molecular diffusion in/from the bulk phases and the kinetic processes occurring inside the adsorbed layer (re-orientation, aggregation, etc.).

As a general rule, optical techniques are inherently limited by the space- and time-resolution of the camera. Improving either of the two comes at the expense of the second. The maximum theoretical resolution of digital images is of 110 nm (half the Abbe limit). Hence, despite the progress of digital cameras and the excellent software programs for image analysis, very small and/or very fast surface deformations cannot be detected.

A brief description of the most popular bubble/drop techniques is provided below.

Pendant drop

"Gold standard" of interfacial techniques, it is specially suited for equilibrium (static) surface tensions, but can be applied also to oscillating drops. A scheme of the experimental setup is reported in Figure 13.2: a droplet of about 2–3 mm in diameter is suspended from a needle and its profile is recorded by a digital (video) camera.

If the drop is static, its shape profile, resulting from a balance of capillary and gravity forces, is fitted against the (axisymmetric) Young-Laplace equation, which relates the surface tension σ to the capillary pressure jump ΔP across the interface:

$$\sigma \left(\frac{1}{R_1} + \frac{1}{R_2} \right) = \Delta P \equiv \Delta P_0 - \Delta \rho g z \quad (13.1)$$

Here, R_1 and R_2 are the principal radii of curvature of the drop; $\Delta\rho gz$ is the hydrostatic pressure at height z from the bottom of the drop, $\Delta\rho$ being the density difference between the two fluids, while ΔP_0 is the pressure at $z = 0$. Once the profile is known, the *equilibrium* surface tension σ can be calculated [214].

If the drop undergoes sinusoidal oscillations, the *dynamic* surface tension can be measured from the time-dependent profile [215]. The surface response to local compression or expansion – deriving from shape and/or volume deformation, as well as from the adsorption/desorption of surface-active species – is quantitatively described by the complex surface dilational modulus [216]:

$$\varepsilon(\nu) = \frac{d\sigma}{d\ln A} = |\varepsilon| \cdot e^{i\phi} \quad (13.2)$$

Where A is the surface area. Hence, by relating ε to the time-dependent amount of adsorbates Γ at the drop surface [216], the technique can also be employed to study the adsorption-desorption processes. Moreover, the amplitude of the surface tension response (real part of Equation 13.2) is proportional to the dilational elasticity, while the phase lag ϕ between the surface tension and the applied area perturbation (imaginary part) is related to the viscosity. Both parameters can therefore be extracted as a function of the oscillation frequency ν .

However, since the underlying models are valid only at (quasi-)equilibrium, the pendant drop technique is limited to small-amplitude and low-frequency oscillations (within the 10^{-3} – 10^{-1} Hz range). A second shortcoming is of experimental origin. Indeed, the sensitivity in the detection of σ depends on the drop dimension R_0 and on σ itself (see Figures 13.2 and 13.3). Namely, below or about the capillary length of the interface – indeed, when σ exerts the highest effect on the drop shape – the shape changes are below the detection limit of optical imaging.

Capillary pressure tensiometry

This method [217,218] can be used in alternative to the pendant drop to investigate higher-frequency oscillations. It allows the determination of dynamic surface tension, as well as of surface viscoelasticity, for instance, over adsorption/desorption kinetics experiments.

The experimental setup, sketched in Figure 13.4, consists of an oil drop or gas bubble of controlled volume, anchored to a glass capillary, immersed in a closed cell containing water or an aqueous solution. Unlike the pendant drop, the drop/bubble must be *spherical* (see figure). This is achieved by keeping the radius R small (of an order of 10^2 μm), with an extra benefit for sensitivity.

Harmonic perturbation of the drop/bubble interfacial area is induced by a piezo system located at the bottom of the cell and oscillating with angular frequency ω . The pressure response

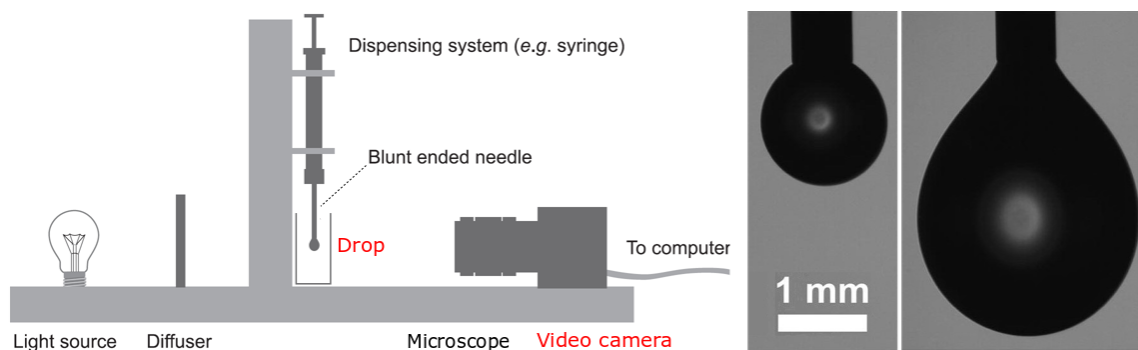


Figure 13.2: *Left:* basic experimental setup for pendant drop tensiometry. *Right:* digital images of two drops. For radii R_0 smaller than the capillary length (left drop) the drop retains a spherical shape, otherwise it is deformed by gravity (right drop). From Equation 3.1 we see that for small R_0 the drop shape is hardly affected by changes in σ , leading to low accuracy in σ measurement, while large drops allow more accurate measurements. Adapted from [214].

of the system is recorded by a sensor. Under linearity conditions, a harmonic response of all of the drop/bubble parameters is expected, including the capillary pressure ΔP between the inner and outer phase: $\Delta P(t) = \Delta P_0 + \bar{\Delta P} \sin(\omega t + \phi)$, with ΔP_0 being the equilibrium (static) value. $\Delta P(t)$ is the parameter of interest to bubble/drop tensiometry and coincides with the Laplace pressure for small spherical bubbles or drops: $\Delta P(t) = \frac{2\sigma(t)}{R(t)}$ (obtainable from Equation 13.1 by imposing $R_1 = R_2 = R$) and is hence related to the dynamic surface tension. Moreover, the viscoelasticity of the interface can be obtained by the phase shift ϕ from the excitation signal. In actual fact, the pressure signal acquired by the detector does not coincide with ΔP , as it contains different bulk pressure contributions. Consequently, specific models of the experimental apparatus and calibration procedures are required to obtain the desired observables.

Concerning the oscillation frequencies, as each tensiometer works properly in a given time scale, a quite broad range could in principle be covered. Limitation in frequency arise from the onset of non radial oscillations [219] as well as by other fluidynamic effects which may set a limit between 100 Hz (for drops and/or highly viscous systems) and 1000 Hz (for bubbles), depending on the experimental setup and conditions [220]. Therefore, for higher frequencies, drop/bubble tensiometers are not longer appropriate and other methods are preferable.

Resonant Droplet Tensiometry

Finally, although not common at all, it is worth signalling the "Resonant Droplet Tensiometry" technique, recently developed at Sofia University [221–223]. The setup, schematised in Figure 13.5,

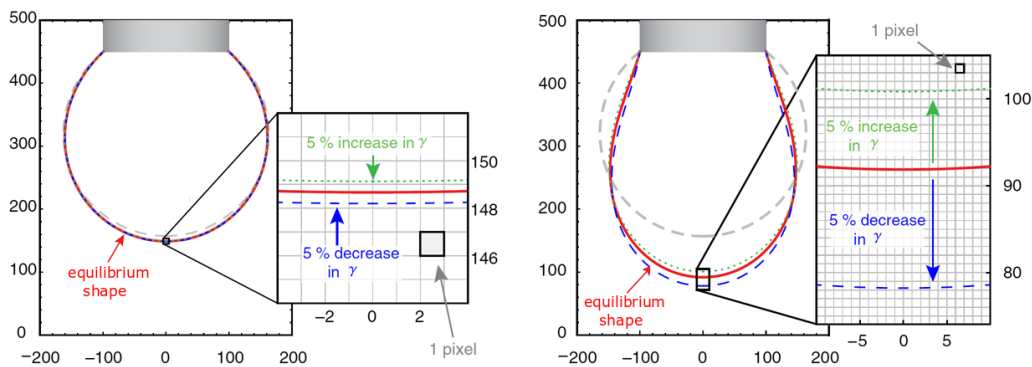


Figure 13.3: σ -dependency of the pendant drop method. *Left:* for high σ (e.g., bare drops or low surface coverages) the shape is only slightly perturbed upon σ variation (e.g. adsorption-desorption of material), resulting in low sensitivity in the optical measurement of σ . *Right:* for low σ (e.g. high surface coverages) the sensitivity is improved. The two drops have the same volume V_0 . Red full lines mark the equilibrium shape, gray dashed profiles the sphere segment corresponding to V_0 . Image adapted from [214].

bears a striking resemblance to our single-bubble apparatus. In brief, a spherical droplet suspended to a needle/electrode, is stimulated by an axial electric field and undergoes axisymmetric oscillations. The instrument is endowed with a camera and shape analysis software, enabling to accurately measure the droplet radius ($\pm 1 \mu\text{m}$). The amplitude and frequency of oscillation are detected by following the time-dependent modulation and/or deflection of a laser source pointed about the droplet bottom, as a function of the applied frequency. Resonance curves similar to ours are obtained, whose analysis allows to estimate several properties like the surface tension (benefiting from the comparison with optical imaging) or the viscosity of the liquid.

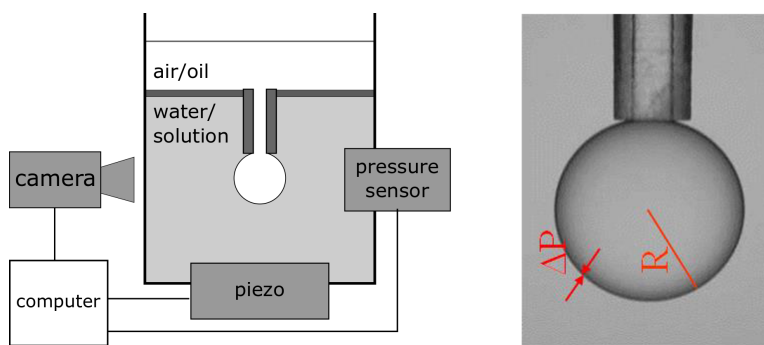


Figure 13.4: Capillary pressure tensiometer. *Left:* sketch of the experimental setup. The camera is optional. *Right:* a typical spherical droplet of radius R . ΔP is the capillary (Laplace) pressure.

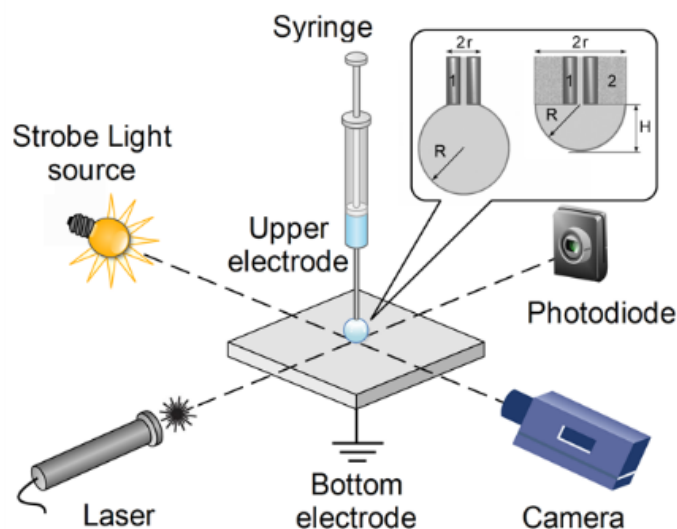


Figure 13.5: Scheme of the Resonance Droplet Tensiometry setup. Image retrieved from [222].

In spite of the similarities with our method, however, the two techniques exhibit markedly different figures concerning the oscillation amplitudes. In fact, typically operated amplitudes are of order of 10–50 μm , with $\pm 1 \mu\text{m}$ sensitivity [222].

13.3 Biomembranes and cells

Measurement of shape fluctuations in biomembranes (biological and biomimetic membranes) and cells also relies on numerous techniques. The vast majority of them are based on far field optical imaging or scattering techniques. Less used methods are x-ray scattering [224], dark field microscopy-based edge detection [225], and defocusing microscopy [226]. An exhaustive review on this topic has been published by Monzel and Sengupta quite recently [11]. Table 13.1, outlining the mostly employed techniques with their merits and limits and related references, is drawn from this review.

Among these methods, RICM (Reflection Interference Contrast Microscopy) -based techniques have been largely employed to investigate the adhesion processes between living cells (or biomimetic models) and solid substrates or supported membranes [2, 235–242, 253]. In recent developments, these techniques have reached a great sensitivity, enabling to detect oscillation amplitudes as small as a few nm [254]. As we will show in Chapter 15, our differential interferometer further improves

Technique	Principle	Resolution	Advantages	Shortcomings
FS [49, 227–230]	Contour analysis (phase contrast)	~10 ms (camera limited); 86 ms	Simple setup	Assumption of refractive index variation; Limited to perimeter
DODS [231, 232]	Displacement of fluorescent membrane in the confocal volume	10 μ s; 20 nm	Simple setup; can measure anywhere on vesicles or cells; applicable to nucleated cells	Single-point information; Fluorescent labelling
TRMFS [233, 234]	Light scattering from object edge	~1 μ s; \leq 1 nm	Label-free; high spatio-temporal resolution	Sophisticated setup; Single-point information
RICM [235–242]	Optical path difference between interfering rays	~10 ms (camera limited); 5 nm	Label-free, topographic information with high axial resolution	Restricted to ~1 μ m from a surface; Requires well defined interfaces of known reflectivity (or approximations)
FLIC [243–248]	Optical path difference between interfering rays	~10 ms (camera limited); ~1 nm	Topographic information with high axial resolution	Requires special substrates; Fluorescent labelling; Sophisticated analysis
DPM [58, 249–252]	Phase shift of scattered light	~10 ms (camera limited); ~1 nm	Label-free, thickness change	Strong assumption on refractive index variation; Requires optically homogeneous samples
DLS []	Elastic light scattering	0.5 μ s–5 ms; ~1 nm	Probing of hydrodynamic theory of membrane dispersion behaviour; probing of membrane structural changes	Averaging of the process over several minutes; Requires homogeneous sample
NSE []	Neutron scattering; dephasing of neutron spins	~1 ps; 1–100 Å	Fluctuations on molecular scales; probing of membrane structural changes	Measurements at spallation neutron source; Limited number of experiments

Table 13.1: Overview of experimental techniques for probing biomembrane fluctuations, with their merits and limits. **FS:** Flicker Spectroscopy; **DODS:** Dynamic Optical Displacement Spectroscopy; **TRMFS:** Time Resolved Membrane Fluctuation Spectroscopy; **RICM:** Reflection Interference Contrast Microscopy; **FLIC:** FLuorescence Interference Contrast; **DPM:** Diffraction Phase Microscopy; **DLS:** Dynamic Light Scattering; **NSE:** Neutron Spin Echo. Adapted from [11].

resolution and allows exploring also the sub-nanometric region. Looking at Table 13.1, we see that these figures are only achieved by neutron-scattering, which, however, relies on accelerator-based neutron sources. By contrast, our setup is definitely compact (as large as an optical bench) and economical (easily retrievable materials, total cost of the apparatus of order of 10000 €).

Chapter 14

Main features of interferometry

In our work, an interferometric apparatus was constructed to study capillary waves rising at the surface of bubbles or drops when they are perturbed from the equilibrium shape by an external oscillating field. The technique here applied allows to measure shape fluctuations in sub-millimetric bubbles and drops, with sub-nanometer accuracy in amplitude.

An exhaustive survey of interferometry is out of our scopes. Rather, we shall provide an essential background to the technique and its main applications and then focus on the interferometric study of bubble and drop oscillations - hereinafter referred to as “Bubble interferometry”. Details of the experimental apparatus and of the measurements performed will be given in Part VI

14.1 Principle

Basically, interferometry measures waves using waves. The detection method relies on the precise determination of the phase difference between two interfering wavefronts originating from a common source.

Any kind of radiation can give rise to interference, so long as it exhibits wave behaviour. In fact, when two wave sources S_1 and S_2 meet up, their wavefronts generate an interference pattern. In particular, if they have the same wavelength λ , this pattern is characterised by an alternating series of fringes of decreasing intensity around the central (maximum) fringe. Here, an intensity signal can be measured of the following form:

$$I(x) = A \left[I_1 + I_2 + 2\sqrt{I_1 I_2} \cos \frac{2\pi x}{\lambda} \right] \quad (14.1)$$

where A is a constant depending on the detection method, I_1 and I_2 are the intensities coming from S_1 and S_2 , respectively, and x is the *path difference* between S_1 and S_2 . The last term in Equation

14.1 is the interference term, which depends on the phase difference $\frac{2\pi x}{\lambda}$ between the two sources. Intensity maxima are only observed when the path difference is equal to an integer multiple of the wavelength:

$$x = m\lambda, \quad m = 1, 2, \dots \quad (14.2)$$

which is the well-known condition of constructive interference.

Equation 14.1 also implies that the pattern shape is extremely sensitive to the spectral properties of the interfering radiation (via λ) and to the system geometry (via x). Therefore, tiny variations in either of the two parameters can be easily detected, especially for small λ (e.g., visible light) and/or large x (e.g., astronomical distances). This makes interferometry ideally suited for ultra-sensitive measurements.

14.1.1 Optical interferometry

Based on the source employed – usually light, radio or sound waves – one can differentiate between optical, radio and acoustic interferometry, respectively. We shall be concerned with optical interferometry and neglect the others in this discussion.

The first light interferometer was developed by Michelson in the 1880s. The technology has improved considerably since – especially owing to the invention of lasers – leading to high standards of accuracy. Nonetheless, the basic functioning principle of the Michelson interferometer, described in Figure 14.1, still remains at the core of interferometry. Indeed, the well-known Fabry-Perot etalon, represented in Figure 14.2, is a “folded” Michelson interferometer: here the multiple reflections occurring inside the cavity result in much better-defined interference fringes.

As a general rule for interferometers (justified in Appendix B), the optical path difference between the two beams CLS1 and CLS2 (x in Equation 14.1) affects directly the character of the observed pattern, for what concerns both the single-fringe intensity and the overall shape of the pattern. As such, noticeable changes are observed upon path variation (e.g., translation of any of the two mirrors in the previous examples). Moreover, since the wavelength of visible light is very short, small variations in the optical path difference can be detected. The actual sensitivity is, of course, dependent on the experimental apparatus.

Notably, as explained in Figure 14.3, the gas-liquid (or liquid-liquid) interface of bubbles or drops provides the optical mirrors for light beam crossing, so that these objects may act themselves as interferometers, where the path length (for central light focusing) is proportional to the radius. Accordingly, an interferometric pattern will be generated whose features – both static and dynamic – are directly related to the bubble (drop) radius.

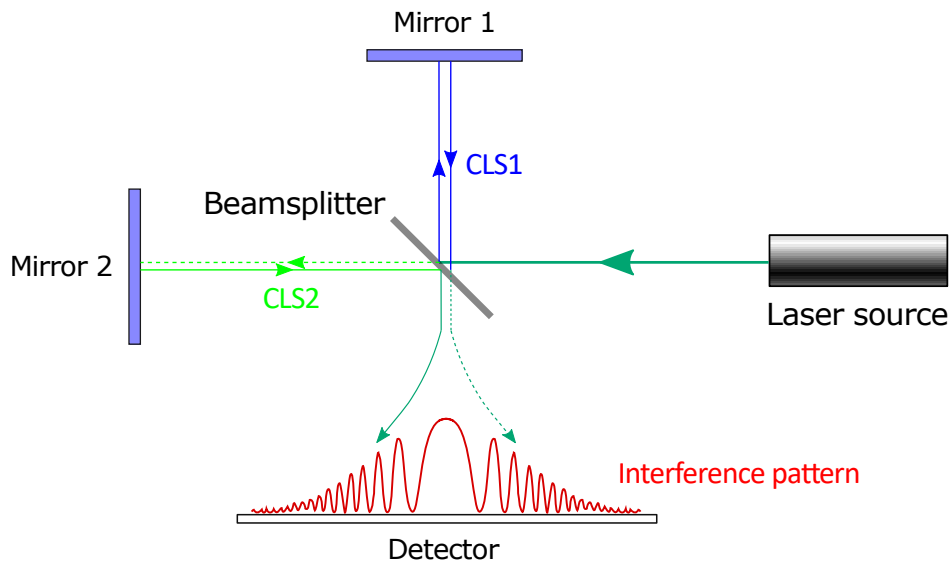


Figure 14.1: Scheme of a Michelson interferometer. It consists of two mirrors and a beamsplitter (partially reflecting mirror). When the incident light goes through the beamsplitter, two coherent light sources are generated with different optical paths (CLS1, going to Mirror 1, and CLS2, to Mirror 2). After being reflected back at the mirrors, the two beams recombine again at the beamsplitter before reaching the detector. The path difference between the two beams causes a phase difference, yielding an interference fringe pattern. In this and in the following figures, incident and reflected beams are represented by filled arrows, while dashed arrows denote transmitted light.

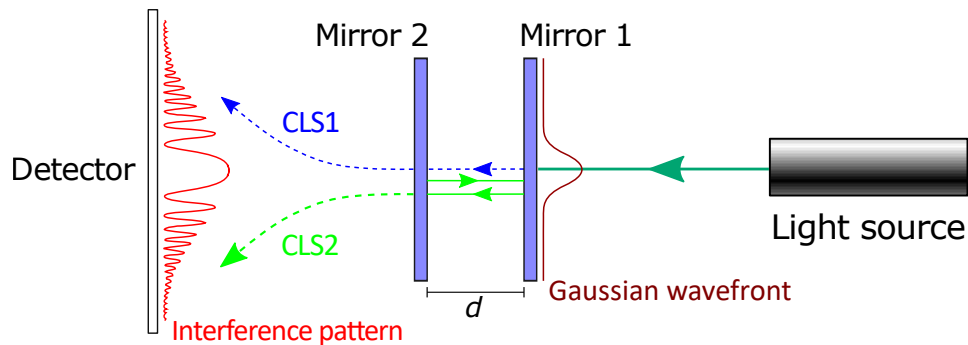


Figure 14.2: Scheme of a Fabry-Perot interferometer. The light source is passed through a pair of parallel, partially reflecting mirrors and undergoes multiple reflections before reaching the detector. Interference yields a coherent light source (of which only two components, CLS1 and CLS2, are shown for simplicity), whose wavelength must satisfy Equation 14.2 and is therefore related to the *cavity width*, i.e. to the distance d between the mirrors ($x = 2d$). Notice how the initially Gaussian wavefront of the laser source finally yields a complex interference pattern.

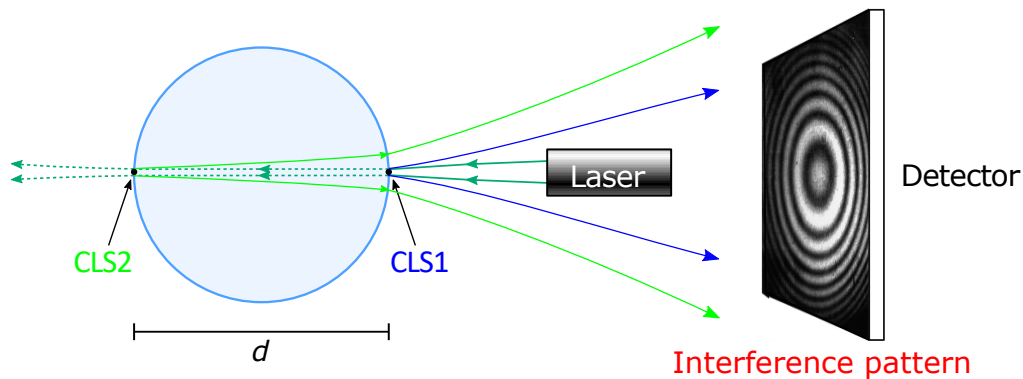


Figure 14.3: A bubble (drop) as a Fabry-Perot interferometer. Due to the refractive index mismatch, the bubble (drop) walls act as partially reflecting mirrors towards a crossing light source (in this case, a laser focused on the bubble centre). Hence, the cavity width d is equal to the bubble diameter. CLS1 and CLS2 denote the interfering light sources generated at the entering and exiting interfaces of the bubble (drop) and directed towards the detector. The divergence of light beams as they cross the interfaces at the indicated points – arising from the curvature difference between the light wavefront and the local bubble surface – was emphasised to illustrate the origin of the observed interference fringes (shown at right).

The above observation is at the basis of "bubble interferometry", which will be the main topic of Chapter 15. In particular, we will be concerned with the *dynamic* features of the interferometric pattern resulting from bubble (drop) dynamic motions.

Landmarks of interferometry: strengths and weaknesses

The most striking features, common to all kinds of interferometry, which make this technique a powerful experimental tool can be summarised as follows:

- Measurements can be performed over a large *bandwidth*, i.e. over a wide range of wavelengths – potentially, all the electromagnetic spectrum. This makes interferometry applicable to a vast number of systems (see Figure 14.4 and next section).
- Interferometry is a *differential* technique, as it measures the difference in path lengths between two coherent radiation sources. As such, it is not affected, to first order, by translations of the system under study¹. This makes interferometric techniques impressively sensitive,

¹This applies only to *linear* systems and proper working conditions.

the theoretical sensitivity being limited by the detection method (e.g., shot noise of photodetectors).

These features make interferometry an ideal candidate for the study of capillary waves at water-gas or water-liquid interfaces, as in the case of oscillating bubbles (drops).

However, potential shortcomings are represented by the following points:

- The sample (and the surrounding medium) must be *transparent* to the incoming radiation. This limits the span of investigable systems: for instance, opaque media are not accessible to optical interferometry.
- Due to the high sensitivity, interferometric measurements are prone to *noise*. Potentially interfering noise sources must therefore be avoided carefully.

Applications

Interferometric techniques have played a crucial role in modern science. Indeed, the underlying basic principle has a potentially infinite range of applications, spanning from fundamental research to instrumental components. A not-exhaustive survey is given below, some examples being illustrated in Figure 14.4.

The sensitivity to spectral properties of radiation (λ in Equation 14.1) may be exploited to measure certain characteristics of the waves themselves and the materials the waves interact with, or, for instance, to construct wavelength filters.

More interestingly, the sensitivity to system geometry (x in Equation 14.1) over a broad bandwidth can be exploited to study small changes in displacement using light waves (see Figure 14.4). This displacement measuring interferometry finds application, for instance, in calibration and mechanical motion control in precision machining, or in the sensing of building structural stability [255]. Moreover, it is of cardinal importance to astronomical observations [256, 257], atomic and molecular spectroscopy [258], structure assessment of macromolecules (one for all, DNA [259]), or to cell and tissue studies [260].

Latest developments have demonstrated the potentialities of this technique in achieving ultimate sensitivities. On this regard, we cannot but mention the Laser Interferometer Gravitational-Wave Observatory (LIGO) [261], which has deserved the 2017 Nobel prize award for Physics [262]. Being able to detect 10^{-18} m displacements (a thousand times smaller than the proton diameter) over a 4 km-long detector, this is the largest and most sensitive interferometer facility ever built.

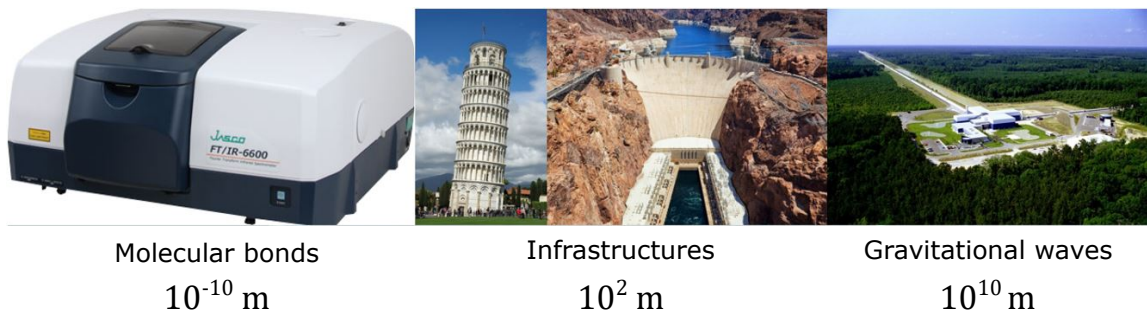


Figure 14.4: An illustration of the scale span of interferometry. *Left image:* an FT-IR spectrophotometer, measuring the strength of molecular bonds by their deformations. *Right image:* the LIGO observatory at Livingston (Louisiana), hosting one of the most popular interferometers for the observation of gravitational waves. *Middle images:* examples of civil infrastructures, whose stability can be monitored non-invasively (by their resonance frequency) using portable interferometric devices. The corresponding wavelengths are indicated at the bottom.

Chapter 15

Interferometric measurement of capillary waves: “(single)-bubble interferometry”

15.1 Idea behind measurements

The possibility to selectively excite distinct oscillation modes of a bubble (drop), together with the idea that the bubble (drop) itself can provide a very simple optical interferometer (see Figure 14.3), lays the basis for a new technique, which we are going to describe in the following sections and address as “bubble interferometry” (Chapter 10).

In brief, an oscillating field is applied on the bubble (drop) to excite its stationary oscillation modes, while a laser beam crosses it in the horizontal direction and is reflected at the entering and exiting air-liquid (or liquid-liquid) interfaces. The deformation from the equilibrium shape is then detected by the change in the optical path of the laser beam inside the bubble (drop) and finally analysed in terms of the bubble (drop) resonance behaviour.

Specifically, the following spectral features are evaluated:

- The oscillation *amplitude*, which is connected to the susceptibility of the bubble (drop) surface to the applied field – the interface tension for shape oscillations;
- The central mode *frequency*, which is related to the restoring forces acting on the vibrating bubble (drop) – the interfacial tension in the simplest situation;
- The resonance *width*, which is determined by the energy dissipation along surface oscillations — i.e. by viscosity for simple systems.

This method is ideally suited for “bubble (drop) spectroscopy”, as it allows the high sensitivity necessary to probe vibration amplitudes that are extremely small (≤ 1 nm) in comparison with the

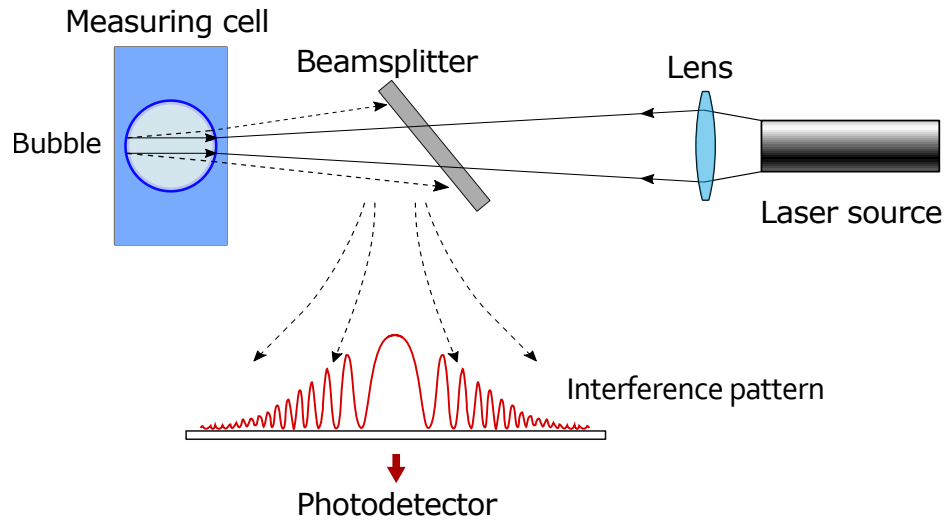


Figure 15.1: Scheme of the (single) bubble interferometer.

bubble (drop) radius (≈ 1 mm). Moreover, this procedure avoids non-linear effects and ensures complete decoupling among the oscillation modes.

In this chapter we shall discuss in general terms the *single*-bubble interferometer, evidencing its functioning and potentialities. The related experimental setup has been extensively employed by our group in recent and ongoing works, as summarised in Section 15.7. The experimental setup developed for studying bubble-bubble interactions will be described in full detail in Chapter 16. We shall see that, in spite of its greater complexity, the underlying principles remain unaltered.

15.2 The single-bubble interferometer

The experimental apparatus, sketched in Figure 15.1, is composed of three main parts, which we are going to discuss in the following sections:

- Optical interferometer
- Measurement cell
- Photodetection system

15.2.1 The optical interferometer

This is the most delicate part of the instrumental apparatus. As any interferometer, it must provide a light source and a means of splitting it into two distinct sources having different path lengths as they recombine after interacting with the sample.

Here, the light source consists of a laser beam focused at the centre of the bubble (drop) by a lens. An essential requirement is that its coherence length be larger than the optical pathway $2d$, that is, to twice the bubble (drop) diameter¹. As described in Section 14.1.1 (Figure 14.3), the bubble walls act as optical mirrors by partially reflecting the incident light and giving rise to two coherent light sources, CLS1 and CLS2, whose optical path difference is equal to twice the bubble diameter. Then, in the backward direction, a circular pattern of interference fringes is formed on any plane perpendicular to the laser beam axis². The origin of this pattern will be explained in Section B, in terms of the Gaussian nature of the light beams. Indeed, according to geometrical optics, CLS1 and CLS2 would be perfectly coincident and no lateral fringes would form.

A portion of the fringe pattern is then deflected by a beamsplitter towards a photodetector, perpendicular to the beam axis and pointed to the central fringe. Substituting $x = 4R$ to Equation 14.1, the measured signal as a function of bubble radius R has the form (for $I_1 \sim I_2$):

$$I(R) \propto 1 + \cos\left(\frac{8\pi R n_i}{\lambda}\right) \quad (15.1)$$

where n_i is the refractive index of the bubble (drop) interior ($n_i = 1$ for air bubbles).

Hence, any change in bubble radius will, in turn, modify the interference pattern in both its shape (the larger R , the narrower the observed fringes, see Appendix B) and its local intensity (Equation 15.1). In particular, if R varies along time – as is the case of oscillating bubbles – a dynamic pattern will be recorded, where a full cycle in the central fringe brightness corresponds to an optical path variation of λ , i.e. to a change in bubble radius $\Delta R = \lambda/4$.

It should be noticed that the above reasoning applies rigorously to central fringe operation, whereby the interferometer is strictly differential. In this case, the optical path difference x depends on the bubble radius R only ($x = 4R$) and not, at first order, on the overall movement of the bubble relative to the laser source or to the detector. In fact, the interferometer can operate in a region where the

¹ For this reason, He-Ne lasers were preferred to semiconductor devices as they offer superior coherence length. In fact, customary semiconductor lasers have coherence lengths shorter than 2 mm.

² Of course, forward reflection at the bubble walls occurs as well, but the resulting signal is superposed to the transmitted light coming from the laser source and cannot be used for measurements.

response function $I(x)$ is nearly linear with x . The interested reader may refer to Appendix C.1 for further information.

15.2.2 The measurement cell

This is the (literally) "pulsating" heart of the experiment. It contains the bubble under study and the excitation electrodes and is a functional part of the optical bench, on which it is mounted, with the bubble acting as a reflecting mirror.

A good measurement cell must be both transparent to the incident radiation – a prerequisite for interferometry – and perfectly clean – an essential requirement due to the extreme sensitivity of the technique.

Actual experiments were performed in hand-crafted cells made of PMMA (a cost-effective material which is transparent, easily washable and does not release contaminants in water at working temperatures) and small in volume (within 1 cm^3). A hydraulic circuit, made of tubes and syringes, enabled the injection and removal of fluid from the cell at every measurement, both for cleaning purposes and to form and position the bubbles (drops). Moreover, any possible care was taken to avoid contaminants in solution, from the cleaning procedure to the use of distinct cells for different substances (e.g., pure water vs SDS solutions). Figure 16.2 shows a cell adopted in two-bubble experiments. The differences between single- and double-bubble cells are merely technical and will be pointed out in Section 16.2.

15.2.3 The detection system

The interference signal produced by the light sources CLS1 and CLS2 is recorded by a photomultiplier tube (PMT) placed on the central fringe axis and having an aperture much smaller than the central-fringe width. By this way the input light is converted into a dynamic voltage output V_{out} proportional to the bubble radius variations (see Figure 15.3 and Appendix C.1).

To ensure linearity conditions (see Appendix C.1) the detection circuitry is devised so that the output signal is split in two components (see Appendix C.2 for further details):

- The former operates as a high pass filter, yielding the time-varying voltage V_{out} , which is in turn collected by the spectrum analyser. In particular the signal-to-noise ratio is optimised for frequencies lying in the range of bubble resonances.
- The latter operates as a low-pass filter, yielding a low-frequency (almost continuous) signal, V_{DC} . The voltage V_{DC} can be read in a display and is used to set the working point (see

Appendix C.1).

Spectrum analyser

Signal analysis may be performed either in *FFT* (Fast Fourier Transform), or in *swept sine* mode. Both of them were exploited in our experiments.

The *FFT* method is the faster and is ideal for a preliminary evaluation of the bubble (drop) spectrum. It converts the time-varying input signal coming from the detector to a frequency spectrum, in accordance with the Fourier theorem [263]. The resulting spectrum displays all the frequency components enclosed in the time signal and is rapidly obtained thanks to the FFT algorithm [263,264].

The *swept-sine* procedure is the more accurate and was employed to obtain the final bubble spectra. Unlike the FFT analyser, which collects all of the frequencies at once, the swept sine measures only one frequency at a time. Basically, it makes use of a comb function, where a frequency interval from ν_0 to ν_f is sampled at n points. At any i -th point, the source supplies a constant frequency (ν_i) input and the analyser selectively collects signals whose frequency is $\nu_i \pm \delta$ ³. The corresponding amplitude $A(\nu_i)$ is averaged over a user-defined number of cycles. After that, the source steps to the $i + 1$ -th point of the sequence. As can be seen, this method is slower than the FFT, but enables optimised amplitude measurements over the entire frequency range. Indeed, as the source is a sine wave, all of its energy is centred at a single frequency value ν_i and the signal noise is therefore minimised.

15.3 Surface excitation

Unexcited bubbles undergo only thermal fluctuations, well described by the damped oscillator model. This can be easily inferred from the RP theory (Section 6.3) by substituting $\alpha = 0$ into Equation 6.12. By contrast, application of an external stimulus may allow for damped-forced oscillations with non-decaying amplitude, from which information on the interface under study can be drawn.

Most commonly, bubble oscillations can be excited either electrically or acoustically. The two excitation modes are analysed and compared below. In Chapters 16 to 18 we will comment on the

³ This procedure, called *lock-in*, is digitally implemented by the analyser by calculating the product between the function applied at step i ($\sin \nu_i$) and the overall (multi-frequency) signal. Recalling the prosthaphaeresis formula: $2 \sin \alpha \sin \beta = \cos p - \cos q$ (where $p = \alpha - \beta$, $q = \alpha + \beta$ and α and β are the frequency components of the applied and the response functions), it can be seen that for any sine function applied only the ν_i -component of the overall signal (corresponding to $p = 0$) is "filtered".

specific case of double-bubble systems.

Electric stimulation

Electric excitation is obtained applying a sinusoidal electric field in the frequency range of bubble (drop) resonance (a few hundred Hz), by means of an electrode in contact or in proximity to the bubble (drop) surface.

This is the most convenient mode when the bubble (drop) interface bears a net electric charge, while no vibration is observed if the surface is neutral.

The electric excitation can be swept in a certain frequency range, the oscillation amplitude being meanwhile recorded by the interferometer. The photodetected signal is measured synchronously by a spectrum analyzer (see Section 15.2.3).

Acoustic stimulation

Acoustic excitation is performed by a piezoceramic emitting a frequency-swept mechanical wave. The pressure gradient induces nonspherical deformations, the restoring force being related to the bubble (drop) interface properties.

Acoustic excitation is a convenient alternative for inducing surface vibrations when the interface is not charged, or when the ionic strength of the solution cannot be kept sufficiently low. If present, here surface charge only affects the mechanical properties of the interface, without entering the excitation process.

Notice that, in terms of symmetry, pressure fields tend to be isotropic, while electric fields are directional. Hence, in order to selectively excite *shape* modes by a pressure field, special care must be paid in the design of the excitation setup. Let us look at Figure 15.2, reporting two different setups for acoustic excitation. In the left one, designed for the detection of volume modes and similar to the setups employed by other researchers, the acoustic pressure is applied at the bottom of the cell and an isotropic field reaches the bubble. Its oscillatory response is therefore related to the surface tension and elasticity and to the compressibility of the gas phase. On the contrary, in the right setup the excitation is provided by a piezo coupled to the anchoring electrode, so that the bubble will sense a highly anisotropic field. Hence, strictly speaking, the acoustic excitation of surface modes can be referred to as a *mechanical* excitation. In this case, the driving force of the excitation is related to the shear exerted on the contacting bubble surface, leading to surface oscillations that are mainly sensitive to the interface properties like surface tension. Details on the two-bubble system are provided in Section 16.2 and Appendix C.2.

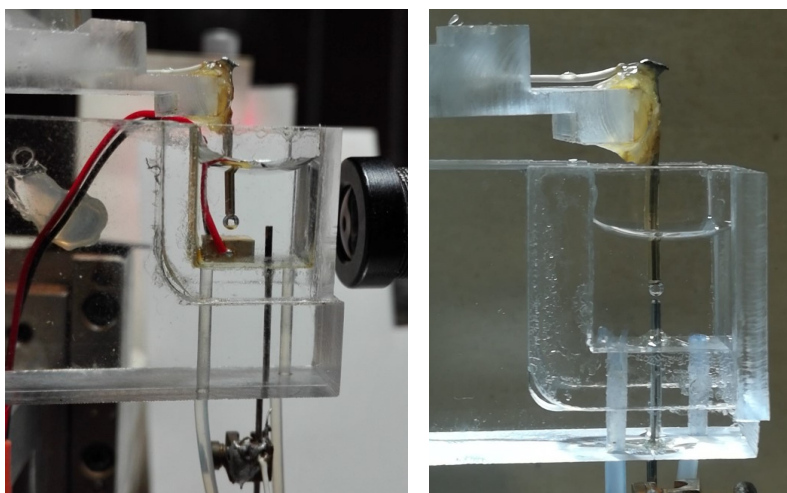


Figure 15.2: Two different setups for the excitation of bubble oscillations. *Left*, measuring cell for the detection of *volume* modes. Bubble excitation (acoustic) is provided by a piezo placed at the bottom of the cell. *Right*, measuring cell for the detection of *shape* modes. Bubble excitation (electric or mechanical) is provided by the contacting anchoring electrode, coupled to a piezo (not visible in the picture – see Figure C.5, detail C, for the two-bubble case).

Moreover, mechanical excitation always yields $A/Q^{-1} = \text{const}$, as expected for linear harmonic oscillators⁴, while this is not the case for electric stimulation, where the amplitude dependence is more articulated, especially in the case of anchored bubbles. A (preliminary) theoretical description of the surface potential at an oscillating anchored bubble, as a function of the applied electrical field, will be given in a later version.

Shape vs volume modes

In Section 6.4 we distinguished between *volume* (breathing) and *shape* (non-spherical) vibration modes. Because of their different physical origin, these two modes respond differently to an applied perturbation. This point must be considered carefully to excite *selectively* either of the two modes, since, according to the theory of coupled oscillators, eigenmodes with similar energy and symmetry are inherently coupled (exactly as happens in molecular orbitals).

Roughly speaking, breathing modes – spherically symmetric and arising from pressure imbalances between the bubble interior and exterior – are best excited by a pressure (acoustic) field,

⁴In this case the amplitude has a Lorentzian frequency dependence, governed by the width parameter: $A(\omega) \propto \frac{\sigma}{(\omega - \omega_0)^2 + \sigma^2}$, where ω_0 is the resonance frequency and σ is half the full width at half maximum. Recalling that the quality factor of resonance is $Q = \frac{2\sigma}{\omega_0}$ and that ω_0 is almost constant, the ratio A/Q^{-1} is a constant as well.

while surface modes – axially symmetric and more sensitive to changes in interfacial properties – are better excited electrically.

By contrast, no significant differences arise between shape (of various order n) and volume modes for what concerns their detection: the interferometric technique will, in any case, detect *local* variations of the bubble radius in the direction of the laser beam, passing through the centre of the bubble (Section 15.2.1), regardless of the excitation method. Therefore, the form of the interferometric response (Equation 15.1) applies to any oscillation mode, as do the observations made in the following section.

15.4 Relationship between excitation, interferometric response and detected signal

Theory of harmonic motion predicts that small applied perturbations will result in small oscillations around the equilibrium position. In the case of an oscillating bubble, this means that (neglecting phase delay with respect to the source) its local radius R will vary about the equilibrium radius R_{eq} such that $R(t) \propto E_{\text{app}}(t)$, the proportionality coefficient depending on the oscillation amplitude. Besides being a convenient assumption for theory, linear oscillations provide the best condition for quantitative measurements, as illustrated in Figure 15.3.

We know from Equation 15.1 that the bubble oscillatory motion is followed by a variation in light intensity at the central pattern fringe $I(R)$ (left panel of the figure). If the interferometric response $I(R)$ is linear with R (i.e., in the neighbourhood of R_{eq} , red point in the figure), it is possible to detect changes in the bubble radius from variations in the detected signal, exploiting the proportionality between $I(R)$ and the output voltage $V(t)$ (right panel). The absolute calibration of the vibration amplitude is easily obtained by comparing the voltage span for the central fringe half cycle with the peak-to-peak voltage output given by the spectrum analyser.

In Appendix C.1 we will explain how to set the working point for linear operation, detailing the calibration procedure, and see what happens when oscillation amplitudes lie out of the linearity range.

15.5 Spectral features

As explained in Section 15.2.3 and in Appendix C.1, the voltage $V_{\text{out}}(t)$ from the detector can be readily converted into oscillation amplitude values as a function of the excitation frequency, that is,

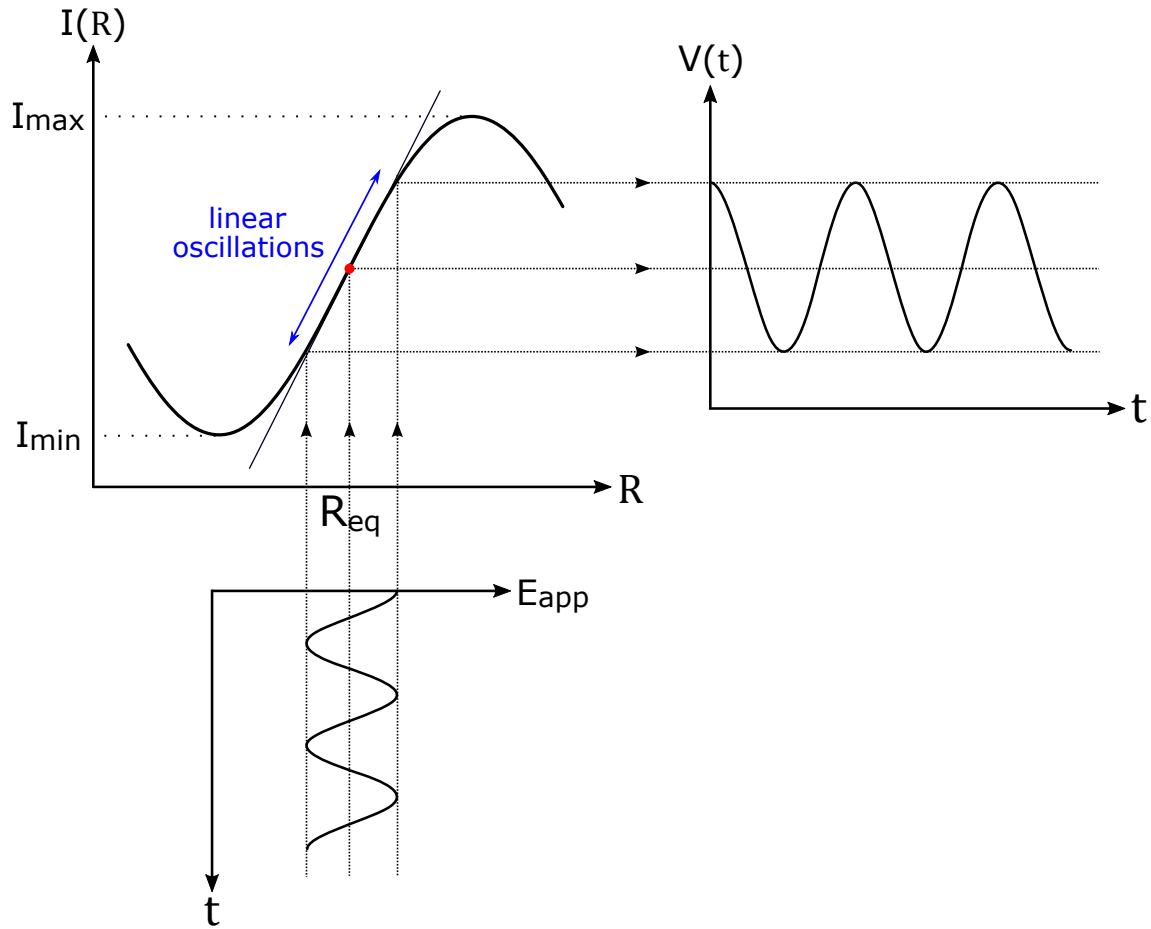


Figure 15.3: Relationship between the applied sinusoidal excitation field E_{app} (bottom), the interferometric response of the bubble I as a function of local radius R (Equation 15.1, left) and the detected signal $V(t)$ (right). In the case of small-amplitude (harmonic) oscillations, $R(t) \propto E_{app}(t)$, where R varies about the equilibrium radius R_{eq} . The bubble oscillatory motion can be interferometrically detected by following the variation of light intensity at the central pattern fringe, $I(R)$ (Equation 15.1). This explains the link between the applied oscillating field and the interferometric response. $I(R)$ is in turn related to the detected voltage $V(t)$, provided it is linear in the neighbourhood of R_{eq} (i.e., $\Delta I \propto \Delta R$). As shown in the figure, this implies that the working point be chosen at the inflection point of $I(R)$ (marked in red). In particular, if the working point is set at the left of an intensity maximum I_{max} (as represented here) the fringe intensity grows with increasing R , while on the right side a local increase in R will be followed by a decrease in I . Within these conditions, if the speed of response of the photodetector exceeds the bubble (drop) oscillation frequency, the voltage $V(t)$ will follow instant variations of I and, hence, of R .

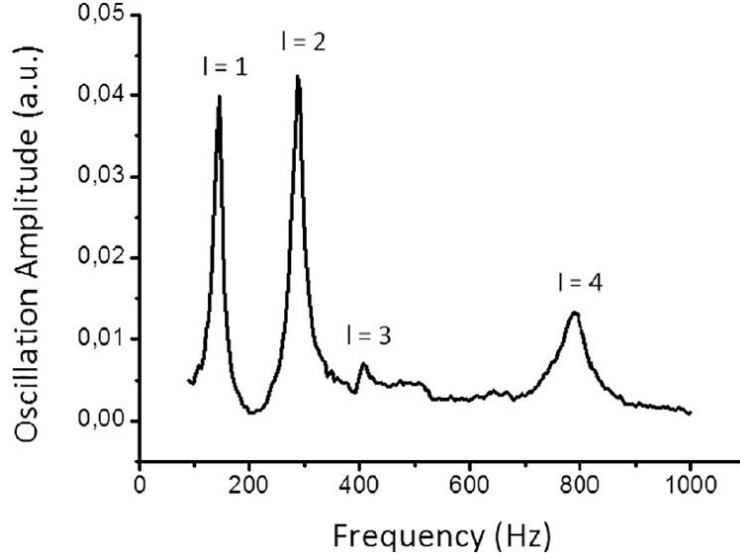


Figure 15.4: Vibrational spectrum of a single anchored bubble (radius $R_0 = 0.64$ mm) in pure water, excited by an inhomogeneous electric field. Different harmonics are clearly visible: $l = 1$ (141 Hz), $l = 2$ (287 Hz), $l = 3$ (410 Hz) and $l = 4$ (786 Hz), with l corresponding to n in our model. Image retrieved from [7].

to a vibrational spectrum of the bubble. A typical example is given in Figure 15.4, where several resonance peaks corresponding to increasing values of n (higher harmonics) are evident.

For small deformations, where linear response dominates and the forced-damped harmonic oscillator model holds, all of the bubble modes are expected to show a simple Lorentzian frequency dispersion [98] (see, for instance, Figure 15.5):

$$a_n(\nu) = \frac{2A_n}{\pi} \frac{\gamma}{4(\nu - \nu_0)^2 + \gamma^2} \quad (15.2)$$

Here, $a_n(\nu)$ is the measured amplitude (proportional to V_{out}) as a function of the frequency ν of the sweeping excitation voltage. A_n is the maximum peak amplitude, corresponding to the resonance frequency ν_0 . Finally, γ is the peak width measured for $a_n(\nu) = A_n/2$ (known as the *full width at half maximum*, FWHM). Subscript n denotes the oscillation mode, such that a whole bubble spectrum (as that of Figure 15.4) is given, within our linear modelling framework, by the sum of all the individual harmonics.

As for any vibrational spectroscopy, spectral analysis of bubble resonance gives precious insights on the system properties. In particular, the following parameters can be evaluated:

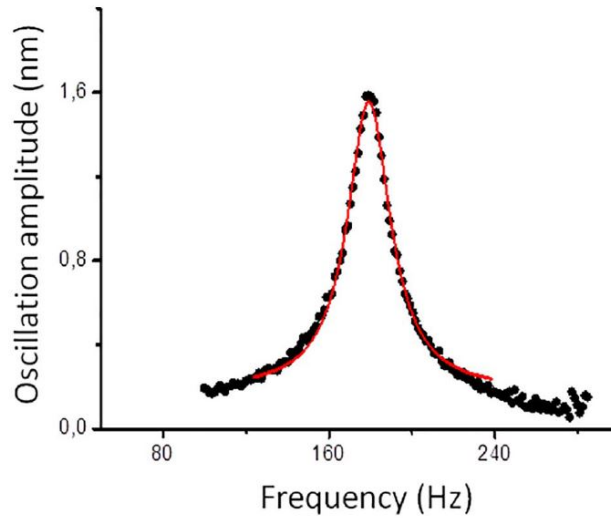


Figure 15.5: Vibrational spectrum (black dots) of an air bubble in water, 0.85 mm in radius, excited by a sweeping sinusoidal voltage of 1 V. The full red line is a Lorentzian fit. Image retrieved from [7].

- The oscillation *amplitude*
- The peak *width*
- The resonance *frequency*

Amplitude

The oscillation amplitude at resonance is connected to the susceptibility of the bubble (drop) interface to the applied field. If excited by an electric field, the oscillation amplitude is connected to the net surface charge on the bubble. If excited by an acoustic wave, the mismatch in compressibility and density is involved.

The oscillation amplitude of a bubble over the excitation frequency, $a(\nu)$ in Equation 15.2, is tightly related to the interaction between the bubble surface and the applied sinusoidal field (acoustic or electric), that is, to the nature of the oscillator and that of the forcing.

In the case of *acoustic* excitation, the forcing consists of an applied sinusoidal pressure. As the RP theory suggests (see Equation 6.9), the coupling between the applied field and bubble oscillation modes derives from the imbalance between the pressure inside and outside the bubble, which forces the bubble radius to vary over time. For this reason, larger amplitudes are observed for the volume modes than for the shape ones (see Section 15.3). The involved physical properties of the bubble are density and compressibility.

When the forcing is of *electric* nature, resonance behaviour entails a polarisation of the bubble surface. The coupling with the excitation field is most effective when the bubble possesses a net surface charge: in particular, at constant surface charge densities, the measured amplitude scales with the square of the radius R^2 , meaning a proportionality with global surface charge [265]. However, the coupling can also take place in the absence of charge, because of the difference in the dielectric constant between the gas within the bubble and the outer liquid. This is, for instance, the case of air-water interfaces. The surface charge density on millimetric air bubbles in pure water was found to be of the order of $1.8 \times 10^{-5} \text{ C}^{-2}$ [265]. The coupling is quadratic in the electric field (i.e., $A \propto \mathbf{E}^2$, with time dependence from the driving $\propto \sin 2\omega t$). Due to their inherent directionality, electric fields couple preferably to surface modes [266].

Frequency

The resonance frequency is connected with the forces restoring the equilibrium bubble shape, and hence, in the simplest case, to the bubble radius and to the interfacial tension (analogously to spring-mass systems).

In line with the theory of harmonic oscillators, the characteristic frequencies of a bubble oscillating at small amplitudes are related to the restoring forces which contrast the applied driving force. Hence, while in a spring-mass system the oscillation frequency depends on the effective mass of the oscillator and on the spring constant, in the case of bubbles the radius and the interfacial tension are involved, respectively (see Equation 6.24). If the bubble undergoes volume oscillations the compressibility of the inner gas comes into play (see Equation 6.14).

Width

The peak width reflects the energy dissipation along surface oscillations, namely viscosity for simple systems.

The bandwidth $\Delta\nu$ of a resonator, given by the full width at half height (the γ coefficient in Equation 15.2) is associated with the rate of energy loss relative to the energy stored by the resonator, that is, to its *damping*. In the case of bubbles, higher damping means a higher viscosity of the surrounding fluid (see Equations 6.13 and 6.21).

A common descriptor for resonators is the dimensionless parameter Q , termed *quality factor*:

$$Q = \frac{\nu_0}{\Delta\nu} \quad (15.3)$$

relating the bandwidth $\Delta\nu$ to the resonance frequency ν_0 .

In the case of bubbles, since the observed resonance frequency is rather independent of fluid viscosity, the peak width, and hence viscous dissipation, is directly proportional to the inverse quality factor, Q^{-1} .

Phase

As mentioned in Appendix B, the interferometric signal always possesses a phase relative to the excitation field, owing to its ondulatory origin.

This phase, that we will refer to as the "*absolute*" phase of the resonance peak, can be directly accessed in experiments performed under electric excitation, since the sweeping sine voltage, generated by the spectrum analyser, coincides with the signal used to excite bubble oscillations. It is interesting to note that one clearly observes a π phase shift when the exciting frequency goes through a peak of the bubble response. This is exactly what is expected when a true harmonic oscillator undergoes resonance. Since opposite charges will have opposite phases, the information on phase gives the sign of the net charge at the bubble interface. Moreover, it allows to estimate the charge adsorbed on a covered bubble, by comparison with the (negative) charge of the bare air-water interface [265]. However, the information on charge is irrelevant to our scopes, since in our experiments we know in advance the sign of the species adsorbed at the bubble surface. Moreover, in the case of acoustic excitation, the phase reference provided by the sweeping voltage is missing, hence the absolute phase is not easy to define (although possible).

The absolute phase is poorly informative about bubble oscillations. By contrast, information on inter-bubble interactions can be gained from the relative phase.

15.6 Covered bubbles

Many kinds of species can be adsorbed at the air-water bubble interface. Among them, we have tested H^+ and OH^- , surfactants, different proteins, porphyrins and gold nanoparticles on single oscillating bubbles. I will not discuss these experiments in my thesis, apart from one remark.

In our studies of covered bubbles based on the interferometric technique, we have observed the existence of an adsorbant-dependent threshold concentration above which resonance spectra display a divergence of the viscous damping (see, e.g., [9]). We have called this threshold the critical *dissipation* concentration (CDC). This phenomenon, resembling a phase transition from a gas-like distribution to a liquid-like assembly (but occurring at much lower concentrations), has lately

been interpreted in terms of a Rayleigh instability of the bubble shape upon charging (submitted article).

15.7 State of the art in the proposed method

The research group, I collaborate with, has been working on the interferometric detection of the vibration modes of bubbles and drops. A short list of the main investigations performed so far is presented as follows:

- Air bubbles and oil drops in water [265];
- Electric vs acoustic excitation;
- Surface oscillations in presence of surfactants [9];
- Sorption-desorption of surfactants from a gas-liquid interface [267];
- Diffusion in presence of oscillating traps [8];
- Anomalies of sub-nanometric oscillation amplitudes [4];
- Adsorption kinetics of model globular and membrane proteins (submitted article).

Most of these cases are summarised in Ref. [7], including a detailed description of the experimental apparatus.

Part VI

**THE *DOUBLE* BUBBLE
INTERFEROMETER.
EXPERIMENTAL RESULTS**

Chapter 16

Double interferometer

The interferometric setup employed so far by the research group to study capillary waves (described in detail in Section 15.2 and related references, e.g. [7]) was extended to allow the study of a system composed of two interacting bubbles by monitoring the vibration parameters of both bubbles at once. This entailed the use of two interferometers, in order to evaluate the correlated motions of the two bubbles, as well as of two excitation sources. For this reason, we refer to this instrument as the *double* bubble interferometer.

16.1 Functioning scheme

Let us first describe the basic requirements for the observation of bubble-bubble hydrodynamic interactions and then extend the discussion to the adopted setup.

A conceptual view of the double-bubble experiment is provided by Figure 16.1. Here, two equal bubbles, denoted as **A** and **B**, are embedded in a cell filled with water. The closest distance between their surfaces is D . Bubble **A** is excited by an oscillating field (e.g., electric). Bubble **B** does not feel the applied field, but may oscillate due to the pressure waves propagating in the fluid, induced by Bubble **A** oscillations. These fluid-mediated bubble-bubble interactions will depend critically on the distance D and may be studied by recording the vibration spectrum of Bubble **B** for different values of D . Individual spectra, like those stacked at the bottom of Figure 16.1, are obtained according to Section 15.2.1.

16.2 Actual setup

The scheme presented in Section 16.1 needs adjusting for real experiments:

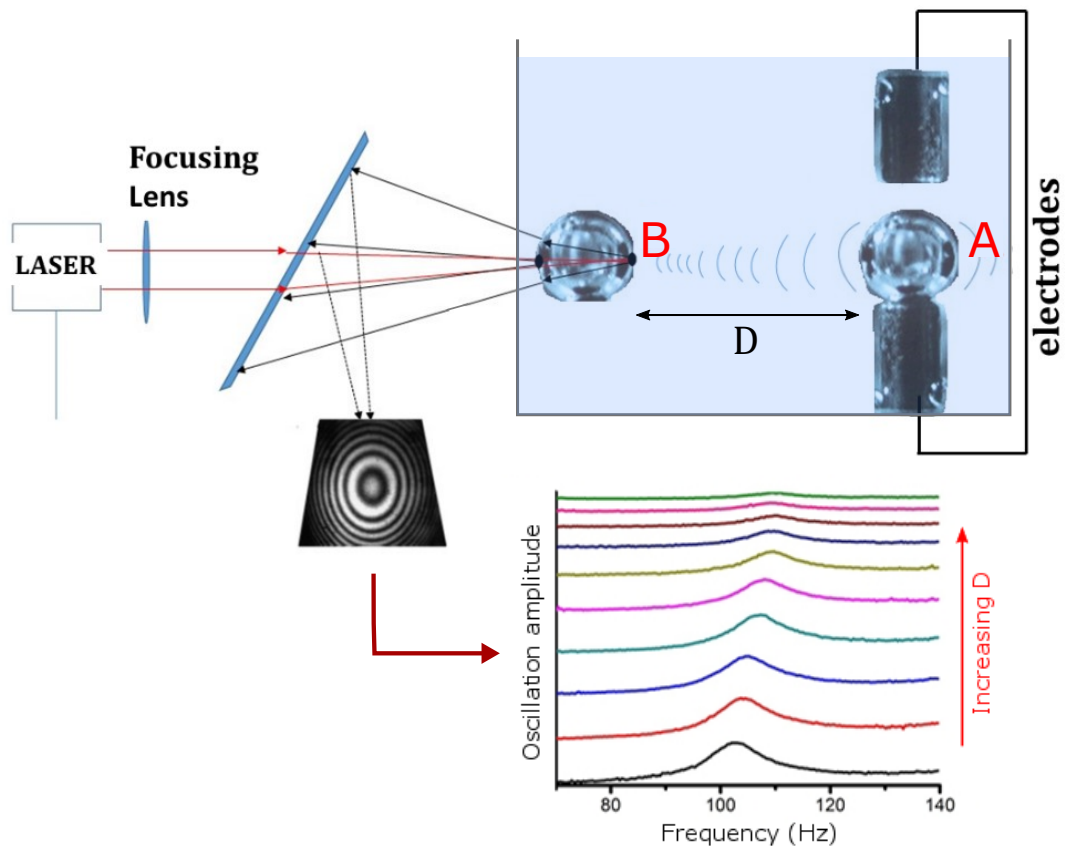


Figure 16.1: Functioning scheme of the double bubble interferometer. Bubbles **A** and **B** are immersed in a water-filled cell and distant D . Bubble **A** is selectively excited by an applied oscillating field: as it vibrates, pressure waves propagate in the surrounding fluid and make Bubble **B** vibrate as well. Bubble **B** oscillations are interferometrically recorded, according to Section 15.2, at several values of D (see spectra at the bottom) and variations in the spectral parameters are evaluated as a function of D .

- To begin with, if we only followed Bubble **B** dynamics we would have a partial view of the bubbles' mutual interactions. Rather, motions of both bubbles must be evaluated at once and independently. This need is met, on the one hand, by splitting the laser source into two halves, each centred on one bubble, so to obtain two independent interferometers; on the other hand, the interferometric patterns must be collected by two independent photodetectors (see Figure C.8). Care must be taken to avoid interference between the light sources going to the detectors.
- To ensure strict differentiability of measurements (i.e., signal depending on bubble radius variation only), bubbles are not buoyed up, but anchored to the electrodes. This point will be covered in Section 16.2.
- Acoustic insulation must be provided to achieve sensitivities of order of 1 \AA (see Appendix C.1).
- Bubbles **A** and **B** are not identical and exhibit distinct vibration spectra (see Section 16.2). Albeit lowering the symmetry with respect to our modelling possibilities, this enables to selectively excite either of the two bubbles and study the effect of its oscillation on the other.

Pictures of the experimental apparatus and related details are provided in Appendix C.2, while Figure 16.2 shows the interacting bubbles. In the following sections we are going to illustrate the peculiarities of the double-bubble interferometer with respect to the single-bubble device discussed in Section 15.2.

Master vs Slave

The double-bubble experiment, conceptually introduced in Section 16.1, entails a role distinction between the two interacting bubbles. Accordingly, in Figure 16.1 we denoted as Bubble **A** the bubble directly excited by the applied field and as Bubble **B** the bubble (not directly excited) whose oscillations are hydrodynamically induced. Apart from this distinction, the two bubbles were assumed to be identical.

In actual experiments the two bubbles are not identical, but can be distinguished by their different geometric constraints, as is clear from Figure 16.2:

- one bubble is held anchored to both an upper and a lower electrodes and may be excited either mechanically or electrically. This was called the *master* bubble.

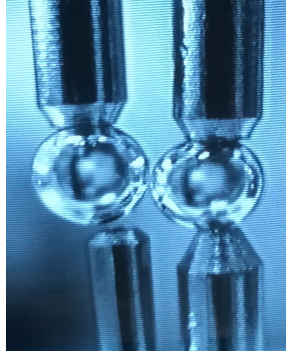


Figure 16.2: Detail of the experimental setup, showing the interacting bubbles (at a mutual distance of about $10\ \mu\text{m}$). *Left:* the *slave* bubble (upper-anchored). *Right:* the *master* bubble (doubly-anchored). The smaller lower electrode on the left is the injection capillary (hollow), while the others (solid) provide the anchoring points. The right electrodes are connected to a piezoelectric feedback, partially visible in Figure C.5, to allow acoustic excitation of the *master* bubble.

- the other is anchored only to an upper electrode and can only be excited electrically. This was called the *slave* bubble.

Notice that, owing to the double constraint along the axial direction, only the $n \geq 2$ modes can be excited in the master bubble, while the $n = 1$ mode is accessible for the slave. In our experiments we excited the $n = 2$ mode of the master and the $n = 1$ mode of the slave. The resulting difference in resonance frequencies ($\omega_{slave} < \omega_{master}$) is further magnified by the smaller size of the master bubble. This enhances the selectivity of the excitation and allows to monitor unequivocally the response of the two bubbles.

Electric vs mechanical stimulation

As discussed in previous Section 15.3, bubble oscillations may be excited either electrically or mechanically. While no significant differences may be observed in single-bubble experiments between these two excitation modes, some differences arise in double-bubble experiments.

Broadly speaking, mechanical excitation can be performed at a constant amplitude over the entire span of distances D , while in the case of applied electric fields a higher intensity is perceived at smaller D and vice versa (and hence, the exciting voltage must be adjusted to ensure constant excitation amplitudes). On the contrary, electrical excitation generally yields narrower peaks and is preferred for some measurement routines, as discussed in Chapter 17.

16.3 Spectral features

Spectra acquisition is the same as in single-bubble experiments. The numerical values of the spectral parameters will vary as a function of the bubble-bubble interactions. In particular, the oscillation amplitude increases with the coupling strength, while the resonance frequency decreases. The peak width, related to viscous dissipation, will depend on both the viscosity of the fluid and on its average kinetic energy, as commented in Section 6.8. Based on the considerations made in Section 11.5, a peak width increase with the coupling strength is expected. Finally, the phase measurements deserve a separate discussion.

Relative phase

In Section 15.5 we mentioned the possibility of recording the phase of oscillation of single bubbles. When it comes to two-bubble system, the *relative* phase of oscillation $\Delta\phi$ can be recorded as well, corresponding to the physical quantity defined in Equation 11.18.

Unlike the absolute phase, that is related to the surface charge of the bubble, the relative phase gives information on the *synchronisation* between the two oscillators. Namely, a stable $\Delta\phi \approx 0$ signal along the oscillation recording means that the two bubbles oscillate in phase (attractively), while $\Delta\phi \approx \pi$ means out-of-phase interactions (due to repulsion) whereby, for equal average distances between the two oscillators, the instantaneous value is maximised. Finally, a non-constant phase difference denotes non-synchronised motions.

In Section 17.6 we will show some examples of phase measurements concerning axisymmetric interacting bubbles and what information can be extracted from them.

Chapter 17

Experiments on double-bubble systems: interacting *axisymmetric* bubbles

In the course of this years, we designed several experiments on two-bubble systems, in collaboration with professor Mario Corti and the LITA laboratory, in Milan (Italy). While I just trained with simple measurement routines, most measurements were made by professor Corti.

The main experiments performed are listed below:

- Bare bubbles in water (Section 17.1)
- SDS-covered bubbles in water (Section 17.2)
- BSA-covered bubbles in water (Section 17.3)
- Bare bubbles in weakly viscous solutions (Section 17.4)
- Bare bubbles in the absence of applied excitation (Section 17.5)

The most typical measurement routine consists in exciting the *master* bubble mechanically (with a 5 mm amplitude) over the 70–160 Hz frequency range, including the characteristic frequency for the $n = 1$ mode of the *slave* bubble. As the $n = 2$ mode for the *master* bubble falls at a much higher frequency, its observed spectrum is flat in this range in absence of any interaction. Then the response spectrum of the *slave* bubble is recorded for different values of the inter-bubble distance D . Notice that in the data reported below D denotes the closest separation distance between the walls of the two bubbles (and not the centre-centre distance). A frequency sweep from ν_0 to ν_f of each experiment took 10 s. All of the spectra were averaged over 3 to 10 replicas.

17.1 Bare bubbles in water

Our first measurements concern the interaction between two air bubbles in ultrapure water. The typical routine described above was followed. The *slave* bubble has an unperturbed radius $R_0 = 0.75 \pm 0.01$ mm). The inter-bubble distance D ranges from 1.5 mm to below contact. The contact distance, falling at about 25 μm due to the presence of a thin water layer between the two bubbles, is evaluated as the distance for which the resonance frequency exhibits a minimum (see Figure 17.3). At lower distances the two bubbles are deformed and the frequency rises over further approaching (as the local radius decreases). Distances below contact are arbitrary and based on the measured electrode displacement with respect to the contact distance. Since the data below contact distance are not relevant to our scopes, they will be disregarded in the other experiments.

The dependence of the observed spectral parameters on the inter-bubble distance is reported below for the case of mechanical excitation:

- The oscillation *amplitude* of the slave bubble decreases of a factor 4-5x with increasing D , up to amplitudes comparable with the *master* vibrations out of resonance (5 nm). The values in Figure 17.1 are normalised against the peak width, to ensure that any variations be due only to bubble-bubble interactions.
- The peak *width* (Equation 15.3) decreases as well (from 12 to 8 Hz), meaning reduced viscous dissipation when the two bubbles are far apart.
- Resonance *frequency* (Figure 17.3) increases with D , from 110 Hz at contact, to 114 Hz (coincident with the characteristic frequency of the *slave* bubble) at 1.5 mm.
- The two bubbles oscillate *out of phase* (Figure 17.4) regardless of the distance. The relative phase shows a π jump in correspondence to the slave bubble resonance, so the inflection point shifts to higher frequencies upon an increase in D .

Several measurements performed on different bubbles (with frequencies of the *slave* bubble lying in the 100–120 Hz) confirm these trends and the order of magnitude of the observed variations.

These results denote synchronisation between the two bubbles (although in phase opposition). The variations in the spectral parameters, especially the the red-shift in the *slave* bubble resonance frequency compared to the isolated system, are a measure of the strength and of the length decay of inter-bubble communication.

Hence, the two bubbles feel each other at very large distances (of order of 1 mm, larger than bubble radii), well beyond the range of intermolecular interaction forces.

Notice that, for all the spectral parameters, the first points of the curve (corresponding to distances within about $100\ \mu\text{m}$) show a different slope with respect to the following ones. One possible explanation for this "transition" could be a change in the coupling mechanism: for instance, it might be purely hydrodynamic at large distances, but influenced by electrostatics at smaller distances. Such distances, however, are much larger than the predictions of pure electrostatic coupling (Section A.1).

17.2 SDS-covered bubbles

We then measured the interaction between two air bubbles covered by Sodium Dodecyl Sulfate (SDS), a standard surfactant possessing a net negative charge.

Notice that amphiphilic molecules like SDS form micelles in water. The critical micellar concentration (CMC) for SDS is of 0.5%, so in our experimental conditions (0.03%) we ensured that the SDS was present in the bulk solution as suspended individual molecules. Generally, for the critical dissipation concentration (Section 15.6) it holds $\text{CDC} \ll \text{CMC}$. For SDS, $\text{CDC} = 0.0015\%$ [9].

The measurements were taken according to the described routine for different values of SDS bulk concentration. At the lowest value, $0.013\ \text{mM}$ (0.0005% , $\approx 1/4\ \text{CDC}$), the two bubbles behave as if they were immersed in pure water, apart from a significant broadening in the peak width (data not shown). The results reported here concern the highest concentration value, $0.1\ \text{mM}$ (0.003% , $\approx 2\ \text{CDC}$). In this case, the master bubble was excited electrically owing to the extremely large peaks obtained under mechanical driving. D was varied in the $20\text{--}2000\ \mu\text{m}$ range. The radius of the unperturbed *slave* bubble was $0.65\ \text{mm}$ (characteristic frequency for the $n = 1$ mode: $120\ \text{Hz}$).

Results show that:

- The oscillation amplitude (Figure 17.5) decreases with D , and is about 12 times that observed in pure water in the case of electric excitation and twice the water values for mechanical excitation.
- Red shift in the resonance frequency (Figure 17.6) as the bubbles get closer: from $120\ \text{Hz}$ at $2000\ \mu\text{m}$, to $107\ \text{Hz}$ at $20\ \mu\text{m}$.
- The Quality factor (Figure 17.7) increases with D (from 0.9 to 2.0 in the case of electric excitation). Resonance peaks obtained from mechanical excitation of the master bubble are much larger, which made measurements rather difficult.

- The two bubbles oscillate out of phase (data not shown) over the entire distance span and for both concentration values.

Asymmetric coverage

After the above measurements, where both the interacting bubbles were covered by SDS, we studied the interactions between a bubble covered by SDS (the master) and one bare bubble (the slave). The idea behind this experiment was to test the capability of the bubbles to exchange chemicals by their oscillations.

The master bubble was formed in a 0.1 mM SDS solution and allowed to adsorb surfactant at its surface. The bulk solution was then rinsed several times until the measured conductivity of the solution matched the value of pure water. In such conditions, the master bubble still retains the adsorbate on its surface without significant losses in the surrounding medium, as it was verified by evaluating the surface charge from the electrically excited resonance spectrum (comparable with those observed in the 0.1 mM bulk SDS solution). The slave bubble was then added and excited indirectly via the master bubble (mechanically driven) as in the previous routines.

The spectra of the slave bubble obtained via this procedure (not shown here) are superimposable to those obtained for ultrapure water and for SDS below the CDC. This observation clearly rules out the hypothesis of an interaction-enhanced exchange of chemicals between the two bubbles, at least in this weak-interaction regime. However, it demonstrates the possibility of studying the interactions between two bubbles bearing different coatings.

17.3 BSA-covered bubbles

Many protein-covered single bubbles were previously studied in our laboratory using different classes of proteins. To extend this study and test the role of adsorbed proteins in bubble-bubble interactions, we chose Bovine Serum Albumine (BSA), a globular protein of $MW = 66.5 \text{ kDa}$ bearing a highly negative charge at neutral pH (isoelectric point: 4.7). For this protein, the CDC is 4.5 nM (0.25 mg/L) and $CMC \gg CDC$. Experiments were performed with 1.5 nM and 2 nM (below CDC) and 6 nM (over CDC) bulk solutions of BSA. The *slave* bubble radius was in both cases of 0.75 mm. The *master* bubble was excited out of resonance, both electrically and mechanically (in the latter case, at the highest concentration the resonances are rather large and difficult to analyse, see Figure 17.14).

Results confirm the the qualitative behaviour observed in SDS-covered bubbles. Namely, below

the CDC the spectral parameters behave similarly to those of pure water, except for higher dissipation, with a resonance frequency span over D of about 5 Hz (see Figures 17.8, 17.9 and 17.10). The frequency span doubles at the higher concentration (Figure 17.11) and the quality factor spans from less than 1 to 2 on increasing D (Figure 17.12). Finally, Figure 17.13 shows the behaviour of the relative phase between the master and the slave bubble oscillating in pure water (black) vs in 0.1 mg/L BSA solution (red), at $D = 350 \mu\text{m}$. Phase going from approximately π , to 0, to $-\pi$. Two inflection points corresponding to resonance frequencies of the two bubbles: the one at about 100 Hz corresponds to the *slave* bubble frequency; that at 135 Hz to the *master* bubble resonance ($n = 1$).

17.4 Weakly viscous solutions

Selective investigation of solvent viscosity effects on bubble-bubble interactions is much more difficult than the cases reported previously. This is mainly due to the fact that peak detection is undermined by broadening. Another major concern is to minimise the adsorption of organic compounds on the bubble surface, which could affect interface properties as well. Therefore, measurements were limited to dilute solutions of small, rather polar, high-purity compounds.

Addition of non-adsorbing solutes to the fluid surrounding the two bubbles should only affect viscous dissipation, i.e. the peak width, without significantly altering interface-related parameters like amplitude and frequency. Experimental results confirm these predictions, evidencing an increase in peak width with increasing solute concentration, while the frequency and amplitude span along inter-bubble distance remain comparable to the values obtained in pure water. Some examples are given below.

Methanol

Figure 17.15 reports the quality factor of resonance Q of the slave bubble in a dilute aqueous solution of methanol (0.005% w/w), as a function of the inter-bubble distance D . As expected, a drastic decrease in Q is observed for methanol compared to pure water.

Sucrose

Ultrapure sucrose (Sigma spectroscopic grade) was added to the water medium, first to a 5% w/w concentration and then to 10%. The spectra of the isolated slave bubble ($R_0 = 0.75 \text{ mm}$, excited

electrically) upon sucrose addition are shown in Figure 17.16. The major effect is the expected increase in the peak width. Moreover, a slight frequency decrease is observed, owing to the increased density of the medium. The conductivity of the solution is unaltered, meaning an absence of charge effects. The master bubble (mechanically driven at 5 nm amplitude) was then introduced into the 10% solution and the *slave* spectra were recorded at different values of D , ranging from contact distance (25 μm) to 2000 μm . Figure 17.17 reports the resonance frequency and Figure 17.18 the peak width.

17.5 Absence of excitation

Finally, we recorded the spectra of two interacting bubbles in the *absence* of any applied excitation. In this experiment the two bubbles were identical ($R_0 \approx 0.7$ mm) and anchored only to the upper electrodes to prevent buoyancy. The interferometric signal of one of the two bubbles was acquired and analysed over the 0–150 Hz frequency interval (having verified that the spectra are flat at larger frequencies) by the FFT mode described in Section 15.2.3, for different values of the inter-bubble distance D . The results are shown in Figure 17.19.

It can be observed that, even in the absence of any excitation, the oscillation amplitudes are still detectable, falling in the 0.1–1 nm range. On increasing the inter-bubble distance the amplitude decreases in intensity, but remains detectable up to a distance of about 400–500 μm .

At first sight, these results may seem counter-intuitive, since the oscillation amplitude is expected to be zero without external excitation (Equation 6.20). What we miss is the effect of *thermal noise*. Indeed, the two bubbles oscillate under the effect of thermal fluctuations (as commented on in Chapter 3, concerning capillary waves at liquid-gas interfaces and membranes), although the amplitudes are not as large as at resonance. These oscillations propagate in the surrounding liquid medium while dissipating a significant part of their mechanical energy before interacting with the nearby bubble. Therefore, the frequency spectra as a function of bubble-bubble distance (in the absence of any excitation) probe the response of the bubble surface to thermal noise, reinforced by the interactions with a nearby bubble.

These capillary spontaneous fluctuations, which we can shortly define as the “sound of silence” (after a famous song by Simon and Garfunkel of the mid-sixties), are worth investigating as they constitute a background in the bubble-bubble (or cell-cell) interaction. Any additional supply of energy (mechanical or electrical excitation in the case of bubbles, enhanced heating due to the metabolic activity in the case of cells) increases the amplitudes of oscillations that, in any case,

never have a zero mean amplitude. It is worth remembering that the detection of such a tiny effect was possible thanks to our differential interferometric apparatus enabling to measure amplitudes in the sub-nanometric scale.

The results shown in Figure 17.19 are still preliminary and demand further study. Notably, it would be useful to repeat the same experiment using a white noise source, far more controlled than the ambient noise (which, by definition, can vary over time according to the external noise sources). In addition, special attention is needed to avoid any spurious signals coming from the measuring apparatus (to which, for instance, the presence of some well-defined, low-frequency peaks in the Figure could be ascribed). This will imply some tailored and not trivial modifications of the setup and the measurement routine.

17.6 Feedback from the *slave*

So far only the effect of the *master* bubble excitation on the slave bubble has been considered. The possibility to excite either of the two bubbles and to detect independently their responses allows also to study the feedback effect exerted by the *slave* bubble on the master, as we are going to show in this section.

A first example, concerning two bare bubbles in ultrapure water as those of Section 17.1, is provided by Figure 17.20. Here, the resonance peak of the *slave* bubble (in black), indirectly excited by the oscillations of the master bubble (set at a distance of 20 μm), is compared to the *master* bubble signal (in red). The latter signal, which should be flat over the selected frequency range, displays a small non-Lorentzian peak corresponding to the *slave* bubble characteristic frequency. This is the "feedback" sent back to the *master* bubble by the *slave*.

Many experiments were performed, both in water and in SDS and BSA solutions, where the *slave* bubble was selectively excited (electrically) over its resonance range and the signal of the master (out of resonance for the isolated system, due to double anchoring) was recorded. Figure 17.21 displays a typical result (SDS 0.03 mM bulk solution). It is observed that, as the two bubbles approach each other, the *master* exhibits an oscillation peak of increasing amplitude about the *slave*'s resonance frequency. Its shape is not Lorentzian, forming a local minimum at the right of the peak (the following rise in amplitude is due to the *master* resonance, falling at frequencies higher than 160 Hz and well separated from the slave resonance). Both the maximum and the minimum intensities decrease with D and their frequencies get closer. The relative phase shows correspondingly a π jump at the frequency of this minimum (and not at the *slave* bubble resonance

frequency), passing from about -20° (nearly in-phase) to -180° (out-of-phase). The inflexion point coincides with the minimum in the master's amplitude. This behaviour is not observed upon mechanical excitation.

Interestingly, the experimental spectra of the master bubble can be reproduced by subtracting a lorentzian peak centred at the inflexion point to a (positive) lorentzian peak centred at the *slave* resonance frequency (both having the same width as the slave peak), as shown in Figure 17.22. This leads to the hypothesis that the slave bubble oscillation may induce a low-frequency in-phase resonance and a higher-frequency, out-of-resonance peak. The latter would therefore subtract to the existing signal at the corresponding frequency range and generate the observed minimum. Further control experiments are needed to confirm this hypothesis, however.

Finally, in Figure 17.23 reports the case of two bubbles of the same size and upper anchored and both excited electrically. One of them is "naked" (the slave bubble, black scatter) and the other covered by SDS over the CDC (the master bubble, red scatter), as described in Section 17.2. The distance D is of $150\ \mu\text{m}$. The peak of the master bubble, significantly higher in intensity and broader due to the SDS coating, exhibits a "valley" at the resonance frequency (identical to the master's one), that can be explained in terms of an out-of-phase peak induced by the slave bubble.

17.7 Comment on the results

From the data described above it can be seen that:

- The interactions between two nearby bubbles undergoing shape oscillations are weak, but attractive. This is mostly evident from the modest red-shift in resonance frequencies when the two bubbles approach each other – of order of 5–10% the resonance frequencies of the isolated bubbles (increasing with surface coverage).
- Such interactions are long-ranged, the decay length being of order of 1 mm (in each set of measurements, no interactions at all can be observed at $D = 2\ \text{mm}$). The same trend can be observed following either of the spectral parameters (mostly the oscillation amplitude).
- The oscillations of the *master* and *slave* bubble are always out of phase, regardless of the coating. This supports the thesis of an interaction mechanism not driven by direct interactions, but by an increase of the inertial mass of the system.
- Oscillating coated bubbles dissipate more than air-water interfaces.

- The adopted experimental setup enables to study the interactions between bubbles bearing different surface coatings.
- Mechanical excitation of the *master* bubble yields broader peaks with respect to electrical stimulation (see, for instance Figure 17.14) and is more difficult to interpret. Further investigation on this behaviour is needed.
- The interactions are mutual and occur in both directions, resulting in complex and non-lorentzian peaks whose interpretation is still to be elucidated.
- As observed in Section 17.1, the region of very-low bubble-bubble distances (up to about 100 μm) is quite interesting and deserves further investigation.

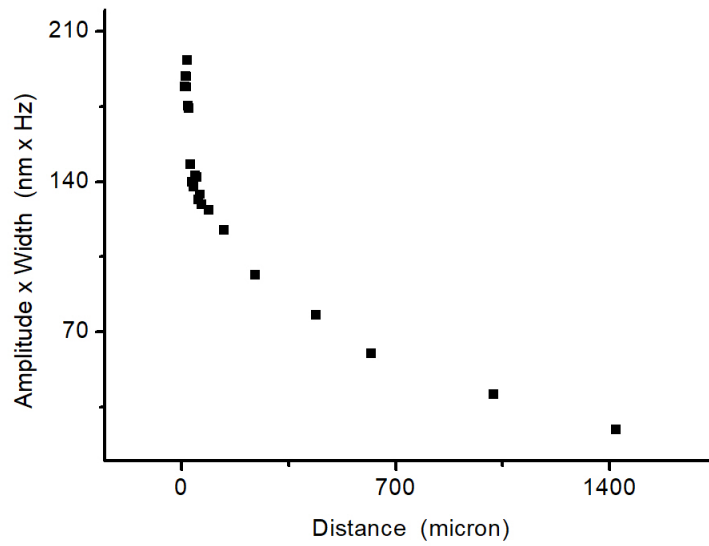


Figure 17.1: *Bare bubbles.* Oscillation amplitude of the *slave* bubble ($R_0 = 0.75$ mm) versus the inter-bubble distance D , normalised against the peak width (Figure 17.2).

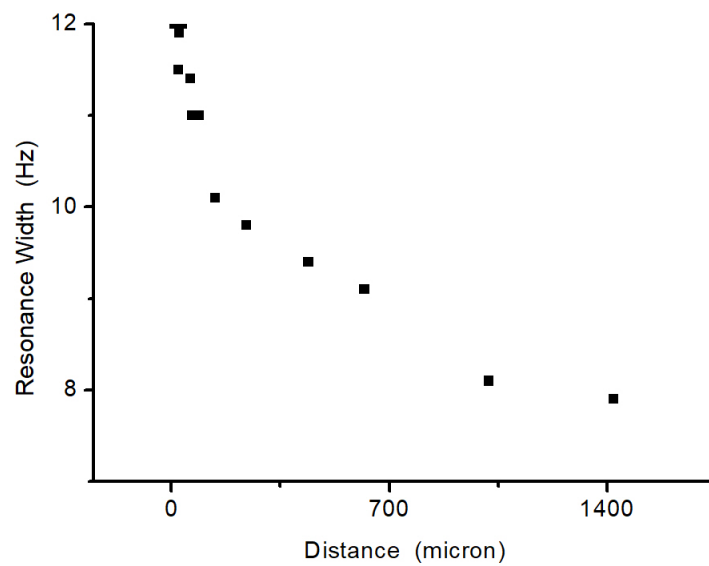


Figure 17.2: *Bare bubbles.* Peak width of the same bubble of Figure 17.1 versus the inter-bubble distance.

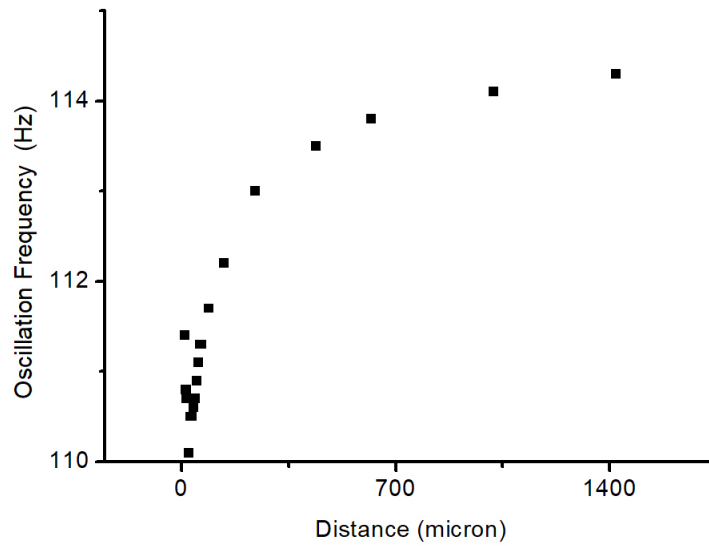


Figure 17.3: *Bare bubbles.* Resonance frequency of the same bubble of Figure 17.1 versus the inter-bubble distance.

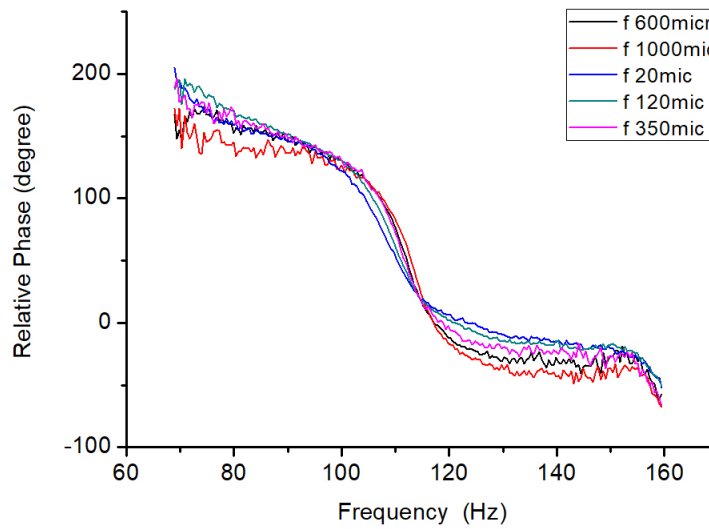


Figure 17.4: *Bare bubbles.* Relative phase of oscillation between the *slave* and the *master* bubble. The inflection points correspond to the frequency values reported in Figure 17.3.

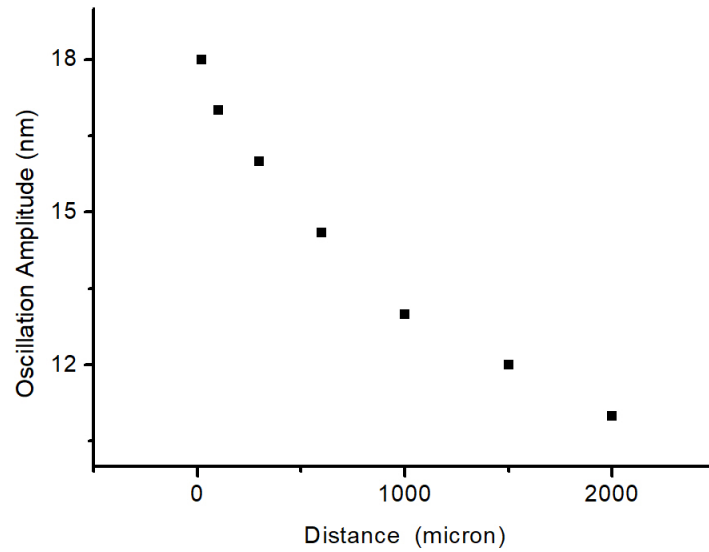


Figure 17.5: *SDS-covered bubbles* (0.1 mM bulk solution, electric excitation). Oscillation amplitude of *slave* bubble ($R_0 = 0.65$ mm, $n = 1$ mode) as a function of the inter-bubble distance D .

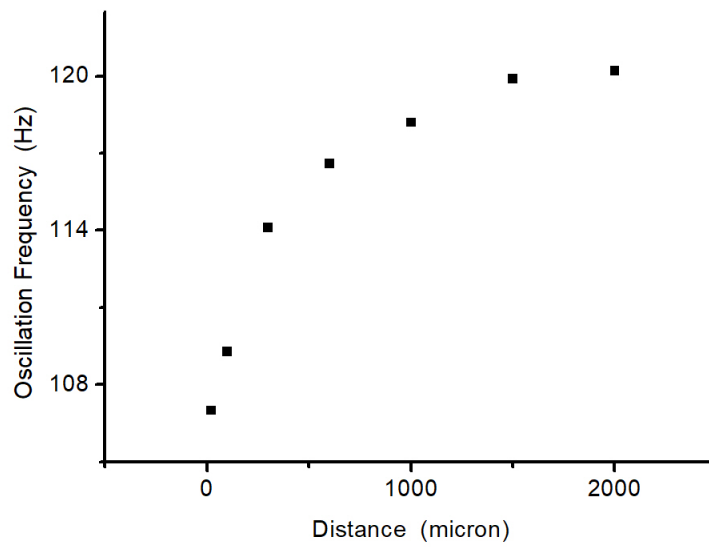


Figure 17.6: *SDS-covered bubbles* (0.1 mM bulk solution, electric excitation). Resonance frequency of *slave* bubble ($R_0 = 0.65$ mm, $n = 1$ mode) as a function of the inter-bubble distance D .

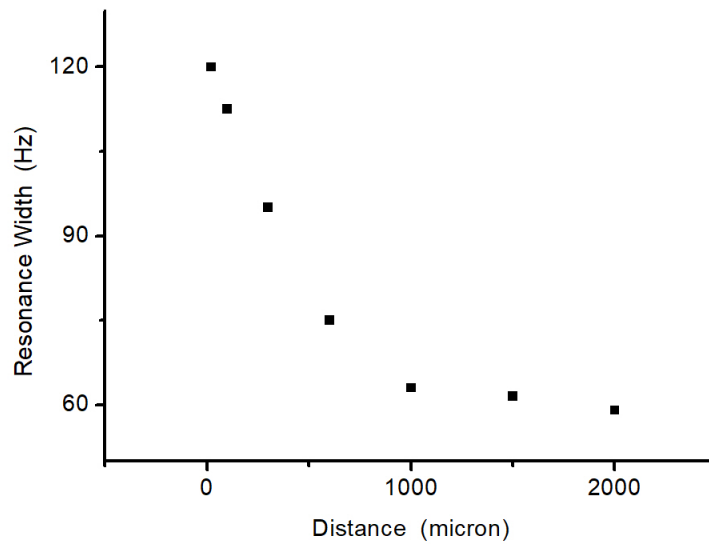


Figure 17.7: SDS-covered bubbles (0.1 mM bulk solution, electric excitation). Resonance peak width of the *slave* bubble ($R_0 = 0.65$ mm, $n = 1$ mode) as a function of D .

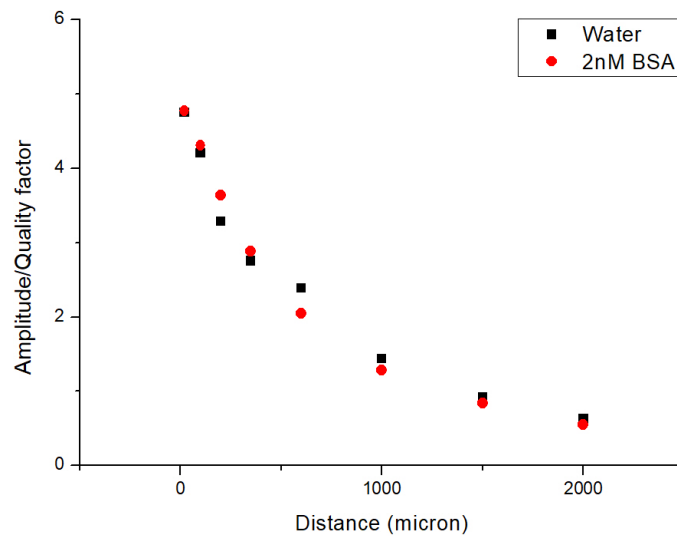


Figure 17.8: Normalised oscillation amplitude of the *slave* bubble versus the inter-bubble distance D for: *black*, ultrapure water; *red*, 2 nM BSA bulk solution. Slave bubble radius $R_0 = 0.75$ mm, mechanical excitation of master bubble.

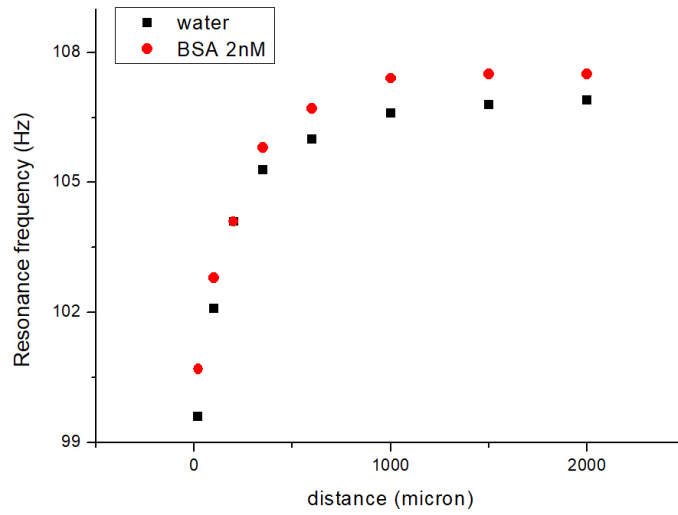


Figure 17.9: Resonance frequency of the *slave* bubble versus the inter-bubble distance D for: *black*, ultrapure water; *red*, 2 nM BSA bulk solution. Slave bubble radius $R_0 = 0.75$ mm, mechanical excitation of master bubble.

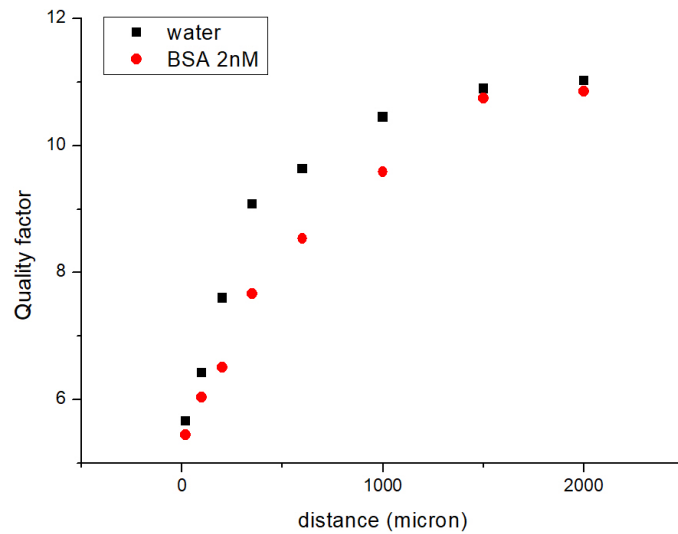


Figure 17.10: Resonance quality factor of the *slave* bubble versus the inter-bubble distance D for: *black*, ultrapure water; *red*, 2 nM BSA bulk solution. Slave bubble radius $R_0 = 0.75$ mm, mechanical excitation of master bubble.

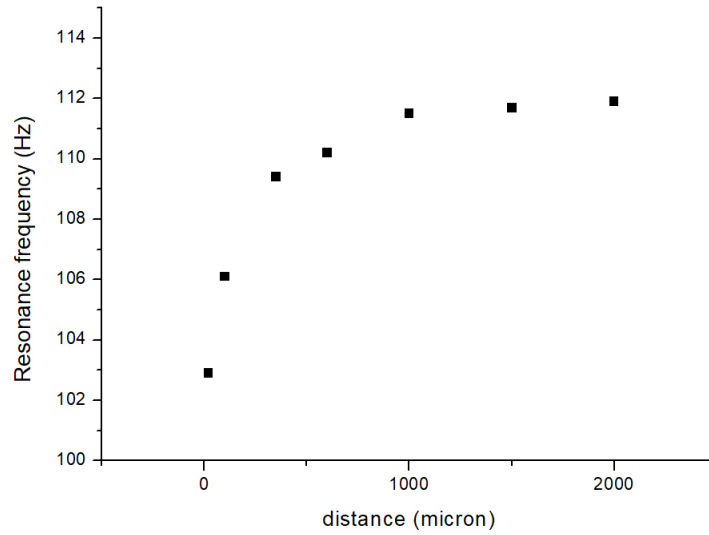


Figure 17.11: *BSA-covered bubbles* (6 nM bulk solution, electrical excitation). Resonance frequency of the *slave* bubble ($R = 0.75$ mm) as a function of bubble-bubble distance D (20–2000 μm).

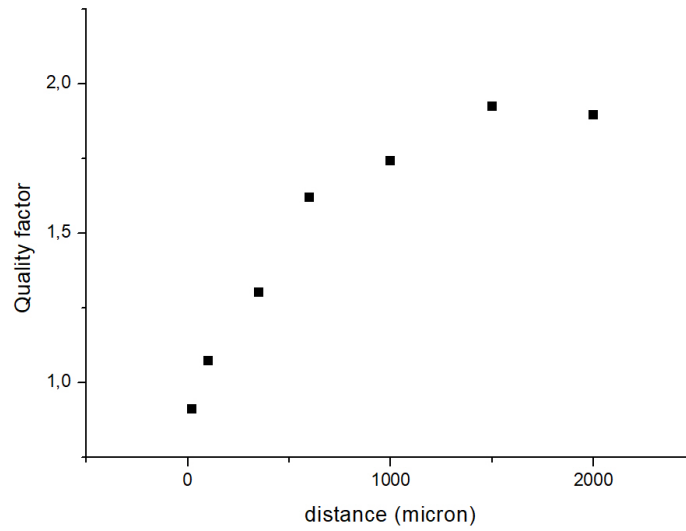


Figure 17.12: *BSA-covered bubbles* (6 nM bulk solution, electrical excitation). Resonance Quality factor of the *slave* bubble ($R = 0.75$ mm) as a function of bubble-bubble distance D (20–2000 μm).

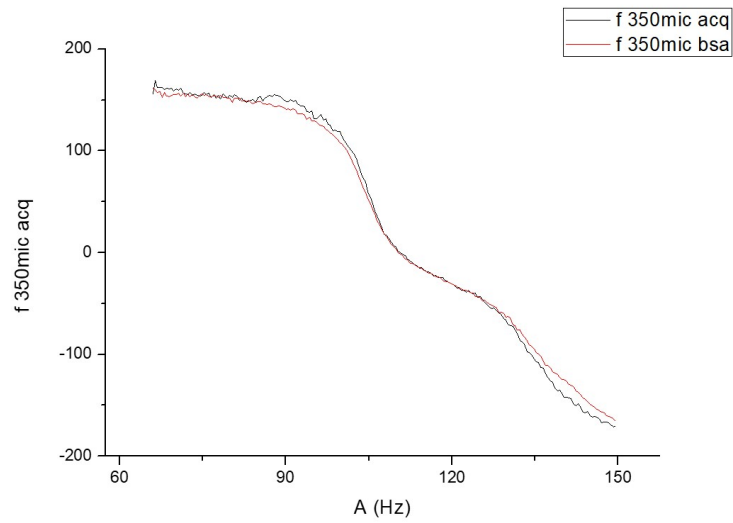


Figure 17.13: Phase difference between *master* and *slave* bubble as a function of frequency. *Black curve:* bubbles in pure water; *Red curve:* bubble in 0.1 mgL^{-1} BSA solution. Methanol added to water medium to avoid bubble disturbance. Electric excitation; inter-bubble distance $D = 350 \mu\text{m}$; bubble radii $R = 0.75 \text{ mm}$.

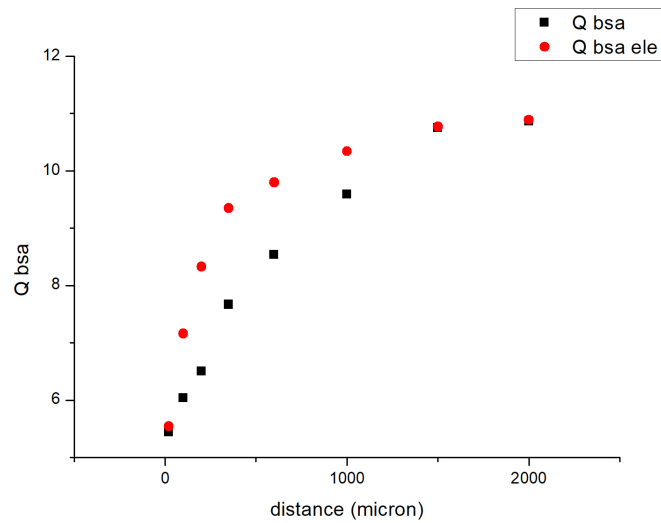


Figure 17.14: Resonance Quality factor of BSA-covered *slave* bubbles (0.4 mg/L bulk solution) versus the inter-bubble distance. *Black,* mechanical excitation of the *master* bubble; *red,* electric excitation. The bubble radius is of 0.75 mm in both cases.

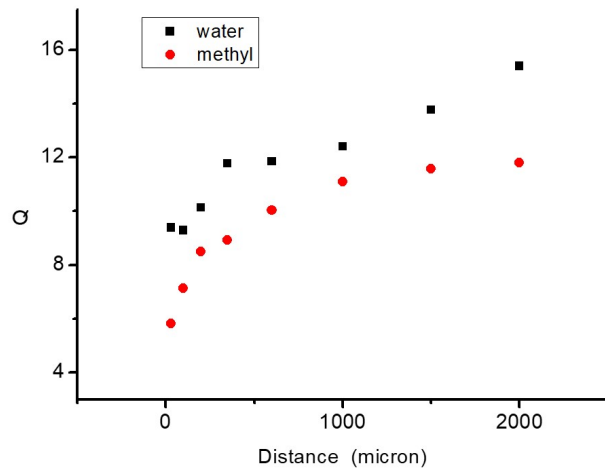


Figure 17.15: Resonance quality factor of bubbles in 0.05% methanol solution (red diamonds), vs pure water (black squares), as a function of inter-bubble distance D . Electric excitation of *master* bubble; bubble radii $R = 0.75$ mm.

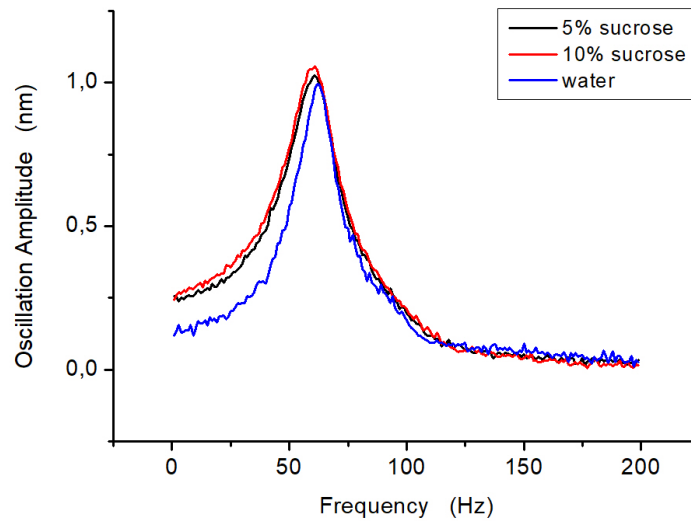


Figure 17.16: Resonance spectra of the isolated *slave* bubble ($R_0 = 0.75$ mm) under different conditions. *Blue*: water (resonance frequency: 120.2 Hz, Quality factor: 10); *black*: 5% sucrose (resonance frequency: 119.6 Hz, Quality factor: 9.06); *red*: 10% sucrose (resonance frequency: 118 Hz, Quality factor: 8.02). Electrical excitation at 5 V/cm. The main effect is an increase in peak width upon sucrose addition, even at the lower concentration, as well as in resonance frequency.

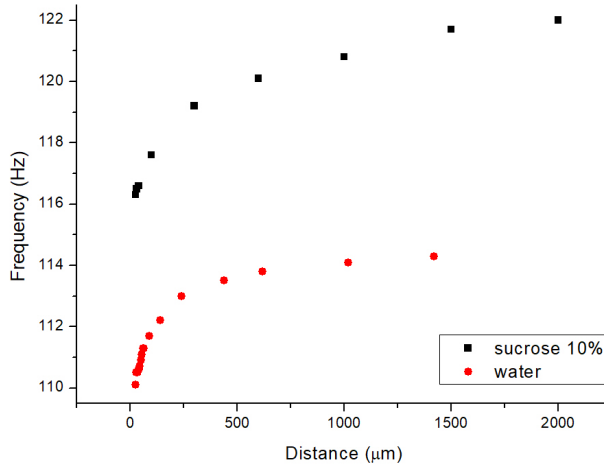


Figure 17.17: Resonance frequency of the slave bubble ($R_0 = 0.75$ mm) excited by the master (mechanically driven out of resonance at a 5 nm amplitude), as a function of inter-bubble distance D . The comparison between data obtained in pure water (*red scatter*) and in 10% sucrose solution (*black*) highlights an overall increase in frequency in the latter case, due to the higher fluid density, while the frequency span over D is comparably small (about 4 and 6 Hz, respectively).

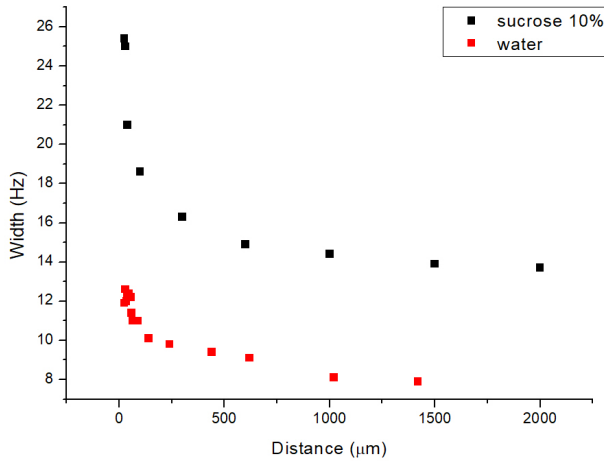


Figure 17.18: Peak width of the slave bubble ($R_0 = 0.75$ mm) excited by the master (mechanically driven out of resonance at a 5 nm amplitude) as a function of inter-bubble distance D . *Red scatter*: pure water; *black*: 10% sucrose solution. Notice that the width increase with D is significantly enhanced in the more viscous solution.

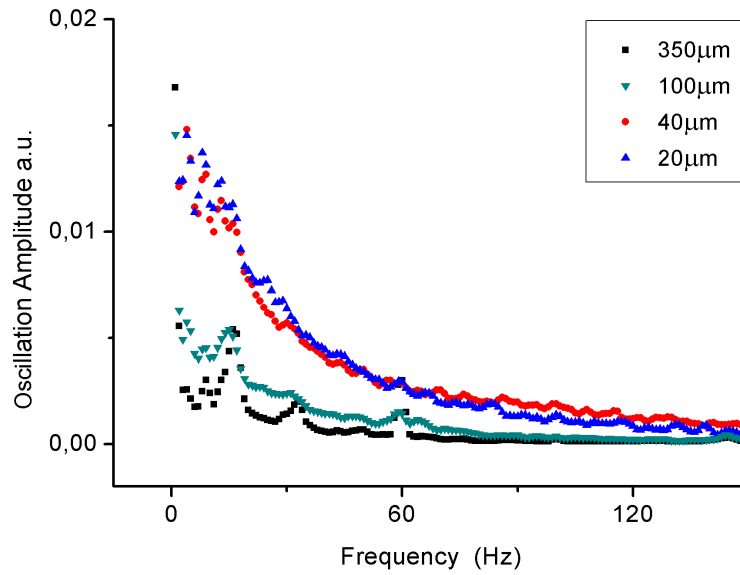


Figure 17.19: Oscillation spectra in the low-frequency range, recorded in the absence of any applied excitation. The system is constituted by two identical, upper-anchored bubbles, set at varying distance D (reported in the inset). The bubble's response to thermal noise is reinforced by the interaction with the other bubble and decreases with D .

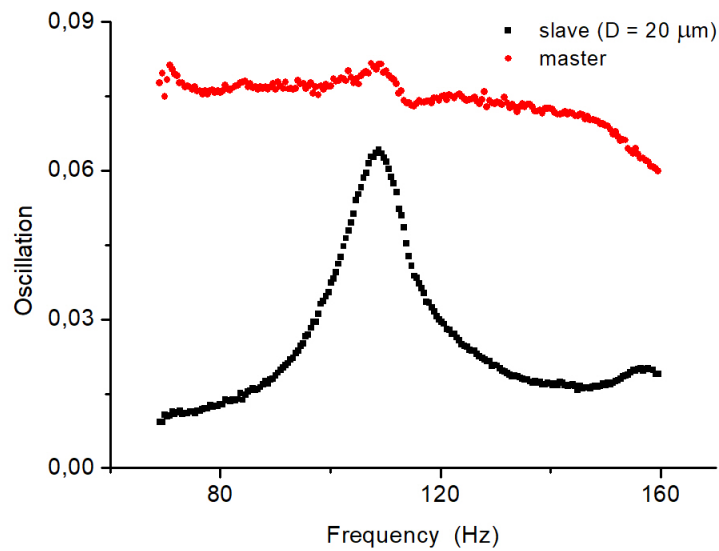


Figure 17.20: *Bare bubbles.* The effect of *slave* bubble oscillations (black scatter) on the *master* bubble out-of-resonance signal (red), consisting of a small non-lorentian peak at the *slave* resonance frequency.

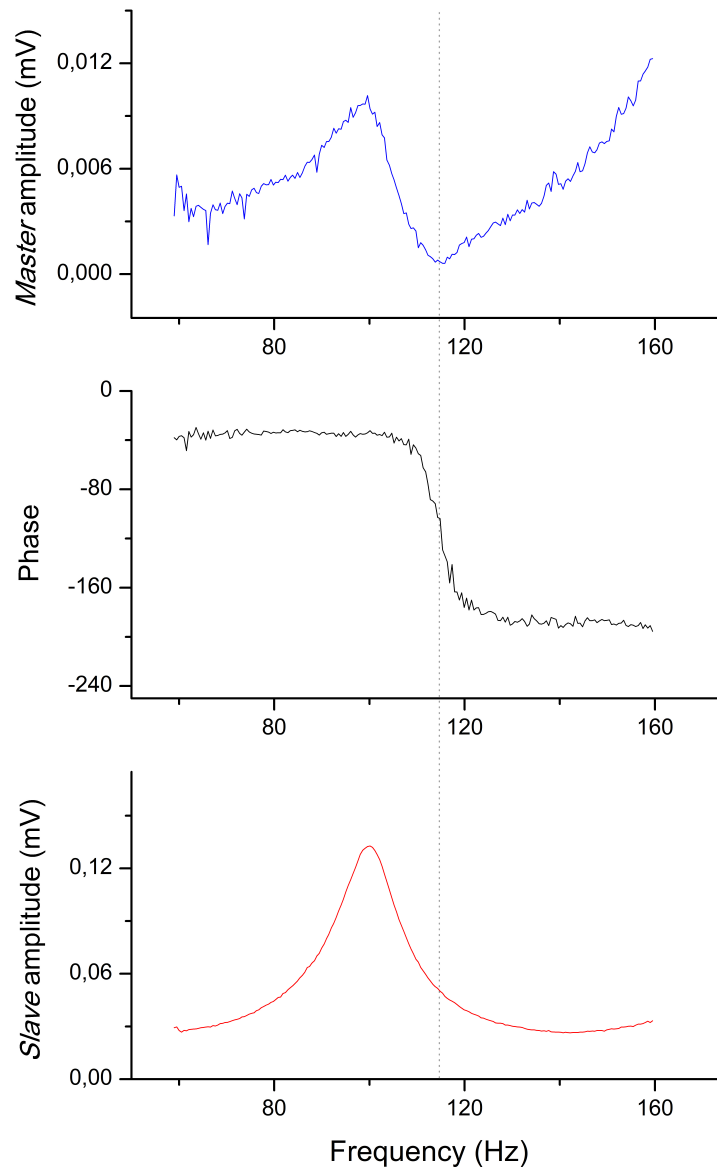


Figure 17.21: *Top:* oscillation amplitude of the *master* bubble (not directly excited). Its natural resonance frequency falls over 160 nm. *Middle:* relative phase of oscillation between the master and slave bubbles. *Bottom:* oscillation spectrum of the *slave* bubble (electrically excited). The dashed vertical line marks the correspondence between the phase inflexion point and the minimum in the *master* signal. Bubble-bubble distance $D = 10 \mu\text{m}$. Measurements were taken in a 0.03 mM SDS solutions, oscillation amplitudes of the slave bubble corresponding to the shown voltages are of about 6 nm. v_{res} slave: 100 Hz; v_{res} minimum: 115 Hz.

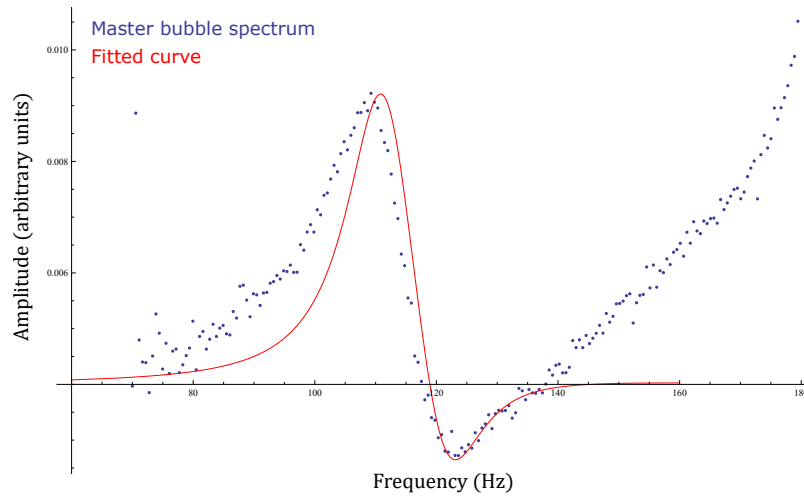


Figure 17.22: Comparison between the experimental spectrum of the *master* bubble (blue scatter), excited indirectly out of resonance by the *slave* bubble (electrically excited), with the fitted spectrum calculated as described in the Section (red curve). Inter-bubble distance $D = 20 \mu\text{m}$.

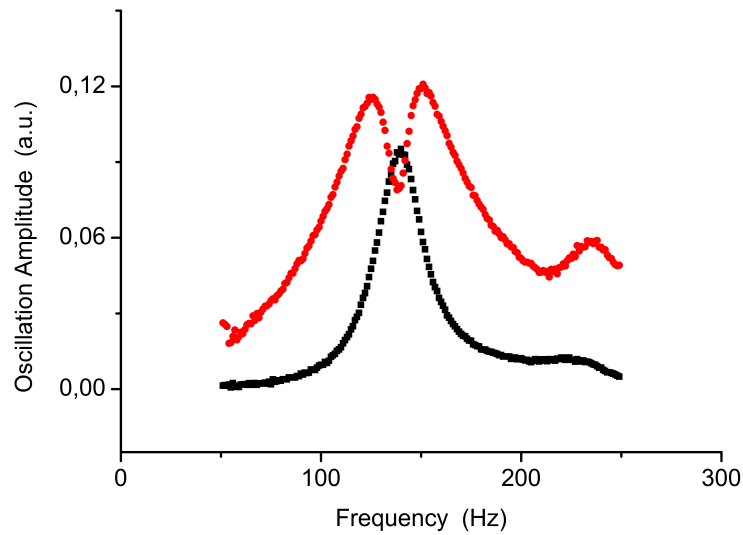


Figure 17.23: Feedback of the *slave* bubble (black scatter) on the *master* (red scatter). The two bubbles are equal in size, anchored only to the top electrode and excited electrically at the same time. The slave bubble is "naked", the master was prepared in SDS solution over the CDC. Inter-bubble distance $D = 150 \mu\text{m}$.

Chapter 18

Experiments on double-bubble systems: interacting *spherical* bubbles

After collecting data on axisymmetric oscillations, we decided to test our experimental method against the simpler and more familiar case where the two bubbles are excited by an isotropic field and undergo volume oscillations.

18.1 Experiment

This kind of study required a different experimental setup with respect to the one described in Chapter 16. The main differences concern the measuring cell, as illustrated in Figures 18.1 (scheme of the experiment) and 18.2 (real measuring cell). Here, both bubbles are pinned to the bottom of needle-shaped electrodes (analogous to those used in the other experiments, see Figure C.6) and their mutual distance D can be regulated via micrometric screws. A piezoceramic mounted at the bottom of the cell enables isotropic acoustic driving of both bubbles with the same exciting

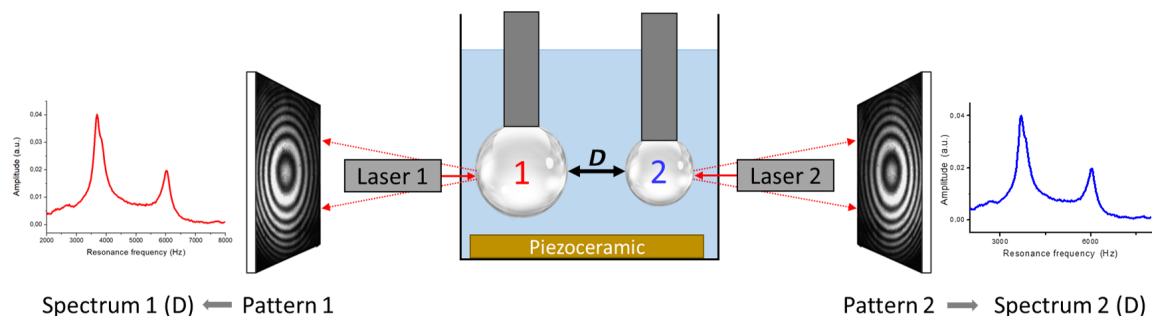


Figure 18.1: Schematics of the experiment on interacting spherical bubbles described in this chapter.

intensity, inducing radial deformations of nanometric amplitude.

Since our focus was on selectively excited shape modes, we only made one such experiment. Further investigations will be performed in a separate study. In order to verify if there were any differences in the oscillating response of the two bubbles, we used two different radii, 0.8 mm (Bubble 1, on the left in Figure 18.1) and 0.6 mm (Bubble 2, on the right), measured with a precision of $10\ \mu\text{m}$. The two bubbles were formed in ultrapure water. Distances were varied from $30\ \mu\text{m}$ to 4 mm (7 distance points). For each chosen value, the spectra of the two bubbles were recorded independently from the respective interferometric patterns.

18.2 Results

Figure 18.3 reports the oscillation spectra of the two isolated bubbles, exhibiting one single resonance peak. The resonance frequencies of Bubbles 1 and 2 are 4025 Hz and 4831 Hz, respectively, in line with the values that can be estimated from Equation 6.14 (corrected for the anchoring). The corresponding quality factors are of 10.5 and 11.2, respectively, values comparable with mechanically excited shape oscillations in ultrapure water.

Figure 18.4 is a typical spectrum observed when the two bubbles interact. The most notable feature is the onset of two resonance peaks, whose frequencies ω_l and ω_h depend on the bubble-bubble distance D . For each observation the values of ω_l and ω_h were equal for the two bubbles, although the oscillation amplitudes differed (being in general one order of magnitude higher for Bubble 2, see Figure 18.3). Both the energy splitting $\Delta\omega = \omega_h - \omega_l$ and the relative intensities of the peaks vary with D . Namely, as the two bubbles approach each other, the value of $\Delta\omega$ increases (due to both an increase in ω_h and a decrease in ω_l) and the amplitude ratio between the low-frequency and the high-frequency peaks increases.

Figures 18.5 to 18.8 show the individual spectral parameters as a function of the inter-bubble distance. The ω_l -peak originates from the contribution of the larger bubble (Bubble 1), the asymptotic value of the frequency at infinite distance being $\Omega_{0,1}$ (Figure 18.5); the high-frequency peak originates from the Bubble 2 mode and tends to $\Omega_{0,2}$ at infinite D (Figure 18.6). The frequency span... The partial overlap between the low- and high- frequency peaks (see Figure 18.4) prevents an accurate fit of peak widths, especially for the high-frequency signals. However, the behaviour of peak widths against D appears to be non-monotonous, as shown in Figures 18.7 and 18.8.

18.3 Comment on the results

Albeit limited to a single system, the data described above show that:

- The two interacting bubbles subject to an isotropic excitation exhibit the same vibration modes. In particular, they may oscillate at a low-frequency, originating from the larger bubble, or at a higher frequency, originated from the smaller bubble.
- The frequency split and the amplitude ratio between these two modes are distance-dependent. The frequency span of the low-frequency peak is of order of 10% the natural resonance of the larger bubble, a figure comparable with the observations made on shape modes. By contrast, the high-frequency mode increases upon bubble approaching of as much as 40% the natural frequency of the smaller bubble (see Figures 18.5 and 18.6).
- The fitted values of peak widths are less reliable, however they suggest a non-monotonous behaviour of viscous dissipation over the distance D (see Figures 18.7 and 18.8).
- The long-ranged decay length of the interactions, observed for the shape modes, is confirmed. Indeed, the interaction between pulsating spherical bubbles seems to persist over larger distances (see Figure 18.5).

Further experiments on different systems (different size ratios between the two bubbles and/or different coverages), as well as computer simulations analogous to those described in Section 12.1, will be performed to validate the results and to compare them with the shape modes of interacting bubbles.

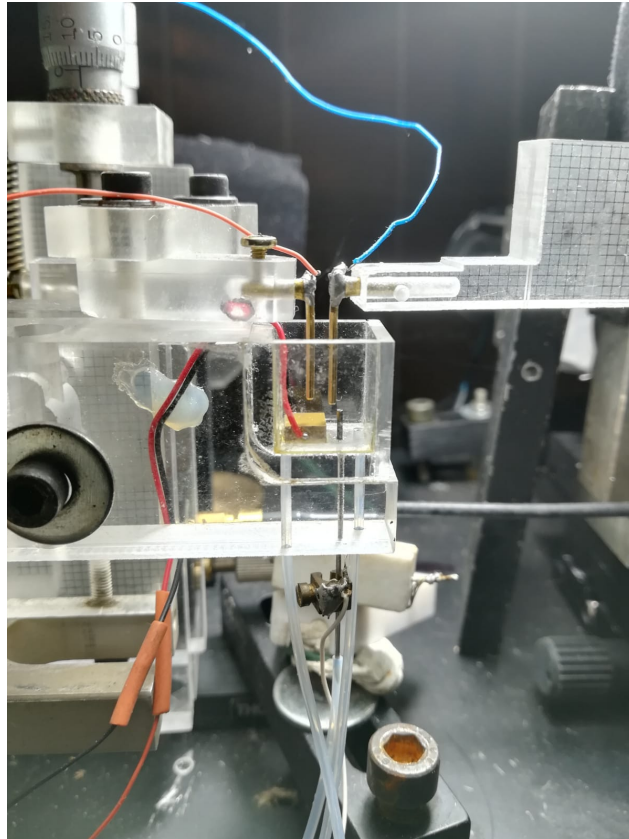


Figure 18.2: Measuring cell for the investigation of volume modes in a two-bubble interacting system. The piezoceramic (the golden block placed at the bottom of the cell) is protected against water damage by a waterproofing coating for electronics.

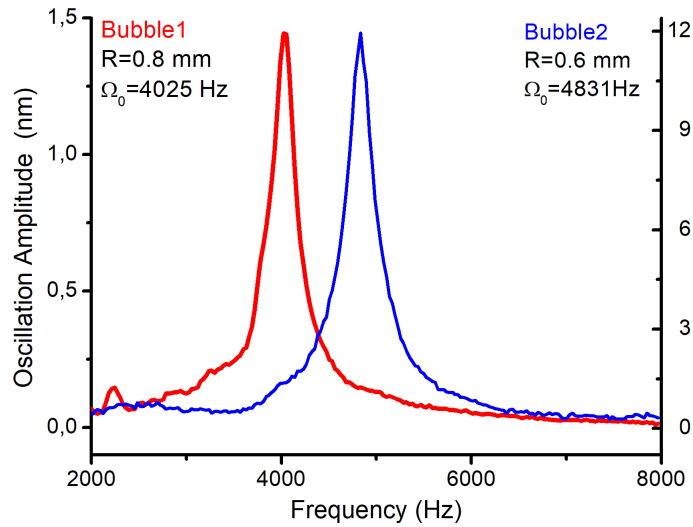


Figure 18.3: Acoustic spectra of the two *isolated* bubbles, each evidencing one single normal mode Ω_i . *Red (left):* Bubble 1 (equilibrium radius $R_1 = 0.8$ mm, $\Omega_{0,1} = 4025$ Hz). *Blue (right):* Bubble 2 (equilibrium radius $R_2 = 0.6$ mm, $\Omega_{0,2} = 4831$ Hz).

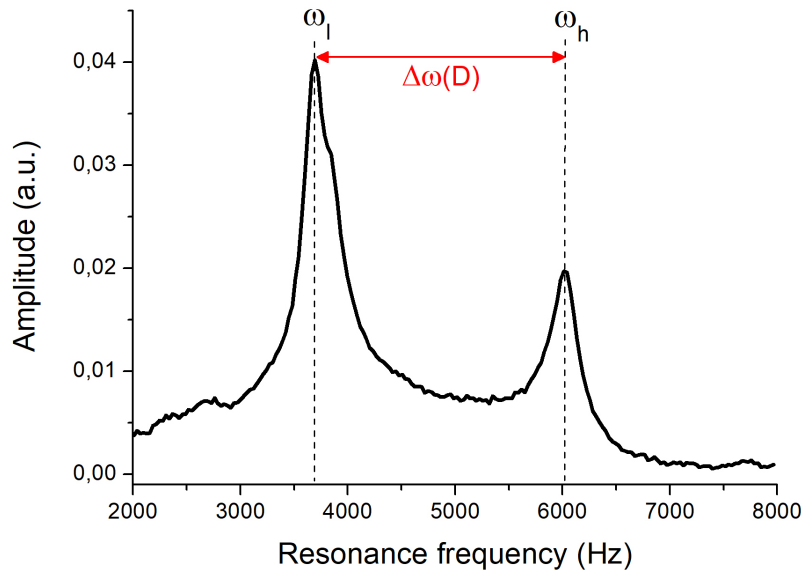


Figure 18.4: Acoustic spectrum of Bubble 2 in the presence of Bubble 1 (inter-bubble distance $D = 370$ μ m). Resonance frequencies: $\omega_{l,1} = 3715$ Hz, $\omega_{h,1} = 6007$ Hz. The difference between the high- and low-frequency modes $\Delta\omega$ increased with D . Bubble 1 and Bubble 2 exhibit almost the same frequencies.

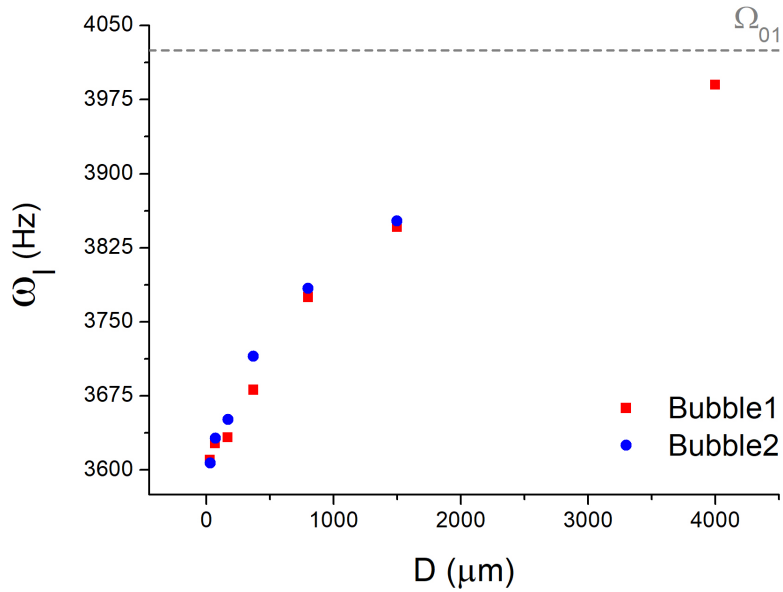


Figure 18.5: Low-frequency resonances ω_l of Bubble 1 (red squares) and Bubble 2 (blue circles), as a function of inter-bubble distance D . As D increases, the resonance frequency approaches the normal mode $\Omega_{0,1}$ of Bubble 1 (the larger bubble), indicated by the dashed grey line.

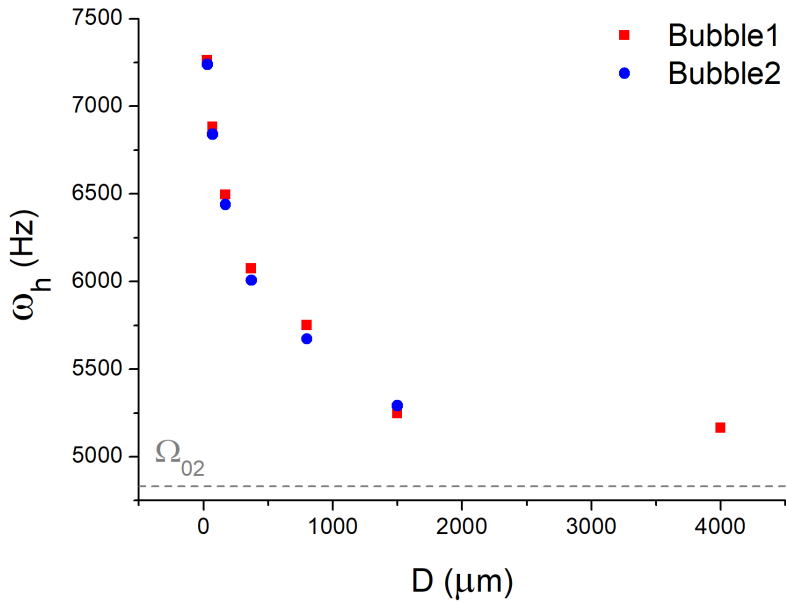


Figure 18.6: High-frequency resonances ω_h of Bubble 1 (red squares) and Bubble 2 (blue circles), as a function of inter-bubble distance D . As D increases, the resonance frequency approaches the normal mode $\Omega_{0,2}$ of Bubble 2 (the smaller bubble), indicated by the dashed grey line.

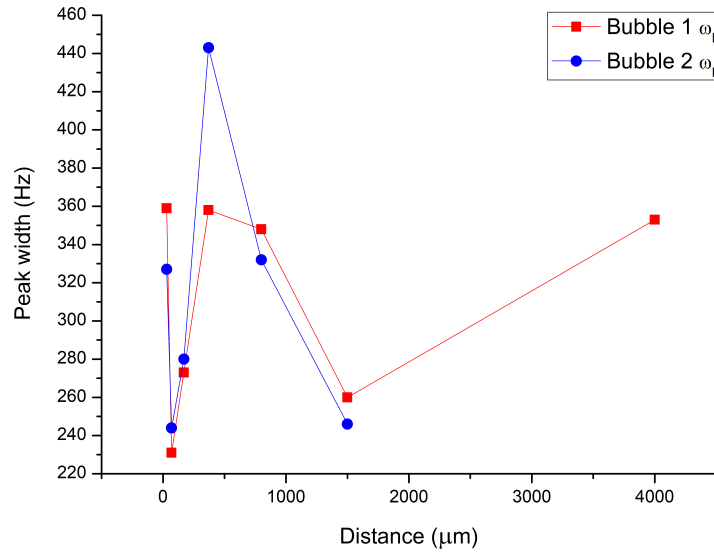


Figure 18.7: Peak width of the low-frequency resonances of Bubble 1 (red squares) and Bubble 2 (blue circles), as a function of inter-bubble distance D .

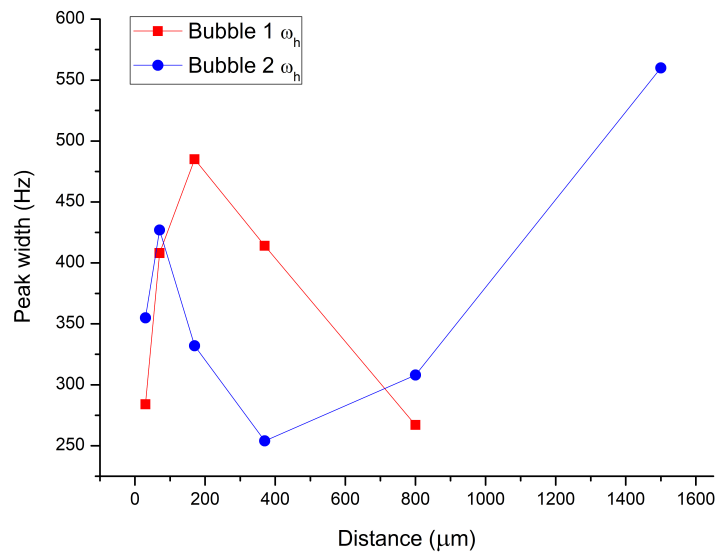


Figure 18.8: Peak width of the high-frequency resonances of Bubble 1 (red squares) and Bubble 2 (blue circles), as a function of inter-bubble distance D .

Part VII

**CONCLUSIONS AND FUTURE
PERSPECTIVES**

Chapter 19

Conclusions

In this thesis work, an innovative method for studying the interactions between two nearby bubbles vibrating in aqueous medium has been developed. Besides the fundamental interest in bubble-bubble interactions, motivated by their widespread occurrence in fluids subject to pressure fields and testified by a growing literature, interacting bubbles also provide a simplified model system of interacting soft, spherical bodies like cells.

The aim of my study was to identify the main determinants of the interaction between two such biomimetic cells, with particular interest in its decay length, which is poorly known in cell systems, albeit crucial to demonstrate the effectiveness of cell-cell hydrodynamic communication.

Accordingly, I have undertaken a collaborative multi-disciplinary study, combining an interferometric method for the detection of bubble oscillations (extending a previously developed single-bubble setup [7]) with theoretical modelling (based on the Rayleigh-Plesset theory of fluctuating interfaces [6]) and computer simulations (based on Lattice-Boltzmann algorithms [205]).

The two bubbles have axial symmetry and sub-millimetric radii. An anisotropic sinusoidal field is selectively applied to one of them to excite linear oscillations of nanometric amplitudes. Special attention has been paid to surface oscillations occurring at constant volume, of relevance to cellular systems, instead of the customary "breathing" modes. The physico-chemical properties of the system – namely the surface charge and interfacial tension and the viscosity of the bulk medium – can be varied in a controlled way, either by addition of chemicals in the measuring cell, or as explicit parameters in the model equations and simulations. Importantly, the range of mutual distances spans from values larger than the bubble dimensions, up to quasi-contact, a much less investigated regime in current studies. Moreover, owing to the extreme sensitivity of the interferometric technique, amplitudes as small as 1 Å can be accurately detected.

19.1 Summary of the achieved results

The study of bubble-bubble interactions is still ongoing and many parts are not yet definitive, especially computer calculations. However, the results obtained so far seem to converge, at least qualitatively, to the following observations.

- Bubble-bubble interactions result in a variation of the (experimental or predicted) spectral parameters – the oscillation amplitude, frequency and width of resonance modes, as well as the relative phase between the two oscillators – dependent on their mutual distances and on the physico-chemical properties of the system.
- On the whole, gradual approaching of the two bubbles from an initially isolated system ("infinite" distances) results in: *a*) an increase in peak amplitude; *b*) an increase in peak width; *c*) a decrease in resonance frequency. The span of these variations is quite modest (see Equations 11.21 and 11.22 and the experimental data), especially for the case of pure water or extremely diluted solutions.
- The decay law for the vibrational parameters with the inter-bubble distance D is faster on increasing the eigenmode number n . For volume oscillations ($n = 0$) the decay roughly behaves as D^{-1} , while it is sharper for surface modes. For the $n = 1$ investigated in our experiments the interactions are still long-ranged, spanning over distances of order of 1 mm, i.e., larger than the bubbles dimensions, at variance with typical intermolecular or inter-particle interactions.
- The bubbles always oscillate *out of phase*, regardless of the surface coverage or their mutual distance. This kind of oscillations allows to maximise the instantaneous distance between the surfaces of the two oscillators (their centre-to-centre distances being fixed), signifying an absence of direct interactions (apart from a slight electrostatic repulsion). Direct, attractive interactions could in principle arise from “sticker” molecules uniformly distributed at the surfaces of both bubbles.
- The interactions are mutual. The forward- and back- propagation of oscillations – from the *master* bubble to the *slave* and vice versa – leads to the observation of complex and non-lorentzian peaks, whose interpretation is still to be elucidated.
- The dissipation behaviour reflects that of the fluid velocity vector in the area between the two bubbles. Our model predicts a peak width decrease with the distance, in accordance with

the experiments concerning shape mode oscillations. Computer simulations and breathing mode measurements, however, seem to suggest a more complex dependence on distance and oscillation modes.

In light of the above, our starting hypothesis on the mechanism of bubble-bubble interactions (formulated in Section 8.1), based on the theory of coupled oscillators, turned out to be wrong. The main evidence lies in: *a)* the modest variation in the spectral parameters over bubble-bubble distance; *b)* more importantly, the observation of out-of-resonance oscillations contrasting the common notion of coupled oscillators.

The model developed in Section 11.2, albeit approximate, suggests that other mechanisms must be advocated to explain bubble-bubble interactions. In particular, the greater fluid velocity in the confined region between the two bubbles, compared to the distal regions near the surface bubble, increases the effective inertial mass of the oscillating system. As a result, the oscillation frequencies of both oscillators are lowered, the effect being more pronounced at short distances.

It should be noticed, however, that many works in the literature do predict the onset of in-phase oscillations, corresponding to lower oscillation frequencies, and out-of-phase oscillations, corresponding to higher oscillation frequencies, for a system of two interacting bubbles. Computer simulations and numerical calculations are expected to provide further insights on this behaviour and on other aspects of bubble-bubble interactions which cannot be addressed by our simplified theoretical description of the involved hydrodynamics.

19.2 Relevance and possible developments

The obtained results pave the way for further studies. In particular, different ideas are presently under investigation concerning the application of oscillating bubbles as biomimetic systems.

As discussed in Chapter 18, we have recently extended the study of two interacting bubbles to the volume oscillation modes ($n = 0$), achieving great accuracy and reproducibility in their excitation and detection. Results are interesting because the spectroscopic parameters are much more sensitive to the inter-bubble distance than the surface modes. While in the experiments shown both bubbles were excited at once, targeted (albeit not trivial) modifications to the measurement cell would enable selective excitation of either of the two bubbles, similarly to the experiments on the shape modes.

A reproducible protocol has been developed to study the interactions between asymmetrically coated bubbles, as demonstrated in Section 17.3 for the case of an SDS-covered bubble and a bare

bubble. This possibility opens the way to interesting applications. By exploiting our previous experience in built-up controlled protein "dresses" of single bubbles and drops, we plan to investigate a ligand-covered bubble interacting, at selected distances, with a receptor-dressed bubble. For instance, the standard biotin-streptavidin ligand-receptor couple may be used. The resulting inter-bubble coupling will change the spectra of slave and master bubbles, enabling accurate measurements of "non-local" effects of intercellular ligand-receptor coupling. Hopefully, this will constitute added value for cell adhesion studies. Indeed, ligand-receptor mediated cell adhesion has been extensively investigated in functionalised biomimetic membranes, typically by the Reflection Interference Contrast Microscopy (RICM) mentioned in Section 13.3 [2, 11]. This technique explores the nanoscale region. In contrast, our apparatus explores the mm to μm scales: this allows to work on a real multi-scale basis (needed for matching molecular binding events to larger-scale motions of fluids), while keeping the model as general as possible.

The surprising response of the slave bubble with the distance from the master bubble even in the absence of excitation of the master, described in Section 17.5, poses interesting questions related to the thermal excitation of vibrational modes. On one hand, the experimental findings confirm the accuracy of our differential interferometric apparatus that is able to detect sub-nanometric oscillation amplitudes. On the other hand, results suggest the need to introduce thermal noise effects when studying systems undergoing small amplitude oscillations. The contemporary presence of deterministic (periodic) and stochastic forcing is a very rich field (often called stochastic resonance) leading, especially in non linear systems, to a stunning variety of interesting phenomena.

Finally, the obtained results could benefit from comparison of other complementary approaches. In particular, my internship activity concerning the interactions between pulsating microbubbles via an optical tweezers setup (which will be reported on in a later version of my dissertation) will provide the opportunity for a fruitful comparison of the two techniques and their potentialities. The ultimate term of comparison for our biomimetic system, of course, would be the interactions between two (or more) real cells. As pointed out in Section 5.3, a growing interest has been raised for the interaction patterns between unicellular organisms, triggered by hydrodynamic waves and leading to biochemical synchronisation (see, e.g., [73]). This would entail rescaling the investigated spatial ranges, oscillation frequencies and amplitudes, to fit in with cellular systems.

Part VIII
Appendices

Appendix A

Theoretical remarks

A.1 Derjaguin approximation (DA)

Background

Dating back to 1934 [202], the Derjaguin approximation (DA) relates the force law $F(D)$ between two spheres of radii R_1 and R_2 to the free energy per unit area $W(D)$ between two planar surfaces by the relation:

$$F(D) = 2\pi R_{\text{eff}} W(D) \quad (\text{A.1})$$

where the *effective radius* R_{eff} is defined such that $R_{\text{eff}}^{-1} = \frac{1}{R_1} + \frac{1}{R_2}$. The underlying principle is that, when the interaction between two bodies decays rapidly (i.e., over a small distance with respect to their sizes), it will depend essentially on *local* properties of the two surfaces in the neighbourhood of the closest distance D .

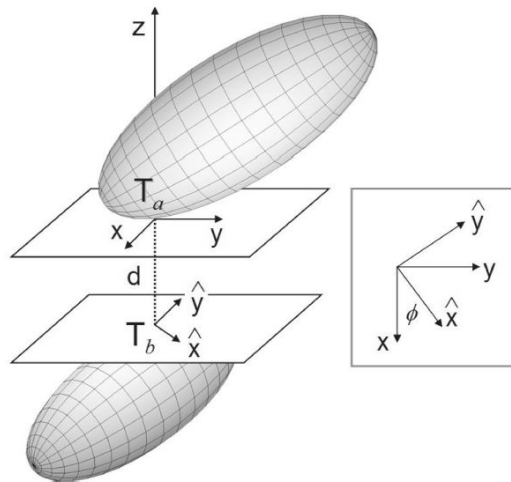
Although it was initially formulated for inverse-power-law potentials between two spheres, the DA is applicable to any kind of force law, be it attractive, repulsive or oscillatory, as well as to non-spherical bodies [201,268]. As such, it has later been generalised and exploited as a simple tool, for instance, to calculate the van der Waals and the electrostatic forces between two particles which do not have a spherical or planar surface [269], to describe the potential energy of interaction between dissimilar spherical colloidal particles for low surface potentials [270], or between macrobodies as a function of their reciprocal orientation [271].

The form of the potential energy between two non-spherical surfaces is useful for modelling purely electrostatic interactions between two bubbles undergoing shape oscillations and will be discussed below.

Extension to non-spherical shapes [269, 271]

Let us consider two convex, smooth bodies a and b as those depicted in the image below. We denote by T_a and T_b the points on their surfaces for which the separation distance is least and let D be this distance of closest approach (i.e., the connecting line between T_a and T_b).

In order to apply the DA to generally-shaped objects, it is convenient to relate the distance between the two bodies to their principal curvatures at the closest-distance points. To this aim, we introduce a Cartesian coordinate system with the origin located at T_a , so that D is contained in the z axis, while axes x and y define the tangent plane and are parallel to the two curvature lines of a at point T_a (parallel and meridian), respectively. A Cartesian coordinate system $(\hat{x}, \hat{y}, \hat{z})$ centred at point T_b is defined similarly. Notice that, because the tangent planes to surfaces a and b at T_a and T_b are parallel, the \hat{z} axis is parallel to the z axis. However, the (\hat{x}, \hat{y}) coordinate system is generally turned away by an angle ϕ from (x, y) , as in the figure.



Applying the DA, the interaction force between a and b is directed parallel to the z axis and is given by:

$$F = \int_{-\infty}^{+\infty} \int_{-\infty}^{+\infty} P(\Delta z(x, y)) dx dy$$

where $P(\Delta z(x, y))$ is the force per unit area between two planar and parallel surfaces at a distance of Δz .

For two curved surfaces, $\Delta z(x, y)$ is evaluated in a small area around T_a and T_b and is expressed as a function of D , of the principal curvatures and of the reciprocal orientation ϕ of the two bodies

[269]. Proper algebra yields:

$$F(D) = \frac{2\pi}{\sqrt{\lambda_1\lambda_2}} \int_D^\infty P(z)dz \quad (\text{A.2})$$

where λ_1 and λ_2 are coefficients depending on the principal curvatures the points of closest approach and on ϕ .

The corresponding electrostatic free energy is given by:

$$U(D) = \frac{2\pi}{\sqrt{\lambda_1\lambda_2}} \int_D^\infty W(z)dz \quad (\text{A.3})$$

$W(z)$ is the potential energy of electrostatic interaction per unit area, which, for two weakly parallel surfaces with dissimilar surface potentials, is given by [201, 268, 270]:

$$W(z) = \frac{\kappa\epsilon_0\epsilon_r}{2} [(\psi_1^2 + \psi_2^2)(1 - \coth \kappa z) + 2\psi_1\psi_2 \cdot \text{csch } \kappa z] \quad (\text{A.4})$$

where κ is the inverse Debye length of the medium, ϵ_0 the vacuum dielectric permittivity, ϵ_r the relative permittivity and ψ_i the electrostatic potential on bubble i surface.

As can be seen from Equation A.4, the final form of $U(d)$ will depend on the local shape and reciprocal orientation of the interacting bodies (through the terms λ_1 and λ_2) and on their surface electrostatic potentials (through $W(z)$). Notably, the ϕ -dependence translates, in terms of energy, into a rotational torque exerted by each body on the other, leading them to align parallelly or perpendicularly [269, 271].

In the simpler case of $\phi = 0$, λ_1 and λ_2 are given by:

$$\lambda_1 = \lambda_{\parallel} = \frac{1}{R_{\parallel 1}} + \frac{1}{R_{\parallel 2}} \quad (\text{A.5})$$

$$\lambda_2 = \lambda_{\perp} = \frac{1}{R_{\perp 1}} + \frac{1}{R_{\perp 2}} \quad (\text{A.6})$$

which are the latitudinal and longitudinal effective curvatures evaluated at the points of closest approach, $R_{\parallel i}$ and $R_{\perp i}$ being the principal radii of curvature of bubble i at the evaluation point (see Section A.1). Since the two interacting bubbles in our system are both vertically symmetric, we will refer to Equations A.5 and A.6 in our calculations.

Applicability conditions

In order to apply DA, the following conditions must be fulfilled [201, 268]:

1. *Low surface potentials.*

This condition is at the basis of the Debye-Huckel, in which the DA is rooted. The electrostatic surface potentials for covered bubbles used in our experiments are always within the limits of this assumption.

2. *The interacting bodies must be smooth in the neighbourhood of the points of closest distance (A and B in Figure 11.4).*

This is, of course, the case for oscillating bubbles, whatever the oscillation mode. More precisely, for any n , the Legendre polynomial $P_n(\cos \theta)$ appearing in Equation 11.1 is a smooth (C^∞) function.

3. *The interaction range between the spheroids is much smaller than the local curvature radii.*

Referring to our case, this translates to: $D \ll R_0 \approx 1 \text{ mm}$, since the effective radii R_{eff} are as large as R_0 for small oscillations. It can be seen from experiments (Chapter 17) that D must be of order of $10 \mu\text{m}$ to observe significant interactions, so the condition is satisfied.

4. *If the bodies are immersed in an electrolyte solution rather than in vacuum, a further condition is necessary, namely: $\kappa^{-1} \ll R_0$. Here $\kappa \propto \sqrt{\sum_i c_i z_i^2}$ is the inverse Debye length, which depends on the concentration c of each z -charged i -th solute and accounts for the electrostatic shield [201].*

κ^{-1} may take very different values, spanning the range of 10^{-1} – 10^3 nm , depending on the solute nature and concentrations. For instance, $\kappa^{-1} = 960 \text{ nm}$ for pure water, while it drops to 0.3 nm for NaCl 1M [201]. In any case, these values are far smaller than the bubble radius ($R_0 \approx 1 \text{ mm}$).

5. *Strictly speaking, DA applies to uniformly charged bodies. However, it may extend to unevenly charged, or globally neutral surfaces, so long as the surface charge distribution scale is larger than the distance D .*

Unlike the previous conditions, this cannot be verified *a priori*, as the redistribution dynamics of the charged species adsorbed at the bubble surface needs to be evaluated on a case-by-case basis.

A.2 Volume conservation

Bubble volume must remain constant during shape oscillations. This implies normalisation of the equilibrium radius R_0 , as described below.

For the quadrupolar mode $n = 2$, the bubble radius is (Equation 11.1):

$$R = R_0 + a_2(t) \cdot P_2(\cos \theta) \quad (\text{A.7})$$

where R_0 is the initial radius of the resting bubble and $P_2(\cos \theta) = \frac{1}{2} (3 \cos^2 \theta - 1)$.

Let us now calculate the volume enclosed by the bubble surface by integrating the volume element dV in spherical coordinates (r, θ, ϕ) :

$$dV = r^2 \sin \theta dr d\theta d\phi \quad (\text{A.8})$$

$$\begin{aligned} V &= \int_0^\pi \sin \theta d\theta \int_0^{2\pi} d\phi \int_0^{R_0} r^2 dr \\ &= \frac{4}{3} \pi R_0^3 \left[1 + \frac{12}{5} x^2 + \frac{16}{35} x^3 \right] \end{aligned} \quad (\text{A.9})$$

where the variable change $x(t) = \frac{a_2(t)}{2R_0}$ was introduced for convenience.

We truncate V to second order and rewrite it as:

$$V \approx V_0 \left[1 + \frac{12}{5} x^2 \right] = V_0 (1 + \varepsilon) \quad (\text{A.10})$$

with $V_0 = \frac{4}{3} \pi R_0^3$ and $\varepsilon = \frac{12}{5} x^2$. The form (A.10) writes, in terms of radius, as:

$$R_{\text{eq}} = R_0 (1 + \varepsilon)^{\frac{1}{3}} \approx R_0 \left(1 + \frac{1}{3} \varepsilon \right) + O(x^3) \quad (\text{A.11})$$

where R_0 is the initial radius of the resting bubble.

Hence we find:

$$R_{\text{eq}} = R_0 \left(1 + \frac{4}{5} x^2 \right) \quad (\text{A.12})$$

Replacing R_{eq} with R_0 in Equation A.7, the local radius of the bubble becomes:

$$R(\theta, t) \approx R_0 + \left[1 + 2x(t) \cdot P_2(\cos \theta) + \frac{4}{5} x(t)^2 \right] + O(x^3) \quad (\text{A.13})$$

Appendix B

Gaussian optics and origin of the fringe pattern [272, 273]

Gaussian optics is a branch of geometrical optics that describes the behaviour of light rays making small angles with the propagation axis. This *paraxial* assumption is well suited to collimated lasers and allows to explain such optical phenomena, like the interference fringes described in Sections 14.1.1 and 15.2.1, not accessible by simpler theories (like the plane-wave approximation).

B.1 Gaussian beams

A light beam is defined to be Gaussian if the transverse profile of optical intensity I is given by the Gaussian function:

$$I(r, z) = \frac{2P}{\pi w(z)^2} \exp\left(-\frac{2r^2}{w(z)^2}\right) \quad (\text{B.1})$$

with P being the power and z and r the propagation and transverse coordinates, respectively. The quantity $w(z)$ is the beam *width*, defined as the distance from optical axis where the intensity drops to $1/e^2$ of the maximum value. This takes the form:

$$w(z) = w_0 \sqrt{1 + \left(\frac{\lambda z}{\pi w_0^2}\right)^2} \quad (\text{B.2})$$

where w_0 is the narrowest beam width, called *waist*, reached at focal point ($z = 0$); λ is the light wavelength.

Equations B.1 and B.2 show that Gaussian beams retain a Gaussian profile along the propagation axis and are entirely described by their waist w_0 (apart from λ). In particular, the form of $w(z)$ implies that:

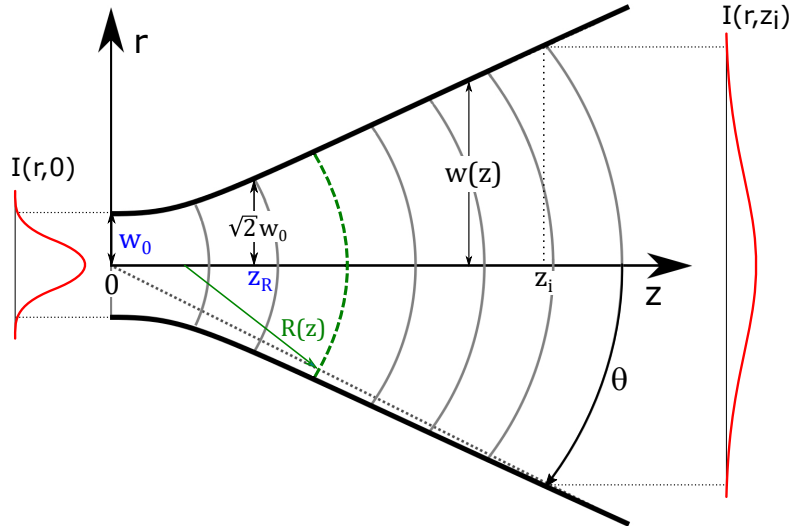


Figure B.1: Beam width $w(z)$ of a (circular) Gaussian beam as a function of the propagation coordinate z (Equation B.2). w_0 is the beam waist, z_R the Rayleigh range and θ the divergence angle, while r is the transverse coordinate. In red are shown the Gaussian transverse intensity profiles $I(r, z)$ (Equation B.1), at the waist (left) and at an arbitrary point z_i (right). The evolution of the wavefront over z , from a flat to a spherical profile, is described by gray lines. $R(z)$ is the curvature radius associated to the green dashed wavefront.

- a) The beam broadens as it propagates from the focus point. $w(z)$ increases slowly for small z , then it rapidly diverges. The *beam divergence* in the so-called "far field" is:

$$\theta = \frac{\lambda}{\pi w_0} \quad (\text{B.3})$$

- b) The smaller the waist w_0 , the larger (B.3) and more rapid (B.2) beam broadening along the optical axis. Hence, the *Rayleigh range* parameter z_R was introduced:

$$z_R = \frac{\pi w_0^2}{\lambda} \quad (\text{B.4})$$

which is the propagation distance corresponding to a width increase of a factor $\sqrt{2}$ and determines the length over which the beam propagates without diverging significantly (i.e. the extent of beam collimation).

The main features of Gaussian beams are summed up in Figure B.1.

Lasers

Collimated lasers are the real optical systems which best match the definition of Gaussian beams.

Lasers are monochromatic light sources narrowly focused along the optical axis with relatively small divergence. In other words, they are spatially and temporally *coherent*:

- Spatial coherence refers to the *collimation* and can be quantified in terms of the beam waist or, equivalently, the Rayleigh range defined above;
- Temporal coherence is related to *monochromaticity*. Unfortunately, real laser sources are not perfectly monochromatic, but display an optical bandwidth $\Delta\nu$. This results in intrinsic interference during light propagation and may therefore affect interferometric measurements. The *coherence length* parameter measures the distance over which temporal coherence is maintained and can be calculated as $L_c = \frac{c}{\pi\Delta\nu}$ (c being the vacuum velocity of light).

The actual performances of laser beams may vary largely as a function of the above parameters (and of the wavelength). Therefore, laser sources must be chosen in accordance with the experimental requirements (e.g., high focusing for precision cutting vs long propagation lengths for laser pointers), possibly making a good compromise between costs and performances.

B.2 Origin of interference fringes

Divergence of Gaussian beams not only results in width broadening, but also in a *curvature* of their wavefront (see Figure B.1). In fact, while at the focus point ($z = 0$) a Gaussian beam is identical to a plane wave of finite extension, during its propagation it acquires a phase shift with respect to a plane wave with the same optical frequency. This phase shift is not uniform along the transverse direction and gives rise to a wavefront curvature (represented in Figure B.1) of radius:

$$R(z) = z \left[1 + \left(\frac{\pi w_0^2}{\lambda z} \right)^2 \right] \quad (\text{B.5})$$

where the appearing symbols were defined in the previous section and in figure.

Equation B.5 shows that the wavefront is flat at $z = 0$ (no phase shift, plane wave) and becomes spherical at infinite z (phase shift $\pi/2$, non-paraxial ray), while for small values of z the curvature is highly sensitive to z .

The phase shift is irrelevant when considering a single beam. Things get different when two beams meet up. In the case of a bubble (drop) crossed by a laser beam, the two light sources backreflected at the bubble (drop) interfaces gain an optical path difference and hence a curvature and a phase difference. The combination of such differently curved wavefronts, therefore, generates a circular interference pattern.

The situation for a "bubble (drop) interferometer" is illustrated in Figure 14.3 of the main text and explained in more detail as follows. A laser beam is focused by a lens on the bubble (drop) surface (point indicated at right in the figure). As it crosses the bubble interior, the beam retains its Gaussian behaviour and undergoes reflection at the air-water (oil-water) interfaces (left and right points in the figure). Two coherent light sources CLS₁ and CLS₂ are therefore generated, with intensities I_i given by Equation B.1 and an optical path difference $x = \Delta z$ related to the bubble radius R ($x = 4R$). Their corresponding wavefronts have both different widths and curvature radii R_i , resulting mainly from the optical path difference and, to a minor extent, from refraction/reflection at the bubble (drop) interfaces¹.

The combination between CLS₁ and CLS₁ yields a light signal of intensity:

$$I = I_1 + I_2 + 2\sqrt{I_1 I_2} \cos \Delta\phi \quad (\text{B.6})$$

which is collected at a screen placed at distance L from the bubble. The last term in Equation B.6 is the interference term, arising from the phase difference between the two wavefronts² on the screen. The phase term takes the form:

$$\Delta\phi = \left(\frac{R_2 - R_1}{R_1 R_2} \rho^2 + \frac{4\pi}{\lambda} R \right) \quad (\text{B.7})$$

where ρ is the radial distance from the propagation axis (centre of the interferometric pattern, see Figure 14.3) and R_i are the curvature radii of the two beams at distance L (Equation B.5). Substituting Equation B.7 into B.6 gives the *shape* of the interferometric pattern. Here, the frequency of the phase term $\Delta\phi$ gives the *spacing*: the larger the radius, the narrower the fringes. It can be seen that, knowing the distance L from the screen, the (static) bubble radius R can be measured from the pattern shape.

¹Indeed, the bubble (drop) acts as a spherical lens, with refractive index determined by the inner fluid and focus dependent on the radius. Hence, back-reflection results in further beam widening and wavefront curvature.

²Recall that the intensity is the square modulus of the electromagnetic field E ($I = |E_1 + E_2|^2$, with $I_i = |E_i|^2$), whose phase component contributes to the interaction between CLS₁ and CLS₁.

If the bubble radius varies, both the pattern spacing and the single-fringe intensity modify. In particular, taking $\rho = 0$ (central fringe) it is obtained:

$$\Delta\phi \approx \frac{4\pi}{\lambda}R \quad (\text{B.8})$$

yielding Equation 14.1 of the main text (*dynamic pattern*). *This relationship allows to quantify the bubble (drop) oscillation amplitude, since for small bubble (drop) deformations the detected intensity will vary linearly with the optical path difference x , and hence, with R .* (see Appendix C.1)

It is worth noticing that the fringe pattern could not be explained in terms of plane-wave optics, since the backreflected beams would have coincident wavefronts (with uniform reciprocal phase dependent on bubble radius). In that case, we would only observe a central spot, as expected from a light beam focused on the centre of a spherical lens (bubble).

Appendix C

Experimental remarks

C.1 Experimental issues and good working practice

Linearity conditions and working point

As pointed out in Section 15.4, measurement results depend on the working point, which is strictly related to the bubble radius R (see Figure 15.3, left panel). In particular, the form of the response function $I(R)$ (Equation 15.1, right panel of Figure 15.3) suggests that bubble vibrations are easily measurable in two extreme cases: very small amplitudes (in the 1–500 Å range) and large amplitudes (greater than a few microns):

- In the first case, the interferometer can operate in a region where the response function $I(R)$ is nearly linear with R , that is, around the inflection point of the response curve, R_{eq} (where the argument of the cosine term in $I(R)$ is equal to an odd multiple of $\pi/2$). This is also the region of highest sensibility for measurements. 1% deviation from linearity is reached with a peak-to-peak vibration amplitude $\Delta R = 13.4$ nm, given the laser wavelength.
- For large vibration amplitudes, simple fringe counting can be used. One fringe count corresponds to a radius variation $\Delta R = 1582$ Å.

Hence, in order to quantitatively measure small-amplitude motions of bubbles, that are in accordance with linearised hydrodynamic theory, it is necessary to set the working point within the region of linear interferometric response. In actual experiments, this is accomplished by letting the bubble reach thermal equilibrium with the surrounding fluid and by monitoring the continuum part of the output voltage V_{DC} . In fact, if the minimum and maximum values are known, the instant value of V_{DC} is informative of the position of the working point on the response curve.

Notice that, if the working point coincides with a maximum (minimum) of $I(R)$, the photodetected signal will be distorted, due to the local quadratic form of the response function. In particular, for bubble radii lying in a maximum, higher harmonics can be detected. By contrast, in correspondence of minima, the output signal is too attenuated to be observed.

Amplitude calibration

Once the interferometer operates in its linear region, the absolute calibration of the vibration amplitude is easily obtained as follows by comparing the measured voltage with the voltage span ΔV for a full light span in the central fringe.

With a 5 mW He-Ne laser source ($\lambda = 633$ nm), a 10^4 -gain photomultiplier the photomultiplier gives a typical variation of $1 \text{ V} = \Delta V$ on a load resistance of $100 \text{ k}\Omega$, for a full light span in the central fringe. From Equation 15.1 we find that ΔV corresponds to $\Delta R = \lambda/8 = 79.1$ nm, in the case of a gas bubble, and to $\Delta R = \lambda/8n$, for a drop of refractive index n . Hence, the amplitude A is given by:

$$A = \frac{V_{\text{out}}}{\Delta V} \cdot \Delta R \quad (\text{C.1})$$

Noise and acoustic insulation

Due to the extreme sensitivity of the interferometric technique, every source of noise must be avoided carefully.

- *Light noise.* Of course, measurements are taken in the dark. Background ambient noise is reduced to a minimum by means of an interference filter placed in front of the photomultiplier aperture.
- *Electrical noise* is mainly due to the shot noise term related to the granular nature of the photodetection process. This gives the theoretical limit for the bubble interferometer sensitivity. In a bandwidth of a few hundred Hz, the root-mean-square voltage is evaluated to be on the order of 10 mV, which, in terms of radius change, corresponds to a few hundredths of nm. Such theoretical sensitivity is very high and could be even improved further, if necessary, using a polarizing interferometer scheme (a polarizing beam splitter and a $\lambda/4$ waveplate), more laser power, and an avalanche photodiode.
- *Acoustic noise.* In practice, in laboratory conditions, due to external acoustic noise, the differential nature of the interferometer may be reduced, at second order, by the coupling of

the overall bubble translational motion to the bubble diameter motions. Nonetheless, very low-amplitude displacements of bubble surface can be measured with confidence, if acoustic noise sources are properly reduced. To this scope, the laboratory is placed in the basement floor; the optical system is tightly mounted on a Newport table inside a sound insulating box and stands on a pneumatically stabilized table (see details *B* and *C* of Figure C.3). The table legs are immersed in sand basins, thus not being in direct contact with the floor. Ultimately, the most delicate measurements are taken at night to avoid disturbances due to people walking around.

In our standard experiments, the actual sensitivity was about 0.1 nm. It is important to notice that such sensitivity can be exploited at best along measurements of vibration amplitudes.

Contaminants and cleaning

Removal of any contaminant that could lead to spurious signals is crucial to benefit from highly sensitive measurements.

Repeated washing of the measuring cell is performed after each experiment. Before the first usage, or after a prolonged period of inactivity, a deep cleaning procedure is followed, involving sonication bath in a (easily removable) surfactant solution and repeated washings with hot water, cold water and milliQ water.

To check if the cell is clean it is sufficient to acquire a single-bubble spectrum in pure water, since the peak amplitude and width are extremely reproducible and extremely sensitive to the presence of contaminants. Other measurements, such as conductivity, have a far higher level of detection and are not indicated.

C.2 Details of the *double* bubble interferometer

Measurement cells

Measurement cells, portrayed in Figure C.5, were fabricated from polished slabs of poly-(methyl methacrylate) (PMMA). This material, cost-effective and easily manipulated (milled and chloroform-welded), has the advantage to be transparent and easily washable. Moreover, contaminant release in water is negligible (lower than glass) under 70 °C. Residual chloroform after manufacturing is evaporated putting the cells in a stove for a couple of hours. For the sake of compactness, the cell volume is kept small (500 or 900 μ l for single- and double-bubble experiments).



Figure C.1: Bubble formation and anchoring to an upper electrode.

The hydraulic circuitry for filling and washing the cell consists of two teflon tubes that are pressure-welded to the bottom of the cell (hole diameter 0.67 mm) and connected to two insulin syringes for the injection/suction of water.

The bubbles (drops) are obtained by injecting a proper volume of air (or hydrophobic liquid), of order of 0.5 μl , with a graduated syringe connected to the injection capillary. Once formed, the bubbles are transferred to the anchoring electrodes, exploiting their higher contact surface with the bubble (see Figure C.1).

The bubbles can be visualised on a screen (see detail *E* of Figure C.3) by positioning a CCD camera in front of the cell (Figure C.5, image magnification $25\times$). The equilibrium radius of the bubbles (R_0 in Equation 6.19 and related) is measured from the image on the screen by means of a digital caliper, taking the upper electrode diameter (exactly 1 mm) as a reference. Precision is of 5 μm . Videometry tools can be used as well.

Optics

The light source is provided by a He-Ne laser beam ($\lambda = 633 \text{ nm}$), coupled to a single-mode fiber (Figure C.7), which is then split into two fibers of about 5 mW in power. Each of the light beams is focused at the centre of the bubble by a lens (focal length 150 mm) and is directed towards the photodetector, after reflection at the bubble walls, by means of mirrors (see Figure C.4).

The fringe visibility is excellent since, after Snell law of reflection, $2\sqrt{I_1 I_2} / (I_1 + I_2) = 0.9998$ (I_1 and I_2 being the interfering light sources defined in Equation 14.1) in the case of a gas bubble in water, with refractive index $n = 1.33$.

Scatterers, like surfactant micelles, present in the medium surrounding the bubble (drop) do not cause problems, since the diffused light gives a flat background to which fringes of much higher intensity are superimposed. Of course, if the solution becomes milky, measurements become difficult. To give an idea, measurements of (single) bubbles immersed in blood plasma were performed in previous studies.

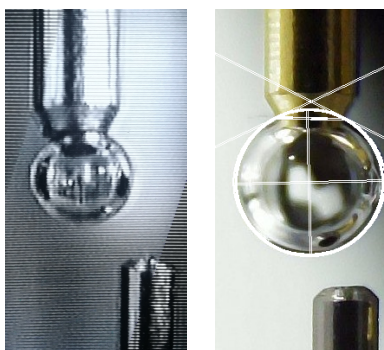


Figure C.2: Two anchored bubbles ($R_0 = 0.7$ mm) at different wetting conditions. *Left:* at low wetting the bubble is unstable and tends to "slide" on the electrode surface. *Right:* at working conditions the contact surface with the electrode is larger (almost equal to the electrode tip) and the bubble is stable. The fit profile of the bubble, used to measure the contact angles (software: *Fiji ImageJ*), is shown. The observed contact angles lie below $\pi/6$, typically around 27° .

Electrodes and excitation circuitry

As can be seen from Figure 16.2, there are two upper and two lower electrodes in the double-bubble setup described in Section 16.2. A better view is provided by Figure C.6. The lower electrode on the left, hollow, is the injection capillary and was obtained from a syringe needle (outer diameter 0.67 mm, inner diameter 0.3 mm) milled to reduce the contact surface with the bubble. The anchoring electrodes (obtained from Xe lamps) are solid and larger than the injection capillary (outer diameter of 1.00 mm) and milled at the extremity (the "tip" diameter is of 0.5 mm for the lower electrode and 0.7 mm for the upper electrodes, with differences of about 0.01 mm from one electrode to another due to the manufacturing process). Note that besides geometry, the electrode wettability is a crucial parameter for modulating bubble anchoring and contact angle, and may impact on the shape of the bubble. Thus, the electrodes must have a rather reproducible hydrophilic surface. In standard working conditions, as in Figure C.6, the contact surface of the bubbles with the electrodes almost coincides with the tip area. Higher wetting leads to larger and non-planar contact surfaces. At low wetting the contact surface is reduced, up to the ideal single-point anchoring limit, but in practice the bubble is unstable and tends to escape. Figure C.2 gives two examples of different wetting conditions and shows the fitted profiles of a typical bubble used to measure the contact angle at the electrode.

The so-called "master" bubble (see Section 16.2 and Figure 16.2) is doubly anchored. The anchoring electrodes allow both electric and mechanical excitation. The lower is fixed at a 2 mm

distance from the injection capillary, while the upper can be moved up-down and left-right through a system of micrometer screws. The "slave" bubble is anchored only on the top and can be excited only electrically (the oppositely charged electrode being supplied by the injection capillary, which is fixed). The anchoring electrode can be moved both top-down and left-right, so that the inter-bubble distance can be varied.

Selective electric excitation of either bubble along the vertical axis is provided by an electrical generator connected to each electrode couple. Frequency, intensity and waveform of the applied field can be finely tuned to meet the experimental needs. Values of the applied electrical field – within the linear response range – correspond to oscillation amplitudes of 0.1–50 nm. Application of voltages of order of 5–10 V, larger than those employed in ordinary measurements (1–5 V), induce deformations on the other bubble of order of 1–2 Å (out of resonance). Acoustic excitation of the master bubble is obtained by a feedback-controlled piezo circuit (see detail C of Figure C.5, illustrating the piezoceramic). Amplitudes are similar to those obtained electrically.

Detection circuitry

The back-reflected light beams from each bubble are directed to a photomultiplier (PMT), generating a cathode photocurrent due to migration of photoemitted electrons (the anode is earthed). Gain depends on the operating voltage and can be as high as 10^6 at 800 V. In our working conditions the voltage is less than 400 V. Avalanche photodiodes, having higher quantum efficiencies in the red (and hence higher sensitivity), could be used instead of PMTs. However, they bear some disadvantages (need of amplification feedbacks, higher shot noise).

As anticipated in Section 15.2.3 of the main text, the overall output signal coming from the photodetector is split in two components:

- The former operates as a high-pass filter, yielding the time-varying voltage V_{out} , which is in turn collected by the spectrum analyser. In particular, the signal-to-noise ratio is optimised for frequencies lying in the range of bubble resonances: signals whose frequencies are lower than 10 Hz cannot be detected, while noise increases for frequencies as high as a MHz.
- The latter operates as a low-pass filter, yielding a continuous (averaged) signal, V_{DC}^1 . This is accomplished by a high-capacity capacitor which integrates the output over a very small bandwidth of order of 1 Hz². The voltage V_{DC} can be read in a display (visible in Figure C.3,

¹i.e., at a much lower frequency than the sweep rate (from v_0 to v_f in 10 s).

²Recall that $R \propto \frac{1}{\nu C}$ in RC circuits, so the electrical resistance vanishes for very low frequencies ν .

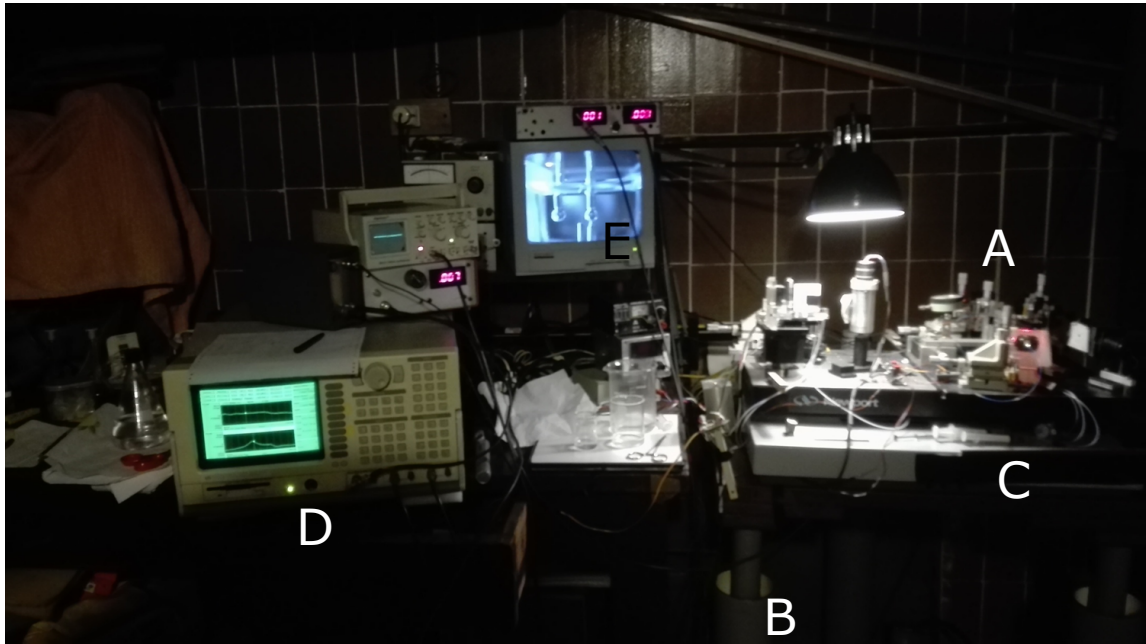


Figure C.3: Front view of the experimental apparatus. *A*) Optical bench with the dual bubble interferometer. *B,C*) Vibrations insulating system. *D*) Digital signal analyser (SR785 Two-Channel Dynamic Signal Analyzer). *E*) Enlarged view of the cell by the CCD camera.

on top of the screen *E*). V_{DC} values range from 50 mV to 100 mV, electrical current (V_{DC}/R) flows over a resistance of about 56 k Ω . These are quite high signals, for which the maximum shot noise is of order of 50 μ V.

While V_{out} is sent to the spectrum analyser (Figure C.3, detail *D*) and used to evaluate bubble radius oscillations, the value of V_{DC} read on the screen is used to set the working point (Appendix C.1).

Phase data are acquired through the "cross spectrum" function of the dual-channel analyser (from the excitation and the photodetected signal, in the case of single bubbles, or from the two independent photodetected signals in the case of interacting bubbles).

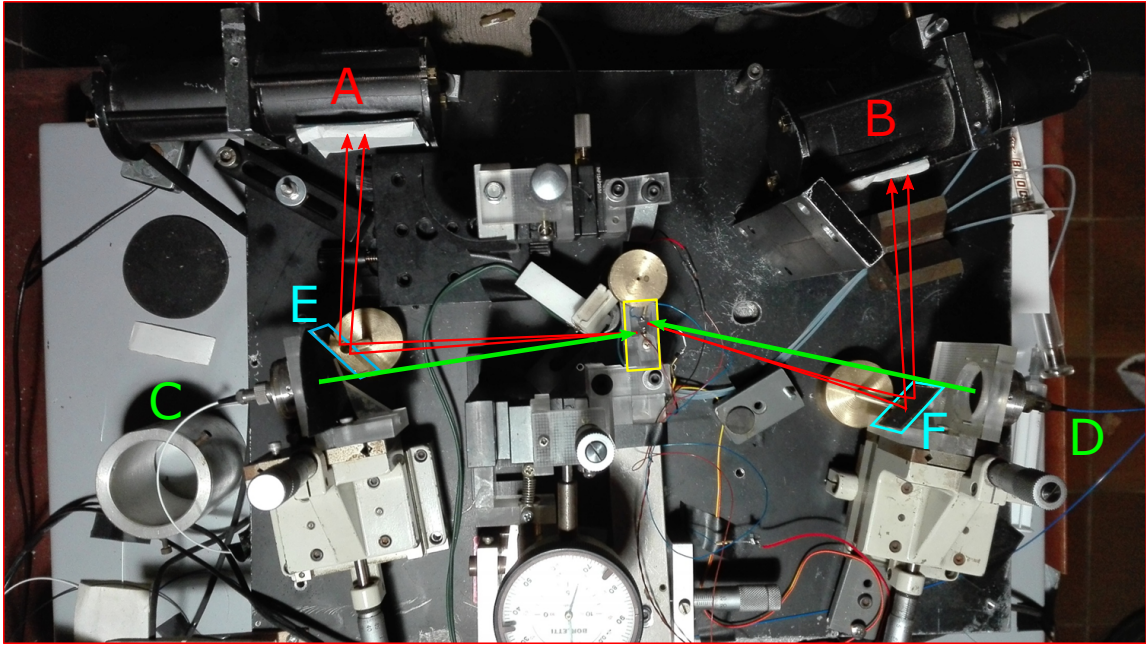


Figure C.4: Top view of the optical bench. *A)* Master bubble interferometer photomultiplier; *B)* Slave bubble interferometer photomultiplier. *C)* Fiber with coupler (PAFA-X-4-A) for the Master bubble-interferometer; *D)* Fiber with coupler (PAFA-X-4-A) for the Slave bubble-interferometer. *E,F)* Mirrors which intercept backward interference fringes from bubbles.

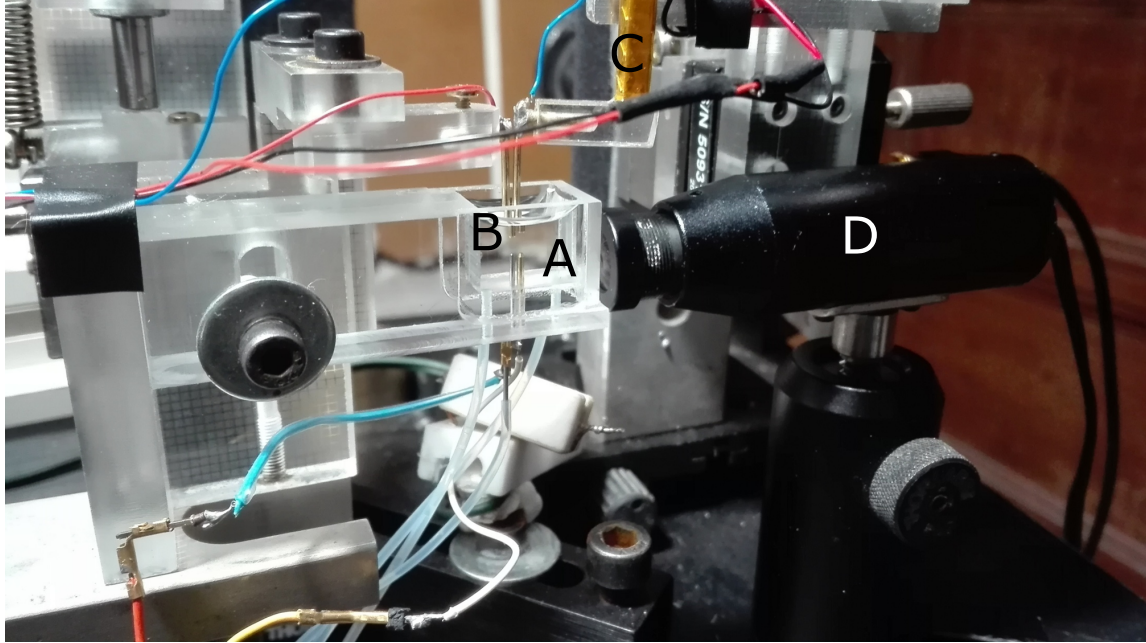


Figure C.5: A closer view of the apparatus. *B*) Upper electrodes to which bubbles are anchored: while the *master* bubble (at right) is held in a fixed position and blocked between upper and lower electrodes, the *slave* bubble (left) is allowed to move in the left-right direction. *C*) Piezoceramic for the mechanical excitation of the *master* bubble. *D*) CCD camera.

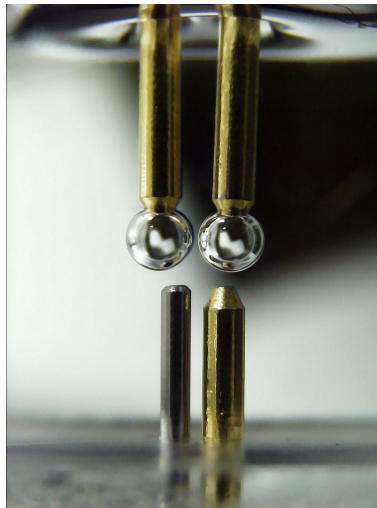


Figure C.6: Detail of the measurement cell, showing the upper and lower electrodes. The two suspended bubbles are in "standard" wetting conditions, where the contact surface of the bubbles with the electrodes almost coincides with the "tip" area (diameter of order of 0.7 mm).

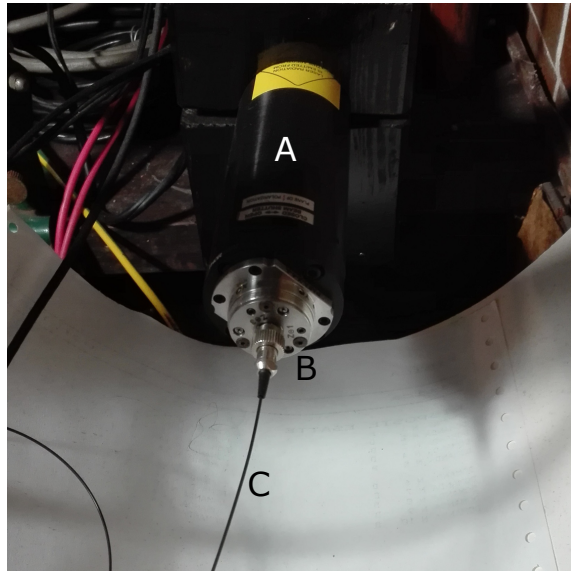


Figure C.7: Detail of the laser source. *A*) Laser He-Ne (Thorlabs HNL21L, 20 mW). *B*) Coupler of the laser beam into the single-mode fiber (Thorlabs Fiber Port PAFA-X-4-A). *C*) Single-mode optical fiber (Thorlabs FC632-50B-FC): the fiber splits into the two fibers which feed the two interferometers (about 5 mW of light power available at each end).

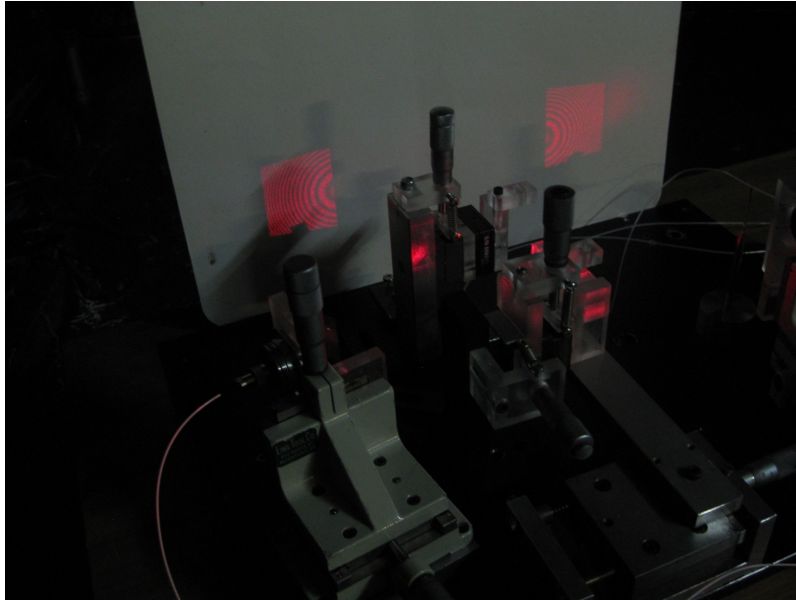


Figure C.8: Partial view of the double interferometer, showing the two interference patterns which allow to monitor both bubbles at once. Optical artifacts arising from interaction between the two light sources are avoided by a proper choice of laser directions and by positioning a blackout screen in-between.

Acknowledgements

I would like to express the deepest appreciation to Mario Corti – ex full professor of Physics at the faculty of Medicine of the university of Milan (Italy), now associated to CNR-IPCF Messina – for his commitment in the experimental part, including the setup of a tailored interferometric apparatus. Without his precious work this study would not have been possible.

I am indebted to Doctor Martina Pannuzzo, Laboratory of Nanotechnology for Precision Medicine, Fondazione Istituto Italiano di Tecnologia (IIT), Genoa (Italy), for her support in the research planning process, for her countless gems of advice, as well as, of course, for her commitment in the computer simulations.

My thanks go to Professor Giovanni Russo and to Clarissa Astuto from the Department of Mathematics of the University of Catania, and to Professor Armando Coco, from Oxford Brookes University, UK, for sharing their numerical calculations on bubble dynamics.

I am grateful to Professor Ayache Bouakaz, UMR Inserm U 1253 – Imagerie et Cerveau, University of Tours (France), for giving me the opportunity to do a traineeship in his laboratory and introducing me to the fascinating field of biomedical research.

I also benefited greatly from many discussions with Professor Alexey Maksimov, V. I. Il'ichev Pacific Oceanological Institute, Russian Academy of Science, Vladivostok, concerning theoretical aspects that I would have ignored otherwise. I am looking forward to a fruitful cooperation.

Finally, the purchase of reactants and instrument components was financed by the French National Center for Scientific Research (CNRS).

Bibliography

- [1] D. Boss, A. Hoffmann, B. Rappaz, C. Depeursinge, P. J. Magistretti, D. Van de Ville, and P. Marquet, *PLoS One*, 2012, **7**(8), e40667.
- [2] E. Sackmann and A.-S. Smith, *Soft matter*, 2014, **10**(11), 1644–1659.
- [3] K. Salaita, P. M. Nair, R. S. Petit, R. M. Neve, D. Das, J. W. Gray, and J. T. Groves, *science*, 2010, **327**(5971), 1380–1385.
- [4] A. Raudino, D. Raciti, and M. Corti, *Langmuir*, 2017, **33**(25), 6439–6448.
- [5] M. Corti, A. Raudino, L. Cantu', J. Theisen, M. Pleines, and T. Zemb, *Langmuir*, 2018, **34**(28), 8154–8162.
- [6] L. Rayleigh, *The London, Edinburgh, and Dublin Philosophical Magazine and Journal of Science*, 1917, **34**(200), 94–98.
- [7] L. Cantù, A. Raudino, and M. Corti, *Adv. Colloid Interface Sci.*, 2017.
- [8] A. Raudino, D. Raciti, A. Grassi, M. Pannuzzo, and M. Corti, *Langmuir*, 2016, **32**(34), 8574–8582.
- [9] M. Corti, M. Pannuzzo, and A. Raudino, *Langmuir*, 2014, **30**(2), 477–487.
- [10] I. Cimrák, M. Gusenbauer, and T. Schrefl, *Computers & Mathematics with Applications*, 2012, **64**(3), 278–288.
- [11] C. Monzel and K. Sengupta, *J. Phys. D Appl. Phys.*, 2016, **49**(24), 243002.
- [12] R. Finn, *Equilibrium capillary surfaces*, Vol. 284, Springer Science & Business Media, 2012.

- [13] J. Bostwick and P. Steen, *Annual Review of Fluid Mechanics*, 2015, **47**, 539–568.
- [14] B. J. Kirby, *Micro-and nanoscale fluid mechanics: transport in microfluidic devices*, Cambridge university press, 2010.
- [15] R. Scardovelli and S. Zaleski, *Annual review of fluid mechanics*, 1999, **31**(1), 567–603.
- [16] O. Voinov, *Fluid dynamics*, 1976, **11**(5), 714–721.
- [17] X. Noblin, A. Buguin, and F. Brochard-Wyart, *The European Physical Journal E*, 2004, **14**(4), 395–404.
- [18] D. Lyubimov, T. Lyubimova, and S. Shklyaev, *Fluid Dynamics*, 2004, **39**(6), 851–862.
- [19] P.-G. De Gennes, *Reviews of modern physics*, 1985, **57**(3), 827.
- [20] E. Lucassen-Reynders and J. Lucassen, *Advances in colloid and interface science*, 1970, **2**(4), 347–395.
- [21] D. Langevin, *Colloids and surfaces*, 1990, **43**(2), 121–131.
- [22] D. Langevin et al., *Light scattering by liquid surfaces and complementary techniques*, M. Dekker, 1992.
- [23] S.-W. Ohl, E. Klaseboer, and B. C. Khoo, *Interface Focus*, 2015, **5**(5), 20150019.
- [24] K. S. Suslick and D. J. Flannigan, *Annu. Rev. Phys. Chem.*, 2008, **59**, 659–683.
- [25] M. Minnaert, *The London, Edinburgh, and Dublin Philosophical Magazine and Journal of Science*, 1933, **16**(104), 235–248.
- [26] A. Unsworth, D. Dowson, and V. Wright, *Annals of the rheumatic diseases*, 1971, **30**(4), 348.
- [27] M. P. Brenner, S. Hilgenfeldt, and D. Lohse, *Reviews of modern physics*, 2002, **74**(2), 425.
- [28] O. Reynolds, *Scientific Papers on Mechanical and Physical Subject*, 1894, **2**, 1900–1903.
- [29] M. S. Plesset and R. B. Chapman, *Journal of Fluid Mechanics*, 1971, **47**(2), 283–290.
- [30] W. Lauterborn and H. Bolle, *Journal of Fluid Mechanics*, 1975, **72**(2), 391–399.

- [31] J. R. Blake and D. Gibson, *Annual review of fluid mechanics*, 1987, **19**(1), 99–123.
- [32] R. E. Arndt, *Annual Review of Fluid Mechanics*, 1981, **13**(1), 273–326.
- [33] R. Knapp, J. Daily, and F. Hammitt, *Cavitation*. engineering societies monographs, 1970.
- [34] P. Marmottant and S. Hilgenfeldt, *Nature*, 2003, **423**(6936), 153.
- [35] I. Lentacker, I. De Cock, R. Deckers, S. De Smedt, and C. Moonen, *Advanced drug delivery reviews*, 2014, **72**, 49–64.
- [36] A. Bouakaz, A. Zeghimi, and A. A. Doinikov in *Therapeutic Ultrasound*; Springer, 2016; pp. 175–189.
- [37] B. H. Lammertink, C. Bos, R. Deckers, G. Storm, C. T. Moonen, and J.-M. Escoffre, *Frontiers in pharmacology*, 2015, **6**, 138.
- [38] C. A. Sennoga, E. Kanbar, L. Auboire, P.-A. Dujardin, D. Fouan, J.-M. Escoffre, and A. Bouakaz, *Expert opinion on drug delivery*, 2017, **14**(9), 1031–1043.
- [39] A. A. Doinikov and A. Bouakaz, *IEEE transactions on ultrasonics, ferroelectrics, and frequency control*, 2011, **58**(5), 981–993.
- [40] V. Bjerknes, *Die Kraftfelder*, number 28, F. Vieweg, 1909.
- [41] U. Parlitz, R. Mettin, S. Luther, I. Akhatov, M. Voss, and W. Lauterborn, *Philosophical Transactions of the Royal Society of London. Series A: Mathematical, Physical and Engineering Sciences*, 1999, **357**(1751), 313–334.
- [42] R. Mettin, *Bubble and particle dynamics in acoustic fields: modern trends and applications*, 2005, pp. 1–36.
- [43] W. Lauterborn and T. Kurz, *Rep. Prog. Phys.*, 2010, **73**(10), 106501.
- [44] W. Helfrich, *Z. Naturforsch. C Bio. Sci.*, 1973, **28**(11-12), 693–703.
- [45] A. Raudino and M. Pannuzzo, *J. Chem. Phys.*, 2010, **132**(4), 01B617.
- [46] A. Pierres, V. Monnet-Corti, A.-M. Benoliel, and P. Bongrand, *Trends in cell biology*, 2009, **19**(9), 428–433.

- [47] H. Wennerström and U. Olsson, *Advances in colloid and interface science*, 2014, **208**, 10–13.
- [48] T. Browicz, *Zbl. med. Wissen*, 1890, **28**(1), 625–627.
- [49] F. Brochard and J. Lennon, *J. Phys.*, 1975, **36**(11), 1035–1047.
- [50] E. S. Chhabra and H. N. Higgs, *Nature cell biology*, 2007, **9**(10), 1110.
- [51] O. T. Fackler and R. Grosse, *J. Cell. Biol.*, 2008, **181**(6), 879–884.
- [52] J. Evans, W. Gratzler, N. Mohandas, K. Parker, and J. Sleep, *Biophys. J.*, 2008, **94**(10), 4134–4144.
- [53] B. Rappaz, A. Barbul, A. Hoffmann, D. Boss, R. Korenstein, C. Depeursinge, P. J. Magistretti, and P. Marquet, *Blood Cells, Molecules, and Diseases*, 2009, **42**(3), 228–232.
- [54] A. Y. Krol, M. Grinfeldt, S. Levin, and A. Smilgavichus, *European Biophysics Journal*, 1990, **19**(2), 93–99.
- [55] A. E. Pelling, F. S. Veraitch, C. Pui-Kei Chu, B. M. Nicholls, A. L. Hemsley, C. Mason, and M. A. Horton, *Journal of Molecular Recognition: An Interdisciplinary Journal*, 2007, **20**(6), 467–475.
- [56] B. Szabó, D. Selmeczi, Z. Környei, E. Madarász, and N. Rozlosnik, *Physical Review E*, 2002, **65**(4), 041910.
- [57] N. Gov and S. Safran, *Biophys. J.*, 2005, **88**(3), 1859–1874.
- [58] Y. Park, M. Diez-Silva, G. Popescu, G. Lykotrafitis, W. Choi, M. S. Feld, and S. Suresh, *Proceedings of the National Academy of Sciences*, 2008, **105**(37), 13730–13735.
- [59] G. Tomaiuolo, *Biomicrofluidics*, 2014, **8**(5), 051501.
- [60] J. Faix and K. Rottner, *Current opinion in cell biology*, 2006, **18**(1), 18–25.
- [61] E. Evans, *Cell motility and the cytoskeleton*, 1989, **14**(4), 544–551.
- [62] R. Shamri, V. Grabovsky, J.-M. Gauguier, S. Feigelson, E. Manevich, W. Kolanus, M. K. Robinson, D. E. Staunton, U. H. von Andrian, and R. Alon, *Nature immunology*, 2005, **6**(5), 497.

- [63] J. P. Hale, G. Marcelli, K. H. Parker, C. P. Winlove, and P. G. Petrov, *Soft Matter*, 2009, **5**(19), 3603–3606.
- [64] K. Khairy, J. Foo, and J. Howard, *Cellular and molecular bioengineering*, 2008, **1**(2-3), 173.
- [65] M. P. Sheetz and D. Sawyer, *Journal of supramolecular structure*, 1978, **8**(4), 399–412.
- [66] G. Schwoch and H. Passow, *Molecular and cellular biochemistry*, 1973, **2**(2), 197–218.
- [67] A. G. Petrov and P. N. Usherwood, *European biophysics journal*, 1994, **23**(1), 1–19.
- [68] B. Martinac, *Journal of cell science*, 2004, **117**(12), 2449–2460.
- [69] A. D. Bershadsky, N. Q. Balaban, and B. Geiger, *Annual review of cell and developmental biology*, 2003, **19**(1), 677–695.
- [70] J. Keener and J. Sneyd in *Mathematical Physiology*; Springer, 2009; pp. 347–384.
- [71] C.-C. Huang, G. Gompper, and R. G. Winkler, *Physical Review E*, 2012, **86**(5), 056711.
- [72] D. Leckband, *Current opinion in colloid & interface science*, 2001, **6**(5-6), 498–505.
- [73] A. Mathijssen, J. Culver, M. S. Bhamla, and M. Prakash, *bioRxiv*, 2018, p. 428573.
- [74] H. Ishida and Y. Shigenaka, *Cell motility and the cytoskeleton*, 1988, **9**(3), 278–282.
- [75] D. R. Brumley, K. Y. Wan, M. Polin, and R. E. Goldstein, *Elife*, 2014, **3**, e02750.
- [76] S. Chandrasekhar, *Proceedings of the London Mathematical Society*, 1959, **3**(1), 141–149.
- [77] A. Prosperetti, *The Physics of Fluids*, 1981, **24**(7), 1217–1223.
- [78] J. Padrino, T. Funada, and D. Joseph, *International Journal of Multiphase Flow*, 2008, **34**(1), 61–75.
- [79] C. Miller and L. Scriven, *Journal of Fluid Mechanics*, 1968, **32**(3), 417–435.
- [80] J. Loshak and C. H. Byers, *Chemical Engineering Science*, 1973, **28**(1), 149–156.
- [81] S.-C. Yao and V. Schrock, *Journal of Heat Transfer*, 1976, **98**(1), 120–126.
- [82] V. G. Levich, *Physicochemical hydrodynamics*, Prentice hall, 1962.

- [83] C. Wong, *Physics Letters B*, 1976, **61**(4), 321–323.
- [84] B. Sommers and J. Foster, *Journal of Physics D: Applied Physics*, 2012, **45**(41), 415203.
- [85] A. R. Nelson and N. R. Gokhale, *Journal of Geophysical Research*, 1972, **77**(15), 2724–2727.
- [86] L. Kelvin, *mathematical and Physical papers*, 1890, **3**, 384–386.
- [87] L. Rayleigh, *Reprinted, Dover, New York*, 1945.
- [88] H. Lamb, *Proceedings of the London Mathematical Society*, 1881, **1**(1), 51–70.
- [89] H. Lamb, *Hydrodynamics*, Cambridge university press, 1932.
- [90] C. Herring, *Theory of the pulsations of the gas bubble produced by an underwater explosion*, Columbia Univ., Division of National Defense Research, 1941.
- [91] J. B. Keller and M. Miksis, *The Journal of the Acoustical Society of America*, 1980, **68**(2), 628–633.
- [92] A. Prosperetti and A. Lezzi, *Journal of Fluid Mechanics*, 1986, **168**, 457–478.
- [93] A. Prosperetti, *The Physics of fluids*, 1987, **30**(11), 3626–3628.
- [94] Q. Wang and J. Blake, *Journal of Fluid Mechanics*, 2010, **659**, 191–224.
- [95] Q. Wang and J. Blake, *Journal of Fluid Mechanics*, 2011, **679**, 559–581.
- [96] A. Prosperetti, L. A. Crum, and K. W. Commander, *The Journal of the Acoustical Society of America*, 1988, **83**(2), 502–514.
- [97] Z. Feng and L. Leal, *Annual review of fluid mechanics*, 1997, **29**(1), 201–243.
- [98] T. Leighton, *The acoustic bubble*, Academic press, 2012.
- [99] C. E. Brennen, *Cavitation and bubble dynamics*, Cambridge University Press, 2014.
- [100] R. Berker, *Handbuch der physik*, 1963, **3**, 1–384.
- [101] T. Leighton, 2007.

- [102] M. Plesset, *Journal of Applied Physics*, 1954, **25**(1), 96–98.
- [103] M. S. Plesset and A. Prosperetti, *Annual review of fluid mechanics*, 1977, **9**(1), 145–185.
- [104] L. A. Crum, *The Journal of the Acoustical Society of America*, 1983, **73**(1), 116–120.
- [105] S. M. van der Meer, B. Dollet, M. M. Voormolen, C. T. Chin, A. Bouakaz, N. de Jong, M. Versluis, and D. Lohse, *The Journal of the Acoustical Society of America*, 2007, **121**(1), 648–656.
- [106] G. Brenn, *Analytical Solutions for Transport Processes*, Springer, 2016.
- [107] A. Prosperetti, *Quarterly of Applied Mathematics*, 1977, **34**(4), 339–352.
- [108] A. Prosperetti, *Journal of Fluid Mechanics*, 1980, **100**(2), 333–347.
- [109] A. A. Harkin, T. J. Kaper, and A. Nadim, *Physics of Fluids*, 2013, **25**(6), 062101.
- [110] J. Vejrazka, L. Vobecka, S. Orvalho, M. Zednikova, and J. Tihon, *Chemical Engineering Science*, 2014, **116**, 359–371.
- [111] V. E. Zakharov, *Journal of Applied Mechanics and Technical Physics*, 1968, **9**(2), 190–194.
- [112] T. B. Benjamin, *Journal of Fluid Mechanics*, 1987, **181**, 349–379.
- [113] A. Maksimov, *Journal of Experimental and Theoretical Physics*, 2008, **106**(2), 355–370.
- [114] C. K. Batchelor and G. Batchelor, *An introduction to fluid dynamics*, Cambridge university press, 2000.
- [115] J. Vejrazka, L. Vobecka, and J. Tihon, *Physics of fluids*, 2013, **25**(6), 062102.
- [116] C. Devin Jr, *The Journal of the Acoustical Society of America*, 1959, **31**(12), 1654–1667.
- [117] A. Prosperetti, *The Journal of the Acoustical Society of America*, 1977, **61**(1), 17–27.
- [118] M. S. Longuet-Higgins, *Journal of Fluid Mechanics*, 1989, **201**, 543–565.
- [119] T. Leighton, *The Journal of the Acoustical Society of America*, 2011, **130**(5), 3333–3338.
- [120] J. Bostwick and P. Steen, *Physics of Fluids*, 2009, **21**(3), 032108.

- [121] J. Vejrazka, L. Vobecka, and J. Tihon In *EPJ Web of Conferences*, Vol. 45, p. 01092. EDP Sciences, 2013.
- [122] A. Prosperetti, *Physics of fluids*, 2012, **24**(3), 032109.
- [123] S. Ramalingam, D. Ramkrishna, and O. A. Basaran, *Physics of Fluids*, 2012, **24**(8), 082102.
- [124] A. Maksimov, *Journal of sound and vibration*, 2005, **283**(3-5), 915–926.
- [125] A. O. Maksimov, T. G. Leighton, and P. R. Birkin In *AIP Conference Proceedings*, Vol. 838, pp. 512–515. AIP, 2006.
- [126] A. Maksimov and Y. A. Polovinka, *Physics of Fluids*, 2013, **25**(6), 062104.
- [127] Y. A. Kobelev and L. Ostrovskii, *Sov. Phys. Acoust*, 1984, **30**, 715–716.
- [128] J. Lighthill, *Journal of sound and vibration*, 1978, **61**(3), 391–418.
- [129] L. Rayleigh, *Phil. Trans. Roy. Soc*, 1884, **175**, 1–21.
- [130] N. Riley, *Annual review of fluid mechanics*, 2001, **33**(1), 43–65.
- [131] M. Campbell, J. Cosgrove, C. Greated, S. Jack, and D. Rockliff, *Optics & laser technology*, 2000, **32**(7-8), 629–639.
- [132] R. J. Adrian, *Experiments in fluids*, 2005, **39**(2), 159–169.
- [133] M. Nabavi, M. K. Siddiqui, and J. Dargahi, *Measurement Science and Technology*, 2007, **18**(7), 1811.
- [134] M. K. Aktas and B. Farouk, *The Journal of the Acoustical Society of America*, 2004, **116**(5), 2822–2831.
- [135] W. L. Nyborg, *The Journal of the Acoustical Society of America*, 1958, **30**(4), 329–339.
- [136] C. Eckart, *Physical review*, 1948, **73**(1), 68.
- [137] S. A. Elder, *The Journal of the Acoustical Society of America*, 1959, **31**(1), 54–64.
- [138] P. Tho, R. Manasseh, and A. Ooi, *Journal of fluid mechanics*, 2007, **576**, 191–233.
- [139] R. Manasseh, *Handbook of Ultrasonics and Sonochemistry*, 2016, pp. 1–36.

- [140] M. S. Longuet-Higgins, *Proceedings of the Royal Society of London. Series A: Mathematical, Physical and Engineering Sciences*, 1998, **454**(1970), 725–742.
- [141] F. Mekki-Berrada, T. Combriat, P. Thibault, and P. Marmottant, *Journal of Fluid Mechanics*, 2016, **797**, 851–873.
- [142] A. A. Doinikov and A. Bouakaz, *Journal of Fluid Mechanics*, 2016, **796**, 318–339.
- [143] A. A. Doinikov, D. Bienaimé, S. R. Gonzalez-Avila, C.-D. Ohl, and P. Marmottant, *Physical Review E*, 2019, **99**(5), 053106.
- [144] M. Faraday et al. In *Abstracts of the Papers Printed in the Philosophical Transactions of the Royal Society of London*, Vol. 3, pp. 49–51. The Royal Society, 1837.
- [145] S. Boluriaan and P. J. Morris, *International Journal of aeroacoustics*, 2003, **2**(3), 255–292.
- [146] K. Petkovic-Duran, R. Manasseh, Y. Zhu, and A. Ooi, *BioTechniques*, 2009, **47**(4), 827–834.
- [147] K. Ward and Z. H. Fan, *Journal of Micromechanics and Microengineering*, 2015, **25**(9), 094001.
- [148] P. R. Birkin, Y. E. Watson, and T. G. Leighton, *Chemical Communications*, 2001, (24), 2650–2651.
- [149] J. F. Polak, *New England Journal of Medicine*, 2004, **351**(21), 2154–2155.
- [150] A. Novell, J. Collis, A. A. Doinikov, A. Ooi, R. Manasseh, and A. Bouakaz In *2011 IEEE International Ultrasonics Symposium*, pp. 1482–1485. IEEE, 2011.
- [151] J. Wu, *Ultrasound in medicine & biology*, 2002, **28**(1), 125–129.
- [152] L. A. Crum, *The Journal of the Acoustical Society of America*, 1975, **57**(6), 1363–1370.
- [153] T. Leighton, A. Walton, and M. Pickworth, *European Journal of Physics*, 1990, **11**(1), 47.
- [154] A. I. Eller and L. A. Crum, *The Journal of the Acoustical Society of America*, 1970, **47**(3B), 762–767.
- [155] A. A. Doinikov, *Bubble and particle dynamics in acoustic fields: modern trends and applications*, 2005, **661**, 95–143.

- [156] N. A. Pelekasis and J. A. Tsamopoulos, *Journal of Fluid Mechanics*, 1993, **254**, 467–499.
- [157] N. A. Pelekasis and J. A. Tsamopoulos, *Journal of Fluid Mechanics*, 1993, **254**, 501–527.
- [158] A. Doinikov and S. Zavtrak, *Physics of Fluids*, 1995, **7**(8), 1923–1930.
- [159] A. Doinikov and S. Zavtrak, *The Journal of the Acoustical Society of America*, 1997, **102**(3), 1424–1431.
- [160] A. A. Doinikov, *The Journal of the Acoustical Society of America*, 1999, **106**(6), 3305–3312.
- [161] N. A. Pelekasis, A. Gaki, A. Doinikov, and J. A. Tsamopoulos, *Journal of Fluid Mechanics*, 2004, **500**, 313–347.
- [162] V. Pandey, *Physical Review E*, 2019, **99**(4), 042209.
- [163] T. B. Benjamin and M. Strasberg, *The Journal of the Acoustical Society of America*, 1958, **30**(7), 697–697.
- [164] M. Versluis, D. E. Goertz, P. Palanchon, I. L. Heitman, S. M. van der Meer, B. Dollet, N. de Jong, and D. Lohse, *Physical review E*, 2010, **82**(2), 026321.
- [165] A. Maksimov and T. Leighton, *The Journal of the Acoustical Society of America*, 2018, **143**(1), 296–305.
- [166] M. Guédra and C. Inserra, *Journal of Fluid Mechanics*, 2018, **857**, 681–703.
- [167] W. Bade, *The Journal of Chemical Physics*, 1957, **27**(6), 1280–1284.
- [168] A. Stone, *The theory of intermolecular forces*, OUP Oxford, 2013.
- [169] G. Kapodistrias and P. H. Dahl, *The Journal of the Acoustical Society of America*, 2000, **107**(6), 3006–3017.
- [170] P.-Y. Hsiao, M. Devaud, and J.-C. Bacri, *The European Physical Journal E*, 2001, **4**(1), 5–10.
- [171] A. Shima, *Journal of Basic Engineering*, 1971, **93**(3), 426–431.
- [172] M. Ida, *Physics Letters A*, 2002, **297**(3-4), 210–217.

- [173] Z. Zeravcic, D. Lohse, and W. Van Saarloos, *Journal of fluid mechanics*, 2011, **680**, 114–149.
- [174] A. A. Doinikov and A. Bouakaz, *Physical Review E*, 2015, **92**(4), 043001.
- [175] T. Barbat, N. Ashgriz, and C.-S. Liu, *Journal of Fluid Mechanics*, 1999, **389**, 137–168.
- [176] A. Harkin, T. J. Kaper, and A. Nadim, *Journal of Fluid Mechanics*, 2001, **445**, 377–411.
- [177] E. Kurihara, T. A. Hay, Y. A. Ilinskii, E. A. Zabolotskaya, and M. F. Hamilton, *The Journal of the Acoustical Society of America*, 2011, **130**(5), 3357–3369.
- [178] L. Jin-Fu, C. Wei-Zhong, S. Wei-Hang, and Q. Shui-Bao, *Chinese Physics Letters*, 2012, **29**(7), 074701.
- [179] E. Kurihara, *SIAM Journal on Applied Dynamical Systems*, 2017, **16**(1), 139–158.
- [180] A. Doinikov and S. Zavtrak, *The Journal of the Acoustical Society of America*, 1996, **99**(6), 3849–3850.
- [181] A. A. Doinikov, *Journal of Fluid Mechanics*, 2001, **444**, 1–21.
- [182] M. Morioka, *Journal of Nuclear Science and Technology*, 1974, **11**(12), 554–560.
- [183] A. Maksimov and V. Yusupov, *European Journal of Mechanics-B/Fluids*, 2016, **60**, 164–174.
- [184] A. Maksimov and Y. A. Polovinka, *The Journal of the Acoustical Society of America*, 2018, **144**(1), 104–114.
- [185] A. Maksimov, *Fluids*, 2018, **3**(4), 90.
- [186] L. L. Foldy, *Physical Review*, 1945, **67**(3-4), 107.
- [187] N. Bremond, M. Arora, C.-D. Ohl, and D. Lohse, *Physics of fluids*, 2005, **17**(9), 091111.
- [188] N. Bremond, M. Arora, C.-D. Ohl, and D. Lohse, *Physical review letters*, 2006, **96**(22), 224501.
- [189] R. Manasseh, G. Riboux, and F. Risso, *International Journal of Multiphase Flow*, 2008, **34**(10), 938–949.

- [190] G. B. Deane and M. D. Stokes, *The Journal of the Acoustical Society of America*, 2008, **124**(6), 3450–3463.
- [191] S. W. Fong, D. Adhikari, E. Klaseboer, and B. C. Khoo, *Experiments in fluids*, 2009, **46**(4), 705–724.
- [192] L. W. Chew, E. Klaseboer, S.-W. Ohl, and B. C. Khoo, *Physical Review E*, 2011, **84**(6), 066307.
- [193] W. Wiedemair, Z. Tukovic, H. Jasak, D. Poulikakos, and V. Kurtcuoglu, *Physics of Fluids*, 2014, **26**(6), 062106.
- [194] A. Rust and M. Manga, *Journal of colloid and interface science*, 2002, **249**(2), 476–480.
- [195] H.-J. Butt, B. Cappella, and M. Kappl, *Surface science reports*, 2005, **59**(1-6), 1–152.
- [196] R. Mettin, I. Akhatov, U. Parlitz, C. Ohl, and W. Lauterborn, *Physical review E*, 1997, **56**(3), 2924.
- [197] I. Bena, C. Van den Broeck, R. Kawai, M. Copelli, and K. Lindenberg, *Physical Review E*, 2002, **65**(3), 036611.
- [198] A. A. Doinikov, *Physical review E*, 2001, **64**(2), 026301.
- [199] A. Oron, S. H. Davis, and S. G. Bankoff, *Reviews of modern physics*, 1997, **69**(3), 931.
- [200] D. C. Grahame, *Chemical reviews*, 1947, **41**(3), 441–501.
- [201] J. N. Israelachvili, *Intermolecular and surface forces*, Academic press, 2011.
- [202] B. Derjaguin, *Kolloid Zeits*, 1934, **69**, 155–164.
- [203] D. J. Struik, *Lectures on classical differential geometry*, Courier Corporation, 2012.
- [204] M. P. Do Carmo, *Differential Geometry of Curves and Surfaces: Revised and Updated Second Edition*, Courier Dover Publications, 2016.
- [205] I. Cimrak, M. Gusenbauer, and I. Jančigová, *Computer Physics Communications*, 2014, **185**(3), 900–907.

- [206] R. Bolaños-Jiménez, M. Rossi, D. F. Rivas, C. J. Kähler, and A. Marin, *Journal of fluid mechanics*, 2017, **820**, 529–548.
- [207] J. Earnshaw and R. McGivern, *Journal of Physics D: Applied Physics*, 1987, **20**(1), 82.
- [208] J. Earnshaw, *Advances in colloid and interface science*, 1996, **68**, 1–29.
- [209] W. Klipstein, J. Radnich, and S. Lamoreaux, *American Journal of Physics*, 1996, **64**(6), 758–765.
- [210] P. Cicuta and I. Hopkinson, *Colloids and Surfaces A: Physicochemical and Engineering Aspects*, 2004, **233**(1-3), 97–107.
- [211] C. Sohl, K. Miyano, and J. B. Ketterson, *Review of Scientific Instruments*, 1978, **49**(10), 1464–1469.
- [212] E. I. Franses, O. A. Basaran, and C.-H. Chang, *Current Opinion in Colloid & Interface Science*, 1996, **1**(2), 296–303.
- [213] J. Drelich, C. Fang, and C. White, *Encyclopedia of surface and colloid science*, 2002, **3**, 3158–3163.
- [214] J. D. Berry, M. J. Neeson, R. R. Dagastine, D. Y. Chan, and R. F. Tabor, *Journal of colloid and interface science*, 2015, **454**, 226–237.
- [215] R. Miller, A. Hofmann, R. Hartmann, A. Halbig, and K.-H. Schano, *Advanced Materials*, 1992, **4**(5), 370–374.
- [216] J. Lucassen and M. Van Den Tempel, *Chemical Engineering Science*, 1972, **27**(6), 1283–1291.
- [217] R. Nagarajan and D. Wasan, *Journal of colloid and interface science*, 1993, **159**(1), 164–173.
- [218] L. Liggieri, V. Attolini, M. Ferrari, and F. Ravera, *Journal of colloid and interface science*, 2002, **255**(2), 225–235.
- [219] V. Kovalchuk, J. Krägel, A. Makievski, G. Loglio, F. Ravera, L. Liggieri, and R. Miller, *Journal of colloid and interface science*, 2002, **252**(2), 433–442.

- [220] M. Leser, S. Acquistapace, A. Cagna, A. Makievski, and R. Miller, *Colloids and Surfaces A: Physicochemical and Engineering Aspects*, 2005, **261**(1-3), 25–28.
- [221] N. Tankovsky and N. Zografov, *Zeitschrift für Physikalische Chemie*, 2011, **225**(4), 405–411.
- [222] N. Zografov In *AIP Conference Proceedings*, Vol. 2075, p. 160016. AIP Publishing, 2019.
- [223] A. Andreeva and N. Zografov In *AIP Conference Proceedings*, Vol. 2075, p. 160015. AIP Publishing, 2019.
- [224] T. Reusch, D. Mai, M. Osterhoff, D. Khakhulin, M. Wulff, and T. Salditt, *Physical review letters*, 2013, **111**(26), 268101.
- [225] L. Mittelman, S. Levin, and R. Korenstein, *FEBS letters*, 1991, **293**(1-2), 207–210.
- [226] J. C. Neto, U. Agero, R. T. Gazzinelli, and O. N. Mesquita, *Biophysical journal*, 2006, **91**(3), 1108–1115.
- [227] H. Strey, M. Peterson, and E. Sackmann, *Biophysical Journal*, 1995, **69**(2), 478–488.
- [228] J. Pécréaux, H.-G. Döbereiner, J. Prost, J.-F. Joanny, and P. Bassereau, *The European Physical Journal E*, 2004, **13**(3), 277–290.
- [229] H.-G. Döbereiner, G. Gompper, C. K. Haluska, D. M. Kroll, P. G. Petrov, and K. A. Riske, *Physical review letters*, 2003, **91**(4), 048301.
- [230] K. Fricke, K. Wirthensohn, R. Laxhuber, and E. Sackmann, *European Biophysics Journal*, 1986, **14**(2), 67–81.
- [231] C. Monzel, D. Schmidt, C. Kleusch, D. Kirchenbüchler, U. Seifert, A.-S. Smith, K. Sengupta, and R. Merkel, *Nature communications*, 2015, **6**, 8162.
- [232] C. Monzel, D. Schmidt, U. Seifert, A.-S. Smith, R. Merkel, and K. Sengupta, *Soft matter*, 2016, **12**(21), 4755–4768.
- [233] T. Betz, M. Lenz, J.-F. Joanny, and C. Sykes, *Proceedings of the National Academy of Sciences*, 2009, **106**(36), 15320–15325.
- [234] T. Betz and C. Sykes, *Soft Matter*, 2012, **8**(19), 5317–5326.

- [235] L. Limozin and K. Sengupta, *ChemPhysChem*, 2009, **10**(16), 2752–2768.
- [236] C. Monzel, S. F. Fenz, R. Merkel, and K. Sengupta, *ChemPhysChem*, 2009, **10**(16), 2828–2838.
- [237] J. Rädler and E. Sackmann, *Journal de Physique II*, 1993, **3**(5), 727–748.
- [238] S. F. Fenz, R. Merkel, and K. Sengupta, *Langmuir*, 2008, **25**(2), 1074–1085.
- [239] C. Picart, K. Sengupta, J. Schilling, G. Maurstad, G. Ladam, A. R. Bausch, and E. Sackmann, *The Journal of Physical Chemistry B*, 2004, **108**(22), 7196–7205.
- [240] J. Schilling, K. Sengupta, S. Goennenwein, A. R. Bausch, and E. Sackmann, *Physical Review E*, 2004, **69**(2), 021901.
- [241] L. Limozin and K. Sengupta, *Biophysical journal*, 2007, **93**(9), 3300–3313.
- [242] K. Sengupta and L. Limozin, *Physical review letters*, 2010, **104**(8), 088101.
- [243] Y. Kaizuka and J. T. Groves, *Physical review letters*, 2006, **96**(11), 118101.
- [244] J. T. Groves, R. Parthasarathy, and M. B. Forstner, *Annual review of biomedical engineering*, 2008, **10**.
- [245] Y. Kaizuka and J. T. Groves, *Biophysical journal*, 2004, **86**(2), 905–912.
- [246] P. V. Ganesan and S. G. Boxer, *Proceedings of the National Academy of Sciences*, 2009, pp. pnas–0901770106.
- [247] C. M. Ajo-Franklin, C. Yoshina-Ishii, and S. G. Boxer, *Langmuir*, 2005, **21**(11), 4976–4983.
- [248] J. M. Crane, V. Kiessling, and L. K. Tamm, *Langmuir*, 2005, **21**(4), 1377–1388.
- [249] H. V. Pham, C. Edwards, L. L. Goddard, and G. Popescu, *Applied optics*, 2013, **52**(1), A97–A101.
- [250] G. Popescu, T. Ikeda, R. R. Dasari, and M. S. Feld, *Optics letters*, 2006, **31**(6), 775–777.
- [251] B. Bhaduri, H. Pham, M. Mir, and G. Popescu, *Optics letters*, 2012, **37**(6), 1094–1096.

- [252] Y. Park, C. A. Best, T. Auth, N. S. Gov, S. A. Safran, G. Popescu, S. Suresh, and M. S. Feld, *Proceedings of the National Academy of Sciences*, 2010, **107**(4), 1289–1294.
- [253] J. Zhao, J. Wu, and S. L. Veatch, *Biophys. J.*, 2013, **104**(4), 825–834.
- [254] M. C. Dos Santos, C. Vézy, and R. Jaffiol, *Biochimica et Biophysica Acta (BBA)-Biomembranes*, 2016, **1858**(6), 1244–1253.
- [255] M. Pieraccini, *Sci. World J.*, 2013, **2013**.
- [256] A. R. Thompson, J. M. Moran, G. W. Swenson, et al., *Interferometry and synthesis in radio astronomy*, Springer, 2017.
- [257] J. D. Monnier, *Reports on Progress in Physics*, 2003, **66**(5), 789.
- [258] J. Schmiedmayer, M. S. Chapman, C. R. Ekstrom, T. D. Hammond, D. A. Kokorowski, A. Lenef, R. A. Rubenstein, E. T. Smith, and D. E. Pritchard in *Atom Interferometry*; Elsevier, 1997; pp. 1–83.
- [259] J. D. Watson, F. H. Crick, et al., *Nature*, 1953, **171**(4356), 737–738.
- [260] D. D. Nolte, *Optical interferometry for biology and medicine*, Vol. 1, Springer Science & Business Media, 2011.
- [261] B. Abbott, R. Abbott, R. Adhikari, P. Ajith, B. Allen, G. Allen, R. Amin, S. Anderson, W. Anderson, M. Arain, et al., *Reports on Progress in Physics*, 2009, **72**(7), 076901.
- [262] B. P. Abbott, R. Abbott, T. Abbott, M. Abernathy, F. Acernese, K. Ackley, C. Adams, T. Adams, P. Addesso, R. Adhikari, et al., *Physical review letters*, 2016, **116**(6), 061102.
- [263] R. N. Bracewell and R. N. Bracewell, *The Fourier transform and its applications*, Vol. 31999, McGraw-Hill New York, 1986.
- [264] P. Welch, *IEEE Transactions on audio and electroacoustics*, 1967, **15**(2), 70–73.
- [265] M. Corti, M. Bonomo, and A. Raudino, *Langmuir*, 2012, **28**(14), 6060–6066.
- [266] T. Bellini, M. Corti, A. Gelmetti, and P. Lago, *EPL (Europhysics Letters)*, 1997, **38**(7), 521.
- [267] M. Corti, M. Pannuzzo, and A. Raudino, *Langmuir*, 2015, **31**(23), 6277–6281.

- [268] H.-J. Butt and M. Kappl, *Surface and interfacial forces*, John Wiley & Sons, 2018.
- [269] P. Schiller, S. Kruger, M. Wahab, and H.-J. Mögel, *Langmuir*, 2011, **27**(17), 10429–10437.
- [270] R. Hogg, T. W. Healy, and D. Fuerstenau, *Transactions of the Faraday Society*, 1966, **62**, 1638–1651.
- [271] L. R. White, *Journal of colloid and interface science*, 1983, **95**(1), 286–288.
- [272] A. E. Siegman, *Mill Valley, CA*, 1986, **37**, 208.
- [273] H. Kogelnik and T. Li, *Applied optics*, 1966, **5**(10), 1550–1567.